Titre: Title:	Esterification of Cellulose Via Ultrasound and Green Solvents
Auteur: Author:	Pierre Dal
Date:	2025
Type:	Mémoire ou thèse / Dissertation or Thesis
Référence: Citation:	Dal, P. (2025). Esterification of Cellulose Via Ultrasound and Green Solvents [Thèse de doctorat, Polytechnique Montréal]. PolyPublie. https://publications.polymtl.ca/68852/

URL de PolyPublie: PolyPublie URL:	https://publications.polymtl.ca/68852/
Directeurs de recherche: Advisors:	Daria Camilla Boffito, & Jean-Marie Raquez
Programme: Program:	Génie chimique

POLYTECHNIQUE MONTRÉAL

affiliée à l'Université de Montréal

Esterification of cellulose via ultrasound and green solvents

PIERRE DAL

Département de génie chimique

Thèse présentée en vue de l'obtention du diplôme de *Philosophiæ Doctor*

Génie chimique

Juillet 2025

POLYTECHNIQUE MONTRÉAL

affiliée à l'Université de Montréal

Cette thèse intitulée :

Esterification of cellulose via ultrasound and green solvents

présentée par **Pierre DAL**

en vue de l'obtention du diplôme de *Philosophiæ Doctor*

a été dûment acceptée par le jury d'examen constitué de :

Robert LEGROS, président

Daria Camilla BOFFITO, membre et directrice de recherche

Jean-Marie RAQUEZ, membre et codirecteur de recherche

Bianca VIGGIANO, membre

Kelly MEEK, membre externe

DEDICATION

To my family and friends for their support and motivation.
À ma famille et mes amis pour leurs soutien et motivation.

ACKNOWLEDGEMENTS

I owe my family the opportunity to have gone so far in my studies! My curiosity and passion for science undoubtedly come from my grandfathers.

Thank you to Gab for your patience, your good humor, and your unfailing support through my many moments of discouragement.

Daria, thank you for your initial project proposal, your trust, and your guidance. Jean-Marie, your good humor is motivating, and your Walloon wit has, in some way, reconnected me with my roots. Thank you for your help and for sharing your experiences.

Arthur, to our lunchtime meals together, our similar journeys, our mutual encouragement, and a friendship that will endure.

To my friends, it's important to be well surrounded and to enjoy quality moments that allow you to think about other things. To my teammates from the Carabins and Parco teams, without rugby, I'm not sure I would have finished this project.

Thank you so much, Martine, Anic, Claire, Gino, Yuan, Matthieu, and Wendell, for your support and help with reagents and equipment.

Thank you Cédric for your assistance and expertise with nuclear magnetic resonance analyses.

Thank you Owen, Askin, and your group, as well as Mark and Oscar for your wonderful welcome.

Finally, I thank the Trottier Energy Institute, Mitacs, and the Canada EPIC Research Chair for their financial support

RÉSUMÉ

La cellulose a de nombreuses applications dans les industries des pâtes et papiers, biochimique, cosmétique et agricole entre autres, ce qui génère une quantité significative de déchets cellulosiques, dont une partie est brûlée ou enfouie. Cependant, la valorisation de la cellulose pose plusieurs problèmes notamment dus à son important réseau de liaisons hydrogène, son caractère amphiphile et sa température de fusion élevée. Ces enjeux compromettent la dissolution de la cellulose ainsi que son traitement, puis les surmonter implique de prétraiter la cellulose, l'utilisation de quantités importantes d'énergie et peut dégrader les chaînes de cellulose. Le présent projet de recherche vise à convertir la cellulose en matériaux thermoplastiques via estérification, par un procédé plus efficace en énergie et en temps que les procédés conventionnels. Nous avons choisi une approche d'intensification des procédés : les ultrasons, et la cavitation acoustique générée, afin d'améliorer les transferts de masse et de chaleur, de diminuer la consommation énergétique et d'accélérer les réactions. La géométrie du réacteur, la fréquence des ultrasons et les propriétés thermodynamiques des solutions de cellulose affectent la cavitation acoustique au sein du réacteur, justifiant l'intérêt de modéliser l'activité des ultrasons. D'un autre côté, l'estérification de la cellulose produit des matériaux thermoplastiques utilisables comme films, grâce au greffage de longues chaînes d'acides gras qui agissent comme plastifiant. La présente thèse se divise en trois parties suivant des objectifs spécifiques et menant à la soumission de trois articles dans des journaux scientifiques.

La première partie traite de la modélisation et de la simulation d'un réacteur cylindrique comportant six transmetteurs d'ultrasons répartis sur les parois et un transmetteur d'ultrasons focalisés à haute intensité placé au bas du réacteur. La section hexagonale du réacteur permet aux ondes de générer des interférences constructives. Le transmetteur d'ultrasons focalisés émet les ondes dans une zone conique du réacteur qui concentre l'écoulement. Les bulles générées lors de la cavitation acoustique affectent la propagation des ondes, c'est pourquoi l'atténuation qu'elles engendrent est implémentée dans le modèle numérique. Les simulations montrent que les bulles de cavitation diminuent la pression acoustique de 80 % et la surface de la zone de cavitation de 85 %. L'espace entre le réflecteur et les transmetteurs latéraux a été fixé à 0.075 m, ainsi le logiciel a déterminé la propagation des ondes et l'activité acoustique dans des solutions de cellulose de concentration

variée et à diverses fréquences d'ultrasons. La plus faible concentration de cellulose étudiée a provoqué la pression acoustique la plus élevée et la zone de cavitation la plus étendue.

La deuxième partie montre l'estérification de cellulose assistée par ultrasons avec des acides gras comportant des longues chaînes. L'optimisation des conditions d'estérification conventionnelle (sans ultrasons) précède l'application d'ultrasons et utilise l'acide oléique et l'acide stéarique comme agents d'estérification. Le meilleur résultat est un degré de substitution de 1.44, obtenu avec l'acide oléique à un ratio molaire de 6 par rapport à la cellulose, à 80 °C pendant 24 h. L'application des ultrasons à 20 kHz et 4.39 W a diminué le temps de réaction à seulement 30 min, produisant des esters de cellulose ayant un degré de substitution de 0.38. Enfin, nous avons analysé les effets de la puissance ultrasonique, du volume réactionnel et des propriétés des solutions de cellulose sur la cavitation acoustique. Les simulations incluent la densité, la viscosité et la vitesse du son des solutions de cellulose, paramètres que nous avons mesurés nous-mêmes. Les simulations avec les conditions expérimentales menant au degré de substitution le plus élevé ont généré le plus faible volume de cavitation et les plus lents jets acoustiques.

La troisième partie a exploré l'estérification de cellulose assistée par ultrasons dans des liquides ioniques. Nous avons d'abord choisi le liquide ionique optimal par estérification conventionnelle, impliquant deux sources de cellulose, quatre liquides ioniques et deux agents d'estérification. Les estérifications conventionnelles à 80 °C pendant 24 h dans le chlorure et dans l'acétate de 1-butyl-3-methylimidazolium avec l'acide oléique et le chlorure de 4-toluènesulfonyle comme catalyseur ont montré les meilleurs résultats. Nous avons alors estérifié deux sources de cellulose dans ces deux liquides ioniques avec l'acide oléique et les ultrasons, auxquels nous avons ajouté le diméthylsulfoxyde comme co-solvant afin de diminuer la viscosité du mélange réactionnel. Les ultrasons durant 30 min à 102 W g^{-1} et 40 °C ont produit des esters avec un degré de substitution de 2.34. Nous avons même pu traiter 75 g L^{-1} de cellulose grâce au co-solvant et aux ultrasons. Les esters de cellulose produits sont moins cristallins que la cellulose non-modifiée, et la calorimétrie différentielle à balayage et la spectroscopie diélectrique ont prouvé la plastification de la cellulose grâce à l'acide oléique greffée.

ABSTRACT

Cellulose finds many applications in papermaking, biochemistry, cosmetics, agriculture, generating significant waste from which a part is burned or buried into landfills. That motivates sustainable valorization pathways of cellulose. However, cellulose valorization meets several challenges because of its hydrogen bond network, its amphiphilicity, and its high melting point. These issues hinder cellulose solubility and processability. Overcoming these issues typically requires a pre-treatment, a lot of energy and can degrade cellulose. This research project aimed to convert cellulose into thermoplastic material via esterification. We chose ultrasound, a process intensification strategy, and its acoustic cavitation activity to enhance heat and mass transfer, accelerate chemical reactions, and reduce energy consumption. The geometry of the reactor, the ultrasound frequency and the thermodynamic properties of the cellulose solutions affect the cavitational activity into the reactor. Esterification grafts long-chain fatty acids that internally plasticize cellulose, making materials suitable for flexible film applications for instance. The thesis includes three parts, meeting sub-objectives and resulting in the submission of three full-length research articles.

The first part examines the numerical modeling and simulation of a cylindrical sonoreactor with six lateral flat transducers along the walls and a concentric high-intensity focused ultrasound transducer at the bottom of the reactor. The hexagonal section reactor design ensures constructive sound waves interference. The high intensity focused ultrasound transducer focuses sound waves in the conic whistle part. Cavitation bubbles affect the propagation of acoustic waves, thus we included its attenuation in our model. It attenuated the acoustic pressure by 80 %, and the active cavitation surface area by 85 %. At a fixed gap of 0.075 m between the reflector and transducers, the software solved the propagation of sound waves and the cavitation surface area in the sonoreactor for various cellulose concentrations and working frequencies. The lowest cellulose esters concentration tested (6.25 g L^{-1}) resulted in the highest acoustic pressure and largest active cavitation surface area.

The second part focuses on the ultrasound-assisted esterification of cellulose with long-chain free fatty acids. Before conducting ultrasound (US)-assisted esterification, we optimized the esterification conditions using stearic acid and oleic acid as esterification agent under silent

conditions (no ultrasound). The best conditions were achieved with oleic acid, with an esterification agent/cellulose molar ratio of 6 and a temperature of 80°C for 24 h, producing esters with a degree of substitution of 1.44. The sonication at 20 kHz and 4.39 W, at room temperature, required 30 min to produce cellulose esters with a degree of substitution of 0.38. Then, we investigated by simulation the effects of the ultrasound input power, reaction volume and properties of cellulose solutions on the cavitation activity. Simulations incorporated the measured density, viscosity and speed of sound of the cellulose ester solutions. Simulations with conditions resulting in the highest degree of substitution with ultrasound revealed the smallest acoustic cavitation volume and the lowest acoustic streaming velocity.

The third part investigated ultrasound-assisted esterification of cellulose in ionic liquids. We first screened the optimal IL in conventional esterification for subsequent US-assisted esterification. The conventional esterification involved two cotton celluloses, four ionic liquids and two long chain free fatty acids. The conventional esterification at 80 °C for 24 h in 1-butyl-3-methylimidazolium chloride, and in 1-butyl-3-methylimidazolium acetate, with oleic acid and p-toluenesulfonyl chloride as a catalyst produced the most esters among conventional experiments. Then we explored the ultrasound-assisted esterification of two cotton celluloses in 1-butyl-3-methylimidazolium chloride and 1-butyl-3-methylimidazolium acetate using oleic acid. Dimethyl sulfoxide was added as co-solvent to reduce the viscosity of the reaction medium. Ultrasound at 102 W g^{-1} and 40 °C for 30 min in 1-butyl-3-methylimidazolium chloride and oleic acid produced cellulose esters with a degree of substitution of 2.34. The US-assisted esterification could treat cellulose at a concentration up to 75 g L^{-1}. Produced ester samples were less crystalline than unmodified cellulose, and differential scanning calorimetry and dielectric spectroscopy evidenced the oleic acid involvement in internal plasticization of cellulose.

TABLE OF CONTENTS

LIST OF TABLES

LIST OF FIGURES

LISTE OF SYMBOLS AND ABBREVIATIONS

Ac	Acetate anion
AGU	Anhydroglucose units
Amim	1-Allyl-3-methylimidazolium
ATR	Attenuated total reflectance
b	Radius of the cone in the whistle area
Bmim	1-Butyl-3-methylimidazolium
Bu	Dibutylamine
c	Speed of sound
C	Constant
CDI	N,N'-carbonyldiimidazole
CI	Confidence interval
Cl	Chloride anion
CPMAS	Cross polarization magic angle spinning
Cr	Crystallinity index
d	Damping factor
D	Thermal diffusivity of the gas
DMAc	N,N-dimethylacetamide
DMAP	N,N-dimethyl-4-aminopyridine
DMF	N,N-dimethylformamide
DMSO	Dimethyl sulfoxide
DOE	Design of experiments
DP	Degree of polymerization

DS	Degree of substitution
DSC	Differential scanning calorimetry
DSS	Sodium trimethylsilylpropanesulfonate
EA	Esterification agent
EDC	1-ethyl-3-(3-dimethylaminopropyl)carbodiimide hydrochloride
Emim	1-Ethyl-3-methylimidazolium
f	Ultrasound frequency
FFA	Free fatty acid
FTIR	Fourier transform infrared
h	Gap between the reflector and transducers
HCl	Hydrochloric acid
HIFU	High intensity focused ultrasound
HRMAS	High-resolution magic angle spinning
i	Imaginary unit
IL	Ionic liquid
k_m	Complex wave number
Li	Lithium cation
LiCl	Lithium chloride
M	Molecular weight of an oleoyl group
MCC	Microcrystalline cellulose
mTBNH	5/7-methyl-1,5,7-triazabicyclo [4.3.0]non-5-enium
m_0	Weight of unmodified cellulose
m_1	Weight of the ester's sample
NaOH	Sodium hydroxide

n_b	Number of bubbles per unit volume
NCC	Nanocrystalline cellulose
NMR	Nuclear magnetic resonance
n_0	Number of moles of unmodified cellulose
P	US power delivered to the liquid
PD	US power density
PEG	Polyethylene glycol
PI	Process intensification
p	Acoustic pressure
p_a	Pressure amplitude
p_c	Threshold pressure for cavitation
p_{HIFU}	HIFU transducer acoustic pressure
p_{LT}	Lateral transducer acoustic pressure
p_{max}	Maximum acoustic pressure
p_{min}	Minimum acoustic pressure
p_T	Total acoustic pressure
p-Tos	P-toluenesulfonyl chloride
p_v	Vapour pressure
p_0	Undisturbed pressure in the bubble position
RMSE	Root mean square error
R_{eq}	Bubbles equilibrium radius
R_0	Incipient radius of a bubble
S	Ultrasound transducer surface area
SH	Specific hypothesis

SI	Supplementary information
SO	Sub-objective
TAC	Triaminocyclopropenium
TBAF	Tetra-n-butylammonium fluoride
T_g	Glass transition temperature
TGA	Thermogravimetric analysis
T_m	Melting temperature
u	Acoustic streaming velocity
US	Ultrasound
v	Total reaction volume
V	Active cavitation zones volume
XRD	X-ray diffraction
Z	Acoustic impedance

Greek letters

α	Acoustic attenuation from the liquid
β	Volume of the gas fraction within the bubbles
ε''	Dielectric loss permittivity
γ	Specific heat ratio of the gas inside bubbles
μ	Viscosity
ρ	Density
σ	Surface tension of the liquid
τ	Relaxation time
Φ	Complex adimensional parameter

χ	Complex function
ω	Acoustic wave angular frequency
ω_0	Resonant angular frequency of bubbles

LIST OF APPENDICES

CHAPTER 1 INTRODUCTION

1.1 Background

Renewability and biocompatibility provide a wide market for cellulose, with applications in papermaking, textiles, agriculture, construction, biology, medicine and biochemistry. The global cellulose market is projected to reach 438 billion CAD in 2026 [1]. However, the abundant cellulose feedstock generates a significant amount of waste. For instance, the pulp and paper industries alone generated 23 million tons of cellulosic waste in the European Union in 2022 [2], of which 28 % was burned to produce energy or buried in landfills, and 61 % of wood waste followed the same fate [3]. In Canada, 3.6 million tons of paper fiber waste were generated in 2022, including newsprint, cardboard and mixed papers [4].

The conversion of cellulose waste into value-added products must overcome several significant challenges:

1 - Structure: Intermolecular and intramolecular hydrogen bonds in cellulose make it insoluble and difficult to process in water and most organic solvents [5].

2 - Amphiphilicity: Energy is required to the break hydrophobic bonds of cellulose, as it has both polar and nonpolar groups [6].

3 - Pretreatment and activation: Dissolution and derivatization of cellulose require pretreatment. These steps are expensive [7], time-intensive [8], and can degrade cellulose [9].

4 - Processability: Unmodified cellulose has a high melting point of 467 °C [10] and poor thermoplasticity, requiring a plasticizer for compounding into products [11].

Current methods to valorize cellulose waste into value-added products, such as cellulose esters, are energy-intensive, reagent-intensive, and toxic [12]. Therefore, process intensification (PI) emerges as a solution to the limitations mentioned above. PI aims to create smaller chemical plants, reduce costs, and lower energy and chemical consumption. The PI strategy improves process safety and energy efficiency with lower costs compared to conventional processes. Ultrasound (US) is a promising PI technology for the conversion of cellulose into cellulose esters. US enhances heat and mass transfer, accelerates chemical reactions, and reduces energy consumption. US as a PI strategy

helps achieve sustainable development goals by enabling more economically viable chemical processes.

1.2 Objectives

The main objective of this project is to valorize cellulose waste to produce value-added products as an alternative to petroleum-based thermoplastic materials.

Underlying assumption: US is a PI technology to convert cellulose waste and produce esters. PI is an innovative strategy that enhances the energy efficiency of chemical processes compared to those using catalysts, chlorinated solvents or inorganic acids and conventional heating processes, as the energy density per molecule of reagents is higher than in conventional processes. The US process has an energy consumption 55 % lower than conventional heating and mixing processes [13], and provides the opportunity to adjust the power delivered to the reaction medium. Moreover, US is an electricity-powered PI technology, with electricity produced in Québec being almost entirely renewable.

Hypothesis: US power density is adjusted to produce thermoplastic cellulose esters by grafting long-chain free fatty acids (FFAs) onto the hydroxyl groups of the cellulose backbone.

The project was divided into three sub-objectives (SOs), each related to a specific hypothesis (SH). Each SO resulted in the submission of a paper to a peer-reviewed scientific journal:

SO-1: Determine the total acoustic pressure and the volume of active cavitation zones for various geometrical parameters, US frequencies, and thermodynamic properties of cellulose ester solutions in a two-part multi-frequency sonoreactor. SH-1: The geometrical parameters of the sonoreactor, the US frequency and the thermodynamic properties of cellulose ester solutions influence the total acoustic pressure intensity and the volume of active cavitation zones.

1. Measurement of the density, viscosity and speed of sound of cellulose ester solutions at three different concentrations.
2. Modelling of a two-part multi-frequency sonoreactor with flat rectangular transducers and a high-intensity focused ultrasound transducer, including attenuation due to cavitation bubbles.
3. Validation of the model through a benchmarking approach.

4. Statistical analysis of the simulation results, screening of the most significant input variables influencing the response variables, and determination of equations to predict the total acoustic pressure and active cavitation zones volume as functions of input variables.

Chapter 3 presents the results of SO-1, reviewed and submitted to Ultrasonics Sonochemistry as a full-length article.

SO-2: Esterify cotton cellulose and cellulose waste under US to produce long-chain cellulose esters with degree of substitution (DS) comparable to that of long-chain cellulose esters produced from fatty acid chlorides, anhydrides, and vinyl esters. SH-2: US at 20 kHz in cellulose ester solutions generates cavitation bubbles and acoustic streaming, promoting heat and mass transfer.

1. Synthesis and purification of long-chain cellulose esters.
2. Characterization of the esters structure and thermal transitions via FTIR, XRD, and DSC analyses.
3. Determination of DS through gravimetric and ^{1}H NMR analyses.
4. Statistical analysis of DS results, screening of the most significant input variables influencing the response variables, and determination of equations to predict DS as function of input variables.
5. Measurement of the density, viscosity and speed of sound of cellulose ester solutions at a cellulose concentration of 25 g L^{-1}.
6. Simulation of the horn-type sonoreactor, including attenuation due to cavitation bubbles, to determine the effect of input variables on acoustic pressure, active cavitation zone volume and acoustic streaming velocity.

Chapter 4 presents the results of SO-2, submitted to Journal of Cleaner Production as a full-length article.

SO-3: Esterify cotton cellulose and cellulose waste under US to produce long-chain cellulose esters in ionic liquids (ILs) and dimethyl sulfoxide (DMSO). SH-3: ILs dissolve a higher amount of cellulose than traditional solvents, such as N,N-dimethylacetamide/lithium chloride (DMAc/LiCl).

ILs act as both a solvent and a catalyst for US-assisted esterification of cellulose. Additionally, ILs cavitate upon US irradiation.

1. Synthesis of triaminocyclopropenium salt.
2. Synthesis and purification of long-chain cellulose esters in ionic liquids.
3. Characterization of the esters structure and thermal transitions via FTIR, XRD and DSC analyses.
4. Determination of DS through gravimetric analysis.
5. Verification of thermoplastic behavior by film formation and dielectric spectroscopy analyses

Chapter 5 presents the results of SO-3, submitted to Carbohydrate Polymers as a full-length article.

1.3 Contributions

The project presented in this thesis advances the research on cellulose waste valorization and on ultrasound modelling and applications:

1. It presents a method to measure the speed of sound in cellulose solutions, and its implementation into simulations of a multi-frequency sonoreactor, showing evidence of the effects of the geometry and viscosity on the volume of active cavitation zones.
2. It presents a valorization process for cellulose esterification, with long-chain FFA acting as internal plasticizers, and in a reaction time eight times lower than in traditional heating and stirring processes.
3. It presents a valorization process for cellulose esterification, resulting in three times more cellulose treated than in traditional heating and stirring processes.

Forestry is an economic pillar of Canada. Cellulose-based products can replace a wide range of petroleum-based products with comparable properties. This project will contribute to:

Produce cellulose esters from cellulose waste and bio-derived fatty acids with properties comparable to those of petroleum-based materials. Minimize waste and pollution from cellulose combustion and landfill disposal. Advance the understanding of ultrasound esterification mechanisms, further supporting Canada’s development and research of process intensification technologies.

Throughout this doctoral project, I wrote three papers, one declaration of invention, and contributed to a literature review:

1. Dal, P., Schieppati, D., Kring, J., Boffito, D.C. (2024). Numerical simulation of a continuous sonoreactor for biomass residues recovery. Submitted to *Ultrasonics Sonochemistry*, available at SSRN 4981947.
2. Dal, P., Jean-Fulcrand, A., Lévêque, J.M., Raquez, J.M., Boffito, D.C. (2025). Ultrasound-assisted esterification of cotton cellulose with long chain free fatty acids. Submitted to *Cleaner Chemical Engineering*.
3. Dal, P., Curnow, O.J., Raquez, J.M., Boffito, D.C. (2025). Ultrasound-assisted esterification of cotton cellulose in ionic liquids. Submitted to *Carbohydrate Polymers*.
4. Dal, P., and Boffito, D.C., Continuous sonoreactor for lignin conversion. Report of invention DIV- 1013.
5. Schieppati, D., Patience, N.A., Galli, F., Dal, P., Seck, I., Patience, G.S., Fuoco, D., Banquy, X., Boffito, D.C. (2023). Chemical and biological delignification of biomass: a review. *Industrial & Engineering Chemistry Research*, 62(33), 12757-12794.

1.4 Coherence of the articles

CHAPTER 2 describes the cellulose origin and structure, its solubility and esterification, in both conventional solvents and ILs. It also explains US-assisted processes and esterification. This chapter helped identify the esterification agent, solvents, experimental conditions, and US parameters for CHAPTER 3, CHAPTER 4 and CHAPTER 5.

The first article (CHAPTER 3) presents the simulation of a model for a two-part multi-frequency sonoreactor with flat rectangular transducers and a high-intensity focused ultrasound transducer, including attenuation due to cavitation bubbles. It investigates the effects of various geometrical parameters, US frequencies, and thermodynamic properties of cellulose ester solutions on the total acoustic pressure and the volume of active cavitation zones. This modeling work provides the theoretical framework used in the subsequent CHAPTER 4.

CHAPTER 4 describes the esterification of cellulose in DMAc/LiCl with long-chain FFAs (potentially bio-derived) and introduces its intensification using US probe irradiation. It also demonstrates the implementation of the model presented in CHAPTER 3 to determine the total

acoustic pressure, the volume of active cavitation zones, and the acoustic streaming velocity, explaining the US effects on the reaction medium.

Since ILs dissolve more cellulose than DMAc/LiCl, and the US-assisted esterification of cellulose in ILs with long-chain FFA remains unexplored, CHAPTER 5 investigates this system. A cosolvent was introduced to minimize IL consumption. The same US setup as in CHAPTER 4 was used, ensuring comparability of results. This chapter thus extends the knowledge from conventional solvents (CHAPTER 4) to ILs, highlighting the advantages and challenges of each medium while building on both the simulation (CHAPTER 3) and the solvent-specific learning.

CHAPTER 6 presents a general discussion of the project, integrating the insights from simulation (CHAPTER 3), conventional solvent experimentation (CHAPTER 4), and IL experimentation (CHAPTER 5), and outlines limitations and future work.

CHAPTER 2 CRITICAL LITERATURE REVIEW

2.1 Cellulose

2.1.1 Cellulose origin

Cellulose is the most abundant natural polymer, with an annual production of $1.5 \cdot 10^{12}$ t [14]. It is the primary structural component of plant cell walls and occurs alongside hemicelluloses, lignin, and extractives or in a pure form. The cellulose content varies depending on the biomass source: it ranges from 40 wt% to 50 wt% in wood and straw, 70 wt% to 80 wt% in flax, and more than 90 wt% in cotton, which is almost pure cellulose. Other sources of cellulose include fungi, algae, and tunicates. Additionally, some bacteria synthesize bacterial cellulose from glucose, producing it in a pure, fibrous network form [5].

2.1.2 Cellulose structure

Cellulose is a homopolymer of D-anhydroglucose units (AGU) in the $^4C_1$ chair conformation (regardless of the source), which corresponds to the lowest energy state [15]. An acetal function between carbon 1 and carbon 4 covalently bonds AGUs through β-1,4-glycosidic linkages (Figure 2.1). Each AGU has three hydroxyl groups: a primary hydroxyl at carbon 6 and two secondary hydroxyls at carbons 2 and 3 [5], which together account for 31 % of the cellulose weight [16]. To maintain structural equilibrium, every second AGU rotates 180° in the plane, forming cellobiose, which is considered the repeating unit of cellulose (Figure 2.1) [14].

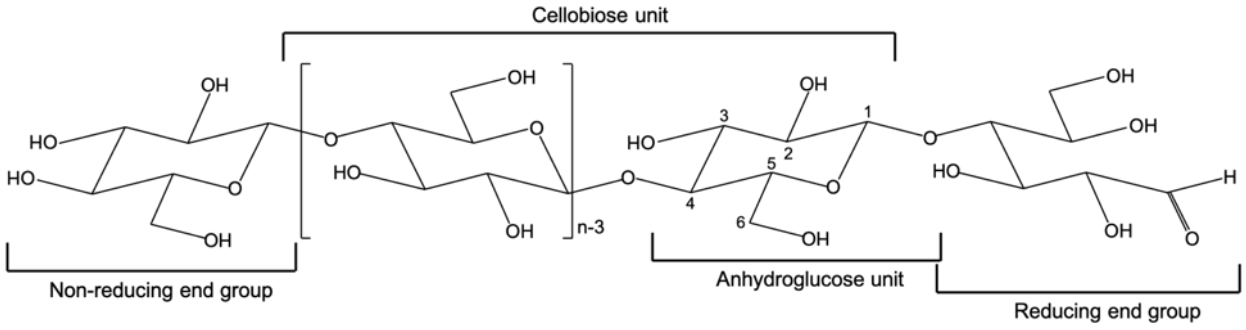

Figure 2.1 Structure of cellulose (n denotes the degree of polymerization).

The two ends of the cellulose chain are distinct: one end features an AGU with a hydroxyl group at carbon 4 (non-reducing end), while the other has a hydroxyl group at carbon 1 in equilibrium with an aldehyde group (reducing end). Bleached wood pulp can contain additional carboxyl and carbonyl groups due to its production process, which affects cellulose reactivity [14]. The degree of polymerization (DP) of cellulose, defined as the number of AGUs in the chain, varies depending on the cellulose source and its treatment. Native and bacterial cellulose, as well as cotton, have a DP ranging from 800 to 10000, while extracted wood pulp typically ranges from 300 to 1700, and microcrystalline cellulose (obtained by acid treatment) has a DP ranging from 150 to 300 [14].

Cellulose has a strong hydrogen bonding network, which influences its solubility, hydrophobicity, hydrophilicity, and crystallinity. Hydroxyl groups and oxygen atoms in AGUs, along with glycosidic bonds, participate in intramolecular and intermolecular hydrogen bonding, creating a three-dimensional structure [5]. Intramolecular hydrogen bonds occur between the hydroxyl group at carbon 3 and the oxygen of the ether link in the adjacent AGU. They also occur between the oxygen of the hydroxyl group at carbon 6 and the hydroxyl group at carbon 2 in a neighboring AGU [17], [18], [19]. These bonds have a dissociation energy of approximately 25 kJ mol^{-1} and contribute to cellulose's rigidity, stiffness, high viscosity in solution, crystallinity, and fibrillar structure [20]. Intermolecular hydrogen bonds form between the oxygen of the hydroxyl group at carbon 3 and the hydroxyl group at carbon 6 of another cellulose chain [21]. These bonds, along with hydrophobic interactions, organize cellulose into layered structures [22].

Cellulose is an amphiphilic polymer, meaning it contains both polar and non-polar groups. The three hydroxyl groups of AGUs are positioned equatorially, forming the hydrophilic regions of cellulose. Conversely, the axial orientation of hydrogen atoms in C-H bonds creates a hydrophobic face. In aqueous environments, these hydrophobic regions tend to aggregate, reducing solubility. The geometric arrangement of polar and non-polar groups plays a crucial role in cellulose solubility [6].

2.1.3 Microcrystalline cellulose

Native cellulose is semi-crystalline, consisting of highly ordered crystalline zones interspersed with amorphous regions containing entangled fibrils. The crystallinity of extracted cellulose ranges from 40 % to 60 %, depending on the treatment method and biomass source [14]. Various processes convert cellulose into microcellulose and nanocellulose, which differ in their DP and crystallinity.

Microcrystalline cellulose (MCC) is produced through alkaline pretreatment with aqueous sodium hydroxide (NaOH), followed by acid hydrolysis, yielding a white powder. During hydrolysis, the DP of cellulose decreases to 150–300 [14]. During hydrolysis, hydronium ions preferentially attack amorphous regions, which are less dense than crystalline regions. This cleaves glycosidic bonds, releasing intact crystalline zones. These crystalline fragments, which are water-insoluble, can rearrange into rod-like structures that are larger than the original microfibrils, with dimensions of approximately 50 μm in diameter and 100 μm to 1 000 μm in length [23], [24]. When MCC is treated with sulfuric acid, sulfate groups are grafted onto the cellulose microfibrils, imparting negative electrostatic charges. This surface modification, combined with mechanical stirring, prevents aggregation, leading to the formation of a in water [5], [23]. In contrast, hydrochloric acid hydrolysis produces MCC without electrostatic charges. As a result, MCC prepared using hydrochloric acid is unstable in suspension, though it exhibits thixotropic behavior at concentrations above 5 wt% and antithixotropic behavior at concentrations below 0.3 wt% [5].

2.1.4 Nanocellulose

The properties of nanocrystalline cellulose (NCC) depend on the cellulose source and processing conditions. NCC production begins with the pretreatment and refinement of biomass, followed by acid hydrolysis, which conventionally converts cellulose into NCC. The hydrolysis method significantly affects NCC stability. Sulfuric acid hydrolysis introduces negative surface charges, enhancing electrostatic repulsion, which makes the NCC more stable in suspension compared to NCC produced using hydrochloric acid [25]. Compared to MCC, NCC contains fewer amorphous regions [26]. NCC typically has a diameter of 5 nm to 20 nm and a length ranging from 100 nm to several micrometers [27].

NCC exhibits remarkable mechanical properties, with an elastic modulus of approximately 150 GPa and a tensile strength of around 7 GPa [28]. In composite materials, NCC reinforces mechanical properties by forming a rigid nanocrystalline network [29]. NCC can be dispersed in polar organic solvents such as DMSO and N,N-dimethylformamide (DMF). Dispersions and films obtained from these solvents exhibit birefringence, a property that can be exploited in optical and functional material applications [30].

2.2 Cellulose solubility

Solubility parameters, such as the Hildebrand and Hansen parameters, are valuable tools for assessing the solubility of polymers in different solvents. According to Mäki-Arvela et al., if the Hildebrand solubility parameter of a solute is close to that of the solvent, the dissolution ability is generally high. However, the Hildebrand parameter considers only molecular dispersion forces and is unavailable for cellulose [31]. In contrast, the Hansen solubility parameter accounts for London dispersion forces, dipole-dipole interactions, and hydrogen bonding interactions, providing a more comprehensive description of solubility behavior. Nevertheless, Hansen and Björkman stated that solubility parameters alone cannot fully explain the interactions between solvents and cellulose [32].

2.2.1 Mechanisms of dissolution

Water and most organic solvents do not dissolve cellulose. While water dissolves glucose, the monomeric unit of cellulose, non-polar solvents do not, due to cellulose's polar nature, its hydroxyl groups, and its ability to form hydrogen bonds. The insolubility of cellulose in water is more complex. The scientific community generally agrees that this is due to intramolecular and intermolecular hydrogen bonding, although Lindman et al. suggest additional interactions are involved [6], [33]. The entropy of mixing is the driving force behind dissolution. For a substance to dissolve, the free energy change must be negative, which is the sum of the enthalpy and entropy contributions. Low molecular weight compounds dissolve more easily than polymers because they have a higher number of individual molecules for the same mass, leading to greater entropy gain and thus a negative free energy change. Flexible polymers dissolve more easily than stiff polymers, as they gain conformational freedom in solution, unlike rigid polymers such as cellulose. Cellulose is relatively stiff and contains both hydrophilic and hydrophobic regions. In aqueous environments, cellulose adjusts its conformation to minimize contact between its hydrophobic regions and water, further hindering dissolution. Additionally, cellulose contains crystalline regions, which further decrease solubility. Crystalline zones have lower energy than amorphous zones, making them more resistant to dissolution. However, Thomas Heinze argued that there is no major difference in the solubility of amorphous and crystalline cellulose [6].

Many studies focus on hydrogen bonding as the primary reason for cellulose's insolubility in water. However, solubility is governed by a balance of multiple interactions, including hydrogen bonds,

Van der Waals forces, and hydrophobic interactions. In aqueous systems, there are interactions not only between cellulose and water but also between cellulose-cellulose and water-water molecules. Hydrogen bonds alone cannot explain cellulose's insolubility, as water can form additional hydrogen bonds with cellulose, which should theoretically promote dissolution. Polyelectrolytes are generally more soluble than non-ionic polymers due to counterion entropy effects. Charging cellulose increases its solubility, explaining why cellulose is more soluble in water at extreme pH values. The amphiphilic nature of cellulose also affects its solubility. In water, its hydrophobic regions tend to aggregate, reducing solubility. Lindman et al. proposed that amphiphilic solvents such as ILs and N-methylmorpholine N-oxide, as well as cosolutes like urea and polyethylene glycol, can disrupt hydrophobic interactions, thus enhancing dissolution [6].

The literature highlights the role of chloride anions in disrupting hydrogen bonds to promote cellulose dissolution. Polar-electrostatic interactions between IL ions and cellulose hydroxyl groups drive the dissolution process. For instance, in DMAc/LiCl, dissolution occurs via chloride anions (Cl) forming hydrogen bonds with the hydroxyl protons of cellulose. Lithium cations (Li) interact with DMAc and cellulose hydroxyl oxygens, forming an intermediate complex (Li - DMAc - cellulose). Cls accumulate around cellulose chains, imparting a negative charge, while Li - DMAc acts as the counterion. Electrostatic repulsion between negatively charged cellulose chains prevents aggregation. Then, osmotic pressure drives the solvent into the cellulose structure, reducing intermolecular forces and dissolving cellulose [34]. A similar polyelectrolyte effect occurs in DMSO and tetra-n-butylammonium fluoride (TBAF), where fluoride anions impart negative charges on cellulose chains, leading to electrostatic repulsion and increased solubility [35]. Other anions besides Cl also dissolve cellulose, such as in 1-ethyl-3-methyl-imidazolium acetate ([Emim][Ac]). Effective cations for cellulose dissolution are often amphiphilic and contain nitrogen or phosphorus atoms [6].

2.2.2 Solubility in aqueous system

Aqueous solvents for cellulose consist of solutions containing inorganic salts and complex compounds. Cellulose with a DP of up to 200 is soluble in a 10 wt% NaOH aqueous solution [36]. Sobue et al. claimed that aqueous NaOH at a concentration of 7 wt% to 10 wt% dissolves cellulose when cooled below -5 °C [37]. According to Liebert, aqueous NaOH dissolves cellulose only when it has low crystallinity and a low DP [38]. Isogai and Atalla described the dissolution of MCC in

water and NaOH. Their optimal procedure involved completely freezing a mixture of 1 g of cellulose in 26.9 mL of an 8.5 wt% NaOH aqueous solution at -20 °C. Upon defrosting the solid at room temperature, it formed a gel. By adding water and shaking the mixture, they obtained a clear cellulose solution containing 2 wt% cellulose and 5 wt% NaOH. When they placed microcrystalline cellulose in an 8 wt % to 15 wt% NaOH solution at 4 °C, it gelled but did not dissolve. This demonstrated that complete freezing of the cellulose mixture is crucial for dissolution to occur, along with the concentration of NaOH from 5 wt% to 7 wt%. They explained that water crystallization within the cellulose fibers disrupts intermolecular bonds, facilitating dissolution. Heating the aqueous solution of cellulose and 5 wt% NaOH caused cellulose to precipitate around 40 °C. This precipitate was no longer soluble in 5 wt% NaOH. Conversely, increasing the NaOH concentration up to14 wt% at a constant temperature led to cellulose precipitation. Adding water to this suspension redissolved the cellulose at NaOH concentrations between 5 wt% and 9 wt%. The researchers tested cellulose from various sources and concluded that aqueous NaOH completely dissolves cellulose with a DP below 200. Cellulose with a higher DP did not dissolve completely unless first regenerated in a SO_2-diethylamine-DMSO system. They also observed that lignin in the samples reduced cellulose solubility in aqueous NaOH, whereas hemicelluloses, which are soluble in NaOH, did not [39].

An aqueous solution of polyethylene glycol (PEG) and NaOH dissolved cellulose with a DP of approximately 800 at concentrations of up to 13 wt%. The solution contained 1 wt% PEG and 9 wt% NaOH [40]. An aqueous mixture of 7 wt% NaOH and 12 wt% urea dissolved cellulose within 2 min at -12 °C [41]. Molten inorganic salt hydrates, such as LiCl and $ZnCl_2$, can dissolve cellulose with a DP of up to 1500 [36].

2.2.3 Solubility in non-aqueous system

Kadokawa et al. also stated that cellulose is not soluble in polar solvents such as water, DMSO, or DMF [42]. However, non-aqueous solvents like DMSO, DMF, and DMAc, when mixed with another reagent, such as LiCl, can dissolve cellulose, even with a “relatively” high molecular weight, without causing degradation. For instance, a mixture of 1,3-dimethyl-2-imidazolidinone and LiCl dissolved cellulose with a DP of 1200 at concentrations ranging from 2 wt% to 10 wt% [36]. Chrapava et al. treated beech sulfite pulp with a DP of 1790 using the DMAc/LiCl system. They found that DMAc/LiCl at 5 °C dissolved higher amounts of cellulose than at 25 °C: 8 wt%

cellulose compared to 6 wt%, in a DMAc solution with 8 wt% LiCl. However, at 25 °C, only 3 wt% LiCl in DMAc was sufficient to dissolve cellulose, whereas at 5 °C, 4 wt% LiCl in DMAc was required. They also observed that above 3 wt% cellulose in DMAc/LiCl, the solution formed a gel, making viscosity measurements impossible [43]. These concentrations remain lower than those achieved by McCormick et al., who dissolved cellulose with a DP ranging from 772 to 4321. They reached cellulose concentrations of up to 15 wt% in 9 wt% LiCl in DMAc. Their process involved dissolving LiCl in DMAc at 100 °C, then heating the solvent and cellulose at 150 °C before cooling the mixture to room temperature. Cellulose dissolution took 1 h for concentrations ranging from 1 wt% to 5 wt%, and 24 h to 48 h for concentrations ranging from 6 wt% to 15 wt% [44]. DMSO and TBAF dissolved 2.5 wt% cellulose with a DP of 950 within 15 min at room temperature, without any pretreatment [45]. It also dissolved bleached cotton fibers within 1 min at 35 °C [46]. The voluminous cation in this system prevents molecules from reattaching. Additionally, the fluoride anion is more basic than Cl (as in the DMAc/LiCl system). The ratio of fluoride anions to AGUs in the DMSO/TBAF system depends on the DP of cellulose: a ratio of 1 is suitable for MCC with a DP of 332, whereas a ratio of 3 is suitable for cotton fibers with a DP of 1198 [5].

2.3 Cellulose esterification

The condensation of a carboxylic acid and an alcohol forms an ester. Since water is a by-product of esterification, most esterification reactions require non-aqueous medium, to prevent the equilibrium from shifting toward the reactants, which would limit the conversion [47]. Cellulose esterification takes place either along the cellulose chain, or on the outer surface of cellulose fibers leaving the crystalline structure intact [8]. Cellulose esters can be either organic or inorganic. Cellulose nitrates are the oldest cellulose esters, synthetized with a mixture of nitric acid and sulfuric acid. This heterogeneous reaction produced esters with a DS ranging from 1.8 to 2.8, with 2.9 being the upper limit due to side reactions between cellulose and sulfuric acid [48]. Homogeneous reaction of phosphoric acid with substituted cellulose produced cellulose phosphate. However, phosphoric acid has lower reactivity than sulfuric acid, leading to cellulose chain degradation. Additionally, cellulose phosphates tend to crosslink, affecting the solubility of the resulting esters [49].

Organic cellulose esters require a carboxylic acid as the esterification agent (EA) in an acid-catalyzed medium. Due to their low reactivity, carboxylic acids alone cannot esterify cellulose; therefore, the reaction typically involves an acid anhydride or an acid chloride as the EA [8]. The most common organic cellulose ester is cellulose acetate, produced using acetic acid and acetic anhydride as EAs, with sulfuric acid as a catalyst. Since acidic EAs and catalysts degrade the cellulose chain, a basic reaction medium with a catalyst such as pyridine is preferred. For the grafting of FFA, acid anhydrides are not reactive enough, so esterification requires acid chlorides as EAs along with a base like pyridine as both solvent and catalyst [49]. Willberg-Keyriläinen and Ropponen esterified cellulose using four different EAs (to graft long aliphatic chains of 8, 12, or 16 carbons) in DMAc/LiCl: acid chloride, acid anhydride, vinyl ester, and FFA [12]. For reactions with acid chloride and acid anhydride, pyridine was added to the cellulose solution along with the chloride or anhydride, and the mixture was heated at 80 °C for 16 h. When using vinyl esters, the EA was added to the cellulose solution and heated at 50 °C for 1 h. In the case of FFA, activation with N,N'-carbonyldiimidazole (CDI) at 60 °C for 3 h was necessary before adding it to the cellulose solution and heating at 80 °C for 16 h. The highest DS (1.3) was obtained with octanoyl chloride. However, acid chlorides generate hydrochloric acid (HCl), which is corrosive and leads to the degradation of both cellulose and the resulting esters. Anhydrides produced cellulose esters with a lower DS in DMAc/LiCl, with octanoic anhydride, reaching a DS of only 0.5. The vinyl ester pathway required the removal of vinyl alcohol by-products. FFAs did not degrade cellulose chains but required activation agents, such as CDI or p-toluenesulfonyl chloride (p-Tos), to increase their reactivity [12], [50]. Zheng et al. esterified cellulose (DP of 630) in DMAc/LiCl using 3-(hydroxyphenylphosphinyl)-propanoic acid as the EA, activated with p-Tos. This homogeneous reaction was conducted at 40 °C for 24 h, yielding esters with a DS of 1.42 [51].

Almasi et al. esterified cellulose nanofibers in pyridine using oleic acid as the EA and p-Tos as the activating agent. The reaction was carried out at 50 °C for 4 h, producing cellulose esters with a DS of 1.82 and a water contact angle of 80°. They observed that increasing the amount of oleic acid decreased the DS, which they attributed to an increase in reaction viscosity and a decrease in miscibility between the oleic acid and cellulose phases [52]. Duchatel-Crépy et al. treated MCC (DP of 150) in DMAc/LiCl and N,N-dimethyl-4-aminopyridine (DMAP) at 80 °C until dissolution. They then added an acid chloride (with chain lengths from 10 to 16 carbons) as the EA and continued heating at 80 °C for 3 h. They reported that DMAP reacted with the HCl produced during

esterification, preventing cellulose hydrolysis. The resulting products were cast into films in chloroform, and they attributed their thermoplastic behavior to the fatty acid chloride chains acting as internal plasticizers [53]. They obtained esters with DS values ranging from 1.7 to 3, which exhibited thermoplastic properties as their DS exceeded 1.5 [54]. All films were hydrophobic (contact angles above 90°), with hydrophobicity increasing with chain length: the contact angle was 97° for esters with 10-carbon chains and 107° for those with 16-carbon chains, both having a DS of 3. Contact angle also increased with DS for esters derived from the same acid chloride, while mechanical properties remained similar [53]. Kulomaa et al. esterified wood pulp in pyridine using FFAs (a mixture of oleic, linoleic, linolenic, and pinolenic acids) modified into acid chlorides. The mixture was heated at 100 °C for 3 h, producing long-chain cellulose esters with a maximum DS of 2.86. These esters were cast into films in chloroform, which exhibited oxygen permeability and relative impermeability to water vapor [55]. The water vapor permeability decreased as the FFA chain length increased [56].

2.4 Ionic liquids

2.4.1 Ionic liquids for cellulose dissolution

Ionic liquids (ILs) are salts composed of ions which have a melting point below 100 °C. They exhibit several notable properties, including low vapor pressure and ionic conductivity [57]. ILs are considered green solvents due to their non-flammability, high thermal stability, and the absence of volatile organic compound emissions [57], [58]. Their properties can be easily tuned by modifying their ionic components, allowing control over parameters such as hydrophobicity, hydrophilicity, viscosity, and melting point [58].

Since ILs are liquid at room temperature, they undergo cavitation when exposed to ultrasound, making them promising alternative solvents for process intensification. In 2002, Swatloski et al. reported that 1-butyl-3-methylimidazolium chloride ([Bmim]Cl) could dissolve cellulose at concentrations up to 25 wt% [59]. Wang et al. suggested that the cellulose-dissolving ability of ILs increases with the hydrogen bond basicity of the anion, as higher basicity enhances polarity. Indeed, cellulose dissolution occurs via hydrogen bonding between the hydroxyl protons of cellulose and the IL anions [60]. Heinze et al. observed the formation of a covalent bond between the carbon at the reducing end of cellulose and the imidazolium cation [61]. Thus, the role of the cation is to solvate and disperse the hydrogen-bonded cellulose-anion complexes [60]. The anion-

to-hydroxyl group ratio is another important parameter in cellulose solubility, as an excess of anions is required, with a ratio ranging from 1.5 to 2.5 [62]. Xu et al. investigated ILs containing the [Bmim] cation and various anions. They found that cellulose solubility increased linearly with the hydrogen bond accepting ability of the anions. Specifically, they dissolved 15.5 wt% of MCC at 70 °C with Ac, 13.5 wt% with $HSCH_2COO^-$, and 12.5 wt% with $HCOO^-$ [62]. The ILs [Emim][Ac] and 1-butyl-3-methylimidazolium acetate ([Bmim][Ac]) dissolved 28 wt% of Avicel cellulose at 110 °C and MCC at 70 °C, respectively [63].

Cations also influence cellulose dissolution. Imidazolium, pyridinium, ammonium, and phosphonium cations, when paired with highly basic hydrogen bond-accepting anions, facilitate dissolution [60]. Imidazolium and pyridinium cations appear to be the most effective, likely due to their aromatic nature, which enhances their polarizability [64] and reduces their electrostatic interaction with anions [65], thereby allowing stronger hydrogen bonding between anions and cellulose. Swatloski et al. demonstrated that increasing the alkyl chain length of the cation reduces cellulose solubility: they dissolved 10 wt%, 5 wt%, and 0 wt% of cellulose pulp at 100 °C in [Bmim]Cl, 1-hexyl-3-methylimidazolium chloride, and 1-octyl-3-methylimidazolium chloride, respectively [59]. Alkoxy and alkoxyalkyl substituents on the imidazolium cation negatively impact cellulose dissolution due to their bulkiness and the presence of oxygen atoms, which interfere with hydrogen bonding between anions and cellulose hydroxyl groups [63]. Some cations may solvate cellulose chains without directly participating in dissolution. The effect of hydroxyl end groups on cations remains debated. While some studies suggest that hydroxyl groups compete with cellulose for hydrogen bonding with anions, thereby decreasing solubility [60], Feng and Chen proposed that hydroxyl groups on cations form hydrogen bonds with cellulose hydroxyl groups, ultimately enhancing solubility [66]. This contradicts earlier findings and is counterintuitive, given that IL anions typically exhibit greater hydrogen bond accepting ability than cellulose hydroxyl groups.

2.4.2 Ionic liquids for cellulose esterification

The synthesis of cellulose esters with a high DS in ILs is challenging. Heinze et al. synthesized cellulose propionate and butyrate in [Bmim]Cl, achieving DS values of 0.9 and 0.4, respectively [61]. Luan et al. enhanced the esterification of MCC (DP of 200) using DMAP as a catalyst in 1-allyl-3-methylimidazolium chloride ([Amim]Cl). Their process, conducted at 30 °C for 30 min

with acid anhydrides as EAs, produced cellulose propionate and butyrate with DS values ranging from 0.9 to 2.9 [67]. Granström et al. esterified MCC in [Amim]Cl using stearic acid, with triethylamine as a catalyst and 1-ethyl-3-(3-dimethylaminopropyl)carbodiimide hydrochloride (EDC) as an activating agent. The reaction, carried out at 60 °C for 24 h, yielded esters with a DS of 0.16. They attributed the low DS to side reactions between the FFA and EDC, which formed stearyl isourea. Stearyl isourea reacted with cellulose but subsequently decomposed into stearyl urea, which was no longer an active EA [68]. Suzuki et al. esterified bagasse in a solvent mixture of [Emim][Ac] and DMSO using vinyl esters as EAs at 80 °C for 30 min. They achieved a DS of 2.7 for long-chain acyl groups. They measured a decrease in tensile strength by 93 % with increasing vinyl ester chain length from six carbons to eighteen carbons [69]. Similarly, the esterification of cellulose (DP of 1072) in [Emim][Ac] with vinyl laurate at 80 °C for 4 h produced esters with a DS of 2.3 [70]. Milotskyi et al. synthesized cellulose laurate from MCC (DP of 86) in [Emim][Ac] with vinyl laurate at 120 °C for 10 min, obtaining thermoplastics with a DS of 2.7. When they added DMSO to the solvent system, they increased the DS to 2.9. They demonstrated that the melt viscosity of cellulose esters depends on the DS: an ester with a DS of 2.73 had a melt viscosity of 0.27 kPa s, while esters with a DS of 1.35 exhibited melt viscosities between 0.94 and 1.12 kPa s [71], [72]. Tarasova et al. esterified various sources of cellulose in the same solvents and EA system, obtained DS ranging from 2.1 to 3.0 and verified the thermoplastic behavior by rheological tests [73]. Lease et al. treated MCC in [Bmim][Ac] using a magnetic mortar at 50 °C, 80 °C, and 110 °C for 4 h, 12 h, and 24 h. They added oleic acid and p-Tos, producing esters with a DS of 0.21 without disrupting the crystalline structure of cellulose. They attributed the low DS to surface modification only, as their process did not alter the internal structure of cellulose [74]. They further observed that DS increased with reaction temperature and duration, peaking at 12 h before slightly decreasing [75]. They explained this decrease as resulting from competition between esterification and hydrolysis, as water—a byproduct of esterification—facilitates ester hydrolysis over extended reaction times [74].

2.5 Ultrasound

Ultrasound (US) refers to mechanical sound waves with frequencies above the audible threshold of 20 kHz [76]. A piezoelectric, electrostrictive, or magnetostrictive transducer transmits mechanical vibrations to a fluid, generating successive acoustic cycles of compression and rarefaction. During compression, positive pressure pushes liquid molecules together, while

rarefaction applies negative pressure, pulling molecules apart. If the pressure amplitude in the rarefaction phase exceeds the tensile strength of the liquid, cavitation bubbles containing vapor form. Generally, pure liquids have a high tensile strength, preventing cavitation [77]. However, liquids contain impurities, particles, and bubbles that lower their tensile strength, promoting cavitation. Two types of cavitation phenomena can occur after bubble formation [76], [77]. Stable cavitation occurs at low acoustic intensity. Bubbles sizes oscillate in phase with the compression and rarefaction cycles, growing slowly over multiple cycles. Due to the minimal variation in bubble size, stable cavitation has no significant chemical effects. Transient cavitation occurs at high acoustic intensity. Bubbles grow rapidly and become unstable after a few cycles, collapsing violently during the compression phase. The bubble size may increase dozens or even hundreds of times its equilibrium radius before collapsing in less than a microsecond. US induces both physical and chemical effects. The collapse of cavitation bubbles generates microjets and localized hotspots with temperatures up to 5000 °C and pressures up to 500 atm [77]. Due to its high reaction rates, US is widely applied in esterification [47], transesterification [78], emulsification [79], and other chemical processes. The energy delivered by US can be tuned to selectively cleave specific bonds [76], [77].

2.5.1 US-assisted esterification

US enhances esterification and transesterification by reducing reaction time by 50 % to 80 %, lowering reaction temperatures, and decreasing solvent and catalyst consumption [80], [81]. Several studies have demonstrated the benefits of US for FFA esterification into biodiesel. In FFA esterification, mass transfer is often limited by the solubility of FFA in alcohol, which limits the reaction rate. Boffito et al. enhanced mass transfer in FFA esterification below 40 °C using a Rosette cell reactor, which combines acoustic and hydrodynamic cavitation. The Rosette cell transesterified 90 % of the feedstock in just 5 min, a 93 % time saving compared to the conventional process [82]. A setup composed of dual-frequency US transducers operating at 25 kHz and 40 kHz and at an US input power of 96 W esterified wheat starch with acetic anhydride for 5 min, producing esters with a DS 34 % and 12 % higher than reactions at 40 kHz and 25 kHz alone, respectively [83]. This enhancement was attributed to cavitation bubbles damaging the surface of starch granules, creating fractures and cracks that increased surface area and facilitated reagent penetration [84].

Few studies have explored the dissolution and esterification of cellulose under US. Extended sonication of polymers cleaves macromolecular linkages, reducing solution viscosity and narrowing molecular weight distribution [85]. The extent of bond cleavage depends on the energy input; only the weakest bonds break under moderate conditions. When the reaction medium contains insufficient dissolved gas, transient cavitation bubbles form, and depolymerization occurs if the US intensity exceeds the cavitation threshold [76]. For example, high-frequency US (525 kHz) selectively depolymerized MCC into glucose at 60 °C in water, where ultrasonic irradiation dissociated water molecules into hydrogen and hydroxyl radicals inside cavitation bubbles [86]. The resulting hydrogen radicals cleaved the glycosidic bonds of cellulose. Bhaumik and Dhepe proposed a mechanism similar to acid hydrolysis, where the anomeric or endocyclic oxygen of the non-reducing glucopyranose unit undergoes protonation [87]. US treatment of cellulose in [Bmim]Cl for 20 min at an US power of 30 W reduced the dissolution time by 68 % compared to conventional methods, though the regenerated cellulose had a DP 28% lower than cellulose dissolved without US [88]. Additionally, US simultaneously degraded and esterified cellulose pulp into NCC. US irradiation at 40 kHz for 0 h to 6 h at 68 °C to 75 °C increased product yield by 77 % and DS by 110 % compared to esterification without US [89]. The authors attributed this effect to US degrading the amorphous regions of cellulose, thereby increasing reagent accessibility to the internal cellulose structure. This phenomenon was linked to the energy imparted by acoustic cavitation, which ranges from 10 kJ mol^{-1} to 100 kJ mol^{-1} comparable to the dissociation energy of hydrogen bonds [77]. Mikkola et al. reported the decrease in dissolution time of 5 wt% MCC in [Amim]Cl from 1 h, under conventional stirring, to 5 min under US [90].

US pretreatment of sugarcane bagasse in pyridine at 30 °C and 40 kHz for 50 min decreased esters yield by 15 % compared to untreated biomass, which they attributed to molecular weight reduction [91]. Ma et al. esterified cellulose with glutaric anhydride in [Bmim]Cl at 85 °C with 40 kHz US irradiation. Increasing the US treatment time from 20 min to 120 min increased the DS by 82 %, although they did not report the DS of untreated samples [92]. In a separate study, the same group esterified cellulose with phthalic anhydride in [Bmim]Cl at 105 °C with US at 40 kHz for 60 min, and it increased the DS by 46% compared to reactions without US [93]. They explained the increase in DS with temperature by the improved reaction rate resulting from enhanced anion and cation mobility. They attributed the increase in DS with US time to prolonged penetration of reagents into

cellulose chains [92]. They added that cavitation bubbles containing vapor of anhydride enhanced mass transfer [93].

An US bath at 40 kHz and 35 °C esterified MCC, in DMAc with oleic acid as EA, DMAP as catalyst, and EDC as dehydrating agent to convert oleic acid into anhydride. They obtained the highest DS of 1.55 after 6 h of reaction, a molar ratio oleic acid/MCC of 6:1 and an US intensity of 300 W m^{-2}. US enhanced reactivity by improving cellulose dissolution, exposing hydroxyl groups, and breaking fiber aggregates, leading to a homogeneous reaction medium which promoted the reaction with oleic acid. The DS of US-prepared esters increased by 281 % compared to conventional esterification. They attributed the increase in DS with power intensity to the cavitation effect [11].

2.6 Originality

This literature review highlighted several important points:

1. US is widely modeled numerically, however models do not often account for cavitation bubbles and are lacking experimentally measured parameters. In this work, we developed a model to quantify the acoustic pressure distribution and the surface area of the active cavitation zones in a continuous cylindrical ultrasonic reactor with six lateral flat transducers along the walls of the reactor. The model accounts for the presence of cavitation bubbles and their effect on sound attenuation. For the first time, we measured experimentally the speed of sound in cellulose esters reaction mixtures, as these were gaps in the literature. The hexagonal section reactor design ensures constructive sound waves interference.
2. Sonication is used for biomass conversion but its effects on cellulose esterification are not completely understood. The present research explores the esterification of cellulose with long chain FFA (oleic acid and stearic acid) to make cellulose thermoplastics, enhanced by US, a combination not previously investigated in the literature so far. Unlike earlier studies, this work integrates the approaches just mentioned to achieve reduced reaction time, lower consumption of harmful chemicals and decreased energy requirements for producing thermoplastic materials or oligomers from cotton linters and cellulose fibers, through acoustic cavitation and acoustic streaming. Additionally, we simulated the US activity to understand the phenomena occurring within the reactor.

3. Though ILs dissolve more cellulose than traditional solvents, their use under US conditions for cellulose valorization is not widely documented. The present research combines US with ILs without the use of a catalyst for the esterification of cellulose with the aim of avoiding the degradation of this latter. We selected oleic acid, and 1-butyl-3-methylimidazolium chloride and 1-butyl-3-methylimidazolium acetate for US-assisted and catalyst-free esterification of two cellulose sources. We added dimethyl sulfoxide as co-solvent to decrease the viscosity of the reaction mixture and the use of ionic liquids in order to obtain cellulose thermoplastics.

CHAPTER 3 ARTICLE 1: NUMERICAL SIMULATION OF A CONTINUOUS SONOREACTOR FOR BIOMASS RESIDUES RECOVERY

Pierre Dal, Julie Kring, Dalma Schieppati, Daria C. Boffito

Submitted in Ultrasonics Sonochemistry on 7 October 2024

Author contributions

Pierre Dal: Conceptualization, Data curation, Formal analysis, Writing – original draft, Methodology, Investigation, Software. Julie Kring: Funding. Dalma Schieppati: Formal analysis, Writing – review & editing, Investigation, Software. Daria C. Boffito: Writing – review & editing, Supervision, Funding, Validation, Conceptualization, Resources.

Abstract

Numerical simulations are a tool for sonoreactors design and reaction parameters choice. We modeled a two parts sonoreactor with six lateral flat transducers along the walls and a concentric high intensity focused ultrasound (HIFU) transducer at the bottom. We examined the effects of the gap between the reflector and transducers (h), cone radii in the lower part and ultrasound frequency (f) on the cavitation activity of cellulose esters solutions. Then, we investigated the effects of the properties of cellulose solutions on the cavitation activity. The simulation accounts for the attenuation due to the cavitation bubbles and considers the propagation of sound waves from the HIFU as linear. We measured the speed of sound in the cellulose esters solutions and included it in our simulations: 1545 m s^{-1} for 6.25 g L^{-1}. h, f, the density (ρ) and the viscosity (μ) of the cellulose solutions have the most significant effects - accounting for 34 % to 61 % of the variance - on the total acoustic pressure (p_T) and active cavitation surface area (V). p_T and V increase as f and ρ increase, and as h and μ decrease. At 78 kHz and h = 0.075 m, with $\mu = 5.3 \cdot 10^{-3}$ Pa.s and ρ = 941.8 kg m^{-3}, the simulation resulted in the highest p_T and largest V: $1.96 \cdot 10^6$ Pa and $3.99 \cdot 10^{-2}$ m^2.

Keywords: Ultrasound, biomass, acoustic cavitation, numerical simulation, sonochemical reactor

3.1 Introduction

Process intensification (PI) is a transformative approach in chemical engineering aimed at increasing the energy efficiency and sustainability of chemical processes. PI encompasses a variety

of strategies and breakthrough technologies that lower the energetic expenditure by 20 % to 80 %, decrease reagents consumptions by 10 to 1000 times, and dramatically reduce the size of the equipment (100 times) [94], [95]. Ultrasound (US) is one of the notable tools in PI, and it has gathered significant attention due to its unique capabilities and benefits, which include the reduction of energy consumption by 20 to 80 % and divides the equipment's size by a hundred [96]. US is a mechanical wave that consists of successive acoustic cycles of compression (positive pressure) and rarefaction (negative pressure). Compression pushes molecules together, while rarefaction pulls molecules apart. In the rarefaction phase, if the pressure amplitude exceeds the tensile strength of the liquid, vapor-filled cavitation bubbles will form. Pure liquids have a high tensile strength and do not cavitate [77]. However, liquids that are impure – i.e. containing particles and bubbles – have lower tensile strength and cavitate more easily. After bubbles formation, stable cavitation or transient cavitation arises [76], [77]. Stable cavitation arises at low intensity (< 0.05 W cm^{-2} at 20 kHz), whereas transient cavitation arises at high intensity (> 0.1 W cm^{-2} at 20 kHz) [76], [97], [98]. During stable cavitation bubbles grow slowly, while during transient cavitation bubbles grow rapidly from dozens or hundreds of times their equilibrium radius before collapsing in less than a microsecond [99]. The collapse of cavitation bubbles originates microjets and localized hotspots of temperature up to 5000 K and pressure up to 500 atm [77], thereby eliciting both physical and chemical effects on the sonicated system. Reactive species form at the liquid – gas interface of the bubbles and inside the bubbles [100]. The transient cavitation in water, cleaves the oxygen – hydrogen bonds, leading to the formation of reactive hydroxyl radicals. For example, at this frequency and acoustic pressure: 52 kHz and 1.5 atm respectively, each bubble generates $6.6 \cdot 10^5$ hydroxyl radicals, and has a maximum bubble radius of 28.9 μm [101]. The sonication of N,N-dimethylacetamide (DMAc) generates radicals of CH_3 and $CH_2N(CH_3)C(O)CH_3$ [102]. Collins et al. sonicated DMAc at 490 kHz and 50 W, which generated 3.8 μg mol^{-1} min^{-1} of radicals [103]. US finds application in many reactions: esterification [47], transesterification [78], emulsification[79], carboxymethylation [104], delignification [105] and others. One can tune the energy delivered by US to the reaction to selectively cleave specific bonds [77].

Acoustic cavitation depends on the reaction parameters and on the reactor's geometry [95]. Numerical simulation is a powerful tool to predict, map, and estimate the extent of the acoustic activity during the design or scale-up of sonoreactors. Rashwan et al. numerically investigated the effect of the US frequency, power and probe immersion depth on the acoustic pressure of the fluid

[106]. They concluded that higher US frequency favors higher pressure amplitude, with a maximum of negative pressure of $-80 \cdot 10^5$ Pa and $-70 \cdot 10^5$ Pa in the range of 60 kHz to 80 kHz. Additionally, they found that the probe immersion depth does not impact the acoustic pressure amplitude [106]. On the contrary, Garcia-Vargas et al. suggested that the sonochemical yield significantly changes when varying the probe immersion depth at constant input power and constant liquid volume [107]. Girard et al. varied the size of the reactor, the probe immersion depth and axial position for the dispersion of nanocellulose [108]. An off-centered configuration of a horn-type probe in a small beaker (60 mL) was the most energy-efficient set-up – it decreased the dead zone volume ration by 61 % and increased the dispersity index by 27 %. Laajimi et al. evaluated the effect of US frequency, probe immersion depth and reactor's diameter on the yield of biolubricant synthesized from canola oil and polyalcohols. They solved the reaction rate numerically in order to calculate the molar concentration of biolubricant. The fluid velocity and the lubricant yield were the highest with a probe immersion depth of 3 cm in 6 cm of liquid: 1.42 m s^{-1} and 94 %, respectively, versus 1.38 m s^{-1} and 81% at 1 cm immersion depth. They attributed these results to the shorter distance between the probe tip and the reactor walls, which promotes sound waves reflection and decreases sound attenuation. Moreover, a US frequency of 100 kHz produced 99 % yield compared to 94 % at 20 kHz, with a difference lower than 10 % between the numerical and experimental results [109]. Similarly, Son et al. investigated the sonochemical oxidation activity through KI dosimetry for various reactor geometries in a 20 kHz US system. The highest triiodide concentration developed with a centered probe at an immersion depth of 6 cm, justifying the highest cavitation activity. They attributed this to the reflections of sound waves at the bottom of the reactor and at the liquid surface. They also observed that the off-centered probe affected negatively the mixing pattern of the fluid and decreased the cavitation activity by 30 % [110]. Fang et al. numerically and experimentally investigated the effect of the shape of the probe tip (flat, truncated and conical) on the acoustic streaming and cavitation activity. The sonochemical activity and the average streaming velocity of the conical tip was ~ 67 % higher and 139 % than that of the flat tip. However, the average streaming velocity measured at a distance of 70 mm to 80 mm from the tip, was 1.6 times higher for the flat tip than for the conical one [111].

Acoustic pressure gradient between the fluid and the inside of the bubble initiates acoustic cavitation, but cavitation itself affects the total acoustic pressure[1] within the reactor [112]. For the sake of simplicity, most numerical simulations omit the presence of cavitation bubbles. However, cavitation bubbles attenuate the propagation of soundwaves and, hence, they must be included for rigor. Commander and Prosperetti first modeled the wave propagation and attenuation in liquids containing multiple cavitation bubbles [113]. Dähnke and Keil adapted it and solved the Helmholtz equation with the volume fraction of bubbles [114], then they approximated it being linearly dependent on the acoustic pressure [115]. They showed that an increased volume fraction of bubbles from 10^{-5} to $2 \cdot 10^{-1}$ completely attenuates the acoustic waves, with attenuation coefficient increasing from 1 to 500 [114]. Dahlem et al. reported the same attenuation close to the probe [116]. Jamshidi et al. modeled an US reactor and investigated the cavitation (i) not considering cavitation bubbles, (ii) considering a constant volume fraction of bubbles (10^{-4}, 10^{-3}, 10^{-2} and 10^{-1}), and (iii) considering a linear volume fraction of bubbles and acoustic pressure relationship. A linear model accounting for the bubbles' volume fraction revealed that sound waves were completely attenuated within 1 to 5 mm from the transducer. Without considering the bubbles, complete attenuation of the sound waves occurred only after 15 mm. They concluded that increasing the US frequency from 10 kHz to 30 kHz increased the attenuation effect of the bubbles by 50 % [112]. Xu et al. simulated the acoustic streaming for two attenuation coefficients, α (0.005 m^{-1} (Eq. (3.10) and 1 m^{-1}, the latter including the attenuation of cavitation bubbles (Eq. (3.4)). The coefficient 0.005 m^{-1} is valid in degassed water, whereas 1 m^{-1} is valid for water containing dissolved gas and cavitation bubbles [117]. They compared it to experimental measurements of fluid velocity obtained through laser Doppler velocimetry [118]. The flow simulated with the coefficient of 1 m^{-1} was close to the experimental results in terms of velocity and pattern: the cavitation bubbles increased the absorption coefficient of sound waves [117]. Jordens et al. modeled a tubular US reactor and calculated numerically, with the model of Commander and Prosperetti, the bubble volume fraction for various US powers, frequencies and reactor diameters. The bubbles volume fraction increased with a logarithmic trend as US power increased. The bubble volume fraction followed a bell shape curve while changing the US frequency and the reactor diameter, with a maximum at 20 kHz and at 4.9 mm, respectively. Frequencies above 20 kHz promoted the attenuation effect of the bubbles. Moreover, the acoustic pressure and bubbles

[1] Sum of the scattered pressure and the background pressure wave

volume fraction followed the same bell-shaped trend, justifying the use of the bubbles volume fraction for the design [119]. Sajjadi et al. simulated the acoustic cavitation in a cylindrical reactor with a cylindrical probe immersed at different depths at 24 kHz and at rated output power from 100 W to 400 W. They concluded that the cavitation bubbles volume increased by 4.95 % for each US power increase of 100 W. Moreover, the more immersed the probe, the smaller the bubbles volume in the reactor: the bubbles volume at a liquid height of 1 cm was 1.45 times smaller than that at a liquid height of 7 cm [120].

Continuous US reactors with multiple lateral transducers are more efficient than horn-type probes or baths. They offer the option for the transducers to emit at different frequencies and promote the constructive interference of sound waves, ensuring a more uniform cavitational activity [95]. Gogate et al. compared the performance of a hexagonal reactor with six lateral transducers to a US bath of 750 mL (22 kHz and 120 W rated output power) and a US probe (22.7 kHz and 240 W rated power dissipation) inserted in a 50 mL reactor. The hexagonal reactor operates at seven different frequency combinations, with a total power dissipation of 900 W and a volume of 7 L. With all transducers emitting at 20 kHz, the cavitation yield in the hexagonal reactor was two times higher than that in the US bath, and 20 times higher than with the US probe [121]. Manickam et al. synthesized biodiesel in a hexagonal multiple frequency reactor. The yield for a triple frequency operating configuration (28 kHz - 40 kHz -70 kHz) was 8 % higher than that of a single frequency (28 kHz), and 3.5 % higher for the double frequency configuration (40 kHz -70 kHz) [122]. Prabhu et al. numerically quantified the cavitation activity in the same reactor reported by Gogate et al. [121], [123]. They concluded that the three frequencies configuration created cavitation bubbles 100 % and 30 % larger than the two frequencies and single frequency configurations [123]. Kumar et al. experimented a hexagonal sonoreactor (radius of 0.060 m and length of 0.30 m) with a central tube and three transducers on each side. They measured the maximum acoustic pressure at 0.18 m from the bottom of the reactor, which they attributed to the influence of every transducer. The acoustic pressure decreased from the side to the center of the reactor: from $2.7 \cdot 10^5$ Pa to $2.0 \cdot 10^5$ Pa at 50 kHz. They confirmed that the acoustic pressure is more uniform than using an immersion probe: 10 % to 30 % of variation in their reactor, against 100 % to 400 % for an immersion probe. They explained it by the higher number of transducers and overlapping of waves of every transducer [124]. In an US bath with five transducers at 37 kHz, the acoustic pressure decreased by a factor of 3 at 100 mm of the transducers [125]. Gogate et al. wrote that hexagonal or

rectangular cross-section reactors form standing waves which increase the cavitational intensity. Transducers mounted on opposite parallel walls of the reactor generate standing waves via constructive interference, which does not occur in reactors with an odd number of walls [126]. Hodnett et al. measured the maximum acoustic pressure in a cylindrical sonoreactor equipped with ten rows of three transducers equally distributed around the reactor. The maximum acoustic pressure was at the center of the reactor. They observed a similar pressure amplitude close to the reactor wall at 500 W and 25 kHz. It induced cavitation close to the walls, which prevented cavitation from occurring towards the center of the reactor due to acoustic pressure attenuation [127]. Chu et al. simulated a hexagonal three-frequency sonoreactor, with each face-to-face transducer at the same frequency (28 kHz, 40 kHz and 70 kHz). Among the three frequencies, 40 kHz had highest absolute pressure amplitudes, which they confirmed by analyzing each frequency separately and by varying the length of hexagon edge. The absolute pressure decreased by 18 % when increasing the length of the hexagon edge by 50 %, which they attributed to attenuation. Each frequency corresponds to a different wavelength, and they selected the reactor size to ensure that sound waves at 40 kHz produced optimal constructive interference [128].

In this work, we developed a model to quantify the acoustic pressure distribution and the surface area of the active cavitation zones[2] in a continuous cylindrical ultrasonic reactor with six lateral flat transducers along the walls and a concentric high intensity focused ultrasound (HIFU) transducer at the bottom of the reactor. The model accounts for the presence of cavitation bubbles and their effect on sound attenuation. We fixed the US frequency and investigated the influence of the size of the gap between the reflector and the transducers, and the dimension of the whistle on the acoustic cavitation throughout the US reactor. Simulations were conducted in COMSOL Multiphysics. For the first time, we measured experimentally the speed of sound in cellulose esters reaction mixtures, as these were gaps in the literature. These media are part of a bigger biomass conversion project in our research group.

[2] Area in which the pressure is above the Blake pressure threshold, where cavitation is considered active

3.2 Mathematical model and governing equations

3.2.1 Equations for acoustic pressure

The Helmholtz equation is a steady state form of the wave equation (the latter characterizes the acoustic pressure distribution in time and space). We assumed that the fluid is homogenous – i.e. bubbles are homogeneously dispersed in the fluid – and incompressible (Section 3.2.3), the sound waves are linear, and the shear stress is negligible [106]. We also assumed that acoustic pressure has a harmonic time dependence: $p(r,t) = p(r).e^{i\omega t}$ [129], where $\omega = 2\pi f$ is the wave's angular frequency in rad s^{-1}, where f is the ultrasonic frequency in Hz. We solved the Helmholtz equation (Eq. (3.1)) for the acoustic pressure distribution in a liquid:

$$\frac{1}{\rho}\nabla^2 p + \frac{\omega^2}{\rho c^2}p = 0 \tag{3.1}$$

US applied to a liquid at a certain intensity and frequency generates acoustic cavitation. Bubbles form and accumulate at the tip of the US probe and attenuate the propagation of sound waves. Wijngaarden developed equations describing the one-dimensional propagation of sound waves in a liquid and bubbles mixture [130]. From the continuity equation and Wijngaarden's equations, Commander and Prosperetti modeled the propagation of sound waves in a liquid containing bubbles. Their model is a modified form of the Helmholtz equation that includes the damping effect of bubbles, arising from viscous, thermal and acoustic effects (factor d defined later). Their model does not work for cases with bubbles resonance effects but works well for bubbles volume fraction up to 2 %. It is only valid for bubble radii ranging from 5 μm to 3 mm and frequencies ranging from 20 Hz to 10 MHz [113]. This model does not consider the ultrasound probe tip as a moving wall as it should. Their modified Helmholtz equation (Eq. (3.2)) is:

$$\nabla^2 p + k_m^2 p = 0 \tag{3.2}$$

where k_m is the complex wave number in m^{-1} in the fluid and bubbles mixture. For a monodisperse bubble distribution, k_m^2 is [112]:

$$k_m^2 = \frac{\omega^2}{c^2}\left(1 + \frac{4\pi c^2 n_b R_0}{\omega_0^2 - \omega^2 + 2id\omega}\right) \tag{3.3}$$

where n_b is the number of bubbles per unit volume in m^{-3}, R_0 is the incipient radius of a bubble in m, ω_0 is the resonant angular frequency of bubbles in rad s^{-1}, i is imaginary unit and d is the damping

factor (a term for the viscous, thermal and acoustic effects respectively [113]) determined from Eq. (3.4):

$$d = \frac{2\mu}{\rho R_{eq}^2} + \frac{p_0}{2\rho\omega R_{eq}^2} Im\Phi + \frac{\omega^2 R_{eq}}{2c} \tag{3.4}$$

where p_0 is the undisturbed pressure in the bubble position in Pa, which is $p_{atm} + (2\sigma/R_{eq})$ where σ is the surface tension of the liquid in N m^{-1}. R_{eq} is the bubbles equilibrium radius in m and it accounts for direct contact coalescence and rectified diffusion, μ is the dynamic viscosity of the fluid in Pa s, and Φ is a complex adimensional parameter. The resonant angular frequency of bubbles ω_0 in Eq. (3.3) corresponds to:

$$\omega_0^2 = \frac{p_0}{\rho R_{eq}^2}\left(Re\Phi - \frac{2\sigma}{p_0 R_{eq}}\right) \tag{3.5}$$

The parameter Φ in Eq. (3.4) and in Eq. (3.5) is a function of the specific heat ratio of the gas inside bubbles (γ), and χ (Eq. (3.7) [131], Eq. (3.6) determines it:

$$\Phi = \frac{3\gamma}{1 - 3(\gamma - 1)i\chi\left[\left(\frac{i}{\chi}\right)^{\frac{1}{2}} \coth\left(\frac{i}{\chi}\right)^{\frac{1}{2}} - 1\right]} \tag{3.6}$$

χ is expressed as:

$$\chi = D/\omega R_{eq}^2 \tag{3.7}$$

with D the thermal diffusivity of the gas. The bubbles number density n_b in Eq. (3.3) depends on β, the volume of the gas fraction within the bubbles in the reactor with respect to the total volume:

$$n_b = \frac{3\beta}{4\pi R_0^3} \tag{3.8}$$

Other authors adopted the same theoretical approach [111], [112], [132] and validated it experimentally, either by: particle image velocimetry [111] or through sonochemiluminescence [132].

3.2.2 Equations for acoustic cavitation zones

We considered that bubbles grow and eventually collapse and generate cavitation when the pressure is above the threshold pressure for cavitation, p_c [133]. This pressure threshold depends on the sonicated fluid, its temperature and its gas content, and is expressed by Eq. (3.9):

$$p_c = p_0 - p_v + \frac{\frac{2}{3\sqrt{3}}\sqrt[3]{\left(\frac{2\sigma}{R_{eq}}\right)^2}}{\sqrt{p_0 - p_v + \frac{2\sigma}{R_{eq}}}} \tag{3.9}$$

where p_0 is the vapour pressure of the sonicated liquid in Pa.

Table 3.1 Values for the pressure threshold for cavitation (p_c).

f, kHz	p_c, Pa
38 - 82	$1.02 \cdot 10^5$
390	$1.04 \cdot 10^5$

3.2.3 Assumptions of the model

For Eq. (3.1) and Eq. (3.2), we assumed:

1. The fluid is incompressible and Newtonian. The reactor intends to treat aqueous solutions of lignin, and solutions of cellulose esters in dimethylacetamide (DMAc) and lithium chloride (LiCl). The compressibility of DMAc – $6.7 \cdot 10^{-4}$ MPa^{-1} [134] – is comparable to that of water – $4.6 \cdot 10^{-4}$ MPa^{-1} [135]. LiCl is an electrolyte, causing electrostriction and reducing compressibility. Wahab and Mahiuddin demonstrated that increasing the concentration of LiCl in methanol decreased the compressibility of the mixture [136]. Given that methanol is an organic solvent, we assume a similar behavior for the DMAc/LiCl system.
2. The bubble to liquid volume ratio is low so the medium's properties are those of the liquid phase [113].

3. The thermodynamic properties of the liquid medium are independent of the temperature and bubble volume fraction.
4. We set the bubble size R_0 equal to 1.6 μm at a US frequency of 40 kHz and to 0.1 μm at a US frequency of 390 kHz. Brotchie et al. and Dehane et al. observed that an increase of the acoustic frequency, decreased the mean size of the cavitation bubbles, and an increase of the acoustic power, increased the mean size of the cavitation bubbles [137], [138]. Servant et al. and Dähnke et al. assumed the bubble radius ranged between $5 \cdot 10^{-6}$ m and $3 \cdot 10^{-3}$ m [139], [140]. Pandit et al. chose a bubble radius ranging from 2 μm to 50 μm with the acoustic frequency ranging from 10 kHz to 80 kHz [141]. We chose a bubble equilibrium radius of 80 μm at a US frequency of 40 kHz and of 5 μm at a US frequency of 390 kHz. It respects the order of magnitude of the Minnaert's equation: $R_{eq} \approx 3/f$ [137]. Under acoustic activity and coalescence, cavitation bubbles grow to about 50 times R_0 [142].
5. The distribution of bubbles is homogeneous in the reactor and β ranges from 10^{-4} to 10^{-1}. For values $\beta > 10^{-1}$ bubbles scatter most of the sound waves [112]. For the computation, similarly to Dähnke et al., we assumed that the volume fraction of bubbles in the reactor linearly depends on the acoustic pressure amplitude in the fluid: $\beta = C \cdot p$ where C is a constant [139]. Jamshidi et al. validated this model in water, with $C = 2 \cdot 10^{-9}$ [112]. We chose the same value for C.
6. The US transducers generate acoustic pressure amplitude, which is the greatest in the middle of the transducers face and decreases as the distance from the center increases [133]. The decrease in pressure amplitude follows a Gaussian function.
7. The assumption of a linear propagation of acoustic waves is valid for: $p << \rho \cdot c^2$. This assumption holds for values of approximately $2 \cdot 10^7$ Pa for our fluids [143]. It also holds as the propagation media is homogeneous [144]. The nonlinearity of waves propagation has more pronounced effects above 100 W cm^{-2} at 1 MHz [145]. Simulations of HIFU transducers with linear propagation assumption was successful and verified experimentally [146].

3.3 Simulation

3.3.1 Geometry and boundary conditions

The reactor is a 12 L stainless steel two-piece vessel (Figure 3.1a and b). The upper part consists of a cylinder (ID: 0.2 m, OD: 0.22 m) with six Ti64 (Ti-6Al-4V alloy) US transducers along its walls (200 mm x 40 mm), and a stainless steel cylindric reflector in the middle (D: variable, H: 0.02 m). The lower part consists of a cylinder (ID: 0.2 m, OD: 0.22 m, H: 0.0365 m) that houses a concentric high intensity focus US transducer (Ti64, 0.125 m curvature radius, 0.065 m radius (Figure 3.1c), and a conic whistle that streamlines the flow towards the upper part of the reactor. The reactor has two liquid feed inlets (I, Figure 3.1a) located at the bottom of the reactor, and four outlets located at very top of the reactor (O, Figure 3.1a). The transducer material and mounting are proprietary information, part of a patent pending and not published yet.

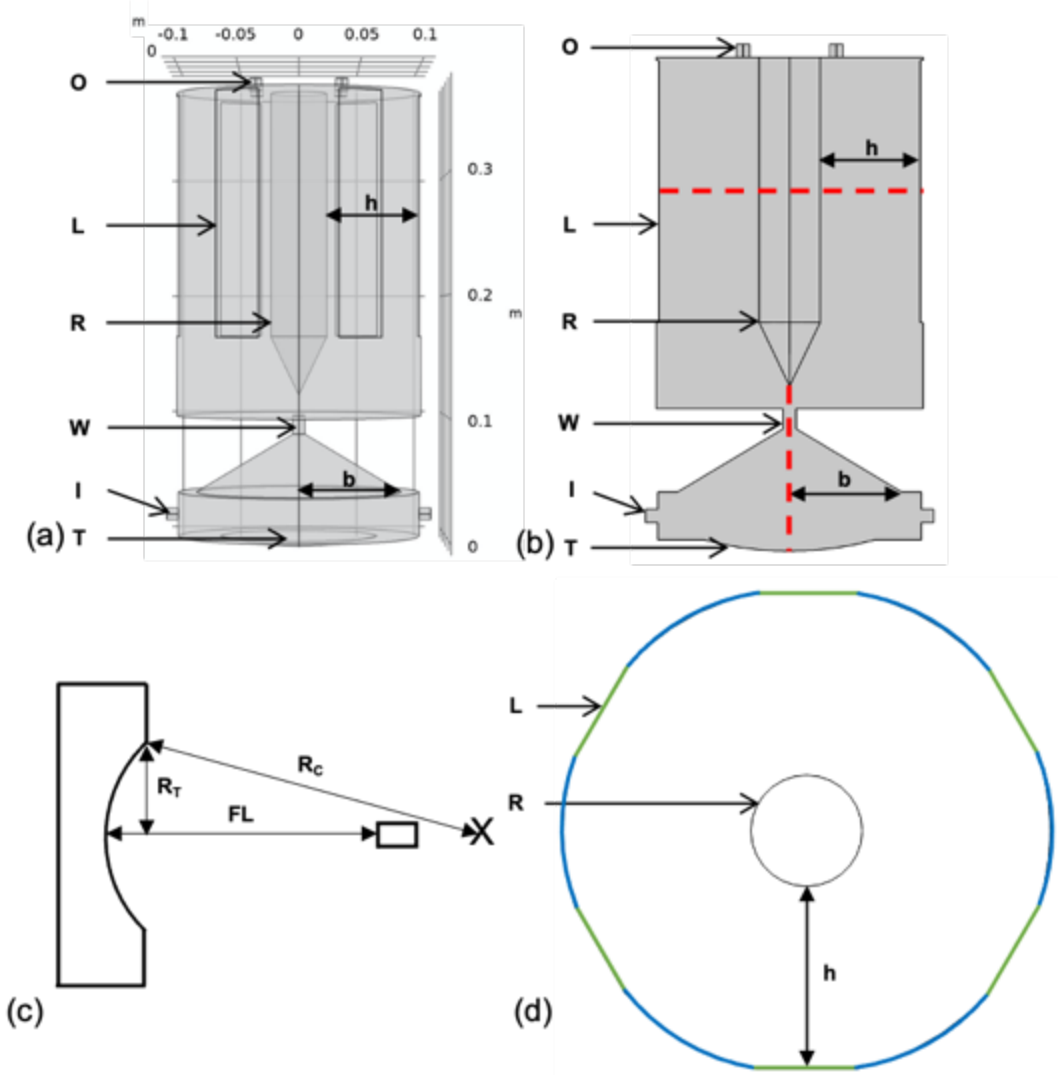

Figure 3.1 Sonochemical reactor (a). Longitudinal section (b), red dashed lines are the mesh sensitivity study measurement segments. HIFU transducer scheme (c). Cross section (d), green lines are the lateral transducers and blue arcs are the reactor's wall. h is the gap between the lateral transducers and the reflector. b is the radius of the cone in the whistle area. O and I correspond to the fluid outlets and inlets, respectively. L and T correspond to the lateral and HIFU transducers, respectively. R and W correspond to the reflector and whistle parts, respectively. FL is the focal length, R_C is the curvature radius and R_T is the radius of the transducer.

The difference of impedance *Z* (product of material's density and speed of sound) at interfaces induces ultrasound reflection. We set the following boundary conditions for the simulations:

- At the reactor's walls, the impedance was: Z = 8010 kg m^{-3} * 3070 m s^{-1} (for stainless steel 304L).

- At the boundary fluid-transducer (non-active), the impedance was: Z = 4470 kg m^{-3} * 4987 m s^{-1}.
- We defined a pressure amplitude p_a (Eq. (3.10)) at the surface of the US transducers:

$$p_a = \sqrt{\frac{2Pc\rho}{S}} \tag{3.10}$$

Where *P* is the US power delivered to the liquid, and *S* is the ultrasound transducer surface area.

3.3.2 Mesh

COMSOL Multiphysics generated the mesh automatically with triangle elements (268 566 elements) for the 2D geometry. A mesh size sensitivity study verified the convergence of the model among three extremely fine mesh element sizes: maximum size of 0.0075 cm and minimum size of 0.00075 cm ; maximum size of 0.075 cm and minimum size of 0.00075 cm ; maximum size of 0.40 cm and minimum size of 0.00079 cm. Moreover, we ensured the maximum mesh element size was 1/5 of the US wavelength (at 390 kHz, λ = 0.38 cm, maximum size of 0.075 cm and minimum size of 0.00075 cm) [108]. Even though other sources suggest at least 8 mesh elements per wavelength [106]. The software calculated the acoustic pressure along the segment located at half of the reflector's length (100 mm, Figure 3.1b) and the segment in the axis of the HIFU transducer (Figure 3.1b).

We applied a quadratic Lagrange discretization to solve the model, which provides more accuracy with fewer elements per wavelength. It better represents the curved geometry. We chose the MUMPS (MUltifrontal Massively Parallel sparse direct Solver) solver as it uses less memory than the PARDISO solver. The Newton method improves the convergence of the solver. We kept an initial damping factor of 1 as the model converged. The maximum number of iterations was 25, which is sufficient to reach convergence for our model in a reasonable time.

3.3.3 Simulation steps

COMSOL Multiphysics 5.5 solved the equations in Section 3.2 and calculated the acoustic pressure distribution throughout the sonoreactor, with and without bubbles attenuation. The software solved the equations in 2D for computation time saving.

The simulation followed two steps for the lateral transducers and for the HIFU transducer:

1. The COMSOL Acoustic Module – Pressure Acoustics solved Eq. (3.1) in the Frequency Domain, modelling a continuous wave and considering the attenuation of the acoustic pressure (α, Eq. (3.11)) intrinsic to the medium [106]. The study calculates the acoustic pressure distribution without cavitation bubbles, which is the starting point for step 2.

$$\alpha = \frac{8\mu\pi^2 f^2}{3\rho c^3} \tag{3.11}$$

2. We included the attenuation due to cavitation bubbles by implementing Eq. (3.2) in the Stabilized Convection-Diffusion Equation and defining Eq. (3.3) to Eq. (3.8) into the parameters. The software calculated β with the acoustic pressure determined in step 1. Then, it solved Eq. (3.8) and Eq. (3.3) to determine n_b and k_m, and it finally solved the modified Helmholtz equation Eq. (3.2) until steady state.

Because the lateral transducers and the HIFU operate at different frequencies, COMSOL Multiphysics resolved Step 1 and Step 2 for the two transducers individually, thereby mapping the acoustic pressure as if the lateral transducers and the HIFU operated one at a time. The total acoustic pressure field (p_T) across the reactor was calculated through the superposition principle using the Parseval's theorem (Eq. (3.12)) [128]. This is possible because the power and frequency chose for this work allow for the simulation of propagating waves as linear, (assumption 7 in Section 3.2.3). [38]:

$$p_T = \sqrt{\frac{1}{2}(|p_{LT}|^2 + |p_{HIFU}|^2)} \tag{3.12}$$

where $|p_{LT}|$ and $|p_{HIFU}|$ are the module of acoustic pressure generated by the lateral transducers and HIFU transducer, respectively.

3.4 Material and methods

3.4.1 Simulations operating parameters and design of experiments

Each lateral transducer emits at 400 W of electrical power and 340 W of nominal power. We assumed that the transducers converted 85 % of the electrical power into acoustic power. The HIFU

transducer emits at 120 W of electrical power, thus its power intensity supports the linear propagation [145]. The HIFU transducer emits at 390 kHz. At frequencies of a few hundreds kHz, cavitation generates mostly chemical effects like radicals generation [95]. The lateral transducers and the HIFU transducer were active separately first, in order to determine the total acoustic pressure and active cavitation surface area. We built two designs of experiments (DOE).

DOE 1 investigated the effect of the geometry (*h* and *b*) and frequency (*f*) on the total acoustic pressure (p_T) and active cavitation surface area (V) within the sonoreactor. The input variables and their associated levels are:

- the ultrasound generator frequency, six levels (Table 3.2). With US frequencies from 20 kHz to 100 kHz, cavitation generates mainly physical effects, like liquid circulation and turbulence, and chemical effects in a lower extent [16].
- the gap between the lateral transducers and the reflector (h), two levels (Table 3.2). We designed the gap between the transducers and the reflector to be a multiple of the wavelength to ensure constructive interference of the waves. We accounted for frequency variations resulting from the probe wearing over time.
- the radius of the cone in the whistle area (b) (Table 3.2).

DOE 2 investigated the effect of the cellulose solutions' parameters on the total acoustic pressure and cavitation surface volume within the sonoreactor (fixed geometry). h = 0.075 m and b = 0.1 m yielded the largest cavitation surface volume in DOE 1, hence DOE 2 adopted these fixed geometric values. The input variables for DOE 2 and their associated levels are:

- The viscosity (μ), density (ρ) and speed of sound (c) of three concentrations of cellulose solution, 3 levels (Table 3.2).
- the frequency, four levels (Table 3.2).

We conducted a statistical analysis, in JMP, to identify significant dependent variables and relationship within the data, and to fit linear models [132]. We first ran a predictor screening analysis with Bootstrap forest partitioning, which identified the dependent variables responsible for the largest variance for the response variables p_T and V. The software generates random forest algorithm to evaluate the contribution of each predictor (input variable) to the response variable. Hundred decision trees are built with bootstrap of the data, thus input variables are ranked from the

most significant to the least significant. We then eliminated the non-significant variables to fit a linear regression model.

Table 3.2 Input variables for DOE 1 and DOE 2, with their levels.

	DOE 1			DOE 2	
Input variable	*f*, kHz	*h*, m	*b*, m	*f*, kHz	Cellulose concentration, g L^{-1}
Levels	38	0.075	0.05	38	6.25
	40	0.077	0.075	40	12.5
	42		0.1	78	25.0
	78			80	
	80				
	82				

3.4.2 Liquid media: preparation and characterization

The objective of the simulations was to calculate the acoustic pressure in cellulose esters in N,N-dimethylacetamide (DMAc). The choice of these media was dictated by ongoing investigations in our research group as a part of a bigger project.

We measured the density and the viscosity at 20 °C, after 2 h of cellulose esterification at 3 different concentrations (25 g L^{-1}, 12.5 g L^{-1} and 6.25 g L^{-1}). An oven dried cellulose at 100 °C for 1 h prior to processing. A solution of 20 mL of DMAc activated 0.50 g of cellulose (or 0.25 g, or 0.125 g depending on the concentration) at 130 °C for 2 h under stirring at 300 rpm. The mixture cooled to 100 °C and we added 1.5 g of lithium chloride (LiCl), to enhance cellulose dissolution and electrostriction [51], [147]. Stirring continued with the heating turned off until the mixture reached room temperature and was completely transparent. We added 3.53 g of p-toluenesulfonyl chloride (p-Tos) as activating agent [51], and 5.26 g of oleic acid, which were *a priori* dissolved in 5 mL of DMAc. Regardless of the cellulose concentration, the molar ratio cellulose : oleic acid : p-Tos remained constant at 1 : 6 : 6. The esterification reaction took place in a thermostatic beaker at 20 °C and 300 rpm for 2 h.

An Anton Paar DMA 4500 density meter determined the density of the cellulose esters' solutions at 20 °C, after reaction. Similarly, a Thermo Scientific Haake Viscotester iQ with a 3 mL coaxial chamber assessed the viscosity of the cellulose solutions after reaction. First, there was a ramp for 120 s at a shear rate of 1 s^{-1}, followed by an increase in the shear rate to 500 s^{-1} in 10 steps over 10 minutes. COMSOL Multiphysics employed the values we measured (Table 3.3) for the numerical simulations.

Table 3.3 Properties of cellulose esters solutions.

Cellulose concentration, g L^{-1}	Speed of sound, m s^{-1}	Density, kg m^{-3}	Viscosity, Pa.s
25	1495.8	936.2	$23.3 \cdot 10^{-3}$
12.5	1529.6	939.1	$14.1 \cdot 10^{-3}$
6.25	1545.0	941.8	$5.3 \cdot 10^{-3}$

3.4.3 Speed of sound measurements

An Olympus V306 immersion transducer determined the speed of sound of cellulose esters solutions. The transducer active element has a diameter of 13 mm and the total diameter of the transducer is 16 mm. The transducer operates at 2.25 MHz and transmits the signal through a polystyrene container filled with 50 mL of the solution. The transducer adhered to the side of the container and we fed the solution with a pipette to prevent movement during the filling and emptying the container, ensuring that the waves transmit perpendicularly to the opposite side of the container. We connected the transducer to an Agilent Technologies 33220A 20 MHz Waveform Generator (signal generator) and to a GW Instek GDS-1000A-U Series oscilloscope.

First, we transmitted a signal through deionized water to measure the round-trip distance the sound wave travelled through the fluid. We assumed the sound wave travelled only in water, at a speed of 1498 m s^{-1}, as measuring the thickness of the gel and the polystyrene wall was impossible. The round-trip travel time corresponds to the interval between the start of each peak (red lines in Figure 3.2). The sound wave travelled a total distance of 0.04467 m. The oscilloscope measured the speed of sound seven times and calculated a mean value. We entered these values into COMSOL Multiphysics for simulations (Table 3.3).

Assuming that the wave traveled only through the fluid led to an underestimation of the speed of sound. In reality, the speed of sound in polystyrene is twice as high in water, oils, and ethanol, for example [148]. Consequently, we overestimated the sound attenuation in the solutions.

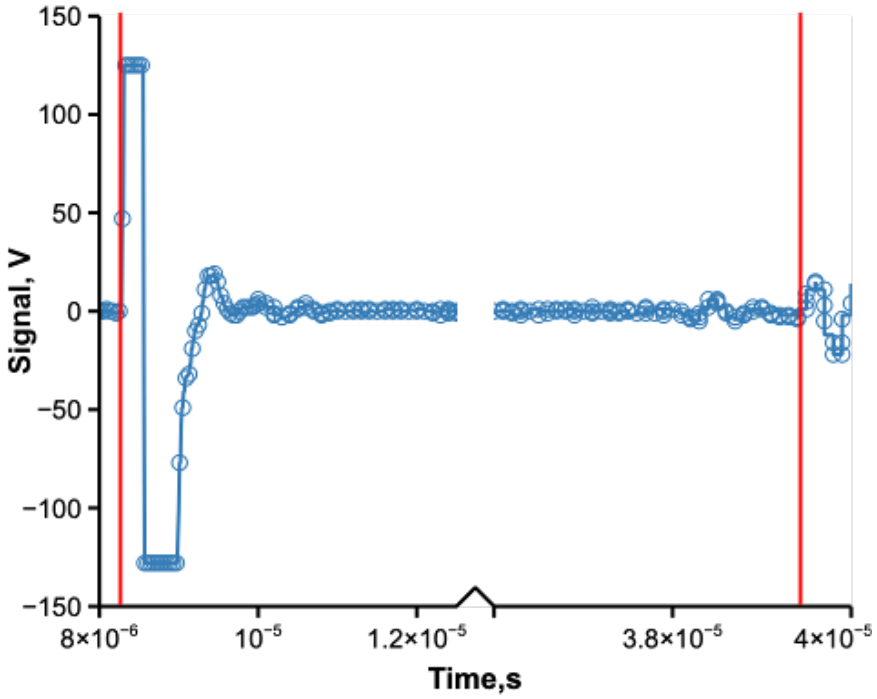

Figure 3.2 Results of the signal in deionized water. Red vertical lines correspond to the signal inbound and outbound.

3.5 Model validation

As the reactor was unavailable for experimental validation, we validated the model through a benchmarking approach. This approach consists in comparing the results of our simulation code with established sources of validated data [124]. We applied our model equations to the published geometry of Kumar et al., using their fluid and US parameters. We compared the simulated acoustic pressure to what they obtained along the radial axis of the reactor. They measured the pressure into the hexagonal reactor with a hydrophone placed at different radial and axial positions [124].

The reactor is a 7.5 L hexagonal vessel (height of 0.3 m and length of side wall of 0.1 m), with three circular US transducers (diameter of 0.06 m, spaced 0.03 m apart, each operating at 50 W and 50 kHz) along each wall. The vessel is filled with water [124].

The acoustic pressure had the same order of magnitude as the local pressure measured by Kumar et al. However, the pressure profiles differed (Figure 3.3). At a radial position of 0.015 m, the pressure of this model was 38 % lower than the measured pressure at 0.005 m away from the bottom of the reactor, whereas it was only 1 % lower at 0.14 m and 0.22 m away from the bottom of the reactor (Figure 3.3). This difference arises from Kumar et al. measuring the local mean pressure, which is time-averaged. In our simulation, COMSOL Multiphysics calculated the absolute value of the instantaneous local acoustic pressure in a stationary phase. Other sources of error include the simulation not accounting for interactions of acoustic waves, or nonlinear acoustic phenomena. Although direct experimental validation remains the preferred approach, benchmarking validation confirms that the acoustic pressure simulated in our model aligns in order of magnitude and similarity with values reported in the literature. This demonstrates that our model produces reliable and credible results.

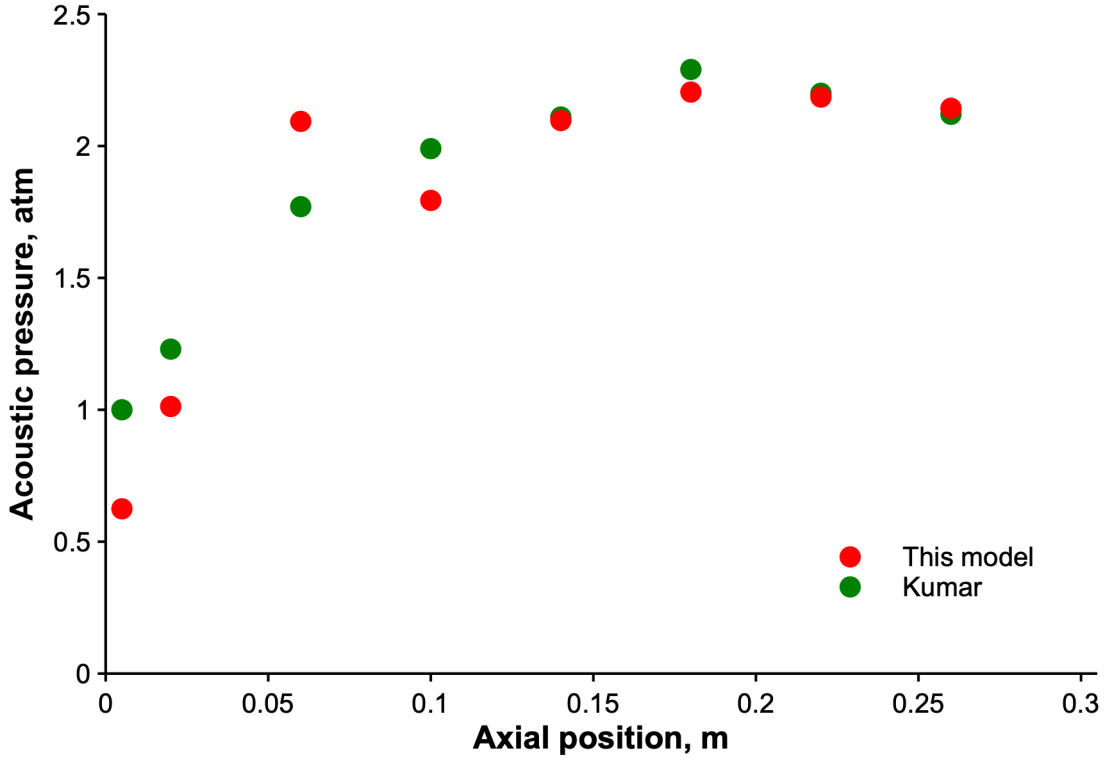

Figure 3.3 Absolute acoustic pressure along the axial position at a radial position 0.015 m, and the comparison with the mean local pressure of Kumar et al. at the radial position 0.015 m [124].

3.6 Results and discussion

3.6.1 Effect of the frequency

p_T increases with the increase of f and decreases as h increases. V increases as f increases and decreases as h increases (Figure A.1). b does not have a significant effect on p_T and V, accounting for 5.1 % and 8.1 % of the variance respectively (Table 3.4). Thus, we selected f and h and neglected b for the linear regressions with a one-degree interaction.

Table 3.4 Predictor screening analysis of p_T and V for DOE 1.

	Predictor		Bivariate fit	
Input variables	p_T*	V*	p_T**	V**
f	60.6 %	57.7 %	0.13 > 0.05	0.76 > 0.05
h	34.3 %	34.1 %	0.04 < 0.05	0.08 > 0.05
b	5.1 %	8.1 %	0.98 > 0.05	0.96 > 0.05

*Portion of the variance explained by the predictor for p_T and V. **p-value of the density ellipse of 0.95 for p_T and V. A p-value above 0.05 means the data are not sufficiently significant to refute the assumption of random distribution within the ellipse. Whereas a p-value below 0.05 suggests the data points are not randomly distributed.

The statistical analysis generated the following regression equation for p_T from 38 kHz to 42 kHz (Figure 3.4):

$$p_T = 6.0 \cdot 10^6 - 4.6 \cdot 10^4 \cdot f - 4.8 \cdot 10^7 \cdot h + 36.9 \cdot 10^6 \cdot (f - 40)(h - 0.076) \quad (3.13)$$

The statistical analysis generated the following regression equation for p_T from 78 kHz to 82 kHz (Figure 3.5):

$$p_T = 32.3 \cdot 10^6 - 1.7 \cdot 10^5 \cdot f - 23.3 \cdot 10^7 \cdot h + 20.2 \cdot 10^7 \cdot (f - 80)(h - 0.076) \quad (3.14)$$

p_T increases with the increase of frequency. However, for h = 0.075 m, from 38 kHz to 42 kHz, p_T decreases (Eq. (3.13)) by 44 %, and from 78 kHz to 82 kHz it decreases (Eq. (3.14)) by 77 %, with a maximum of $1.96 \cdot 10^6$ Pa at 78 kHz. For h = 0.077 m, from 38 kHz to 42 kHz, p_T decreases by 10 %, and from 78 kHz to 82 kHz it increases by 26 %. The increase of amplitude of acoustic pressure with f was also observed by Rashwan et al. [106].

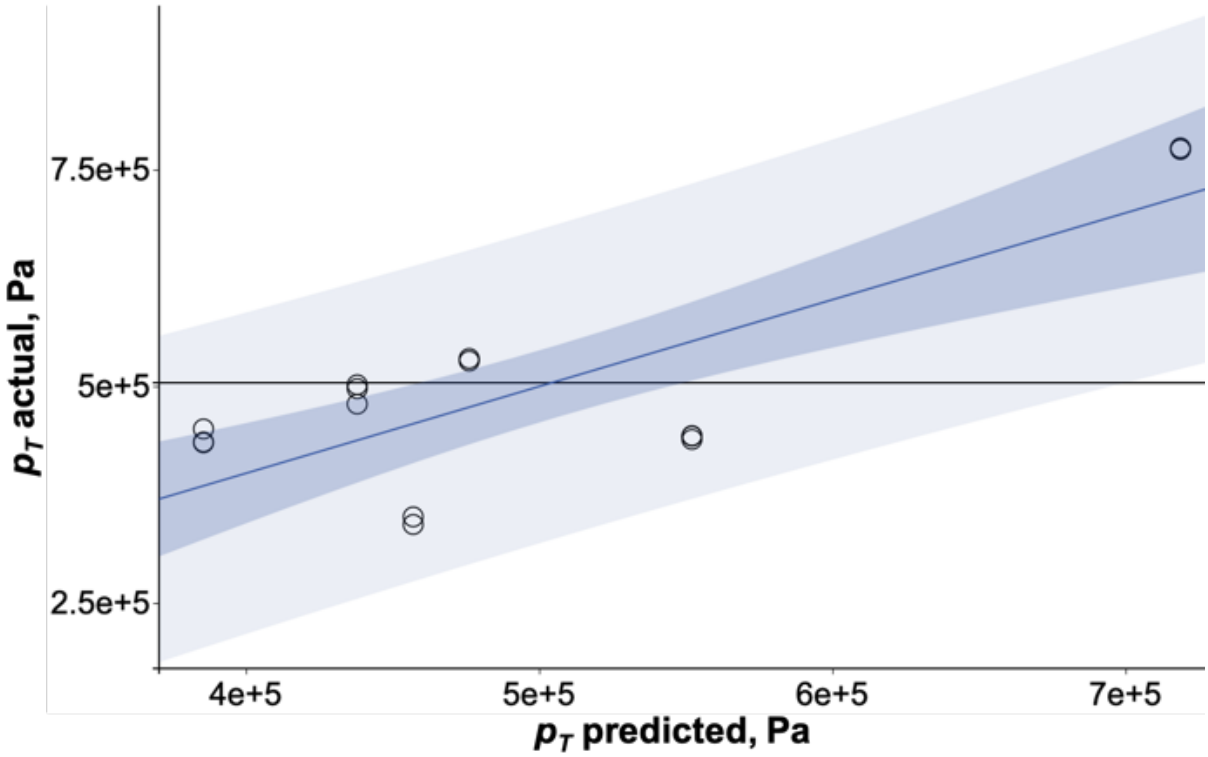

Figure 3.4 Actual by predicted p_T (○) for frequencies from 38 kHz to 42 kHz. Regression, 95 % CI of prediction, RMSE = 88699, R^2 = 0.655, p-value = 0.0015, Mean of response (504582 Pa), Prediction interval.

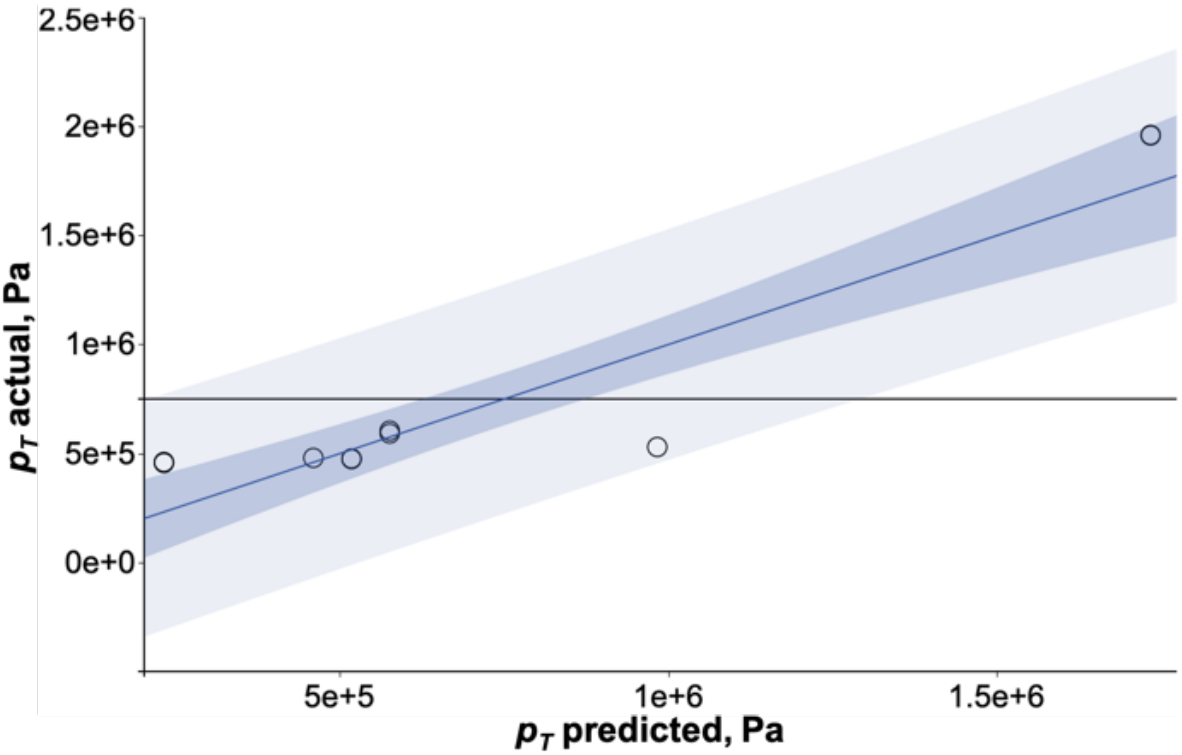

Figure 3.5 Actual by predicted p_T (○) for frequencies from 78 kHz to 82 kHz. Regression, 95 % CI of prediction, RMSE = 257947, R^2 = 0.820, p-value < 0.0001, Mean of response (750281 Pa), Prediction interval.

The statistical analysis generated the following regression equation for V from 38 kHz to 42 kHz (Figure 3.6):

$$V = 0.036 + 3.9 \cdot 10^{-4} \cdot f - 0.27 \cdot h + 1.5 \cdot (f - 40)(h - 0.076) \quad (3.15)$$

The statistical analysis generated the following regression equation for V from 78 kHz to 82 kHz (Figure 3.7):

$$V = 0.20 - 21.6 \cdot 10^{-4} \cdot f - 2.0 \cdot h + 2.4 \cdot (f - 80)(h - 0.076) \quad (3.16)$$

V increases as the frequency increases and follows the same trends as p_T. For h = 0.075 m, from 38 kHz to 42 kHz, V decreases (Eq. (3.15)) by 14 %, and from 78 kHz to 82 kHz it decreases (Eq. (3.16)) by 26 %, with a maximum of $3.99 \cdot 10^{-2}$ m^2 at 78 kHz. For h = 0.077 m, from 38 kHz to 42 kHz, V increases by 31 %, and from 78 kHz to 82 kHz it increases by 34 %. When the frequency increases, the collapse of cavities is more violent and the power dissipation increases, which increases p_T and increases V [124]. The increase of V with f can be explained by a larger number

of cavitation bubbles generated, and shorter collapse time [109]. This phenomenon explains the increase of yield with *f* that Laajimi et al. observed [109].

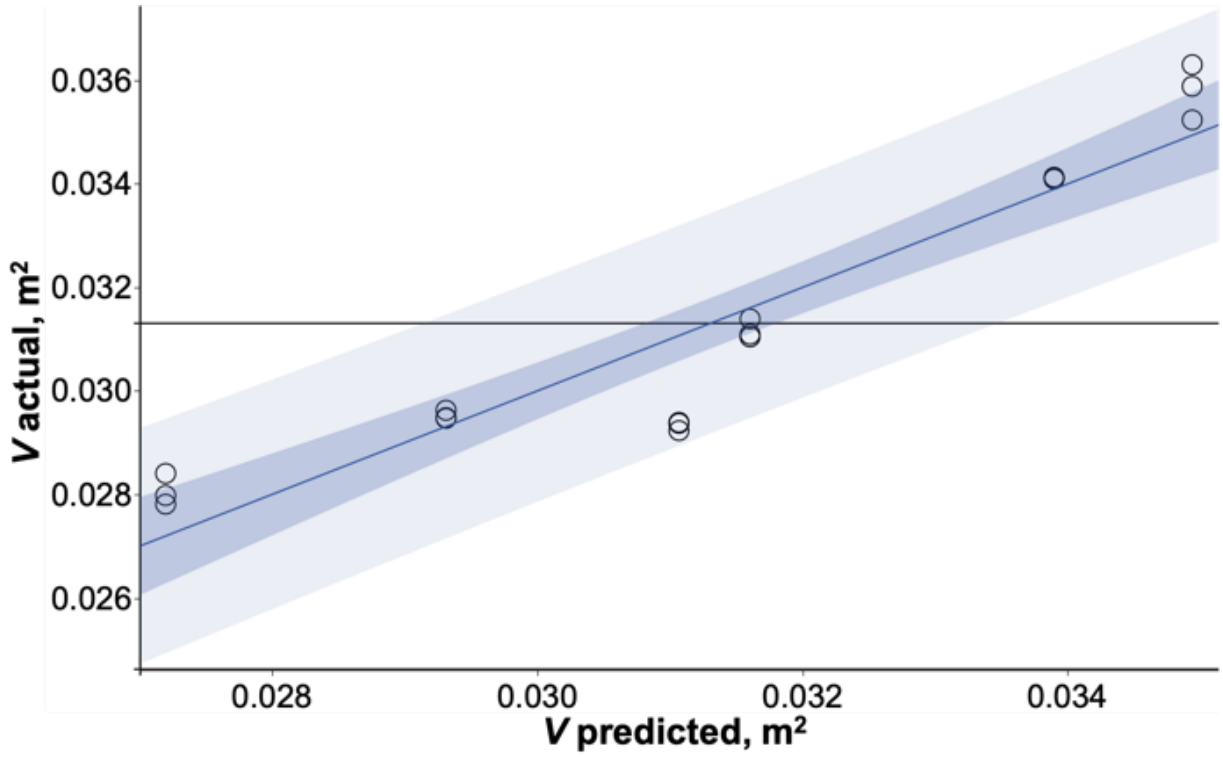

Figure 3.6 Actual by predicted *V* (○) for frequencies from 38 kHz to 42 kHz. Regression, 95 % CI of prediction, RMSE = 0.866, R^2 = 0.889, *p*-value < 0.0001, Mean of response (0.0313 m^2), Prediction interval.

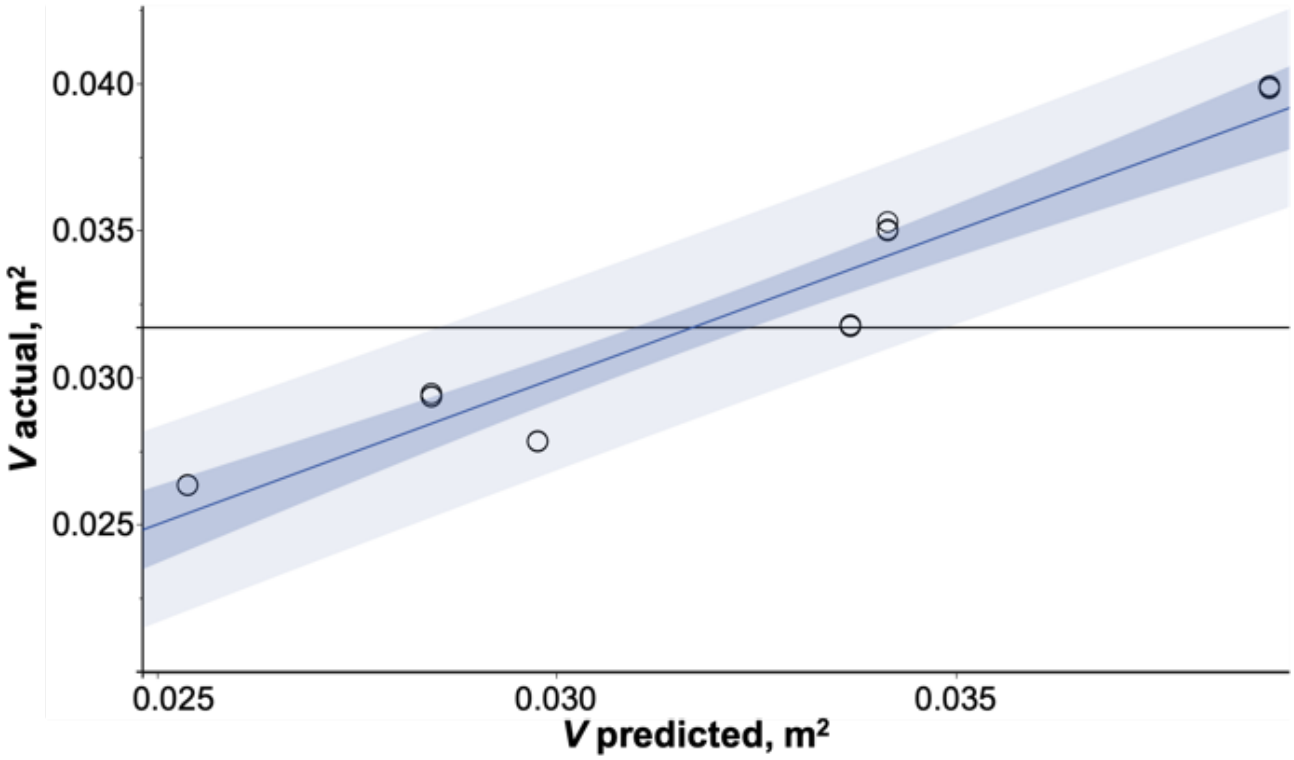

Figure 3.7 Actual by predicted V (○) for frequencies from 78 kHz to 82 kHz. Regression, 95 % CI of prediction, RMSE = 0.001, $R^2 = 0.913$, p-value < 0.0001, Mean of response (0.0317 m^2), Prediction interval.

3.6.2 Effect of the geometrical parameters h and b

p_T decreases as the gap between the reflector and transducers (h) increases (Eq. (3.13) and Eq. (3.14)). As h increases from 0.075 m to 0.077 m, p_T decreases by 76 % (at 78 kHz) and by 23 % (at 40 kHz) for instance, with a maximum of $1.96 \cdot 10^6$ Pa at 78 kHz for h = 0.075 m and b = 0.1 m (Figure 3.8).

V decreases as h increases (Eq. (3.15) and Eq. (3.16)) and follows the same trend observed for p_T. As h increases from 0.075 m to 0.077 m, V decreases by 34 % (at 78 kHz) and by 6 % (at 40 kHz) for instance, with a maximum of $3.99 \cdot 10^{-2}$ m^2 at 78 kHz for h = 0.075 m and b = 0.1 m (Figure 3.8 and Figure A.2). When h increases, sound waves travel a longer distance in the fluid, leading to greater sound attenuation, which in turn reduces both p_T and V [128]. Studies of Kumar et al., Gogate et al., Hodnett et al. and Chu et al. [124], [126], [127], [128] confirm our results analysis, which attest to the importance of considering the geometry together with the frequency wavelength when designing the reactor.

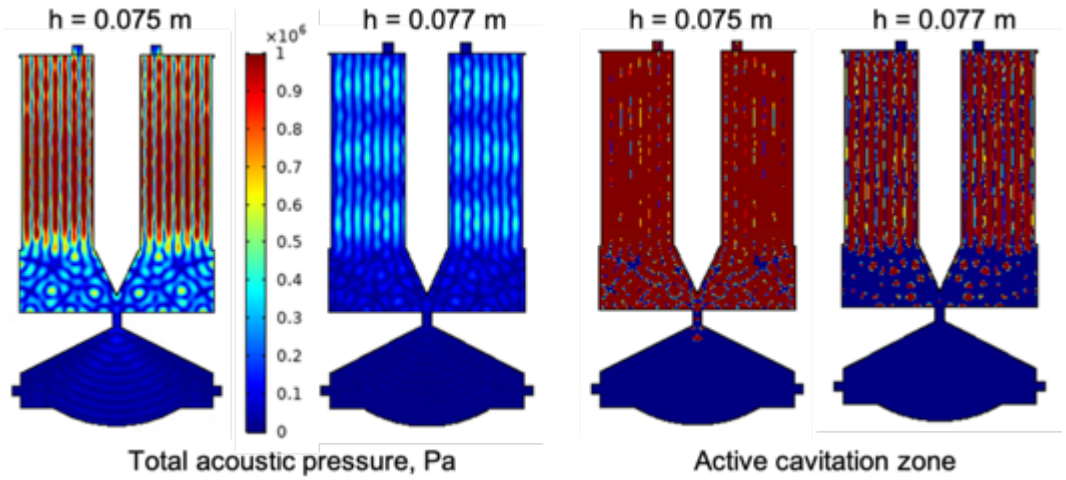

Figure 3.8 Total acoustic pressure and active cavitation zones at 78 kHz and b = 0.1 m. Comparison between h = 0.075 m and h = 0.077 m.

3.6.3 Effect of the concentration of cellulose

p_T decreases as μ increases and as ρ decreases. V decreases as μ increases and as ρ decreases. c does not have a significant effect on p_T and V, accounting for 5.2 % and 5.5 % of the variance respectively (Table 3.5). Thus, we selected μ, ρ and f, and neglected c for the linear regressions with a one-degree interaction.

Table 3.5 Predictor screening analysis of p_T and V for DOE 2.

	Predictor		Bivariate fit	
Input variables	p_T*	V*	p_T**	V**
f	48.5 %	21.0 %	0.25 > 0.05	0.85 > 0.05
μ	28.6 %	37.1 %	0.14 > 0.05	0.0032 < 0.05
ρ	17.8 %	36.4 %	0.14 > 0.05	0.0032 < 0.05
c	5.2 %	5.5 %	0.17 > 0.05	0.0048 < 0.05

*Portion of the variance explained by the predictor for p_T and V. **p-value of the density ellipse of 0.95 for p_T and V. A p-value above 0.05 means the data are not sufficiently significant to refute the assumption of random distribution within the ellipse. Whereas a p-value below 0.05 suggests the data points are not randomly distributed.

The statistical analysis generated the following regression (Figure 3.9) equation for p_T:

$$p_T = -77.1 \cdot 10^6 + 8.2 \cdot 10^4 \cdot \rho + 7.6 \cdot 10^3 \cdot f - 7.3 \cdot 10^5 \cdot (f - 59)(\mu - 0.014) \qquad (3.17)$$

p_T decreases as μ increases and as ρ decreases (Eq. (3.17)). At 78 kHz, when μ increases from $5.3 \cdot 10^{-3}$ Pa.s to $23.3 \cdot 10^{-3}$ Pa.s, and ρ decreases from 941.8 kg m^{-3} to 936.2 kg m^{-3}, p_T decreases by 75 %. The more viscous the fluid is, the greater the sound attenuation and the lower the resulting acoustic pressure [149]. Denser fluids require more energy to cavitate, thus a larger acoustic pressure.

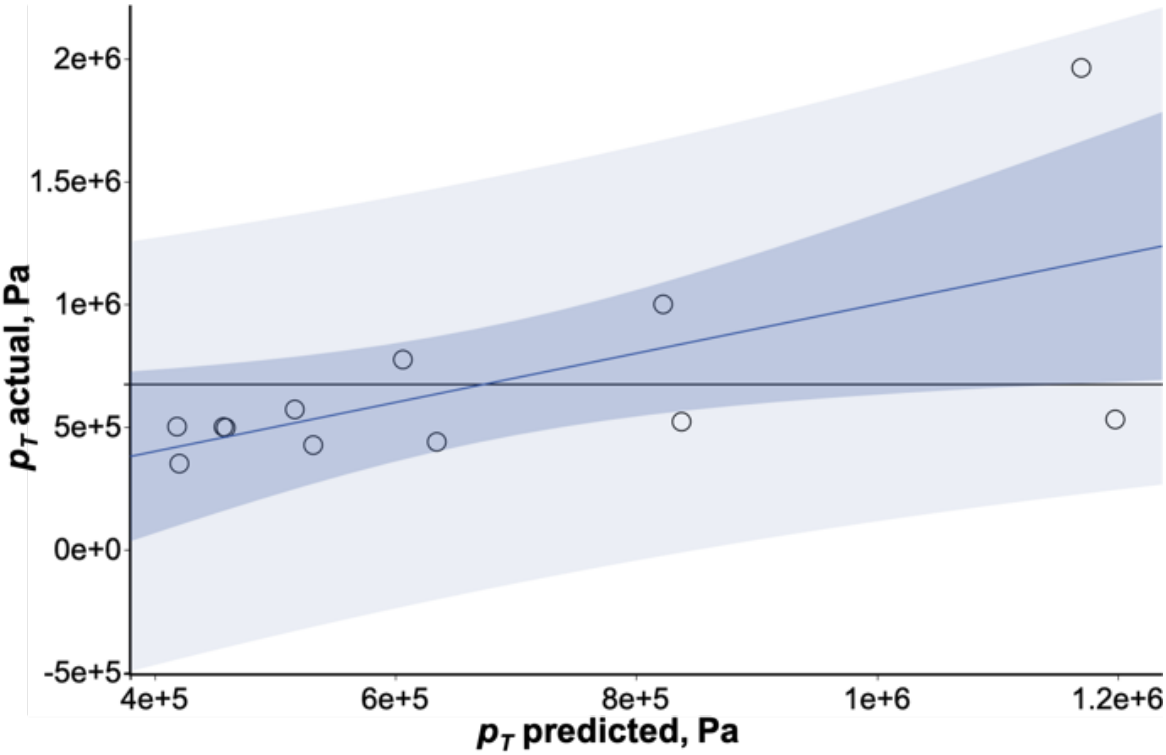

Figure 3.9 Actual by predicted plot of p_T (○). _ Regression, _ 95 % CI of prediction, RMSE = 403169, $R^2 = 0.393$, p-value = 0.2383, _ Mean of response (672635 Pa), _ Prediction interval.

The statistical analysis generated the following regression (Figure 3.10) equation for V:

$$V = 7.5 - 2.9 \cdot \mu - 8.0 \cdot 10^{-3} \cdot \rho \tag{3.18}$$

V decreases as the μ increases and as ρ decreases (Eq. (3.18)). At 78 kHz, when μ increases from $5.3 \cdot 10^{-3}$ Pa.s to $23.3 \cdot 10^{-3}$ Pa.s, and ρ decreases from 941.8 kg m^{-3} to 936.2 kg m^{-3}, V decreases by 37 %. Less viscous fluids produce more intense shock waves, leading to enhanced cavitation activity and larger V. A higher fluid density requires more energy to induce cavitation, reducing bubbles formation of bubbles and decreasing V. Schieppati et al. explained similar effects of μ and ρ on p_T and V [132].

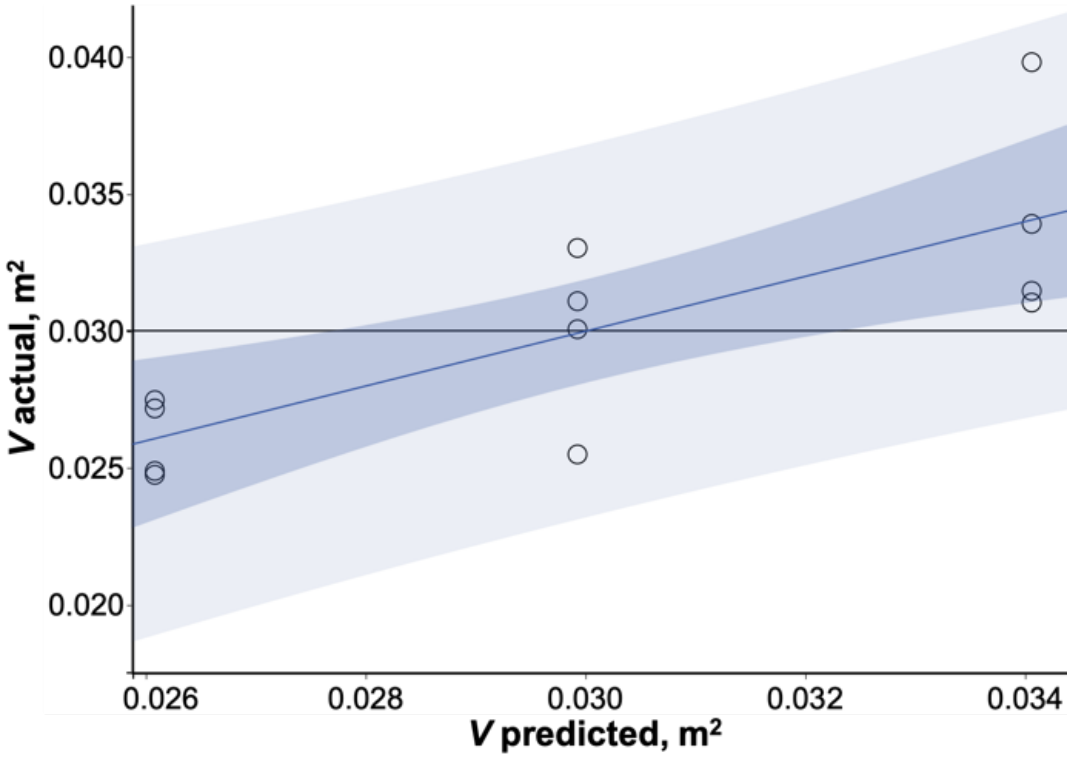

Figure 3.10 Actual by predicted plot of V (○). Regression, 95 % CI of prediction, RMSE = 0.003, R^2 = 0.597, p-value = 0.0167, Mean of response (0.0300 m^2), Prediction interval.

Although c does not have a significant effect on p_T and V (Table 3.5), a higher c means that sound waves propagate faster and vibrate more, which increases the acoustic pressure and bubbles collapse, originating larger active cavitation zones. The negligible effect of c may explain why, despite the gap being designed to be twice the wavelength at 40 kHz with a speed of sound of 1495.8 m s^{-1}, the 0.075 m gap did not yield the highest p_T nor the largest V.

3.7 Conclusions

In this study, we characterized the cavitation activity in a cylindrical ultrasonic reactor with six lateral flat transducers along the walls and a concentric high intensity focused ultrasound transducer at the bottom of the reactor. The hexagonal section reactor design ensures constructive sound waves interference. The HIFU transducer focuses US waves in the conic whistle part, which streamlines the flow towards the upper part of the reactor. COMSOL Multiphysics analyzed the propagation of sound waves and the active cavitation zones in the sonoreactor at various geometrical configurations and operating frequencies. At a fixed gap of 0.075 m between the reflector and

transducers, the software solved the propagation of sound waves and the cavitation surface area in the sonoreactor for various cellulose concentrations and working frequencies. Cavitation bubbles affect the propagation of acoustic waves, thus we included its attenuation in our model. It attenuated the acoustic pressure by 80 %, and the active cavitation surface area by 85 %. The cellulose esters concentration of 6.25 g L^{-1} resulted in the highest p_T and largest V. At 78 kHz and h = 0.075 m, with $\mu = 5.3 \cdot 10^{-3}$ Pa.s and ρ = 941.8 kg m^{-3}, the simulation generates $p_T = 1.96 \cdot 10^{6}$ Pa and $V = 3.99 \cdot 10^{-2}$ m^2.

These simulations calculated the activity throughout the entire reactor geometry, coupling the activity of lateral and HIFU transducers which are working at different frequencies. We included the root mean-squared acoustic pressure of two harmonics in the equation $\beta = \mathrm{C} \cdot p$. A future work will consider simulations of the HIFU transducer in the nonlinear regime, through simulation in the time domain. This study assumed a constant bubble equilibrium radius. As the pressure increases beyond the Blake threshold, the bubble size distribution widens, leading to nonuniform bubbles. Larger bubbles attenuate sound waves more than smaller ones, thus the present study underestimated sound waves attenuation. To improve the accuracy of the simulation, future works will include a dynamic bubble size distribution model.

Notes

We could not validate experimentally the simulations reported in this manuscript as the reactor is under construction and not yet operational at the date of submission.

Acknowledgements

Pierre Dal is thankful to Institut de l'Energie Trottier for awarding him a graduate scholarship to support his studies. We acknowledge the financial support from Khepra (United States, AL) and of the Natural Sciences and Engineering Research Council of Canada (NSERC). This research was undertaken in part, thanks to funding from the Canada Research Chairs Program.

CHAPTER 4 ARTICLE 2: ULTRASOUND-ASSISTED ESTERIFICATION OF COTTON CELLULOSE WITH LONG CHAIN FREE FATTY ACIDS

Pierre Dal, Annelise Jean-Fulcrand, Jean-Marc Lévêque, Jean-Marie Raquez, Daria C. Boffito

Submitted to Cleaner Chemical Engineering on 7 April 2025

Abstract

This study produced cellulose esters with varying degrees of substitution (*DS*) using ultrasound (US) power input, leveraging free fatty acids as esterification agent (*EA*) as a bio-based alternative to traditional chlorides, anhydrides and vinyl esters. The best conditions without US were achieved with oleic acid, with an *EA*/cellulose molar ratio of 6 and a temperature of 80°C for 24 hours, producing esters with a DS of 1.44. Applying US at 20 kHz and 4.39 W at room temperature, required less than 30 minutes to produce cellulose esters with a DS of 0.38. Then, simulation investigated the effects of the US input power, reaction volume and properties of cellulose solutions on the cavitation activity. The density, viscosity and speed of sound in the cellulose esters solutions were measured and defined them in the simulations as 936.2 kg m^{-3}, $23.3 \cdot 10^{-3}$ Pa.s, and 1495.8 m s^{-1} for 25 g L^{-1}. Simulations with conditions resulting in the highest *DS* with US were characterized by the smallest volume acoustic cavitation volume and the lowest *u*: $9.60 \cdot 10^{-8}$ m^3 and 40.06 m s^{-1}. US-assisted esterification produced thermoplastic esters with 18 W g^{-1} of cellulose against 93 W g^{-1} for conventional esterification.

Keywords: Cellulose, Esterification, Free Fatty Acids, Ultrasound, Sonochemistry, COMSOL

4.1 Introduction

Cellulose is the primary structural component of plant cell walls and the most abundant bio-based polymer. It consists of anhydroglucose units (AGU) linked by glycosidic bonds. Due to its strong hydrogen bonding network, cellulose is poorly soluble, and difficult to process in most organic solvents and in its melted form. Converting waste cellulose into esters with thermoplastic properties offers a biomass-based alternative to petroleum-derived thermoplastics. Long chain cellulose esters with a degree of substitution (*DS*) higher than 0.7 are thermoplastic and can be processable without the need for plasticizer [54].

Conventional esterification reactions can be carried out in either homogeneous or heterogeneous phases. Homogeneous reactions typically produce esters with a controlled *DS* [150] and a uniform distribution of functional groups along the cellulose chains [50]. However, these esterification reactions use lithium chloride/N,N-dimethylacetamide (LiCl/DMAc) as a solvent, which is expensive, difficult to recycle [12], non-volatile and toxic [90]. In the case of heterogeneous esterification, it involves an excess of esterification agent (*EA*) and pyridine or sulfuric acid as a catalyst [50]. Drawbacks include uneven functionalization, low *DS*, long reaction times (5 h to 16 h) [12], side reactions [50] and degradation of cellulose [49].

Common esterification agents (*EA*) include chlorides, anhydrides, and vinyl esters [12]. Chlorides generate hydrochloric acid (HCl), which is corrosive and degrades the cellulose and esters [12], [151]. Anhydrides produce cellulose esters with low *DS* in LiCl/DMAc. Vinyl esters require the removal of the vinyl alcohol formed [12].

As an alternative, free fatty acids (FFA) offer key advantages as they are derived from biomass, require mild reaction conditions and form limited amounts of by-products [12], [55], [152]. Unlike other esterification routes, FFA do not degrade the cellulose chains but require an activating agent to increase their reactivity [12]. For instance, Willberg-Keyriläinen and Ropponen esterified cellulose with various *EA* in LiCl/DMAc, achieving the highest *DS* (1.3) with octanoyl chloride [12]. However, it generated HCl, requiring neutralization by N,N-dimethyl-4-aminopyridine (DMAP) to prevent cellulose from hydrolysis [53]. Vinyl esters produced the lowest *DS* (below 0.1) and required the removal of the vinyl alcohol formed [12].

Using p-toluenesulfonyl chloride (p-Tos) as an activating agent alongside 3-(hydroxyphenylphosphinyl)-propanoic acid enabled to produce thermoplastic esters with a DS of 1.42 in LiCl/DMAc at 40 °C for 24 h [51]. Similarly, Almasi et al. produced cellulose nanofibers esters in pyridine and p-Tos, achieving a *DS* of 1.82, with oleic acid at 50 °C for 4 h [52]. Uschanov et al. esterified cotton linters cellulose with oleic acid for 4 h, resulting into a DS of 1.25 [153]. Costa et al. reported α-cellulose esters with a *DS* of 2.45 with stearic acid, at 80 °C for 5 h [154]. In contrast, Granström et al. used 1-ethyl-3-(3-dimethylaminopropyl) carbodiimide hydrochloride (EDC) to esterify microcrystalline cellulose (MCC) esters in 1-allyl-3-methylimidazolium chloride, but side reactions led to a *DS* of 0.16 due to the formation of side products.

Process intensification (PI) aims to enhance efficiency by reducing plant size, cutting costs and energy use by 20–80%, and decreasing chemical consumption by factors of 10 to 1000 [94]. Mechanochemistry such as ball milling, is effective for cellulose esterification. Huang et al. obtained a *DS* of 0.041 after 150 min at 500 rpm, with acetic anhydride improving oleic acid reactivity [155]. Hou et al. esterified MCC in DMAc with DMAP, EDC, and oleic acid, reaching a *DS* of 2.55 after 4h at 500 rpm [156]. Lease et al. produced esters with a *DS* of 0.21 from MCC, oleic acid and p-Tos in 1-butyl-3-methylimidazolium acetate using a magnetic mortar at 100 °C for 12 h, preserving cellulose crystallinity. They attributed the low *DS* to surface modification rather than bulk esterification [75].

Ultrasound (US) is a relevant PI technology that intensifies processes via macro shear rates and acoustic cavitation. The implosion of cavitation bubbles creates extreme localized conditions, with temperature of ~5 000 K, pressure up to 500 atm, fluid microjets, and reactive radicals [77]. These conditions improve heat and mass transfer, and accelerating chemical reactions, especially esterification [47]. In liquid-liquid systems, US emulsifies phases, increasing interfacial surface area and reaction rates [95]. In liquid-solid systems, cavitation bubbles collapse on solid surfaces, producing high-speed jets, localized temperatures and pressures, and enhancing liquid-solid mass transfer [157].

US has been rarely used for cellulose dissolution and esterification, because extended sonication can reduce molecular weight by cleaving polymer linkages [85]. At 525 kHz, high-frequency US selectively depolymerizes MCC into glucose at 60 °C by generating H• and •OH radicals inside the cavitation bubbles, from the unmodified cellulose and solvent [86]. These radicals break glycosidic bonds on the cellulose surface. Bhaumik and Dhepe noted that US irradiation disrupts hydrogen bonds and reduces cellulose crystallinity, as US energy exceeds the 21 kJ mol^{-1} required for hydrogen bond dissociation [87], [158].

Treating cellulose with US decreased the dissolution time by 68 % [88] to 92 % [90] compared to silent conditions. However, regenerated cellulose after US showed a 28% drop in degree of polymerization (DP) compared to cellulose dissolved without US [88]. In another study, US simultaneously degraded and esterified cellulose pulp into NCC at 40 kHz during 5 h at 70 °C, increasing yield by 77 % and *DS* by 110 % compared to silent conditions [89]. They attributed this behavior to selective degradation of the amorphous regions, improving reagent accessibility to the

internal structure of cellulose, as US energy (10–100 kJ mol^{-1}) exceeds the hydrogen bond dissociation thresholds [77].

Despite these benefits, US pretreatment can sometimes reduce esterification efficiency. Liu et al. pretreated sugarcane bagasse in pyridine at 30 °C using US at 40 kHz for 50 min, resulting in a 15% decrease in ester yield compared to non-pretreated biomass, which was attributed to a reduction in molecular weight [91]. US enhanced esterification in ILs as Ma et al. reported an 82% *DS* increase when extending US treatment from 20 to 120 min during cellulose esterification with glutaric anhydride in 1-butyl-3-methylimidazolium chloride ([Bmim]Cl) at 40 kHz and 85 °C [92]. Similarly, *DS* increased by 46 % compared to silent conditions with phthalic anhydride in [Bmim]Cl at 105 ˚C, US at 40 kHz for 60 min, [93].

An US bath operating at 40 kHz and 35 °C was adopted to esterify MCC, in DMAc with DMAP**,** EDC and oleic acid as *EA* [11]. DMAP acted the catalyst, and EDC as the dehydrating agent to convert oleic acid into anhydride. They obtained the highest *DS* of 1.55 in DMAc after 6 h of reaction, a molar ratio oleic acid/MCC of 6:1 and a US intensity of 300 W m^{-2}. US improved reactivity by enhancing cellulose dissolution, exposing hydroxyl groups, and breaking fiber aggregates, leading to a homogeneous reaction medium that promotes the reaction with oleic acid [11].

The present research explores the esterification of cellulose with long chain FFA (oleic acid and stearic acid) to make cellulose thermoplastics, enhanced by US, representing a combination not previously investigated in the literature so far. Unlike earlier studies, this work integrates the approaches just mentioned to achieve reduced reaction time, lower consumption of possibly harmful chemicals and decreased energy requirements for producing thermoplastic materials (long chain FFA act as an internal plasticizer) or oligomers from cotton linters and cellulose fibers, through acoustic cavitation and acoustic streaming. Additionally, COMSOL Multiphysics simulated the US activity – acoustic pressure, active cavitation volume and acoustic streaming velocity – to understand the phenomena occurring within the reactor. The proposed process offers a promising way for the conversion of renewable feedstocks into biodegradable and potentially compostable thermoplastic materials or depolymerized cellulose esters with biomass-derived FFA, an area documented in a limited extent.

4.2 Material and methods

4.2.1 Materials

All chemicals were used as received, i.e. N,N-dimethylacetamide (DMAc, 99 %, Thermoscientific), lithium chloride (LiCl, 99 %, Sigma), p-toluenesulfonyl chloride (p-Tos, 98 %, Thermoscientific), pyridine (99 %, Sigma) oleic acid (90 %, Aldrich), stearic acid (Anachemia), oleoyl chloride (89 %, Sigma), anhydrous ethanol (Commercial Alcohols).

This study included two sources of cellulose: cotton linters cellulose (C1, DP = 138, Sigma), and cellulose fibers (C2, DP = 926, Recyc php). This latter is recycled from used diapers by Recyc php.

4.2.2 Esterification of cellulose

The esterification consisted to dissolve cellulose as it follows: 10 mL of DMAc at 130 °C were added to activate 0.25 g of cellulose for 2h at 1150 rpm, we added 0.75 g of LiCl [5]). When the cellulose is fully dissolved and the mixture is transparent, we added p-Tos and oleic acid with a *EA*/cellulose/p-Tos of 1:6:6 molar ratio (Figure 4.1). Further reaction details are found in the Appendix B.

We built three designs of experiments (DoE), applying a fractional factorial layout to all. The first one included six experiments, the second ten, and the third nine. The first DoE aimed to confirm the effect of the molar ratio of *EA*/cellulose, temperature, cellulose source and FFA (saturated or not) on the esterification of cotton cellulose without US. The independent variables are:

- Molar ratio of EA/cellulose, 3 and 6;
- Temperature, 40 °C, 60 °C and 80 °C;
- Cellulose, C1 and C2;
- FFA, oleic acid and stearic acid.

The second and third DoE investigated the US-assisted esterification of C1 with oleic acid, the independent variables are:

- Temperature, 20 °C, 40 °C, 60 °C and 80 °C;
- US power (P), 4.39 W, 6.70 W and 9.01 W;
- Total reaction volume (v), 32.2 mL, 21.5 mL and 10.7 mL.

The response variables are the *DS* determined by ^{1}H NMR-HRMAS spectroscopy for the conventional esterification and by gravimetric analysis for the US-assisted esterification (for US-assisted esterification exclusively as it provided a larger sample set and enabled a more reliable comparison with *DS* by ^{1}H NMR analysis). For the sample obtained with oleoyl chloride in pyridine (Table 4.1), we determined the *DS* by ^{1}H NMR analysis. Table 4.1 lists all the experiments and operating conditions. Gravimetric analysis tends to overestimate the *DS* because it cannot differentiate substitution from residual solvents and FFA or reaction by-products. It is emphasized as the esterification agent is a long-chain FFA like oleic acid, which persist into the cellulose structure after purification [159]. ^{1}H NMR analysis provides a more selective determination of the *DS*. It distinguishes substituted and unsubstituted cellulose groups [160]. However it has limitations such as wrong *DS* determination in case of inadequate preparation [161], or limited sample solubility and poor resolution in case of low *DS* [162].

Statistical analysis identified significant dependent variables and the relationship within the data. Initially, a predictor screening analysis with Bootstrap forest partitioning, identified the dependent variables contributing the most variance to the response variables. Then, we eliminated the non-significant variables to develop a linear regression model that predicted the response variables with a 95 % confidence interval (CI) accuracy. We plotted the actual vs predicted responses, where the actual refers to the *DS* obtained experimentally, whereas predicted refers to the *DS* determined by the prediction regression.

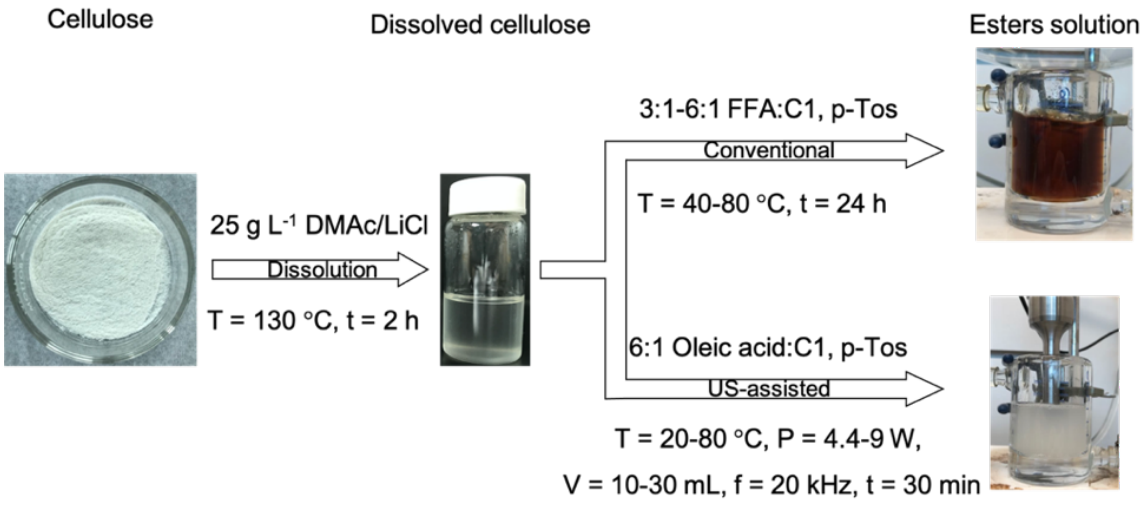

Figure 4.1 Cellulose dissolution and esterification steps, for conventional or US-assisted method. Precipitation in ethanol follows the esterification.

The labeling of the sample names is detailed as follows, with all parameters provided in Table 4.1. The reference parameters for sample preparation involve using cellulose C1 and oleic acid as the *EA*, with an *EA*/cellulose ratio of 6. Samples prepared without US are labeled as C#, while those prepared with US are labeled as U#. The first number in the label represents the esterification temperature, ranging from 20 °C to 100 °C. For samples prepared under silent conditions (without US), the second identifier denotes specific parameters. C80_2 was prepared using cellulose C2, C80_3 used a *EA*/cellulose ratio of 3:1, and C80_S used stearic acid as the *EA* instead of oleic acid.

C100 serves as a reference material, produced at 100 °C using oleoyl chloride as the *EA*.

For US-assisted esterification, the second digit in the label corresponds to the *P*, ranging from 1 (4.39 W) to 3 (9.01 W). The third digit indicates the power density (*PD*), ranging from 1 (139 W L^{-1}) to 6 (839 W L^{-1}). For example, U20_1_1 was prepared at 20 °C, with a *P* of 4.39 W and a *PD* of 139 W L^{-1}. In Table 4.1, the mentioned power is the US power delivered to the reaction medium, calculated by calorimetric calibration [163].

The first experiment (#1) in Table 4.1 corresponds to the experiment in pyridine with oleoyl chloride. The second part of the table (experiments #2-#7) corresponds to the DoE of conventionally stirred esterification (silent conditions). The third part (experiments #8-#17) corresponds to the DoE of US-assisted esterification with DS determined by ^{1}H NMR as a response. The fourth part (experiments #18-#26) corresponds to the DoE of US-assisted esterification with DS determined by gravimetric analysis as a response.

Table 4.1 Design of experiments.

#	Experiment	Cellulose	*EA*	*EA*/cellulose (mol mol-1)	Temperature (°C)	Time (h)	*P* (W)	*PD* (W L-1)	*DS*
1	C100	1	Oleoyl chloride	6	100	1	-	-	2.62 ± 0.40
2	C40	1	Oleic Acid	6	40	24	-	-	0.87 ± 0.15
3	C60	1	Oleic Acid	6	60	24	-	-	0.61 ± 0.11
4	C80	1	Oleic Acid	6	80	24	-	-	1.44 ± 0.25
5	C80_2	2	Oleic Acid	6	80	24	-	-	0.37 ± 0.06
6	C80_S	1	Stearic Acid	6	80	24	-	-	0.13 ± 0.02
7	C80_3	1	Oleic Acid	3	80	24	-	-	0.33 ± 0.06
8	U40_1_4	1	Oleic Acid	6	40	0.5	4.39	409	0.21 ± 0.04
9	U60_1_4	1	Oleic Acid	6	60	0.5	4.39	409	0.14 ± 0.02
10	U80_1_4	1	Oleic Acid	6	80	0.5	4.39	409	0.14 ± 0.02
11	U40_2_5	1	Oleic Acid	6	40	0.5	6.70	624	0.17 ± 0.03
12	U40_3_6	1	Oleic Acid	6	40	0.5	9.01	839	0.029 ± 0.005
13	U40_1_2	1	Oleic Acid	6	40	0.5	4.39	204	0.15 ± 0.02
14	U40_1_1	1	Oleic Acid	6	40	0.5	4.39	136	0.18 ± 0.03
15	U20_1_1	1	Oleic Acid	6	20	0.5	4.39	136	0.38 ± 0.06
16	U20_2_2	1	Oleic Acid	6	20	0.5	6.70	208	0.32 ± 0.05
17	U20_3_3	1	Oleic Acid	6	20	0.5	9.01	280	0.30 ± 0.05
18	U40_1_1	1	Oleic Acid	6	40	0.5	4.39	136	0.59 ± 0.11
19	U60_1_1	1	Oleic Acid	6	60	0.5	4.39	136	0.67 ± 0.03
20	U80_1_1	1	Oleic Acid	6	80	0.5	4.39	136	0.48 ± 0.02
21	U40_2_2	1	Oleic Acid	6	40	0.5	6.70	208	0.74 ± 0.03
22	U40_3_3	1	Oleic Acid	6	40	0.5	9.01	280	0.42 ± 0.02
23	U40_1_2	1	Oleic Acid	6	40	0.5	4.39	204	0.30 ± 0.01
24	U20_1_1	1	Oleic Acid	6	20	0.5	4.39	136	1.79 ± 0.03
25	U20_2_2	1	Oleic Acid	6	20	0.5	6.70	208	1.58 ± 0.04
26	U20_3_3	1	Oleic Acid	6	20	0.5	9.01	280	1.20 ± 0.10

4.2.3 FTIR attenuated total reflection (ATR) analysis

The functional groups of ester samples were identified by a Perkin Elmer Spectrum 65 Fourier-transform infrared (FTIR) spectrometer with an attenuated total reflectance Miracle ATR accessory. We used 32 scans with a resolution of 2 cm^{-1} from 4000 cm^{-1} to 600 cm^{-1}.

4.2.4 Determination of the DS

We determined the *DS* after high-resolution magic angle spinning (HRMAS) ^{1}H NMR in dimethylsulfoxide (DMSO) with sodium trimethylsilylpropanesulfonate (DSS) as a standard. The equipment was a Bruker AVANCE II operating at 400 MHz with a probe cross polarization magic angle spinning (CPMAS). We described the procedure in Section B.3.

For these calculations, it is assumed that the molecular weight of the oleic acid chain was at 265.5 g mol^{-1} by considering that during esterification a hydroxyl group is converted into ester. All the oleic acid in each sample was grafted onto the cellulose chains, which is confirmed by FTIR spectra (Figure 4.3).

Additionally, we verified the *DS* by gravimetric analysis. After drying and weighing cellulose esters samples, we calculated the *DS* with the following equation:

$$DS = \frac{m_1 - m_0}{(M - 1) \cdot n_0} \tag{4.1}$$

where m_1 is the weight of the ester's sample, m_0 is the weight of unmodified cellulose, n_0 is the number of moles of unmodified cellulose, M is the molecular weight of an oleoyl group (M = 265.5 g mol^{-1}), and 162 is the molecular weight of AGU in g mol^{-1}.

4.2.5 X-ray Diffraction (XRD)

A Bruker D8 Advance diffractometer was employed to scan unmodified cellulose, sample U20_1_1 (lowest power density and temperature, highest *DS*) and sample U80_1_1 (highest temperature) from 2° to 50° of 2θ. It is essential to determine whether esterification preserves or disrupts the cellulose structure.

4.2.6 Thermal behavior

Prior to differential scanning calorimetry (DSC), a TA Instruments thermogravimetric analyzer (TGA) Q500 was used to determine the weight loss of the sample C80, which had the highest *DS*

after conventional esterification. The sample was heated from 25 °C to 500 °C at 10 °C min^{-1} under a 40 mL min^{-1} nitrogen flow.

The transition temperatures of the ester samples were determined with a TA Instruments calorimeter Q200 with an RSC 90 cooling system using a heating ramp from -70 °C to 180 °C at 20 °C min^{-1} and with a nitrogen flow of 50 mL min^{-1}. The sample weight was around 3 mg. It reveals glass transition and melting temperatures of the esters to identify operating temperatures for further processing.

4.2.7 Viscosity and density measurements

The numerical simulations aimed to calculate the minimum acoustic pressure (p_{min}), maximum acoustic pressure (p_{max}), cavitation zones volume (V) and acoustic streaming velocity (u) in cellulose esters solution at 25 g L^{-1}. We approximated the fluid to Newtonian, and measured its density (ρ) and viscosity (μ) as data to feed to COMSOL Multiphysics. We measured ρ and μ at various temperatures, after 2 h of cellulose esterification at 25 g L^{-1}.

An Anton Paar DMA 4500 density meter instrument was used to determine ρ. μ was measure with a Thermo Scientific Haake Viscotester iQ. The rheometer has a coaxial cylinder configuration and holds 3mL samples. The ramp was: 120 s at a shear rate of 1 s^{-1}, followed by an increase in the shear rate to 500 s^{-1}.

Table 4.2 Properties of cellulose esters solutions at 20 °C.

Cellulose concentration, g L^{-1}	Speed of sound, m s^{-1}	Density, kg m^{-3}	Viscosity, Pa·s
25	1495.8	936.2	$23.3 \cdot 10^{-3}$

4.2.8 Speed of sound measurements

The speed of sound (c) in cellulose ester solutions was measured using an Olympus V306 immersion transducer. The transducer's active element has a diameter of 13 mm. Operating at a frequency of 2.25 MHz, the transducer transmitted signals through a polystyrene container holding 50 mL of the cellulose ester solution. It was affixed to the container’s side, and the solution was introduced using a pipette to minimize movement during filling and emptying, ensuring the acoustic waves propagated perpendicularly to the opposite container wall. The transducer was

connected to an Agilent Technologies 33220A 20 MHz waveform generator and a GW Instek GDS-1000A-U Series oscilloscope for monitoring.

Initially, a signal was transmitted through deionized water to measure the round-trip distance of the sound wave within the fluid. It was assumed that the wave propagated solely through the water, with a speed of 1498 m s^{-1}, since it was not feasible to determine the thickness of the gel and the polystyrene wall. The wave covered a total distance of 44.67 mm. Seven measurements of the sound speed were taken via the oscilloscope, and an average value was calculated. These results were subsequently input into COMSOL Multiphysics (Table 4.2).

This assumption that the wave traveled exclusively through the liquid underestimated the actual speed of sound. In reality, the speed of sound in polystyrene is approximately twice that in water, oils, or ethanol [148], which overestimated the attenuation of the sound waves in the solutions.

4.3 Mathematical model and simulation

COMSOL Multiphysics 6.1 solved the Helmholtz equation, a steady state form of the wave equation, to determine p_{min} and p_{max} in the sonoreactor (Figure 4.2). To determine V, we considered the acoustic pressure above the cavitation pressure threshold (Figure 4.2). The turbulent flow module calculated u, solving the Navier-Stokes equation (Figure 4.2).

It is assumed that the fluid is incompressible and Newtonian, the sound waves exhibit linear behavior, and the shear stress could be neglected. The bubble to liquid volume ratio is low so the system is computed as a single-phase fluid [113]. The properties of the sonicated fluid are independent of the temperature and bubble volume fraction.

US waves reflect with a deviation of acoustic impedance (Z). Z is product of the material's density and speed of sound. The following boundary conditions were applied:

1. At the boundary liquid-glass, Z = 2230 kg m^{-3}·5640 m s^{-1}, for steps 1 and 2a. For step 2b, we applied a no-slip boundary condition.
2. At the boundary liquid-air Z = 1.2 kg m^{-3}·343 m s^{-1}, for steps 1 and 2a. For step 2b, we applied a pressure outlet, with a pressure of 0 Pa.
3. At the boundary liquid-probe Z = 4470 kg m^{-3}·4987 m s^{-1}, for steps 1 and 2a. For step 2b, we applied a slip boundary condition.
4. At the tip of the probe, a pressure amplitude p_a was set for steps 1 and 2a.

We detail, in Section B.4, the equations solved during the simulations, the assumptions, the geometry, the boundary conditions (Figure B.2) and the mesh of the model [132].

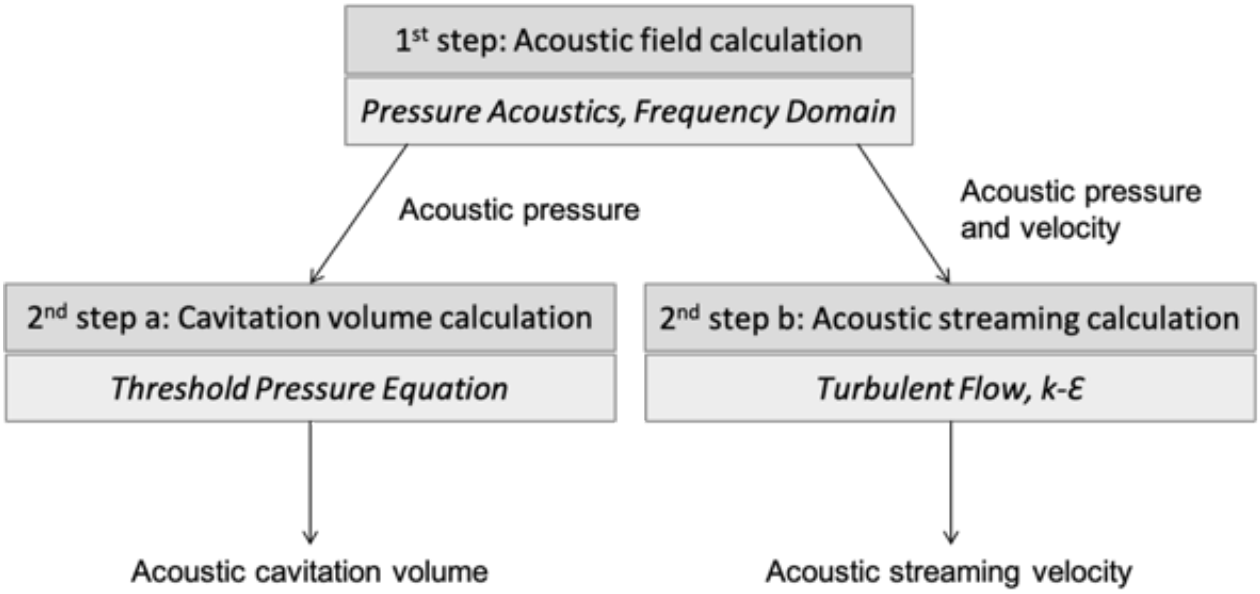

Figure 4.2 Simulation steps for acoustic pressure, cavitation volume and acoustic streaming velocity determination.

The independent variables for these simulations are:

- P, 4.39 W, 6.70 W and 9.01 W;
- v, 32.2 mL, 21.5 mL and 10.7 mL;
- Temperature, 20 °C, 40 °C, 60 °C and 80 °C;

The response variables are p_{min}, p_{max}, V and u. A statistical analysis identified significant dependent variables and relationship within the data, as in Section 4.2.2.

4.4 Results and discussion

4.4.1 Cellulose sources and fatty acids effects

Before conducting US-assisted esterification, we investigated the use of long chain FFA instead of acyl chlorides and anhydrides to produce cellulose esters, aiming for safer, less expensive and biomass-derived *EA*. During the synthesis process, the influence of parameters such as the *EA*/cellulose ratio, the source of cellulose, and the type of FFA, was investigated on the *DS.* The

results are presented in Table 4.1. We obtained a *DS* five times higher, with oleic acid at a molar ratio p-Tos/*EA*/cellulose of 6:6:1 compared to 3:3:1 (1.44 against 0.33). Hou et al. observed the same trend due to an increased frequency of interactions between the OH groups of cellulose and the *EA* [11]. When we compare the nature of *EA*, the use of stearic acid resulted in lower *DS* than oleic acid, with a *DS* of 0.13 against 1.44, respectively. In our case, the chain length remains unchanged, but the degree of saturation differs, with only one C=C unsaturation on the oleic acid chain. Crépy et al. produced cellulose stearate with a *DS* of 2.3 and cellulose oleate with a *DS* of 2.9. They mentioned that the unsaturation facilitates the reaction, but gave no further details [164]. The double bond in oleic acid restricts chain mobility, but its *cis*-configuration makes it less thermodynamically stable than stearic acid, and thus more reactive [165]. The double bond in the alkyl chain increases the electron density, making the carboxylic group of oleic acid more reactive toward attack from the hydroxyl group of cellulose than the carboxylic group of stearic acid. The unsaturation also reduces Van der Waals interactions among the oleic acid molecules, which increases the diffusion of oleic acid and reduces its melting point, increasing the contact with cellulose hydroxyl groups. The reduced Van der Waals interactions among the oleic acid molecules also decreases the viscosity of the reaction medium, facilitating the mixing [159].

We synthetized esters from two different sources of cellulose, C1 with a DP of 138, and C2 with a DP of 926 (Figure B.1). C1 and C2's esters had a *DS* of 1.44 and 0.37, respectively. Similarly, Willberg-Keyriläinen et al. and Uschanov et al. observed that reduction in cellulose molecular weight increased with the *DS* of esters produced [153], [166]. Willberg-Keyriläinen et al. increased the *DS* by a factor of 3 when molecular weights decreased from 520 kg mol^{-1} to 80 kg mol^{-1}. They explained it by the increased accessibility of the cellulose surface for reaction [166].

In this study, the degree of substitution (*DS*) increases with the EA/cellulose ratio when using C1 and decreases when using C2. The *DS* also increases with oleic acid and decreases with stearic acid. A possible explanation for the low *DS* obtained could be the precipitation of solid, forming heterogeneous phase, as we noticed during the esterification reaction. This affects the mixing efficiency, as the reaction mixture had a stationary solid layer on top and a lower liquid layer [167].

The comparison of FTIR spectra of cellulose, FFA, and esters samples show the progress of esterification and the impact of our different steps used for washing and extraction. Following a rigorous washing and extraction method, all samples do not exhibit any traces of solvent nor FFA

(Figure 4.3). Esters samples (C80 and C80_3) have characteristic peaks at 1740 cm^{-1} and 1150-1160 cm^{-1} (Figure 4.3), which correspond to the vibration of C=O and C-O from ester groups, respectively, confirming the formation of ester bonds onto the cellulose backbone. This observation is supported by a decrease in the intensity of the peak at around 3340 cm^{-1}, characteristic of -OH groups, shifting towards higher wavenumber (Figure 4.3). This suggests the substitution of hydroxyl groups into esters [53], reducing hydrogen bonding and enabling the dissolution of cellulose [6], [60].

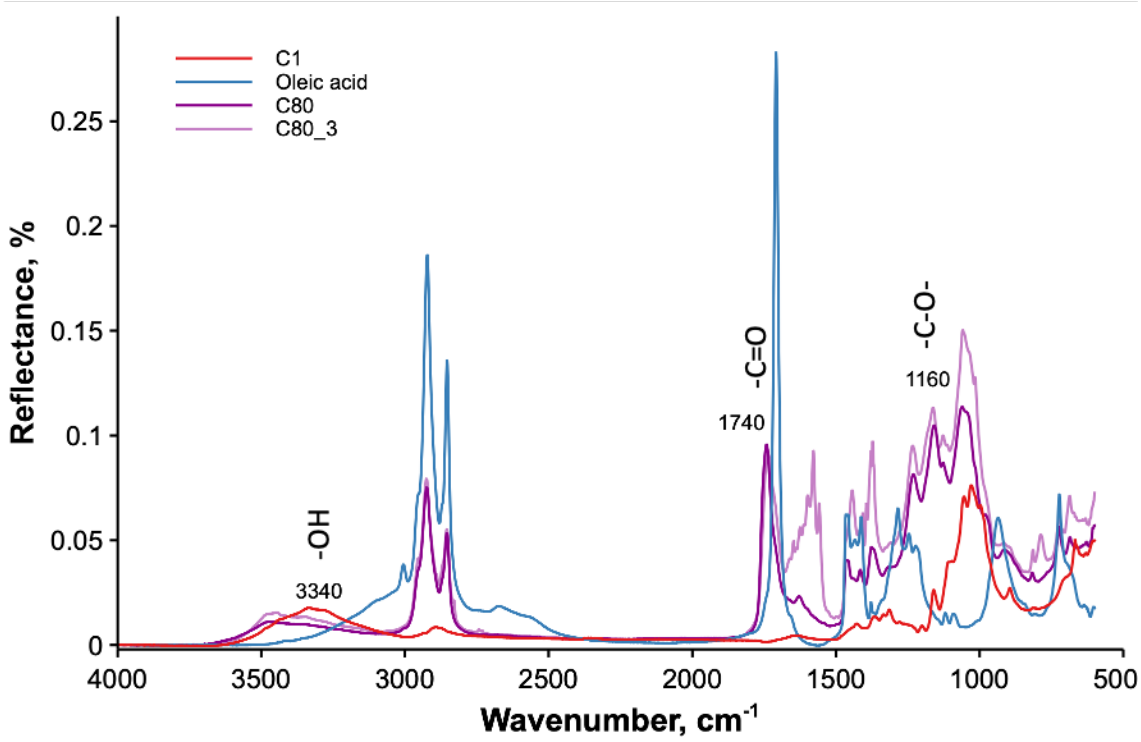

Figure 4.3 FTIR spectra of the unmodified cellulose C1, unmodified oleic acid and cellulose esters produced with various *EA*/cellulose ratios, 6:1 and 3:1.

In the TGA, the degradation took place in two stages for C1 and in three stages for C100 and C80 (Figure 4.4). The initial weight loss is attributed to the evaporation of adsorbed water [168]. Esters samples started to decompose at lower temperatures (210 °C for C100, and 170 °C for C80) compared to unmodified cellulose (295 °C), as reported by Costa et al. [154]. Grafting long chains FFA to cellulose decreased the materials crystallinity, which lowers decomposition temperature of cellulose derivatives [168]. The lower decomposition temperature of cellulose esters also occurs due to the fact that FFAs alone have a lower decomposition temperature than cellulose [153].

The primary degradation step of unmodified cellulose occurs at 340 °C, resulting in the breakdown of cellulose into carbon dioxide and water. In contrast, for cellulose esters (358 °C for C100 and 300 °C for C80), this step involves the degradation of the cellulose backbone, ester groups, and unsaturated bonds of oleic chains. The third degradation step of esters corresponds to the decomposition of oleic acid alkyl chains into volatiles [11]. This step results from the crosslinking and crystallization of aliphatic chains of saturated free fatty acids (FFA) into ordered structures during heating. Jandura et al. observed this last degradation in the range of 300 °C to 400 °C for oleic acid cellulose esters with a *DS* as low as 0.08 [168].

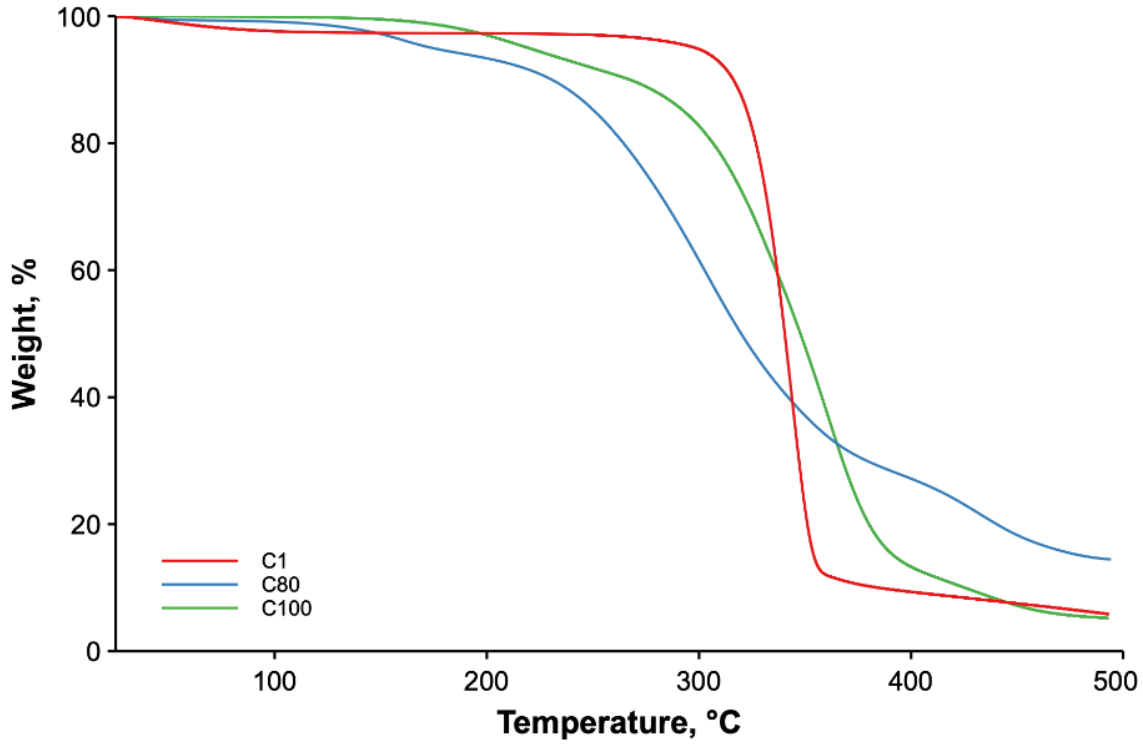

Figure 4.4 Weight loss of unmodified cellulose (C1) and esters treated at two different temperatures (C80 and C100) and exhibiting the best *DS*.

4.4.2 Effect of temperature

The reaction temperature affects both the conventional and the US-assisted processes. In conventional esterification, the *DS* increases by 66 % from 40 °C to 80 °C. For the DoE of conventional esterification, the regression (Figure 4.5) resulted in the following equation:

$$DS = -0.499 + 0.285 \cdot \frac{T - 60}{20} + 0.464 \cdot \frac{\frac{EA}{C} - 4.5}{1.5} + C \cdot \begin{pmatrix} 1 \rightarrow 0.444 \\ 2 \rightarrow -0.444 \end{pmatrix} + EA \cdot \begin{pmatrix} \mathrm{Ol} \rightarrow 0.564 \\ \mathrm{St} \rightarrow -0.564 \end{pmatrix} \quad (4.2)$$

All dependent variables have a significant effect on the *DS*, accounting for a percentage of the variance on the same order of magnitude (Table 4.3). The *DS* increases with temperature (*T*) (Eq. (4.2)).

Lease et al. reported a similar behavior with *DS* increasing nearly 200-fold when the temperature was raised from 50 °C to 100 °C [75]. Jebrane et al. quantified esterification by measuring the intensity of the FTIR peak corresponding to the C=O vibration, which increased from 0.2 to 0.6 as the temperature rose from 90 °C to 125 °C, confirming the increase in *DS* [169]. Mikkola et al. also reported an increase in the *DS* from 0.01 at 60 °C to 0.31 at 100 °C [90].

Table 4.3 Predictor screening analysis of *DS* determined by ^{1}H NMR for esters produced with conventional conditions.

Predictor	Portion*
Temperature	31.6 %
EA	30.8 %
EA/Cellulose	23.1 %
Cellulose	14.5 %

*Portion of the variance from the prediction.

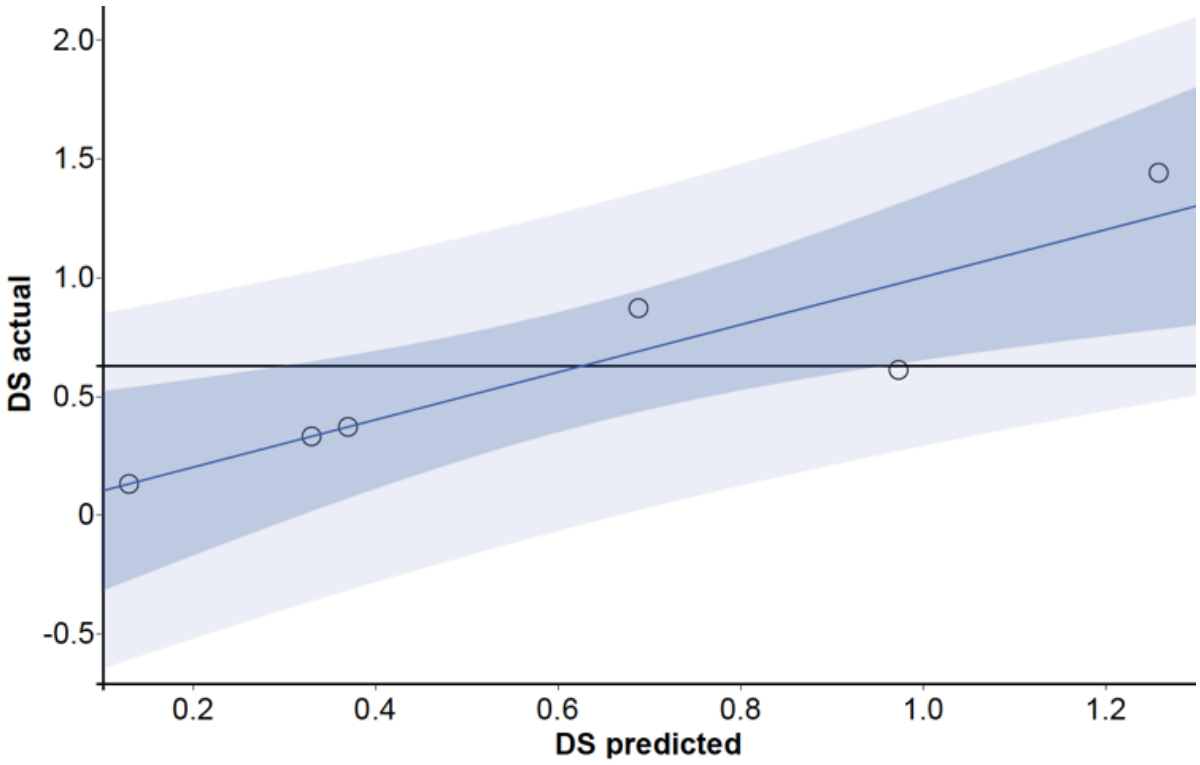

Figure 4.5 Actual vs. predicted *DS* (○) determined by ^{1}H NMR for esters produced with conventional conditions. _ Regression, ▪ 95 % CI of prediction, RMSE = 0.445, R^2 = 0.823, *p*-value = 0.0125, _ Mean of response (0.625), ▪ Prediction interval.

The peaks at 2920 cm^{-1} and 2850 cm^{-1} (Figure 4.6) are characteristic of the CH_2 stretching of alkyl chains from FFA. The unsaturation of oleic acid is indicated by the peaks at 3005 cm^{-1} (C-H stretching) and 1630 cm^{-1} (C=C stretching), respectively. Additionally, the peak at 1460 cm^{-1} is characteristic of C-H scissoring in CH_2 and CH_3 [169], and the peak at 920 cm^{-1} corresponds to the C-H bending of -CH=CH- groups [170]. The carbonyl stretch vibration (C-O) is observed at 1235 cm^{-1} [171]. Peaks at 720 cm^{-1} are characteristic of at least four CH_2 groups linked [53]. These peaks are present in all our samples spectra, however, they alone do not confirm esterification, as they could be attributed to unreacted FFA. Thus, we determined the *DS* by gravimetric and ^{1}H NMR analyses.

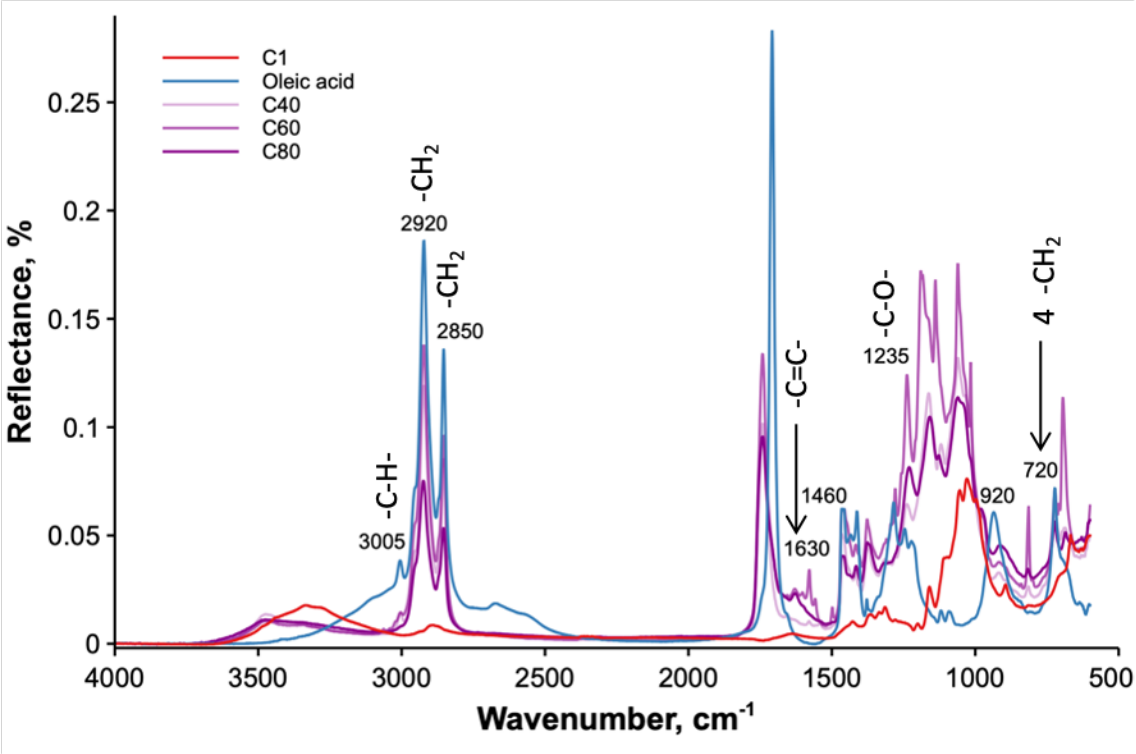

Figure 4.6 FTIR spectra of reference cellulose C1, oleic acid and cellulose esters produced at various temperatures.

Regarding samples prepared with US (with *DS* determined by gravimetric analysis) at a fixed *PD* of 136 W L^{-1}, an increase in reaction temperature from 20 ˚C to 80 ˚C resulted in a decrease in the *DS* from 1.79 to 0.48 (Table 4.1). However, Ma et al. showed the opposite trend by reporting that the increase of reaction temperature from 70 ˚C to 95 ˚C increased the *DS* by 124% (with glutaric anhydride), and from 95 ˚C to 120 ˚C increased the *DS* by 48 % (with phthalic anhydride). They attributed it to enhanced reaction rate with better diffusion of *EA* in the reaction media [92], [93]. We attribute our observed decrease of *DS* to the possible generation of H• and •OH radicals from the dissociation of water (formed during esterification) inside cavitation bubbles. These radicals can cleave the glycosidic bonds of cellulose or the ester links, decreasing the *DS* [86].

At a fixed cellulose concentration, the increase in temperature affects the reaction mixture's properties, such as μ and ρ, which in turn influences acoustic cavitation. From 20 °C to 80 °C, μ dropped by 75 %, and ρ by 4 %. Simulation results show that the increase of the reaction temperature from 20 °C to 80 °C at 25 g L^{-1}, is independent of p_{max}, p_{min} and u. However, it increases V by almost 10 times for a reaction volume of 32.2 mL. A predictor screening of V determined that,

in a reaction volume of 32.2 mL, μ explains 57 % of the variance. Viscosity affects the acoustic attenuation, as more viscous liquids are prone to fewer shock waves and release less energy during cavitation, hence smaller *V*. This corroborates the abovementioned hypothesis about the decrease of *DS* with increasing temperature.

The thermal transitions of cellulose esters produced at different temperatures without US are presented in Figure B.3. Similarly to the starting material C1, C80, C60 and C40 have a T_g close to 5 °C. Pure oleic acid undergoes a polymorphic transformation with a transition from γ to α-form at -16 °C, followed by α-form melting at 13 °C [172]. The thermal behavior of the cellulose esters synthesized with US at a *PD* of 136 W L^{-1} and at four different temperatures is presented in Figure 4.7. The *DS* for US-produced cellulose esters varies with reaction temperatures, reaching 1.79 at 20 °C, 0.59 at 40 °C, 0.67 at 60 °C, and 0.48 at 80 °C (Table 4.1). A melting endotherm linked to alkyl side chains of FFA occurs around -20 °C, with the melting temperature (T_m) decreasing from -21 °C to -23 °C as reaction temperature increases. From 40 to 80 °C, the low *DS* suggests that the alkyl side chains are more mobile and less densely packed, resulting in a decrease in T_m. This results in a single broad melting peak with a slight shoulder at around -10 °C, that indicates limited polymorphism [173]. However, at 20 °C, the higher *DS* hints at tightly packed alkyl chains. The melting region for the US-prepared ester exhibits two distinct melting endotherms at -21°C and 1 °C suggesting the presence of different crystal domains [174].

This is reflected as well with the increase in T_g from 22 °C to 47 °C as the *DS* increases from 0.48 to 1.79 (Figure 4.7). We attribute it to the increase of steric hindrance which increases the stiffness of the cellulose chains as more FFA are grafted onto cellulose backbone [174]. However, it is not always the case. Depending on the structure and length of the chain, a decrease of T_g was observed with increased *DS* and was interpreted as a plasticizing effect of the long chain FFA [53], [150].

The T_g of cellulose esters increases with increasing DP, because the chains begin to entangle, limiting their mobility [73]. Thus, we suggest that the T_g we obtained are lower than those mentioned in the literature due to the depolymerization of cellulose chains, which decreases the DP.

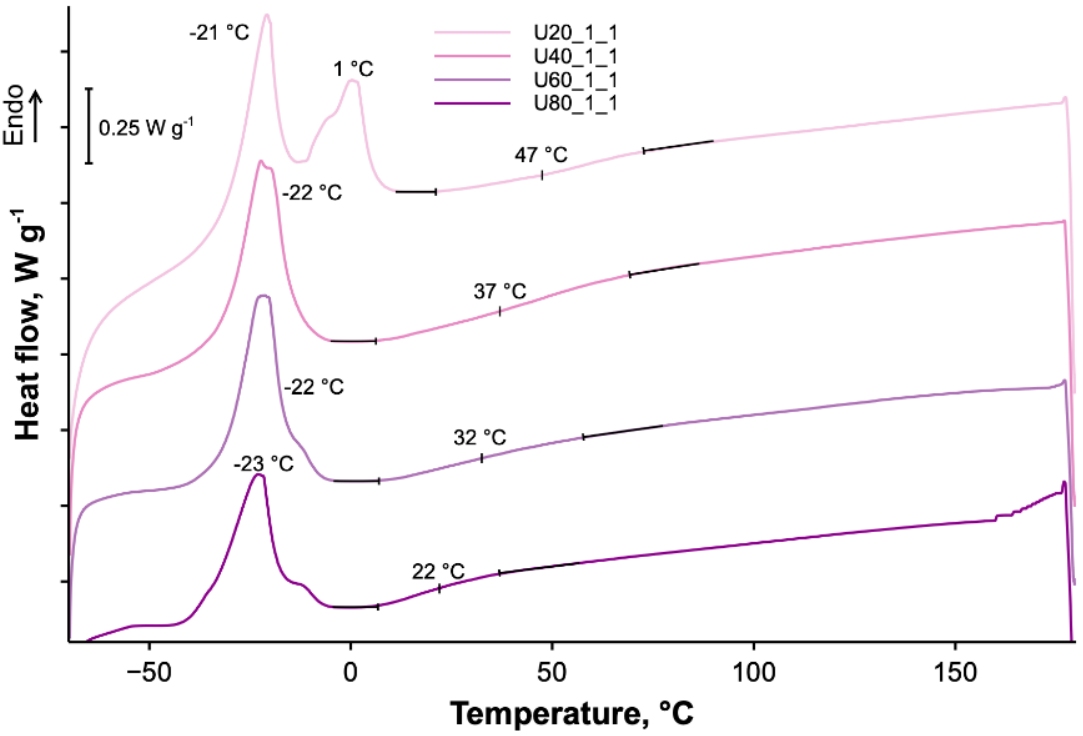

Figure 4.7 DSC curves of cellulose esters produced with US at 136 W L^{-1} and various temperatures.

Alteration of the crystalline structure of cellulose due to dissolution, sonication and esterification of is also confirmed by the decrease of intensity of crystalline reflexes (Figure 4.8). Unmodified cellulose (C1) shows peaks of cellulose Iβ: 14.8°, 16.0°, 20.0°, 22.0°, 34.5°, corresponding respectively to crystals planes 101, 110, 021, 200, 004 [170]. Ester cellulose produced with US at 20 and 80 °C exhibit a decrease in crystalline peak intensity and form amorphous peaks at 18° and 19.8°. Moreover, a new peak at 5.0° in the diffractogram of ester celluloses, confirms the crystallization of grafted fatty chains [175], with its intensity increasing with the *DS*.

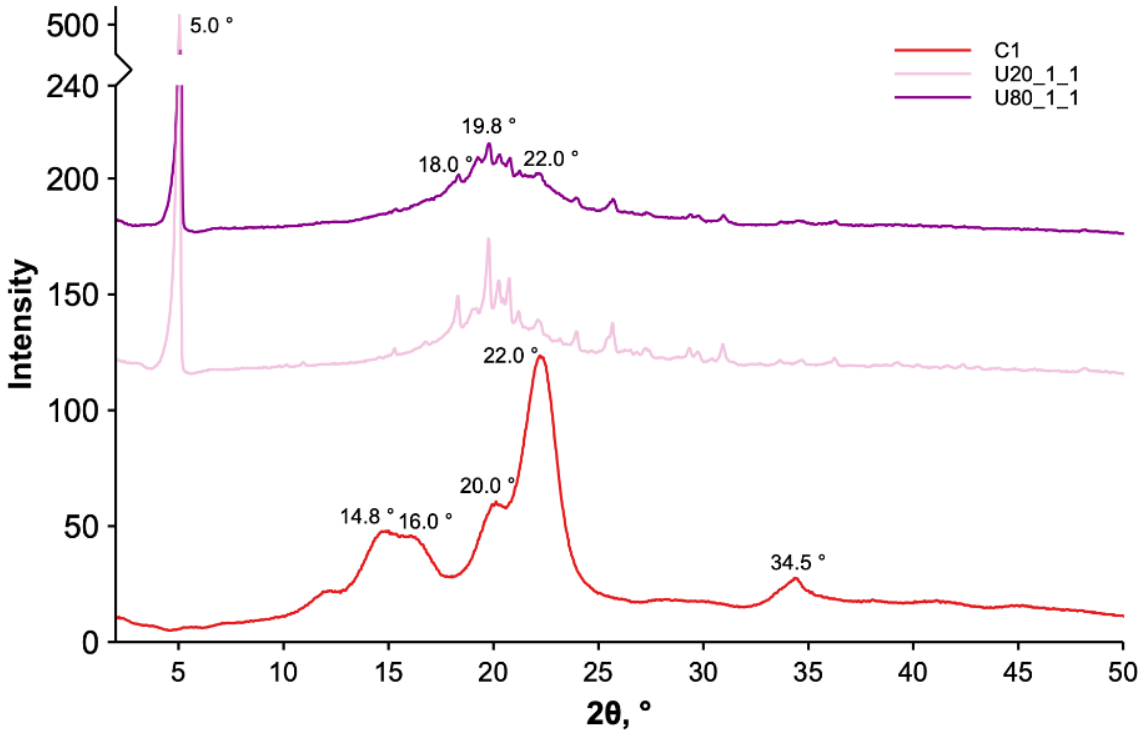

Figure 4.8 XRD diffractogram of unmodified cellulose (C1), and esters treated at two different temperatures (U20_1_1 and U80_1_1).

4.4.3 Comparison of esterification under sonication and silent condition

The effect of process intensification compared to the conventional method (silent conditions) on esterification was investigated with different *P* ranging from 4.39 W to 9.01 W, in a fixed volume of 10.7 mL. After US-assisted esterification, sharp peaks are observed at 1740 cm^{-1} and 1185 cm^{-1}, characteristic of C=O and C-O esters bond stretching (Figure 4.9). At 9.01 W (sample U40_3_6), both peaks have lower intensities, which suggests a small degree of esterification (Figure 4.9).

Our US-produced cellulose esters exhibit intense hydroxyl peaks at 3340 cm^{-1} and 685 cm^{-1}, characteristics of OH covalent bonds and C-OH groups, respectively. These peaks are more pronounced compared to silent conditions, which reflect low level of oleic acid substitution (Figure 4.9). The FTIR results are in accordance with the change in *DS* measured by ^{1}H NMR analysis. As the increase of *P* from 0 W to 4.39 W (3.31 W cm^{-2}) to 9.01 W (6.79 W cm^{-2}), the *DS* dramatically decrease from 0.87 to 0.21 to 0.029 (Figure 4.10a), respectively. However, it is noteworthy that under US, cellulose was esterified within only 30 min against 24 h under conventional heating and

stirring. This partial esterification of the cellulose surface results from insufficient amount of energy supplied to the reaction mixture and/or time. A 24 h US-assisted esterification was not performed due to the erosion of US probe and the excess energy supplied, which would negate the benefits of intensification, and degrade cellulose. Additionally, the *DS* was also determined at 40 ˚C by gravimetric analysis. As *P* increased from 0 W to 4.39 W, so did the *DS* from 0.33 (predicted by Eq. (4.4)) to 0.59. A further increase of *P* to 9.01 W decreased the *DS* to 0.42, with a peak of 0.74 at 6.70 W (Figure 4.10b).

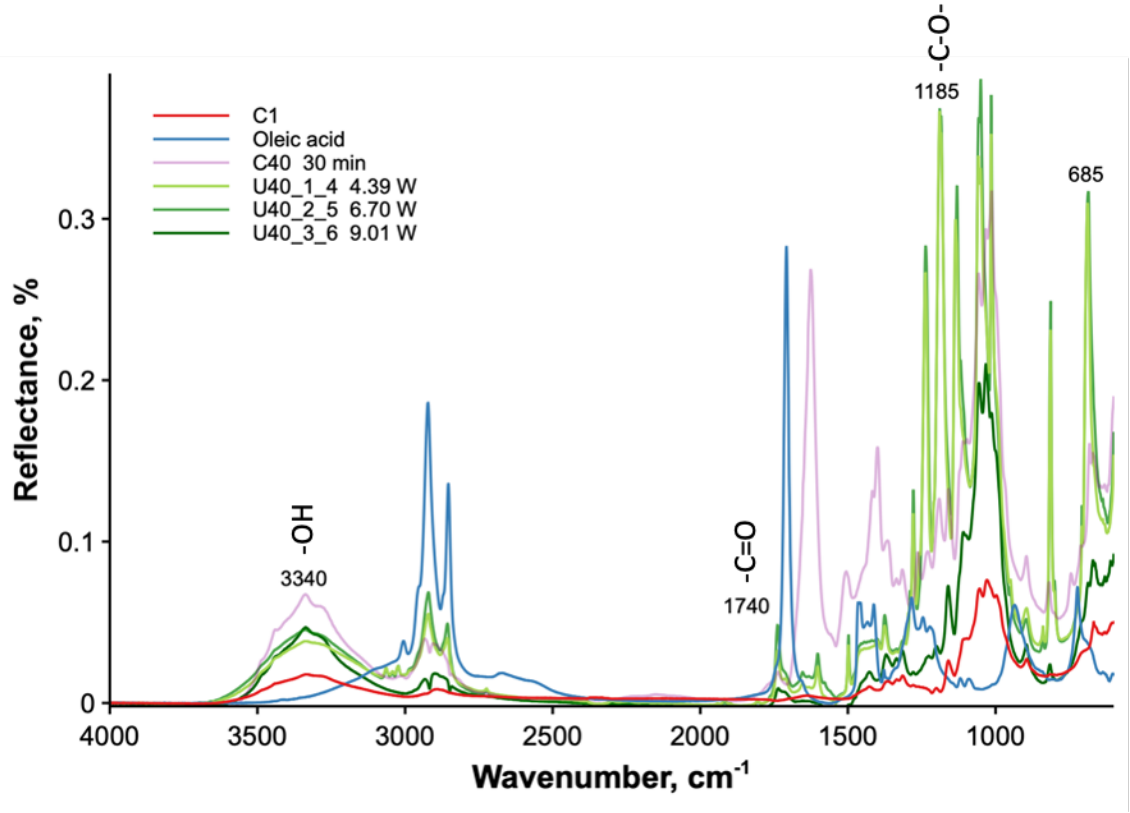

Figure 4.9 FTIR spectra of cellulose esters produced at different ultrasonic powers, and esters produced in silent conditions after 30 min.

At 80 ˚C, the increase in *P* from 0 W to 4.39 W, decreased the *DS* from 1.44 to 0.14. A further increase of *P* to 9.01 W increased the *DS* to 0.87 (predicted by Eq. (4.3)). We obtained the maximum *DS* at 20 ˚C, indeed, the *DS* increased from 1.29 at 0 W (predicted by Eq. (4.4)) to 1.79 at 4.39 W (the peak), then decreased to 1.20 at 9.01 W (Figure 4.10b)

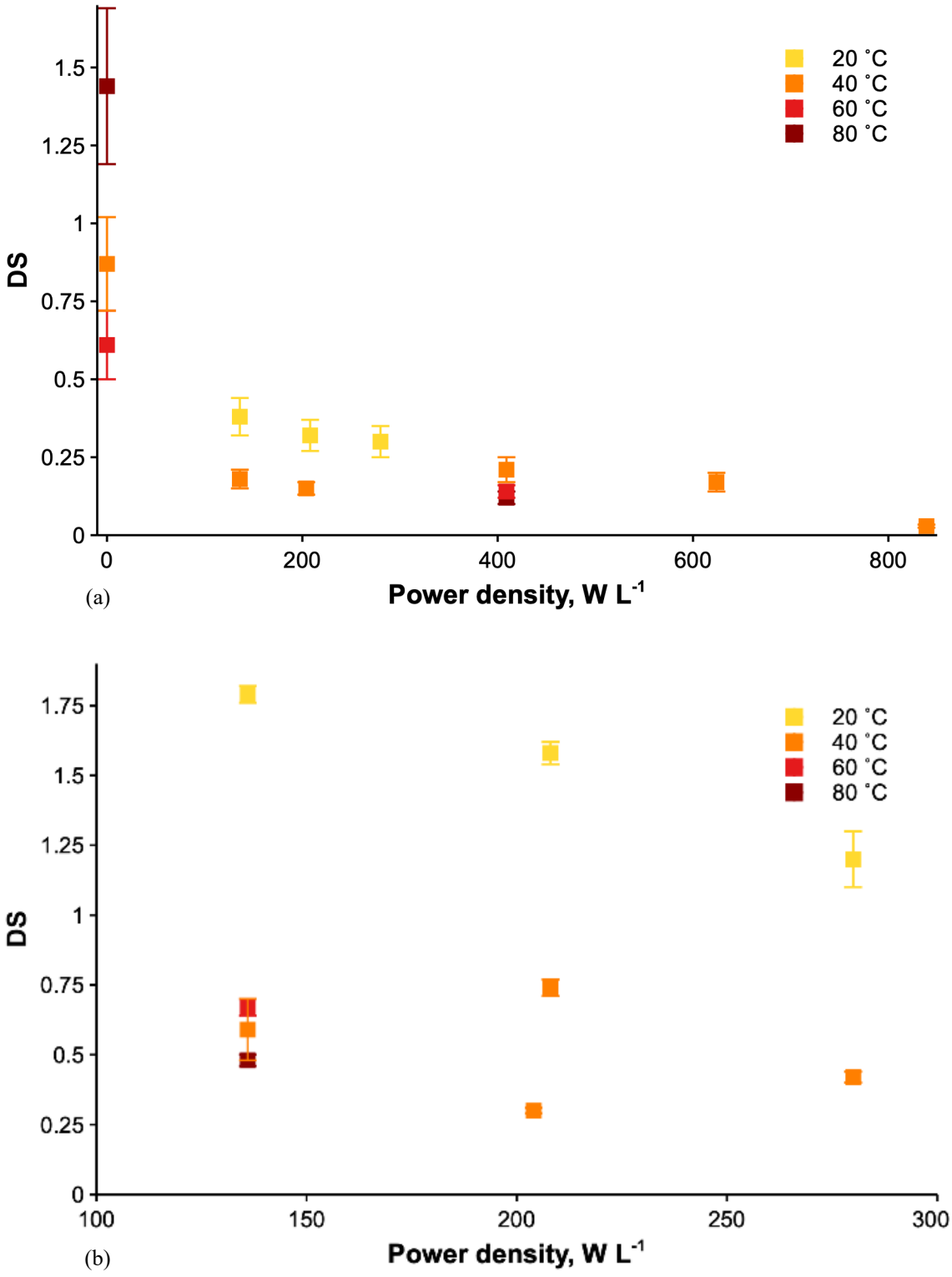

Figure 4.10 *DS* determined by (a) ^{1}H NMR and (b) gravimetric analysis vs. power density at various temperatures.

The *DS* of US-produced ester determined by ^{1}H NMR analysis, resulted in the regression in Figure 4.11 and the following equation:

$$DS = -0.335 + 6.43 \cdot 10^{-2} \cdot P + 4.96 \cdot 10^{-4} \cdot PD + 3.80 \cdot 10^{-2} \cdot \left(\frac{T-60}{20}\right)(\mathrm{P} - 5.78) + 6.30 \cdot 10^{-4} \cdot \left(\frac{T-60}{20}\right)(PD - 365) - 1.37 \cdot 10^{-4} \cdot (P - 5.78)(PD - 365) \quad (4.3)$$

All dependent variables have a significant effect on the *DS*, accounting for a percentage of the variance in the same order of magnitude (Table 4.4). The *DS* increases with *P*, up to 560 W L^{-1}, then it decreases with the increase of *P* (Eq. (4.3)). As *P* increases, US generates more cavitation bubbles, which increases *V* [132]. It suggests that above a certain pressure threshold, cavitation promotes radicals' formation, thus glycosidic bonds and/or esters cleavage, decreasing the *DS* [176], [177].

Table 4.4 Predictor screening analysis of *DS* determined by ^{1}H NMR analysis for esters produced with US.

Predictor	Portion*
Temperature	63.4 %
PD	23.7 %
P	12.9 %

*Portion of the variance from the prediction.

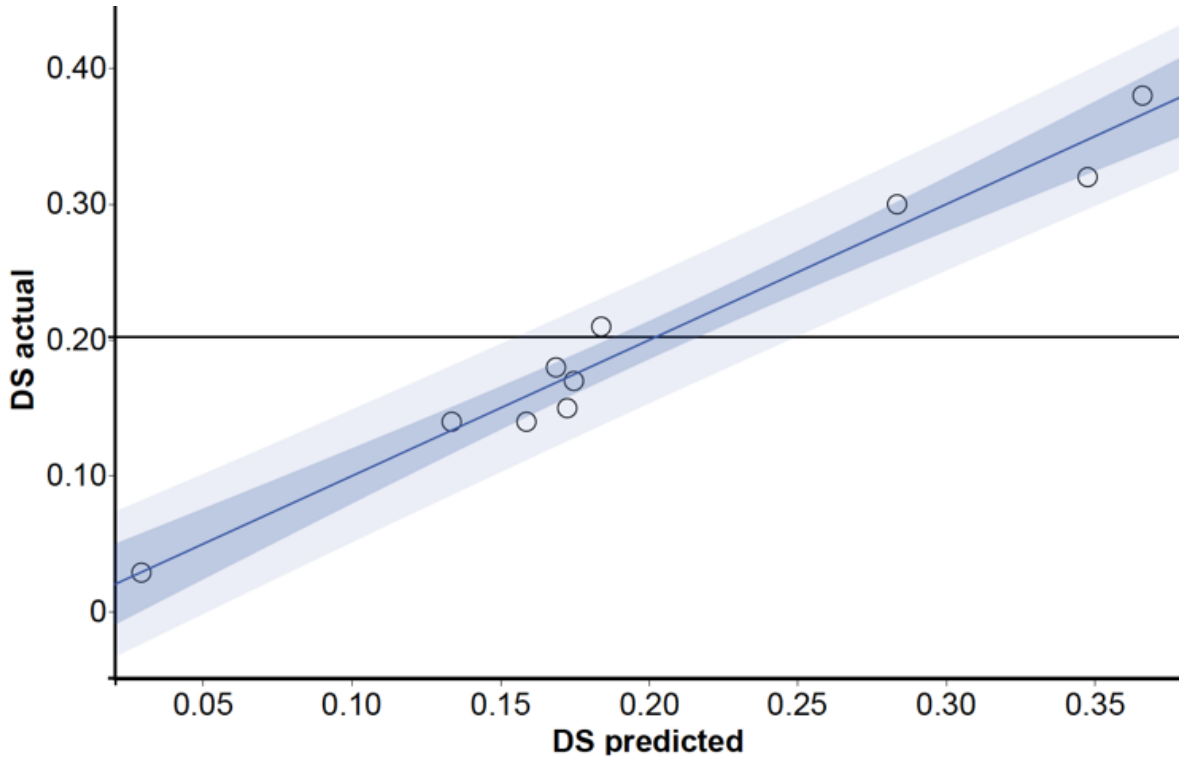

Figure 4.11 Actual vs. predicted *DS* (○) determined by ^{1}H NMR analysis for esters produced with US. _ Regression, _ 95 % CI of prediction, RMSE = 0.0272, R^2 = 0.970, *p*-value < 0.0001, _ Mean of response (0.202), _ Prediction interval.

For esters produced with US and for which we determined the *DS* by gravimetric analysis, the regression (Figure 4.12) resulted in the following equation:

$$DS = 0.437 - 0.108 \cdot \frac{T-60}{20} + 0.249 \cdot \left(\frac{T-60}{20}\right)^2 - 0.179 \cdot (P-5.93)^2 + 1.86 \cdot 10^{-2} \cdot \left(\frac{T-60}{20}\right)(P-5.93) + 5.02 \cdot 10^{-3} \cdot (P-5.93)(PD-192) \quad (4.4)$$

The effect of US on the *DS* is similar to that of the previous DoE. All dependent variables have a significant effect on the *DS*, accounting for a percentage of the variance in the same order of magnitude (Table 4.5). The *DS* increases with *P*, up to 5.93 W, then decreases with the increase of *P* (Eq. (4.4)). However, the *DS* values are substantially higher when determined by the gravimetric analysis than by ^{1}H NMR HRMAS analysis (Table 4.1). This discrepancy can be attributed to an underestimation of *DS* by ^{1}H NMR, as the quantification heavily depends on the surface being analyzed and the dissolution extent of the sample. During sample preparation, incomplete dissolution suggests that primarily the surface was only quantified [164], [178]. The limitation of

solubility as the *DS* increases is attributed to partial crosslinking of sugar rings depolymerized, as evidenced by the formation of a gel during precipitation [176], [177].

Table 4.5 Predictor screening analysis of *DS* determined by gravimetric analysis for esters produced with US.

Predictor	Portion*
Temperature	82.8 %
PD	10.0 %
P	7.20 %

*Portion of the variance from the prediction.

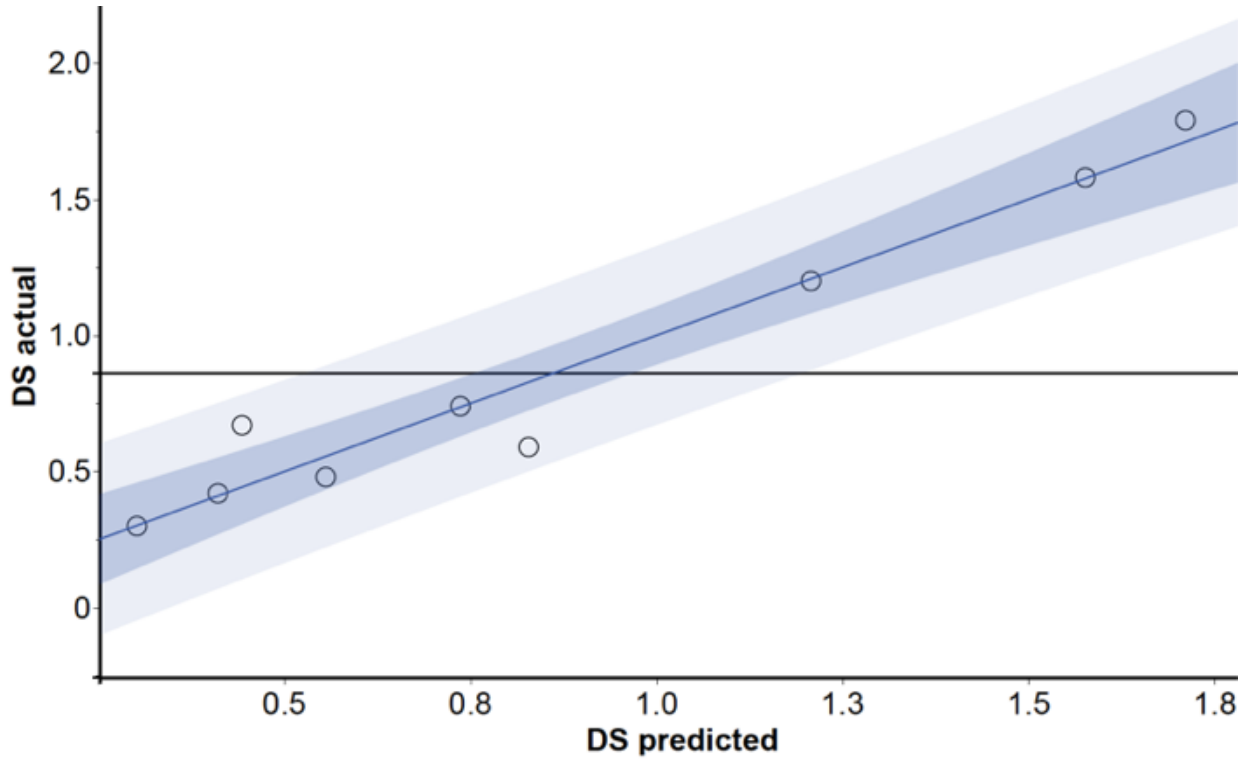

Figure 4.12 Actual vs. predicted *DS* (○) determined by gravimetric analysis for esters produced with US. Regression, 95 % CI of prediction, RMSE = 0.200, $R^2 = 0.947$, *p*-value < 0.0001, Mean of response (0.863), Prediction interval.

Hou et al. increased US intensity from 0 to 300 W m^{-2} resulting in a 281 % raise in the *DS* from 0.38 to 1.42. However, MCC had to be regenerated because its crystalline structure and intra and intermolecular hydrogen bonds reduced reactivity. Pretreatment liberated hydroxyl groups, but

cellulose fibers still aggregated. Acoustic cavitation broke aggregates, with higher US intensity enhancing the effect [11].

Lease et al. esterified cellulose with oleic acid under ball milling for 4 h and 24 h, decreasing the *DS*, from 0.030 to 0.001 [75]. The drop in *DS* arises from simultaneous competing reaction, that are esterification and ester hydrolysis by water produced during esterification [74]. The hypothesis that the *DS* decreases due to hydrolysis of esters formed is less conceivable in our case, as it is usually promoted in basic medium [179]. In this study, it is assumed that above a certain pressure threshold, cavitation promotes radicals' formation, thus glycosidic bonds and/or esters cleavage, decreasing the *DS* [176], [177].

4.4.4 Effect of ultrasound power and power density

Equations (4.3) and (4.4), predicting the *DS* from ^{1}H NMR and gravimetric analysis, follow the same trend, indicating a correlation between *P* and *PD*. *DS* determined by ^{1}H NMR analysis increases with *PD* up to 4.80 W and *P* up to 560 W L^{-1}, then it declines (Eq. (4.3)). Whereas *DS* determined by gravimetric analysis increases with *P* up to 5.93 W, then it decreases (Eq. (4.4)).

The decrease in *DS* suggests the de-esterification and reformation of hydroxyl groups of cellulose. In our process, above 5.93 W, which correspond to 4.47 W cm^{-2}, the locally high temperature and pressure generated by US promote the cleavage of glucose rings and its conversion into pyrazines [180].

Cavitation bubbles grow under positive pressure, collapse and release energy under negative pressure. Simulations determined that at 25 g L^{-1} of cellulose and 20 °C, p_{min} decreases with the increase of *P* (for instance by 43 % from 4.39 W to 9.01 W at 32.2 mL) and rises as *v* decreases (e.g. by 99 % from 32.2 mL to 10.7 mL at 9.01 W). A statistical analysis revealed that p_{min} decreases with the increase of *PD* below 19.4 mL and increases above the threshold:

$$p_{min} = 1.59 \cdot 10^5 - 8.89 \cdot 10^3 \cdot v + 94.9 \cdot PD - 3.32 \cdot 10^3 \cdot (P - 6.70)(v - 21.5) + 46.5 \cdot (v - 21.5)(PD - 382) \quad (4.5)$$

p_{max} is located directly under the tip of the US probe and increases as *P* increases. p_{max} increases as *PD* increases, up to 7.84 W and then decreases (Eq. (4.6)). The reaction volume does not have a significant effect on p_{max} with only 4 % of the variance. As *P* increases, the energy transferred to the fluid increases, as does the amplitude of the sound waves, then the acoustic pressure.

$$p_{max} = 1.84 \cdot 10^5 + 2.78 \cdot 10^4 \cdot P + 13.1 \cdot PD - 208 \cdot (P - 6.70)(v - 21.5) - 12.2 \cdot (P - 6.70)(PD - 382) \quad (4.6)$$

Cavitation bubbles accumulate at the vicinity of the probe emitting surface, which attenuates the propagation of sound waves. Including the attenuation due to cavitation bubbles into our model reduces the volume of cavitation zones by 86 % to 99 %. *V* increases as *P* increases up to a reaction volume of 21.5 mL, then decreases, whereas *V* decreases as the *PD* increases up to a reaction volume of 16.6 mL, then increases. The increase of input US power generates more and larger cavitation bubbles, which collapse more frequently and intensely, which increases *V*. On the other hand, as the fluid's volume decreases, so does the fluid's height between the tip of the probe and the bottom wall (keeping the immersion depth constant). The fluid's height is three times less than the wavelength; thus, bubbles have less time to collapse, which reduces cavitation zones volume [106]. Sivakumar and Pandit observed the same trend, with the increase of cavitation activity up to a maximum, then a decrease because of the decrease of fluid's volume, hence fluid's height [181]. Above 16.6 mL, the increase in *V* is dependent on the increase of *PD*, whereas below 16.6 mL, the decrease in *V* is dependent on the decrease of fluid's volume.

u increases with *PD* (20 % increase from 136 W L^{-1} to 280 W L^{-1} at 32.2 mL), and with the decrease of *v* (22 % drop from 32.2 mL to 10.5 mL at 9.01 W) (Figure 4.13). The increase of input US power increases the acoustic pressure amplitude, which in turn increases the volumetric force (Eq. (B.11)), resulting in higher *u*. The interaction of acoustic waves with the acoustic streaming also increases *u*. *u* increases with the decrease of *v* (which decreases the fluid's height). Xu et al. and Laajimi et al. observed a different effect, with the maximum acoustic streaming velocity increasing with the fluid's height, reaching a peak, and decreasing. They attributed the decrease of velocity to the attenuation due to the liquid height [109], [117].

The simulation with the lowest *V* and *u* corresponds to the experimental parameters that produced the highest *DS* values. In contrast, the simulation resulting in the second highest *u* produced the lowest *DS*. The lowest *DS* obtained is in 10.5 mL of reaction mixture. As the probe is located near the bottom of the vessel, the bottom wall blocks the US waves, resulting in a lower mixing efficiency than in 32.2 mL (although our simulations gave a higher *u*) [109]. The cavitation intensity (number and size of bubbles) increases with the *PD* but becomes too high above 255 W L^{-1}: at the tip of the probe, the bubbles collapses generate less radicals [133]. We assume that excessive high velocities generate bubbles in the reactor that form between the reagent molecules,

preventing their contact and hindering the reaction. This contradiction also highlights limitations of simulations and modelling in this study. Indeed, it assumes the fluid homogeneous and Newtonian, with thermodynamic properties unchanged during the reaction. However, the increase in *DS* increases the hydrophobicity of cellulose esters, creating phase separation and changing the viscosity and solubility of the cellulose [182], which are not accounted for by the numerical simulation. This affects the mixing, mass transfer and acoustic waves propagation. Thus, the reaction is dominated by interfacial process and does not depend on the mixing and mass transfer anymore, which the present simulation did not include [182].

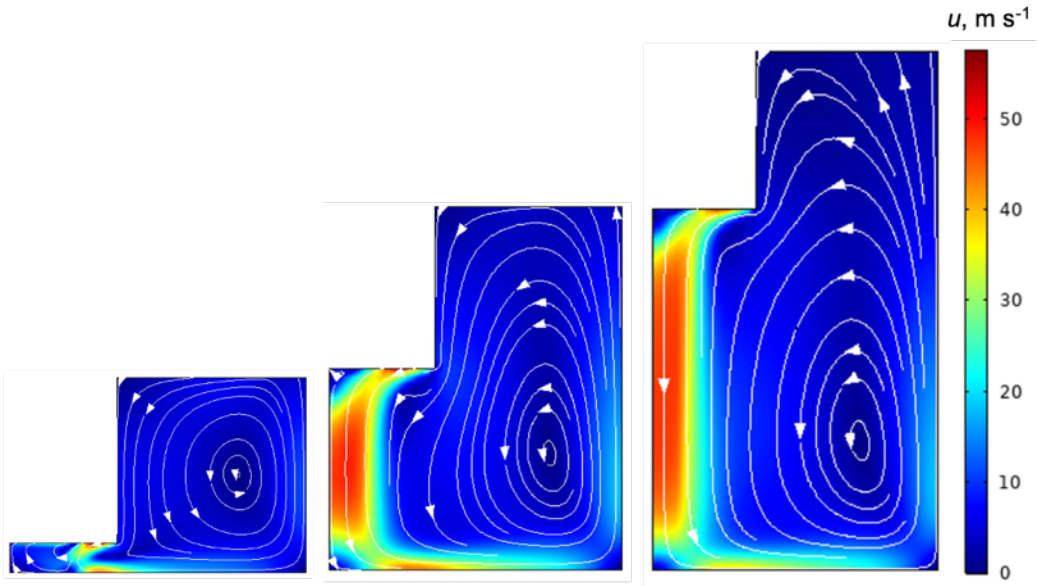

Power Density	839 W L^{-1}	409 W L^{-1}	280 W L^{-1}
Velocity	58.27 m s^{-1}	51.30 m s^{-1}	47.96 m s^{-1}

Figure 4.13 *u* of cellulose esters' reaction at 25 g L^{-1} at 9.01 W. *u* decreases with the increase of reaction's volume.

At a reaction temperature of 20 °C and in a volume of 32.2 mL, two endothermic peaks between -25 °C to -21 °C and between -9 °C to 1 °C are present, followed by a subtle change in T_g (Figure 4.14). We attribute the first endothermic peak to the melting of crystals formed by alkyl side chains of FFA. The first peak T_m decreases by 4 °C with the US power. We ascribe the second endothermic peak to the melting of a highly viscous liquid crystalline phase formed during the cooling [183]. The area of this second melting peak decreases by 77 % with the increase of US power and decrease of *DS*, suggesting a decrease in the amount and/or size of liquid crystals. The two endothermic

peaks suggest a polymorphic behaviour with various crystals sizes and arrangements. The T_g increases from 22 °C to 47 °C as the US power decreases from 9.01 W to 4.39 W and as the *DS* increases from 1.20 to 1.79 (Figure 4.14). We attribute it to the increase of steric hindrance. However, there is no clear evidence of the trend of T_g with the *DS* [11]. Thus, we conclude that the *PD* does not have a clear effect on the T_g and fusion peak (Figure B.4).

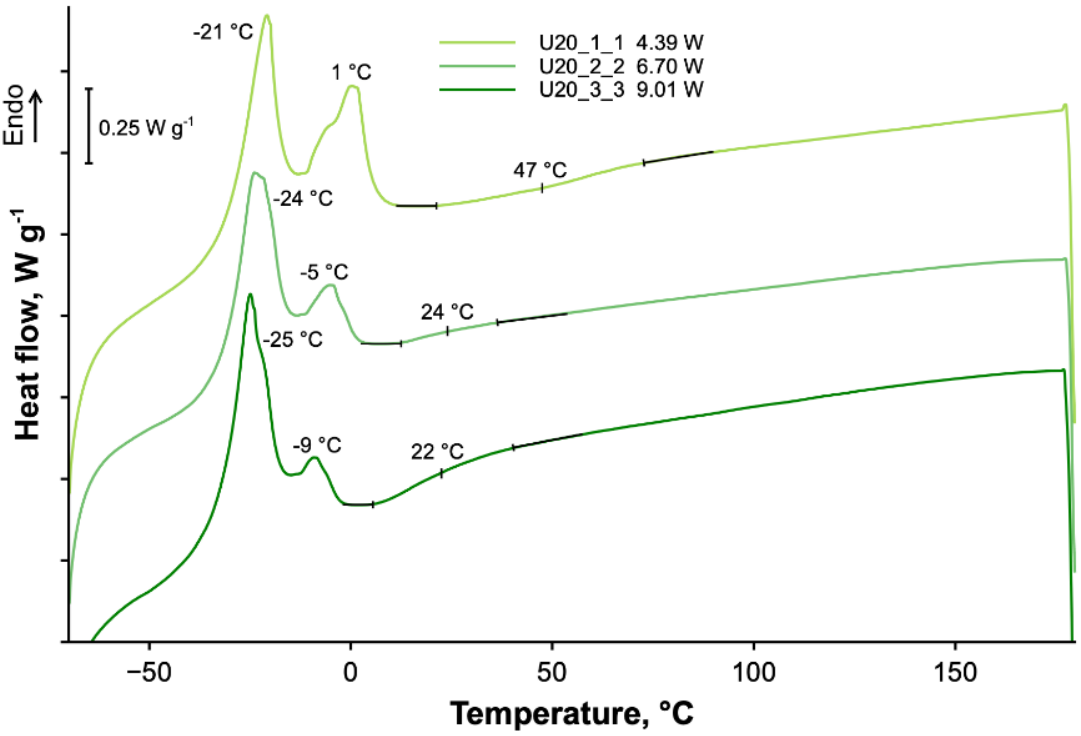

Figure 4.14 DSC curves of cellulose esters produced at 20 ˚C at various US powers.

4.5 Conclusion

This work aimed at producing cellulose esters using long chain fatty acids as a green esterification agent and ultrasound (US) as an alternative energy vector to intensify and decrease the reaction's energy requirements. Prior to US-assisted esterification, oleic acid and stearic acid were used to esterify two sources of cellulose in silent conditions, at various temperatures. Among conventional esterification samples, the reaction at 80 °C for 24 h resulted in the highest *DS* of 1.44. Among US-assisted esterification samples, the reaction at 20 °C and 136 W L^{-1} for 30 min resulted in the highest *DS* of 0.38 (1.79 determined by gravimetric analysis). The conventionally esterified sample

required 93 W g^{-1} of cellulose whereas the US-esterified sample required 18 W g^{-1} of cellulose to achieve the same *DS*. The sample prepared with US displayed a thermoplastic behavior, as confirmed by DSC, with a T_g at 47 °C. Future work will focus on cellulose esterification in ionic liquids, which act simultaneously as both solvent and catalyst.

We characterized the cavitation activity with COMSOL Multiphysics 6.1 in cellulose esters solution in a horn-type cylindrical ultrasonic reactor. A temperature of 20 °C, a cellulose concentration of 25 g L^{-1}, a ultrasound power of 4.39 W in 32.2 mL were the conditions resulting in the highest *DS* in US-assisted esterification. However, the simulation with these parameters resulted in the smallest active cavitation volume (*V)* and the lowest acoustic streaming velocity (*u)*: $9.60 \cdot 10^{-8}$ m^3 and 40.06 m s^{-1}. Future work will consider the kinetic of cellulose esterification with long chain FFA, through simulation with the module *transport of concentrated species* for esters' yield and molar concentration predictions.

CRediT authorship contribution statement

Pierre Dal: Conceptualization, Data curation, Formal analysis, Writing – original draft, Methodology, Investigation, Software. **Annelise Jean-Fulcrand:** Writing – review & editing. **Jean-Marc Lévêque:** Writing – review & editing. **Jean-Marie Raquez:** Writing – review & editing, Supervision. **Daria C. Boffito:** Writing – review & editing, Supervision, Funding, Validation, Conceptualization, Resources.

Acknowledgements

The authors are thankful to Cédric Malveau for providing assistance during the nuclear magnetic resonance experiments. The authors are thankful to Jean Provost and his group for the material for speed of sound measurements. Pierre Dal is thankful to Institut de l'Energie Trottier, and MITACS, for awarding him graduate scholarships to support his studies. The authors are thankful to Dalma Schieppati for advices about designs of experiment and simulations. This work was undertaken, in part, thanks to the support of the NSERC - Natural Sciences and Engineering Research Council of Canada Research Chairs.

CHAPTER 5 ARTICLE 3: ULTRASOUND-ASSISTED ESTERIFICATION OF COTTON CELLULOSE IN IONIC LIQUIDS

Pierre Dal, Owen J. Curnow, Jean-Marie Raquez, Daria C. Boffito

Submitted to Carbohydrate Polymers on 14 May 2025

Abstract

We have developed a method for the controlled ultrasound (US)-assisted esterification of cellulose in ionic liquids (ILs). We first screened the optimal IL in conventional esterification (no US) for subsequent US-assisted esterification. The conventional esterification involved two cotton celluloses, four ILs and long chain free fatty acids (oleic acid and stearic acid), as a bio-based alternative to commonly used chlorides, anhydrides and vinyl esters. The conventional esterification at 80 °C for 24 h in 1-butyl-3-methylimidazolium chloride ([Bmim]Cl), and in 1-butyl-3-methylimidazolium acetate ([Bmim][Ac]), with oleic acid and p-toluenesulfonyl chloride as a catalyst produced the most esters among conventional experiments. Then we explored the US-assisted esterification of two cotton celluloses in [Bmim]Cl and [Bmim][Ac] using oleic acid. ILs play the simultaneous role of solvent and catalyst. We added dimethyl sulfoxide as co-solvent to reduce the viscosity of the reaction medium. US at 102 W g^{-1}, at 40 °C for 30 min in [Bmim]Cl and oleic acid produced cellulose esters with a *DS* of 2.34. The US-assisted esterification could treat cellulose at a concentration up to 75 g L^{-1}. Ester samples produced were less crystalline than unmodified cellulose, and differential scanning calorimetry and dielectric spectroscopy showed evidence of oleic acid involved in internal plasticization of celluloses.

Keywords: Cellulose, Esterification, Ultrasound, Ionic liquid, Sonochemical reactor

5.1 Introduction

Cellulose is the most abundant natural polymer. It is widely used in industries such as paper, textiles, and packaging, leading to significant waste generation. For example, in 2022, Canada alone, generated 3.6 million tons of paper waste [4]. Despite its abundance and biodegradability, the valorization of cellulose is often limited by long reaction times [12], the use of toxic chemicals [90], and possible degradation of the cellulose backbone decreasing the yield [49]. These limitations underscore the need for innovative strategies to enable more sustainable and efficient cellulose valorization. Process intensification (PI) is an approach to process engineering that has

the potential to improve process efficiency. Further, it provides electrification opportunities for the chemical industry, particularly for feedstock substitution, including, among others, cellulose and its waste forms [184], [185].

Our team has previously demonstrated how ultrasound (US) as a PI technology can increase reaction rate. With the US-assisted esterification, the reaction time decreased from 24 h to 30 min and the temperature from 80 °C to 20 °C compared with conventional processes to esterify cellulose into thermoplastic esters. At 20 °C in N,N-dimethyl acetamide (DMAc) and lithium chloride, with US at 20 kHz for 30 min, the *DS* was 0.38, whereas with conventional heating and stirring at 80 °C for 24 h, the *DS* was 1.44 (Dal et al., 2025). Further, it was demonstrated that US-assisted esterification of cellulose in DMAc and lithium chloride, with p-toluenesulfonyl chloride (p-Tos) and oleic acid at 136 W L^{-1} and 20 kHz produced esters whose glass transition temperature (T_g) increased with the degree of substitution (*DS*), while the reaction temperature decreased from 80 °C to 20 °C. The observed increase in T_g with *DS* contrasts with literature reports, where T_g typically decreases as *DS* increases, due to the plasticizing effect of the grafted long-chain fatty acids. In this study, the lower T_g observed at lower *DS* - and at higher reaction temperatures - suggests cellulose depolymerization. This degradation likely reduces chains entanglement, enhancing molecular mobility and thereby lowering T_g [73]. Additionally, the difficulty to dissolve the resulting samples indicates partial crosslinking of esterified cellulose [176], [177]. Indeed, in conventional solvents, the esterification reaction is limited due to the occurrence of secondary competing reactions, particularly cellulose depolymerization and crosslinking reactions [91], [176], [177], [186]. These secondary competing reactions are more likely to occur at elevated temperatures in conventional solvents, reinforcing the need for milder processing conditions. In this regard, ionic liquids (ILs) represent an interesting alternative for cellulose dissolution and modification [73], [187], [188], [189]. ILs are liquid salts composed of ions that ideally remain liquid below 100 °C [57]. ILs are considered green solvents due to their non-flammability, high thermal stability, and the absence of volatile organic compound emissions [57], [58]. In 2002, Swatloski et al. reported that 1-butyl-3-methylimidazolium chloride ([Bmim]Cl) dissolved cellulose up to 25 wt% [59]. Moreover, ILs have the potential to act as both solvent and catalyst for cellulose esterification [187], [188], [190]. Gao et al. reported the transesterification of microcrystalline cellulose (MCC) at 4 wt% in 1,8-diazabicyclo[5.4.0]undecyquin-7-ene chloride with vinyl acetate in 40 min at 100 °C, and the obtention of a degree of substitution (*DS*) of 2.82,

attributed to the catalytic activity of their IL and to hydrophobic interactions between their IL and cellulose chains [187]. Todorov et al. esterified MCC in 5/7-methyl-1,5,7-triazabicyclo [4.3.0]non-5-enium acetate ([mTBNH][Ac]) with isopropenyl acetate at 80 °C for 20 h, they obtained a *DS* of 1.75. They attributed it to the catalytic activity of their superbase IL, preventing the competing formation of anhydride during reaction as elsewhere reported [188].

Although ILs are considered greener than conventional solvents, cellulose esterification in ILs requires the use of chlorides [167], [191], [192], anhydrides [92], [93], vinyl esters [71], [187], [188], [190], or free fatty acids (FFA) and a catalyst [68], [75], [193], as esterification agent (EA) to achieve *DS* high enough to obtain a product showcasing thermoplastic properties (*DS* of 1.5 [54]). The cellulose esterification in [Bmim]Cl, with lauroyl chloride at 80 °C for 2 h resulted in a *DS* of 1.5 [167]. They observed the precipitation of cellulose esters during the reaction, impeding formation of superior *DS*. Ma et al. esterified cellulose with phthalic anhydride [93], and glutaric anhydride in [Bmim]Cl, in an US bath operating at 40 kHz and 180 W [92]. US treatment at 105 °C for 60 min increased the *DS* by 86% compared to silent conditions (no US). Sonication for 45 min, from 95 °C to 120 °C increased the *DS* by 48% [93]. The increase of sonication time from 20 min to 120 min increased the *DS* by 445% at 85 °C. Sonication for 60 min, from 70 °C to 95 °C increased the *DS* by 124%. They explained the *DS* increase by the improved reaction rate resulting from enhanced anion and cation mobility. They attributed the increase of *DS* with US time to prolonged penetration of anhydrides into cellulose chains [92]. The cellulose esterification with methyl benzoate in [Bmim]Cl and dimethyl sulfoxide (DMSO), for 24 h at 115 °C, resulted in a *DS* of 0.69 while catalyzing the reaction with triazabicyclodecene [190]. The MCC treatment in 1-butyl-3-methylimidazolium acetate ([Bmim][Ac]) in a magnetic mortar, with oleic acid and p-Tos, produced esters with a *DS* of 0.21, without altering the crystalline structure of cellulose. The *DS* increased by 59% as the reaction time increased from 4 h to 12 h, before slightly decreasing by 3% [75]. They explained the decrease of *DS* after 12 h due to a competition between esterification/hydrolysis events [74]. Men et al. esterified cotton linter cellulose in [Bmim][Ac] with lauric acid and p-Tos and obtained a *DS* of 1.5 [193]. A chlorinating agent like p-Tos degrades cellulose. It hydrolyzes the oxygen of the β-1,4-glycosidic bond between glucose rings [194]. In some cases, co-solvents such as DMSO can be employed to reduce the solution viscosity during cellulose esterification, without compromising the IL recyclability [73], [189], [190]. For instance, cellulose esterification at 2.5 wt% in [Bmim]Cl with 30 wt% of DMSO, produced esters with a *DS*

of 0.40. The co-solvent enhances both solubility and reusability of the solvent system. They recovered 97% of the mixture [Bmim]Cl/DMSO and successfully reused it to produce esters [190].

For the first time, the present research combines US with ILs without the use of a catalyst for the esterification of cellulose with the aim of avoiding the degradation of this latter. It first investigates the conventional esterification of two cellulose sources in four recyclable ionic liquids - 1-butyl-3-methylimidazolium chloride, 1-ethyl-3-methylimidazolium chloride, 1-butyl-3-methylimidazolium acetate, and a triaminocyclopropenium salt (potentially biodegradable [195]) - with long chain free fatty acid (stearic acid and oleic acid) and various catalysts (sulfuric acid, triethylamine and p-toluenesulfonyl chloride). Based on the extent of esterification, we selected oleic acid, and 1-butyl-3-methylimidazolium chloride and 1-butyl-3-methylimidazolium acetate for US-assisted and catalyst-free esterification of two cellulose sources. We added dimethyl sulfoxide as co-solvent to decrease the viscosity of the reaction mixture and the use of ionic liquids in order to obtain cellulose thermoplastics. This process offers a greener approach and a reduced reaction time along with improved selectivity for the valorization of cellulose waste into internally plasticized esters.

5.2 Material and methods

5.2.1 Materials

All chemicals and solvents were used as received: acetone (≥ 99.8%, Fisher), sulfuric acid (99%, Ermanz), 1-butyl-3-methylimidazolium chloride ([Bmim]Cl, 98%, AK Scientific), 1-ethyl-3-methylimidazolium chloride ([Emim]Cl, 98%, AK Scientific), oleic acid (90%, Aldrich), stearic acid (Anachemia), anhydrous ethanol (Commercial Alcohols), p-toluenesulfonyl chloride (p-Tos, 98%, Thermoscientific), dimethyl sulfoxide (DMSO, 99.9%, Fisher), 1-butyl-3-methylimidazolium acetate ([Bmim][Ac], ≥ 95%, Sigma).

Two sources of cellulose were esterified: cotton linters cellulose (C1, degree of polymerization (DP) = 138, Sigma), and cellulose fibers (C2, DP = 926, Recyc php, Quebec) recycled from used diapers after a separation process.

5.2.2 Designs of experiments and statistics

The study includes two designs of experiments (DoE). The DoE1 aimed to identify the effect of the cellulose source, solvent, catalyst and FFA on the esterification of cotton cellulose without US. DoE1 identified the optimal IL and FFA for US-assisted esterification, considering the peaks intensity in FTIR spectra. The DoE2 determined which experimental conditions – power density (*PD*), cellulose concentration and IL type – produced the highest *DS*, and the associated esters thermal transitions. For cellulose esters used in thermoplastics, thermal transitions are essential for compounding. Limited tests were repeated three times and the reported result is the arithmetic average. The error was deduced for the other tests.

We ran statistical analysis to identify significant independent variables and relationships within the data. We first ran a predictor screening analysis with Bootstrap forest partitioning, which identified the independent variables responsible for the largest variance for the response variables. We then eliminated the non-significant variables to fit a linear regression mode that predicted the response variables with an accuracy within a 95% confidence interval (CI).

5.2.3 Conventional esterification of cellulose

Before esterification, cellulose was first dissolved in ILs at a concentration of 25 g L^{-1}. Specifically, cellulose was dissolved in 5 mL of IL in a 50 mL round bottom flask at 110°C and 500 rpm for 1 h until reaching a transparent solution. FFA was then dissolved in 2.5 mL of IL, at a molar ratio FFA/cellulose of 6. 1 mL of triethylamine or sulfuric acid, or 0.89 g of p-Tos was added to the reaction mixture (Table 5.1) [68], [193]. The reaction occurred at 80°C and 1500 rpm for 24 h under nitrogen atmosphere. The reaction mixture was precipitated in 50 mL of anhydrous ethanol and stirred at 300 rpm for 30 min. It was filtered on Whatman paper n°1 and washed twice with 50 mL of anhydrous ethanol, then 3 times with 50 mL of deionized water, or centrifuged at 6000 rpm for 15 min to separate solid and liquid phases. The solid samples dried at 50 °C for at least 24 h before analysis.

Table 5.1 DoE1.

Experiment	Cellulose	IL	FFA	Catalyst
C1BOT	1	[Bmim]Cl	Oleic acid	Triethylamine
C1BOA	1	[Bmim]Cl	Oleic acid	Sulfuric acid
C1BST	1	[Bmim]Cl	Stearic acid	Triethylamine
C1BSA	1	[Bmim]Cl	Stearic acid	Sulfuric acid
C1EOT	1	[Emim]Cl	Oleic acid	Triethylamine
C1EOA	1	[Emim]Cl	Oleic acid	Sulfuric acid
C2BOT	2	[Bmim]Cl	Oleic acid	Triethylamine
C2BOA	2	[Bmim]Cl	Oleic acid	Sulfuric acid
C1BuOT	1	$[C_3(NBu_2)_3]Cl$	Oleic acid	Triethylamine
C1BOp	1	[Bmim]Cl	Oleic acid	p-Tos
C1BaOp	1	[Bmim][Ac]	Oleic acid	p-Tos

C1# or C2# corresponds to the cellulose source. The second identifier denotes the IL: B for [Bmim]Cl, E for [Emim]Cl, Ba for [Bmim][Ac] and Bu for [C3(NBu2)3]Cl (Section C.1, Figure C.1 and Figure C.2). The third identifier denotes the FFA, O for oleic acid and S for stearic acid. The last identifier refers to the catalyst: T for triethylamine, A for sulfuric acid and p for p-Tos.

5.2.4 US-assisted esterification

Prior to US-assisted esterification, the same dissolution procedure as aforementioned was performed in a thermostatic beaker, and the cellulose concentration ranged from 25 g L^{-1} to 75 g L^{-1} (Table 5.2). When the cellulose was almost dissolved, the same weight of DMSO as IL was added to the reaction mixture, to reduce the viscosity. The temperature decreased to 40 °C or 80 °C and oleic acid was added dropwise to reach a molar ratio FFA/cellulose of 6. The ultrasonic liquid processor was a Vibra Cell from Sonics & Materials Inc. with a nominal output power of 500 W and 20 kHz frequency. The transducer was a piezoelectric ceramic transducer made of a Ti-6Al-V alloy and with a diameter of 13 mm [104]. The probe was placed in the center of the beaker and immersed 5 mm. The sonication during the reaction lasted for 30 min, according to the set of experiments (Table 5.2). The US power delivered to the reaction medium was calculated by calorimetric calibration, as it depends on the sonicated mixture [163]. The washing procedure was

the same as described above, except that the anhydrous ethanol was cooled to 0 °C. The separated solids were dried in a vacuum oven at ambient temperature for at least 24 h before analysis. As reference tests, oleic acid esterified cellulose on a stirring plate at 80 °C for 24 h and 30 min in [Bmim]Cl/DMSO and in [Bmim][Ac]/DMSO without US or any catalyst (Table 5.2). [Bmim]Cl/DMSO and [Bmim][Ac]/DMSO are well established reaction media for cellulose dissolution without chain degradation [73], [196].

Table 5.2 DoE2.

Experiment	Cellulose		IL	Temperature, °C	Time, h	US *PD*, W g^{-1}	*DS*
	Source	Concentration, g L^{-1}					
C1B	1	25	[Bmim]Cl	80	24	-	0.73 ± 0.05
C1Ba	1	25	[Bmim][Ac]	80	24	-	0.04 ± 0.003
C1B_30	1	25	[Bmim]Cl	80	0.5	-	0.13 ± 0.009
C1Ba_30	1	25	[Bmim][Ac]	80	0.5	-	0.0
C1B20_80	1	25	[Bmim]Cl	80	0.5	29.5	0.83 ± 0.06
C1B20	1	25	[Bmim]Cl	40	0.5	29.5	0.92 ± 0.06
C2B20	1	50	[Bmim]Cl	40	0.5	14.7	1.05 ± 0.07
C3B20	1	75	[Bmim]Cl	40	0.5	9.8	0.33 ± 0.02
C3B30	1	75	[Bmim]Cl	40	0.5	21.9	0.34 ± 0.02
C3B40	1	75	[Bmim]Cl	40	0.5	33.9	0.41 ± 0.03
R1B20	2	25	[Bmim]Cl	40	0.5	29.5	1.09 ± 0.08
R1B40	2	25	[Bmim]Cl	40	0.5	101.7	2.34 ± 0.16
C1Ba20	1	25	[Bmim][Ac]	40	0.5	41.2	0.16 ± 0.01
C1Ba20_80	1	25	[Bmim][Ac]	80	0.5	41.2	1.62 ± 0.11

C# or R# corresponds to the cellulose source, C1 and C2 respectively. The first number in the label represents the cellulose concentration, ranging from 1 (25 g L^{-1}) to 3 (75 g L^{-1}). The third identifier denotes the IL: B for [Bmim]Cl and Ba for [Bmim][Ac]. The next digits indicate the power amplitude, ranging from 20% to 40%. The last identifier _80 indicates samples prepared at 80 °C, _30 indicates samples prepared for 30 min. For example, C1B20_80 was prepared with C1 at 25 g L^{-1} in [Bmim]Cl/DMSO at 80 °C, with a US power amplitude of 20%, corresponding to a US power density of 29.5 W g^{-1}.

5.2.5 Fourier transformed infrared spectra (FTIR) analysis

The functional groups of ester samples were identified by a Bruker Alpha FTIR spectrometer with an attenuated total reflectance Platinum ATR accessory. A single beam scanned the samples 32 times with a resolution of 2 cm^{-1} in a spectral range from 4000 cm^{-1} to 600 cm^{-1}.

5.2.6 Determination of the DS

For samples of DoE2, the *DS* was determined with the following equation:

$$DS = \frac{m_1 - m_0}{(M - 1) * n_0} \tag{5.1}$$

where m_1 is the weight of the ester's sample, m_0 is the weight of unmodified cellulose, n_0 is the number of moles of unmodified cellulose, M is the molecular weight of an oleoyl group (M = 265.5 g mol^{-1}), and 162 is the molecular weight of an AGU in g mol^{-1}.

5.2.7 Thermal behavior

The transition temperatures - glass transition temperature (T_g) and melting temperature (T_m) - of the esters samples were determined with a TA Instruments calorimeter Q200 with an RSC 90 cooling system. During measurements the heating ramp was from -70 °C to 180 °C at 20 °C min^{-1} and with a nitrogen flow of 50 mL min^{-1}. The sample size was around 5 mg.

5.2.8 X-ray Diffraction (XRD)

A Bruker D8 Advance diffractometer was used to scan unmodified celluloses and esters samples (DoE2) from 2° to 50°. The crystallinity index (Cr) of unmodified cellulose was estimated from the ratio of the area of crystalline peaks (around 14.5°, 16.0°, 20.0°, 22.0° and 34.5°) to the total area under the curve [197].

5.2.9 Formation of film

Unmodified and esterified cellulose was placed between two polyimide sheets, sandwiched between copper plates, and hot-pressed in a temperature-controlled chamber using a Carver press at 120 °C to 180 °C under 1 MPa for 10 min. The pressed samples were then cooled to room temperature and subsequently in ice.

5.2.10 Dielectric spectroscopy

Dielectric spectroscopy measured the complex dielectric permittivity of pressed films from 10^{-1} Hz to 10^{6} Hz for 50 frequencies with a Novocontrol Alpha-A system equipped with a BDS 1200 sample cell. Samples were placed between two brass electrodes (diameter of 20 mm). A sinusoidal voltage of 3 V was applied. Scans were registered every 10 °C between - 10 °C and 140 °C.

5.3 Results and discussion

5.3.1 Determination of the optimal IL

To determine the best IL solvent for cellulose esterification, the reaction was first performed in silent conditions (absence of US) at 80 °C for 24 h, prior to US-assisted esterification [68], [193]. Among the first set of experiments, esters obtained with oleic acid and sulfuric acid of p-Tos and with stearic acid and sulfuric acid, i.e. C1BOA (Figure 5.1), C1BSA (Figure C.3), C1BaOp (Figure C.4), respectively, were the three samples having a peak at 1740 cm^{-1}, suggesting the formation of ester bonds to the cellulose (C=O bonds) (Table 5.1) [198]. This is supported by a decrease in the intensity of the peak at around 3330 cm^{-1} (characteristic of the -OH groups), and its shift towards higher wavenumber (around 3400 cm^{-1}), confirming the substitution of OH for esters [55]. By contrast, esterified samples C1BOA, C1BOp, C1BST and C2BOA show a lower intensity of the peak at 3330 cm^{-1} than the unmodified cellulose (Figure 5.1, Figure C.3 and Figure C.5), which suggests the decrease in hydrogen bonding due to the dissolution of cellulose [6], [60]. The shoulder at 1725 cm^{-1} for C1BOA (Figure 5.1) and C1BuOT (Figure C.6) suggests that the esterification started only onto the cellulose surface but was incomplete [199]. Indeed, after cellulose esterification in $[C_3(NBu_2)_3]Cl$, we obtained a yellowish powder (Figure C.7), very similar to unmodified cellulose instead of a gel or a film, signs of crosslinking of depolymerized glucose or regenerated cellulose [200]. The peaks at 2850 cm^{-1} and 2920 cm^{-1} are present within all spectra and are characteristic of aliphatic C-H bonds of fatty long chains from the FFA.

At 80 °C, the viscosity of [Emim]Cl is half that of [Bmim]Cl, more than twice that of [Bmim][Ac] [60], and one-third that of $[C_3(NBu_2)_3]Cl$ [201]. Therefore [Emim]Cl represents an interesting solvent for cellulose esterification. However we observed a better solubility of EA and catalysts in [Bmim]Cl, [Bmim][Ac] and $[C_3(NBu_2)_3]Cl$ than in [Emim]Cl.

As far as the catalysts are concerned, the cellulose esterification is impacted by the nature of catalysts used. When a base like triethylamine was used, it usually increased the esterification extent of cellulose by enhancing the nucleophilicity of the carboxylic acid of FFA towards esterification [68]. Although sulfuric acid can promote cellulose esterification [202], the acidic media can lead to the cellulose degradation. When FFA is used, p-Tos activates the carboxylic acid through its conversion into chloride acid moieties resulting a chlorinated EA being more reactive with the hydroxyl groups of cellulose than carboxylic acids [203]. This explains that esters obtained with this catalyst had higher esters peaks in FTIR spectra than samples catalyzed with sulfuric acid and triethylamine. Based on the reactivity and viscosity, [Bmim]Cl, [Bmim][Ac], FFAs and catalysts were then selected for the esterification of cellulose. To adopt a greener approach, we decided to avoid the use of catalysts in order to employ the IL as the solvent and catalyst simultaneously.

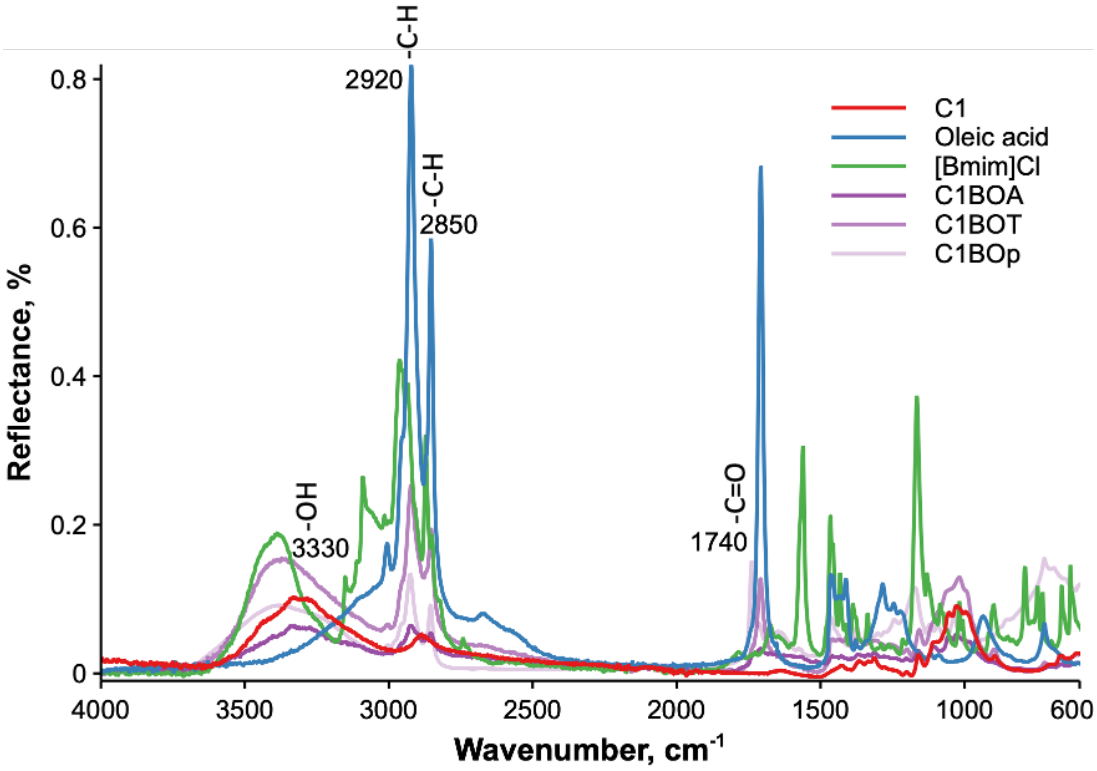

Figure 5.1 FTIR spectra of cellulose esters produced in [Bmim]Cl with oleic acid, sulfuric acid (C1BOA), triethylamine (C1BOT), and p-Tos (C1BOp). Labels are the wavenumber (in cm^{-1}) of the associated peak.

In order to conduct US-assisted esterification reactions, we purposely added a co-solvent - DMSO - to the reaction mixture to decrease its viscosity. Such addition has a positive effect on decreasing the temperature in a way to conduct these reactions at ambient conditions thus reducing the occurrence of competing reactions, as previously observed [186]. Practically, DMSO was added after cellulose dissolution tests at 75 g L^{-1} in [Bmim]Cl at 80 °C and the resulting solution was cooled down to room temperature. This behavior has been already reported elsewhere. For instance, [mTBNH][Ac] was unable to dissolve more than 2 wt% of cellulose. The viscosity of a 2 wt% cellulose solution in [mTBNH][Ac]/DMSO decreased by 84% as the ratio shifted from 1:0 to 1:3. Adding DMSO to [mTBNH][Ac] enhanced cellulose dissolution by improving mass transport through reduced viscosity. Since DMSO alone is not an effective solvent for cellulose, its presence reduced the *DS* of cellulose laurate by 50% [189].

From Table 5.2, we first made a comparison between the silent conditions and the US-based esterification with two different ILs. In silent conditions, the reaction was conducted at 80 °C, and we determined the *DS* after 30 min and after 24 h of reaction. With US, the reaction was conducted in much milder conditions at 40 °C for 30 min. The samples derived from C1B_30 and C1Ba_30 obtained at 80 °C for 30 min under silent conditions, in [Bmim]Cl/DMSO and [Bmim][Ac]/DMSO respectively, exhibit a *DS* of 0.13 and 0.0 respectively, which are lower than *DS* of samples C1B20 and C1Ba20 obtained with US for 30 min at 40 °C, 0.92 and 0.16 respectively (Table 5.2). This supports the benefits of US for the process proposed in this study. To confirm the accomplishment of esterification reactions, we conducted FTIR analyses. Indeed, C1Ba and C1Ba20 have a peak at 1725 cm^{-1}, corresponding to C=O stretching from esters (Figure 5.2). C1Ba_30 and C1Ba20 also exhibit a peak at 3330 cm^{-1}, and C1Ba20 shows a shoulder around 3400 cm^{-1}, whereas C1Ba shows a lower intensity at 3330 cm^{-1}. This suggests the presence of residual hydrogen bonding [204] or ethanol in C1Ba_30 and C1Ba20.

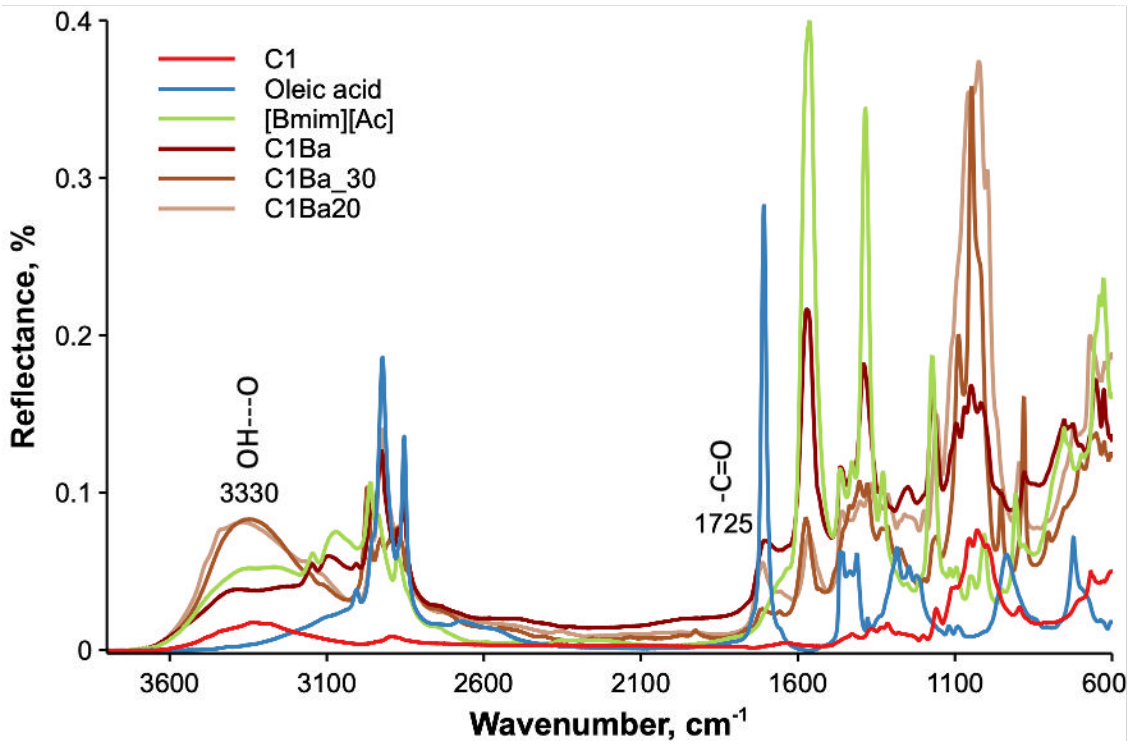

Figure 5.2 FTIR spectra of cellulose esters produced in [Bmim][Ac]/DMSO with oleic acid, without US at 80 °C for 24 h and for 30 min, and with US at 40 °C for 30 min.

A next step covered the analysis of the influence of the IL type and the reaction temperature during US-assisted esterification, which account for 6% and 11% of the variance, respectively (Table 5.3). The *DS* of esters obtained in [Bmim][Ac] is 95% higher than those obtained in [Bmim]Cl, after 30 min of sonication at 80 °C (Table 5.2). A 13 wt% cellulose solution in [Bmim][Ac] is 5 times less viscous than in [Bmim]Cl at 85 °C [205]. At 25 °C, an equimolar ratio of [Bmim][Ac]/DMSO is 5 times less viscous than [Bmim]Cl/DMSO [206], [207]. Schieppati et al. have previously demonstrated that acoustic streaming velocity and active cavitation volume increased as the viscosity of the IL decreased. Hence, we attribute the increase of *DS* to enhanced cavitation activity and mixing, and increasing interaction of molecules [132]. [Bmim]Cl/DMSO at a weight ratio of 15:0.05 dissolved 4 wt% of cellulose. Adding DMSO to [Bmim]Cl decreased the viscosity of the cellulose solution by 33% [208]. For instance, adding DMAc to [Bmim][Ac], decreased the system's viscosity from 0.477 Pa.s at a weight ratio [Bmim][Ac]/DMAc of 10, to 0.001 Pa.s at a ratio of 1:9 [196].

Table 5.3 Predictor screening analysis of the DS for DoE2.

Predictor	Portion*
US *PD*	51%
Cellulose source	19%
Concentration of cellulose	12%
Temperature	11%
IL	6%
Time	1%

*Portion of the variance from the prediction.

5.3.2 Effect of the source of cellulose

In the second set of experiments, we obtained esters from two different sources of cellulose with different molecular weight and crystallinity. FTIR spectra (Figure 5.3) show that US esterified to a certain extent both sources of cellulose, as indicated by the peaks at 1725 cm^{-1} (C=O) and 1160 cm^{-1} (C-O). However, the peak at 1725 cm^{-1} explains a partial esterification of cellulose, and the peak at 1160 cm^{-1} can be attributed to residual [Bmim]Cl.

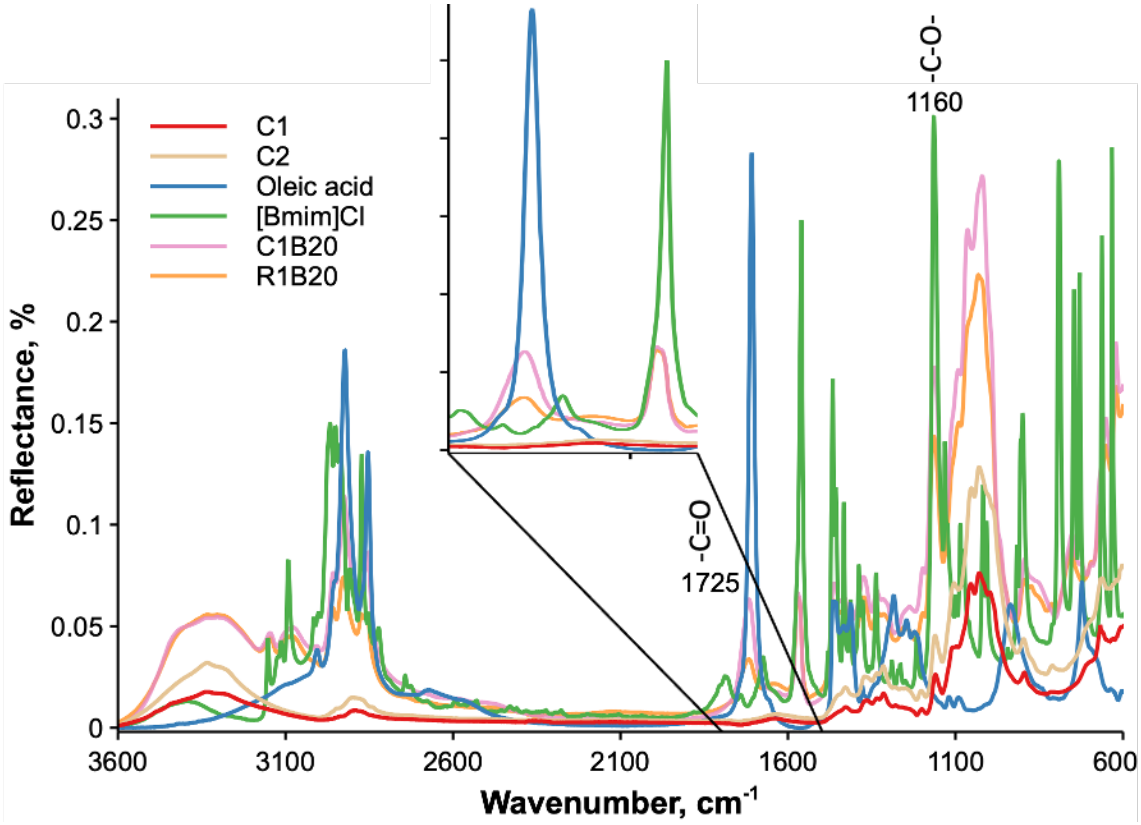

Figure 5.3 FTIR spectra of cellulose esters produced in [Bmim]Cl/DMSO with oleic acid and various sources of cellulose.

The *DS* is generally higher for C2, which also carries a higher molecular weight (Table 5.2). At 25 g L^{-1} and 29.5 W g^{-1}, the *DS* increases by 18% as the DP increases from 138 to 926 and sample R1B40 also has the highest *DS* among all samples (Table 5.2).

When the DP of cellulose increases, it means that the length of cellulose chains also increases. Literature data generally report that *DS* decreases with the increase of DP of cellulose. The *DS* increases by 49% with the DP decreasing from 227 to 82 [209], and by 267% with the DP decreasing from 346 to 93 [166]. They attributed this effect to a larger specific surface area of cellulose chains accessible for modification at lower DP. Tarasova et al. observed an opposite effect, the *DS* increased by 10% as the DP increased from 150 to 1000. They explained it with the crystallinity index (Cr) of unmodified celluloses: the *DS* increase followed a decrease in Cr from 84% to 76%. A lower Cr implies less crystallites and a less ordered structure, suggesting that more hydroxyl groups are accessible for esterification [73]. In our case, C1 has a higher crystallinity index than C2: 86.5% against 83.9% respectively (Figure C.8).

5.3.3 Effect of the concentration of cellulose

We produced esters from cotton cellulose at various cellulose concentrations as confirmed by FTIR spectra (Figure C.9). The *DS* decreases as the concentration of cellulose increases (Table 5.2). As the concentration of cellulose increases, the amount of oleic acid needs to increase to maintain the cellulose/FFA molar ratio constant and equal to 1:6. An increase of the concentration of both reagents is expected to favor the contact between oleic acid and cellulose hydroxyl groups, increasing overall intrinsic kinetics. However, as the cellulose loading increases, the solution viscosity drastically increases: Rieland et al. observed an increase of zero shear viscosity from 0.5 Pa.s to 1510 Pa.s as the cellulose concentration increases from 1 wt% to 15 wt%. The increase of viscosity limits the mass transfer and the reactivity between oleic acid and cellulose hydroxyl groups, decreasing the *DS* [210]. Puss et al. formed a gel-like solution while sonicating 5 wt% lignocellulose in water. The gel formed around the US probe inhibits the waves' transmission into the solution [211].

5.3.4 Effect of the US power

We produced cellulose esters at various US powers and various cellulose concentrations, thus at various US *PD*. In another study, we showed that a US power increase, other conditions being the same, does not necessarily favor the grafting of more FFA [186]. The US *PD* explains 51% of the *DS* variance, *p*-value: 0.0008 (Table 5.3). The *DS* increases with the increase of *PD* (Figure 5.4). US-assisted esterification at 29.5 W g^{-1} for 30 min at 40 °C produced esters with a *DS* 26% higher than in silent conditions at 80 °C for 24 h, demonstrating the benefit of using US (Table 5.2). With C1 at 75 g L^{-1} the *DS* increases by 24% as *PD* increases from 9.8 W g^{-1} to 33.9 W g^{-1} (Table 5.2). With C2 at 25 g L^{-1} the *DS* increases by 115% as *PD* increases from 29.5 W g^{-1} to 101.7 W g^{-1} (Table 5.2). Generally, the increase of US power in ILs increases the number and size of cavitation bubbles, hence increases the cavitation volume [95]. Indeed, the increase of US power from 20 W to 60 W, increases the acoustic streaming velocity by 50% in [Bmim][Ac] and [Bmim]Cl, at 20 kHz [132]. Acoustic cavitation and streaming are both effects derived from sonication that can occur in ILs-based media to different extents. Cavitation bubbles promote reactive radicals' formation [95], and acoustic streaming enhances mixing for homogeneous dispersion of cellulose chains and reagents [11]. The increase of US *PD* increases the temperature locally, boosting the reaction kinetics and decreasing the viscosity. The decrease of viscosity promotes mixing and mass

transfer [81], [95]. The combination of these effects enhances cellulose esterification. However too vigorous US agitation can degas the solution, which decreases the nuclei for cavitation activity [212].

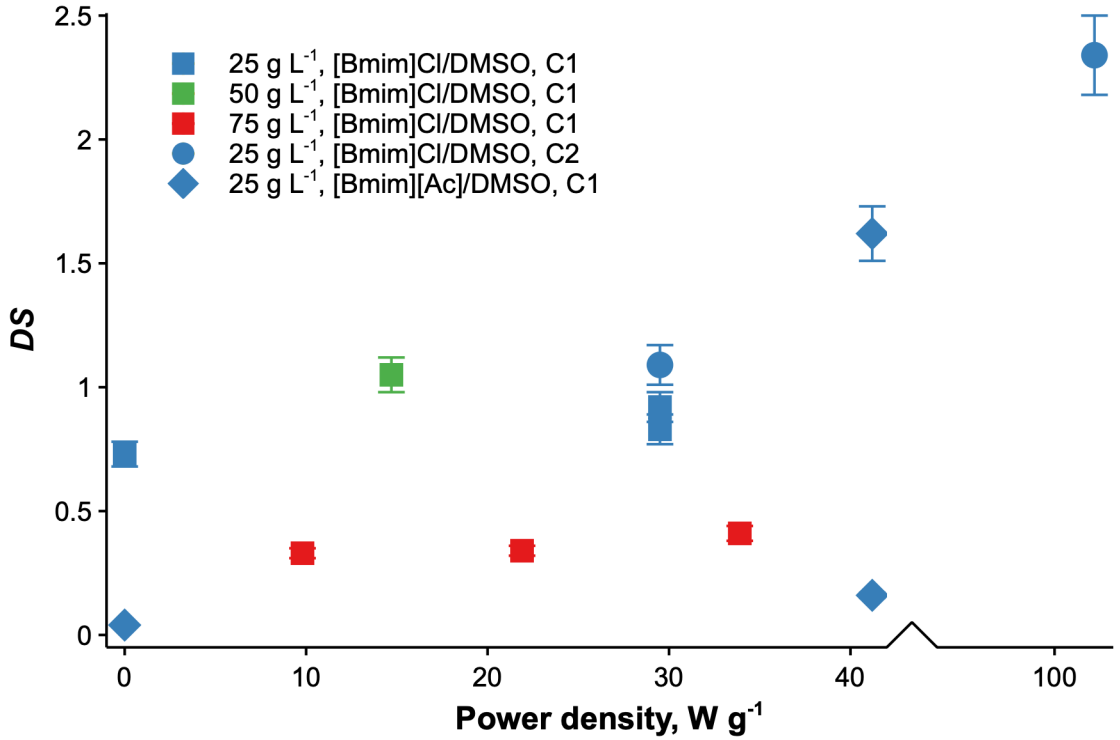

Figure 5.4 *DS* vs. power density for cellulose esters prepared at various concentrations. Squares represent samples prepared in [Bmim]Cl/DMSO from C1, circles represent samples prepared in [Bmim]Cl/DMSO from C2, and diamonds represent samples prepared in [Bmim][Ac]/DMSO from C1.

5.3.5 Thermoplasticity

XRD was employed to verify the amorphization of cellulose esters. XRD diffractograms of C1B20, C2B20 and R1B40 show a decrease in the intensity of crystalline lattices, evidencing the alteration of the crystalline structure of cellulose due to dissolution, sonication and esterification (Figure 5.5). The samples show a broad peak at 20.0° - 22.0° corresponding to an amorphization of cellulose esters and a change of structure to a cellulose II polymorph [73]. The shoulder at 34.5° (Figure 5.5), compared to the peaks at 34.5° for unmodified celluloses (Figure C.8) explains a decrease of peak intensity of crystal plane 004 [170]. This shoulder is the lowest for R1B40, produced at the highest *PD*. Moreover, a new shoulder emerges at 4.5° in the diffractogram of C2B20, confirming

the crystallization of grafted fatty chains [175]. Crystalline peaks observed on DSC curves of C1B20 (Figure C.10) and R1B40 (Figure C.11), characteristic of melting of crystals formed by side chains of fatty acid, do not emerge on the XRD diffractogram. Indeed, melting takes place at -21 °C, -56 °C and -13 °C, whereas XRD analyses were at room temperature.

Peaks at 31.7° and 45.4° for sample R1B40 (prepared at the highest *PD*) are ascribed to residual [Bmim]Cl [213] or eroded Ti-6Al-V alloy from the probe [214], respectively (Figure 5.5).

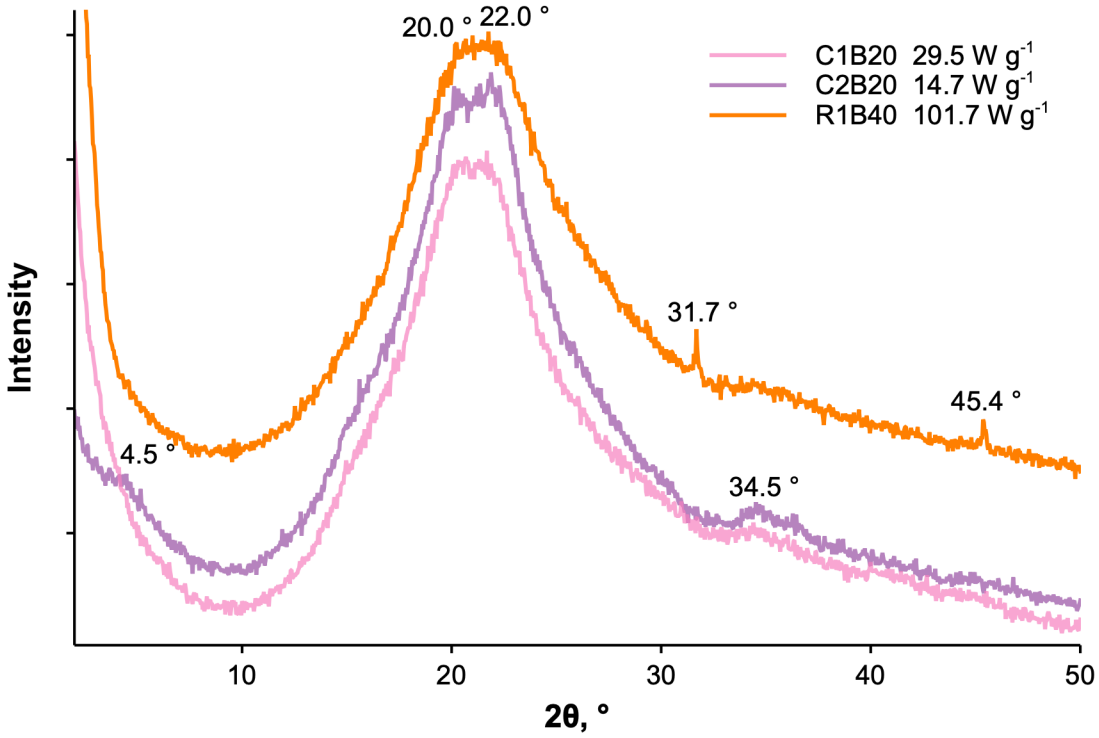

Figure 5.5 XRD diffractogram of samples produced with C1 at different concentrations, C1B20 and C2B20, produced at 29.5 W g^{-1} and 14.7 W g^{-1} respectively, and sample with the highest *DS*, produced with C2 at 101.7 W g^{-1}.

Even though the esterification produces less crystalline materials than the unmodified cellulose, the T_g and thermoplasticity are verified by DSC. The T_g increases with the *DS* to a maximum, then it decreases (Figure 5.6). The decrease of T_g as the *DS* increases is a result of more FFA grafted, which enhances chains mobility and results in an internal plasticizing effect [53], [150]. Hou et al. verified the increase of chains mobility with the *DS* by rheological tests [156]. R1B20 and C2B20 have a similar DS, however R1B20 produced from the cellulose with the highest DP and at the lowest concentration, formed a transparent and flexible film (Figure 5.6). In contrast, C2B20 formed a dark brown wax instead of a film (Figure 5.6), suggesting the simultaneous softening and

degradation during pressing [175]. That explains the higher T_g for R1B20 than C2B20 (Figure 5.6). 1B40, produced at higher PD than R1B20, formed a dark brown material after pressing, sign of degradation and of a non-thermoplastic material. C3B20 formed a stiff, brittle and fibrous plate, as expected due to its low *DS* and absence of T_g in DSC (Figure C.12-C.13). Although C1Ba20 exhibits a lower *DS* than C1Ba20_80, both have similar T_g values, likely due to cellulose degradation in C1Ba20, which reduces chain entanglement and thereby counteracts the expected T_g increase (plasticizing effect of higher substitution). This degradation evidenced by the brittle, brownish and heterogeneous film of C1Ba20, undermines thermoplasticity, whereas the transparent and homogeneous film of C1Ba20_80 reflects a more favorable structure for thermoplastic behavior.

C1B20 was obtained from a cellulose source with lower DP and higher Cr than R1B20. C1B20 has an endothermic peak at -12 °C and a transition at 60 °C, while R1B20 has an endothermic peak at -43 °C and at -15 °C, and a transition at 125 °C (Table C.1 and Figure C.10). The endothermic peaks are attributed to the melting of crystals formed by lateral chains of fatty acid grafted onto cellulose [215]. The higher size of the peak for R1B20 than for C1B20 is in line with more oleic acid grafted onto unmodified cellulose C2 than onto C1 (Table C.1). The increase of T_g from 60 °C to 125 °C is explained by a higher DP of C2, which increases steric hindrance and entanglement of cellulose chains, decreasing their mobility and thus capacity to change phase [73]. The two distinct endotherm peaks for R1B20 suggest the presence of various crystalline domains [174].

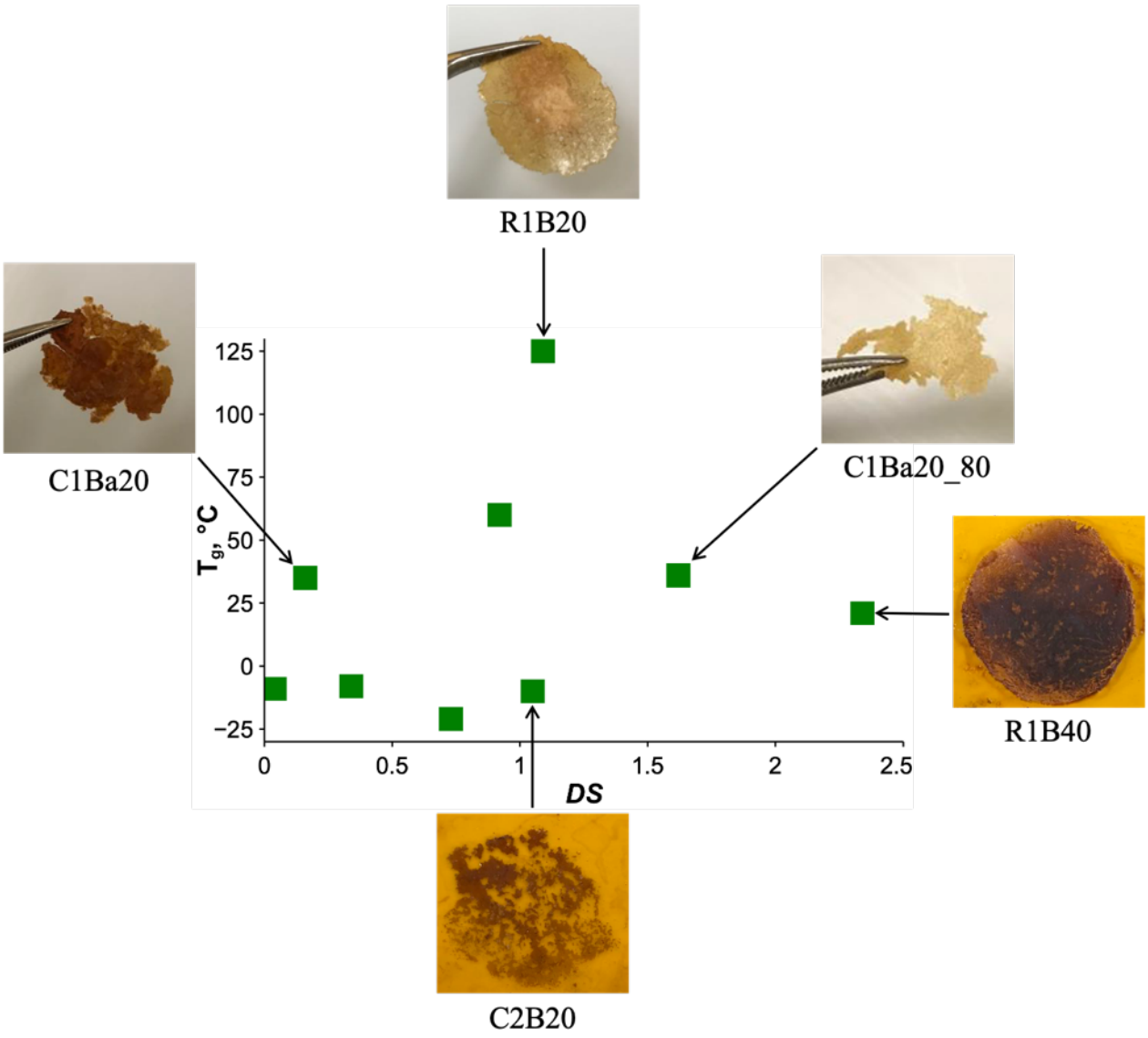

Figure 5.6 T_g vs. *DS* for cellulose esters prepared in various conditions. Squares represent samples data points.

Some samples exhibited multiple T_g values or melting endotherms. To assess the homogeneity of the cellulose esters, we conducted dielectric spectroscopy. Dielectric spectroscopy provides information on material relaxation over a broad range of frequencies and temperatures, from 10^{-1} Hz to 10^6 Hz and from -10 °C to 140 °C, respectively. As the temperature increases, the dielectric loss permittivity (ε'') spectrum shifts towards higher frequencies. This shift is due to enhanced chain mobility, as thermoplastic materials require less relaxation time (τ) for dipole reorientation at higher temperatures [216].

As previously mentioned (Figure 5.5), esterification reduces the crystallinity of cellulose esters; with ester groups preventing the recrystallization of cellulose chains [53], [73], [175]. This loss of crystallinity increases the dielectric permittivity (Figure C.14), as explained by Dawy and Nada, who attributed it to the formation of disordered regions, allowing greater freedom of movement for unmodified hydroxyl groups [217]. However, esterification with oleic acid introduces polar carbonyl (C=O) groups and non-polar aliphatic side chains with eighteen carbon atoms. These non-polar groups explain the decrease in dielectric permittivity as the frequency increases, as well as the absence of a peak around the glass transition temperature of the samples. The non-polar side chains exert a shielding effect, hindering chain mobility and thereby lowering the dielectric permittivity of the cellulose esters [217], [218].

Although no dielectric permittivity peak was observed within the measured frequency and temperature ranges, the thermoplastic behavior of the pressed samples is confirmed by Figure 5.7. Indeed, dielectric spectroscopy revealed two relaxation modes within the explored temperature range (Figure 5.7), each corresponding to a specific molecular domain.

The primary alpha-relaxation, occurring at higher temperatures (lower 1/T), is attributed to the relaxation of alkyl side chains and is associated with the glass transition [219]. The secondary beta-relaxation, observed at lower temperatures (higher 1/T), is related to the relaxation of the main cellulose chain [220].

The similar slopes observed for beta-relaxation in the three ester samples suggest a comparable activation energy, indicating that the cellulose backbone remained intact and was not degraded. Moreover, the beta-relaxation slopes of the esterified samples are lower than that of unmodified cellulose, suggesting that the ester groups facilitate chain mobility, which is an effect typically produced by plasticizers [219].

The alpha-relaxation exhibited varying slopes, indicating differences in activation energy among the samples. The activation energy increased in the order: R1B20 < C1Ba20 < C3B20. Thus, C3B20 requires more energy for alkyl side chain motion than C1Ba20 and R1B20. This trend reflects the weaker plasticizing effect of oleic acid, consistent with the absence of a detectable T_g in DSC measurements (Figure C.13 and Table C.1). R1B20 showed a T_g of 125 °C and a *DS* of 1.09, whereas C1Ba20 had a T_g of 35 °C and a *DS* of 0.16. These values explain the lower activation energy observed for alpha-relaxation in R1B20 compared to C1Ba20, and correlate with the

transparent appearance of the R1B20 film, in contrast to the brownish, degraded film of C1Ba20. We proved the formation of thermoplastic cellulose esters avoiding the degradation of cellulose chains and secondary reactions. These results also suggest that esters have uniform substitutions as only one relaxation attributed to side chains was observed.

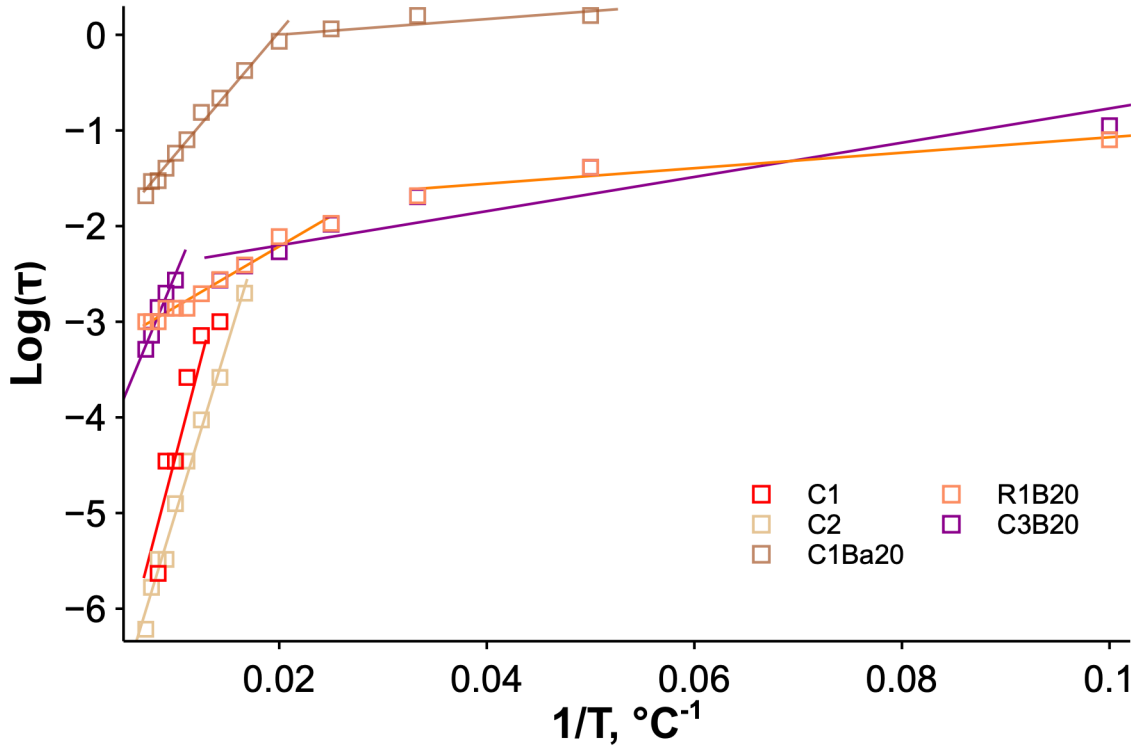

Figure 5.7 Dielectric relaxation time as a function of temperature for unmodified celluloses and pressed samples C1Ba20, R1B20 and C3B20 (regressions parameters in Table C.2).

5.4 Conclusion

In this study, we adopted US to intensify the esterification of two sources of cotton cellulose at various concentrations in four ionic liquids with two esterification agents: oleic acid and stearic acid. Among conventional (no US) esterification reactions at 80 °C for 24 h, [Bmim]Cl and [Bmim][Ac] as solvents and oleic acid and p-toluenesulfonyl chloride as esterification agents resulted in the highest esterification extent. In [Bmim]Cl with oleic acid as esterification agent, a US power per unit of weight of cellulose of 102 W g^{-1}, at 40 °C for 30 min resulted in the highest *DS* of 2.34. Globally the increase of US power density increased the *DS*. The samples displayed a thermoplastic behavior, as confirmed by DSC and dielectric spectroscopy, and melting peaks ascribed to crystals formed by grafted fatty acid chains. XRD analysis also showed the partial

amorphization of cellulose esters following dissolution and US-assisted esterification. Amorphization enables the formation of translucent or transparent materials. In [Bmim]Cl with oleic acid as esterification agent, a US power per unit of weight of cellulose of 29.5 W g^{-1}, at 40 °C for 30 min resulted in a transparent film. Overall, the proposed US process provides faster reactions and higher *DS*, at lower temperatures than conventional process, avoiding the use of a catalyst. The process preserves the cellulose chains from degradation and simultaneously produces a thermoplastic material with the ability of forming translucent films. Future work will consider improving the esters purification procedure along with ILs separation and recovery.

CRediT authorship contribution statement

Pierre Dal: Writing – review & editing, Writing – original draft, Validation, Methodology, Investigation. **Owen J. Curnow:** Writing – review & editing, Investigation, Resources. **Jean-Marie Raquez:** Writing – review & editing, Investigation, Supervision. **Daria C. Boffito:** Writing – review & editing, Supervision, Funding, Resources.

Acknowledgements

The authors are thankful to Cédric Malveau for providing assistance during the nuclear magnetic resonance experiments. The authors are thankful to Eric David and Laura Makatia for providing assistance during the dielectric spectroscopy experiments. Pierre Dal is thankful to Institut de l'Energie Trottier, Mitacs, the Canada Research Chair EPIC, and the National Sciences and Engineering Research Council of Canada (NSERC) for awarding him graduate scholarships to support his studies.

CHAPTER 6 CONCLUSION

6.1 General discussion

This research project successfully valorized cellulose waste with ultrasound-assisted esterification to produce thermoplastic materials. First, we determined the total acoustic pressure and the volume of active cavitation zones for various parameters, US frequencies, and thermodynamic properties of cellulose ester solutions in a two-part multi-frequency sonoreactor using COMSOL Multiphysics. The cavitation activity was characterized in a cylindrical ultrasonic reactor equipped with six lateral flat transducers along the walls and a concentric high-intensity focused ultrasound transducer at the bottom. The hexagonal cross-section design of the reactor promotes constructive interference of sound waves. The HIFU transducer focuses ultrasound waves in the conical "whistle" part, streamlining the fluid flow toward the reactor's upper part. The propagation of acoustic waves and the distribution of active cavitation zones under various geometrical configurations and operating frequencies were modeled using COMSOL Multiphysics. The gap between the reflector and lateral transducers was fixed at 0.075 m. COMSOL calculated the acoustic pressure and the active cavitation surface area into the reactor for different cellulose concentrations (different viscosities, densities and speeds of sound) and US frequencies. The model accounts for the attenuation due to cavitation bubbles as cavitation bubbles alter the sound waves propagation. Cavitation bubbles attenuated the acoustic pressure by 80 % and decreased the active cavitation surface area by 85 %. The cellulose ester concentration of 6.25 g L^{-1} yielded the highest p_T and the largest V. At 78 kHz and h = 0.075 m, with μ = 5.3·10^{-3} Pa.s, ρ = 941.8 kg m^{-3} and c = 1545 m s^{-1}, the simulation generated p_T = 1.96·10^{6} Pa and V = 3.99·10^{-2} m^2. The simulations coupled the activity of lateral and HIFU transducers, working at different US frequencies, to determine the activity within the entire reactor. We included the root mean-squared acoustic pressure of two harmonics into the linear equation $\beta = \mathrm{C} \cdot p$.

The second and third part of the project contributed to the understanding of the US-assisted esterification of cellulose. The sonication for cellulose esterification remains unexplored, even more so in ionic liquids. In the second part the objective was to produce cellulose esters using long chain fatty acids as a green esterification agent and US as an alternative energy vector to intensify the process and decrease the reaction's energy requirements. Preliminary reactions under silent conditions using oleic acid and stearic acid to esterify two sources of cellulose at various

temperatures, resulted in the highest *DS* of 1.44 after 24 h of reaction at 80 °C. US-assisted esterification resulted in the highest *DS* of 0.38 (1.79 determined by gravimetric analysis) after 30 min of reaction at 20 °C and 136 W L^{-1}. Compared to the conventional heating and stirring process, sonoprocessing is 48 times faster and at temperature 4 times lower, even though it produced a *DS* 4 times lower. The conventionally esterified sample required 93 W g^{-1} of cellulose whereas the US-esterified sample required 18 W g^{-1} of cellulose to achieve the same *DS*. The sample prepared with US displayed a thermoplastic behavior, as confirmed by DSC, with a T_g at 47 °C. However, the increase in T_g with *DS* suggests cellulose depolymerization, and the difficulty to dissolve the resulting esters indicates competing crosslinking reactions. Using the same model as presented in CHAPTER 3, we determined the total acoustic pressure, the volume of active cavitation zones, and the acoustic streaming velocity, explaining the US effects on the cellulose ester solution in a horn-type cylindrical ultrasonic reactor. A temperature of 20 °C, a cellulose concentration of 25 g L^{-1}, an ultrasound power of 4.39 W in 32.2 mL were the conditions resulting in the highest *DS* in US-assisted esterification. However, the simulation with these parameters resulted in the smallest active cavitation volume (*V)* and the lowest acoustic streaming velocity (*u)*: $9.60 \cdot 10^{-8}$ m^3 and 40.06 m s^{-1}. At 10.5 mL the probe is located near the bottom of the vessel, the bottom wall blocks the US waves, resulting in a lower mixing efficiency than in 32.2 mL. Excessively high velocities generate bubbles in the reactor that form between the reagent molecules, preventing their contact and their reaction.

Based on these results, we chose to treat cellulose in IL. In this third part, we produced long-chain cellulose esters with US in IL and DMSO. The first experiments aimed at identifying the optimal ionic liquid for subsequent US-assisted esterification of cellulose. The conventional (no US) esterification involved two sources of cotton cellulose in four ionic liquids with two esterification agents: oleic acid and stearic acid. Among conventional esterification reactions at 80 °C for 24 h, [Bmim]Cl and [Bmim][Ac] as solvents and oleic acid and p-toluenesulfonyl chloride as esterification agents resulted in the highest esterification extent. Then, we adopted US to intensify the esterification of cellulose at various concentrations. ILs and DMSO dissolved and esterified cellulose at a concentration of 75 g L^{-1} against 25 g L^{-1} in the mixture DMAc/LiCl. In [Bmim]Cl with oleic acid as esterification agent, a US power per unit of weight of cellulose of 102 W g^{-1}, at 40 °C for 30 min resulted in the highest *DS* of 2.34. Globally the DS increased with the US power density. DSC and dielectric spectroscopy confirmed the thermoplastic behavior of the ester's

samples. DSC showed melting peaks ascribed to crystals formed by grafted fatty acid chains. XRD analysis confirmed the partial amorphization of cellulose esters following dissolution and US-assisted esterification. In [Bmim]Cl with oleic acid as esterification agent, a US power per unit of weight of cellulose of 29.5 W g^{-1}, at 40 °C for 30 min resulted in a transparent film and a T_g of 125 °C. The proposed process avoids the use of a catalyst while preserving the cellulose chains from degradation and simultaneously producing a thermoplastic material.

6.2 Limitations and future research

This research project advances the knowledge in modelling and simulation of ultrasound activity and US-assisted esterification of cellulose. First, the present model and simulation include a linear model for acoustic sound waves propagation. In the perspective of an improved reactor design for scale-up, a next step in the simulation of the lateral and HIFU transducers is the incorporation of a non-linear regime, simulation occurring in the time domain. The present project assumed a constant bubble equilibrium radius. As the pressure increases beyond the Blake threshold, the bubble size distribution widens, leading to non-uniform bubbles. Larger bubbles attenuate sound waves more than smaller ones, thus the present study potentially underestimated sound waves attenuation. To improve the accuracy of the simulation, future work will include a dynamic bubble size distribution model.

The simulations and the cellulose treatments were conducted at a laboratory scale, however the scale-up for potential industrialization or implementation in a biorefinery would involve several challenges. This study explored two sources of cellulose that are pure and extracted from cotton. However, that does not completely represent the cellulose waste stream diversity. Different cellulose sources (different molecular weight, crystallinity, purity…) would alter the dissolution, thus the reaction mixture viscosity, the mixing and mass transfer for instance. A future work should treat other cellulose wastes. The ionic liquid recycling was not tested in this study. Efficient purification and recycling reduce solvent waste generation and potentially the cost of operation. Finally, material's erosion could limit the scale-up. Indeed, ultrasound probe erodes with time and contaminates the reaction medium. The US-assisted esterification could be tested with the probe emitting sound waves pulsations, instead of emitting continuously.

REFERENCES

[1] "Cellulose Market." Accessed: Mar. 09, 2025. [Online]. Available: https://www.fortunebusinessinsights.com/cellulose-market-102062

[2] M. Imani *et al.*, "Investigating waste mineral-filled cellulose sourcing in circular economy for regeneration into composite: Matching existing market volumes of oil-based plastics for packaging," *Cleaner and Circular Bioeconomy*, vol. 8, p. 100089, Aug. 2024, doi: 10.1016/j.clcb.2024.100089.

[3] S. Searle and C. Malins, "Availability of cellulosic residues and wastes in the EU," Oct. 2013.

[4] Statistics Canada, "Waste materials diverted, by type and by source," Tableau : 38-10-0138-01.

[5] T. Heinze, "Cellulose: Structure and Properties," in *Cellulose Chemistry and Properties: Fibers, Nanocelluloses and Advanced Materials*, vol. 271, Springer,Cham, 2015, pp. 1–52. doi: 10.1007/12_2015_319.

[6] B. Lindman, G. Karlström, and L. Stigsson, "On the mechanism of dissolution of cellulose," *J Mol Liq*, vol. 156, no. 1, pp. 76–81, Sep. 2010, doi: 10.1016/j.molliq.2010.04.016.

[7] A.-L. Dupont, "Cellulose in lithium chloride/N,N-dimethylacetamide, optimisation of a dissolution method using paper substrates and stability of the solutions," *Polymer (Guildf)*, vol. 44, no. 15, pp. 4117–4126, Jul. 2003, doi: 10.1016/S0032-3861(03)00398-7.

[8] Y. Wang, X. Wang, Y. Xie, and K. Zhang, "Functional nanomaterials through esterification of cellulose: a review of chemistry and application," *Cellulose*, vol. 25, no. 7, pp. 3703–3731, Jul. 2018, doi: 10.1007/s10570-018-1830-3.

[9] O. A. El Seoud, L. C. Fidale, N. Ruiz, M. L. O. D'Almeida, and E. Frollini, "Cellulose swelling by protic solvents: which properties of the biopolymer and the solvent

matter?," *Cellulose*, vol. 15, no. 3, pp. 371–392, Jun. 2008, doi: 10.1007/s10570-007-9189-x.

[10] C. Krumm, J. Pfaendtner, and P. J. Dauenhauer, "Millisecond Pulsed Films Unify the Mechanisms of Cellulose Fragmentation," *Chemistry of Materials*, vol. 28, no. 9, pp. 3108–3114, May 2016, doi: 10.1021/acs.chemmater.6b00580.

[11] D.-F. Hou *et al.*, "Sustainable conversion regenerated cellulose into cellulose oleate by sonochemistry," *Front Chem Sci Eng*, vol. 17, no. 8, pp. 1096–1108, Aug. 2023, doi: 10.1007/s11705-023-2317-9.

[12] P. Willberg-Keyriläinen and J. Ropponen, "Evaluation of esterification routes for long chain cellulose esters," *Heliyon*, vol. 5, no. 11, p. e02898, Nov. 2019, doi: 10.1016/j.heliyon.2019.e02898.

[13] M. C. Bubalo *et al.*, "A comparative study of ultrasound-, microwave-, and microreactor-assisted imidazolium-based ionic liquid synthesis," *gps*, vol. 2, no. 6, pp. 579–590, Dec. 2013, doi: 10.1515/gps-2013-0086.

[14] D. Klemm, B. Heublein, H. Fink, and A. Bohn, "Cellulose: Fascinating Biopolymer and Sustainable Raw Material," *Angewandte Chemie International Edition*, vol. 44, no. 22, pp. 3358–3393, May 2005, doi: 10.1002/anie.200460587.

[15] V. S. R. RAO, P. R. SUNDARARAJAN, C. RAMAKRISHNAN, and G. N. RAMACHANDRAN, "Conformational Studies of Amylose," in *Conformation of Biopolymers*, Elsevier, 1967, pp. 721–737. doi: 10.1016/B978-1-4832-2843-3.50024-8.

[16] D. N.-S. Hon, "Cellulose and Its Derivatives: Structures, Reactions, and Medical Uses," in *Polysaccharides in Medicinal Applications*, 1st Edition., Routledge, 1996. doi: 10.1201/9780203742815.

[17] K. Kamide, K. Okajima, K. Kowsaka, and T. Matsui, "CP/MASS 13C NMR Spectra of Cellulose Solids: An Explanation by the Intramolecular Hydrogen Bond Concept," *Polym J*, vol. 17, no. 5, pp. 701–706, May 1985, doi: 10.1295/polymj.17.701.

[18] A. J. Michell, “Second derivative F.t.-i.r. spectra of celluloses I and II and related mono- and oligo-saccharides,” *Carbohydr Res*, vol. 173, no. 2, pp. 185–195, Mar. 1988, doi: 10.1016/S0008-6215(00)90814-0.

[19] C. Y. Liang and R. H. Marchessault, “Infrared spectra of crystalline polysaccharides. I. Hydrogen bonds in native celluloses,” *Journal of Polymer Science*, vol. 37, no. 132, pp. 385–395, Jun. 1959, doi: 10.1002/pol.1959.1203713209.

[20] H. A. Krässig, *Cellulose : structure, accessibility, and reactivity*. Yverdon: Gordon and Breach Science, 1993.

[21] K. H. Gardner and J. Blackwell, “The structure of native cellulose,” *Biopolymers*, vol. 13, no. 10, pp. 1975–2001, Oct. 1974, doi: 10.1002/bip.1974.360131005.

[22] Y. Nishiyama, P. Langan, and H. Chanzy, “Crystal Structure and Hydrogen-Bonding System in Cellulose Iβ from Synchrotron X-ray and Neutron Fiber Diffraction,” *J Am Chem Soc*, vol. 124, no. 31, pp. 9074–9082, Aug. 2002, doi: 10.1021/ja0257319.

[23] M. M. de Souza Lima and R. Borsali, “Rodlike Cellulose Microcrystals: Structure, Properties, and Applications,” *Macromol Rapid Commun*, vol. 25, no. 7, pp. 771–787, Apr. 2004, doi: 10.1002/marc.200300268.

[24] D. Trache *et al.*, “Microcrystalline cellulose: Isolation, characterization and bio-composites application—A review,” *Int J Biol Macromol*, vol. 93, pp. 789–804, Dec. 2016, doi: 10.1016/j.ijbiomac.2016.09.056.

[25] H. Angellier, J. Putaux, S. Molina-Boisseau, D. Dupeyre, and A. Dufresne, “Starch Nanocrystal Fillers in an Acrylic Polymer Matrix,” *Macromol Symp*, vol. 221, no. 1, pp. 95–104, Jan. 2005, doi: 10.1002/masy.200550310.

[26] D. Haldar and M. K. Purkait, “Micro and nanocrystalline cellulose derivatives of lignocellulosic biomass: A review on synthesis, applications and advancements,” *Carbohydr Polym*, vol. 250, p. 116937, Dec. 2020, doi: 10.1016/j.carbpol.2020.116937.

[27] S. Mishra, P. S. Kharkar, and A. M. Pethe, “Biomass and waste materials as potential sources of nanocrystalline cellulose: Comparative review of preparation methods

(2016 – Till date)," *Carbohydr Polym*, vol. 207, pp. 418–427, Mar. 2019, doi: 10.1016/j.carbpol.2018.12.004.

[28] L. J. Kroon-Batenburg, J. Kroon, and M. G. Northolt, "Chain modulus and intramolecular hydrogen bonding in native and regenerated cellulose fibres," *Polymer communications (Guildford)*, vol. 27, no. 10, pp. 290–292, 1986.

[29] V. Favier, H. Chanzy, and J. Y. Cavaille, "Polymer Nanocomposites Reinforced by Cellulose Whiskers," *Macromolecules*, vol. 28, no. 18, pp. 6365–6367, Aug. 1995, doi: 10.1021/ma00122a053.

[30] D. Viet, S. Beck-Candanedo, and D. G. Gray, "Dispersion of cellulose nanocrystals in polar organic solvents," *Cellulose*, vol. 14, no. 2, pp. 109–113, Mar. 2007, doi: 10.1007/s10570-006-9093-9.

[31] P. Mäki-Arvela, I. Anugwom, P. Virtanen, R. Sjöholm, and J. P. Mikkola, "Dissolution of lignocellulosic materials and its constituents using ionic liquids—A review," *Ind Crops Prod*, vol. 32, no. 3, pp. 175–201, Nov. 2010, doi: 10.1016/j.indcrop.2010.04.005.

[32] C. M. Hansen and A. Björkman, "The Ultrastructure of Wood from a Solubility Parameter Point of View," *Holzforschung*, vol. 52, no. 4, pp. 335–344, Jan. 1998, doi: 10.1515/hfsg.1998.52.4.335.

[33] B. Lindman, B. Medronho, L. Alves, C. Costa, H. Edlund, and M. Norgren, "The relevance of structural features of cellulose and its interactions to dissolution, regeneration, gelation and plasticization phenomena," *Physical Chemistry Chemical Physics*, vol. 19, no. 35, pp. 23704–23718, 2017, doi: 10.1039/C7CP02409F.

[34] B. Medronho and B. Lindman, "Brief overview on cellulose dissolution/regeneration interactions and mechanisms," *Adv Colloid Interface Sci*, vol. 222, pp. 502–508, Aug. 2015, doi: 10.1016/j.cis.2014.05.004.

[35] Å. Östlund, D. Lundberg, L. Nordstierna, K. Holmberg, and M. Nydén, "Dissolution and Gelation of Cellulose in TBAF/DMSO Solutions: The Roles of Fluoride Ions and Water," *Biomacromolecules*, vol. 10, no. 9, pp. 2401–2407, Sep. 2009, doi: 10.1021/bm900667q.

[36] T. Heinze and T. Liebert, “Unconventional methods in cellulose functionalization,” *Prog Polym Sci*, vol. 26, no. 9, pp. 1689–1762, Nov. 2001, doi: 10.1016/S0079-6700(01)00022-3.

[37] H. Sobue, H. Kiessig, and K. Hess, “Das System Cellulose–Natriumhydroxyd–Wasser in Abhängigkeit von der Temperatur,” *Zeitschrift für Physikalische Chemie*, vol. 43B, no. 1, pp. 309–328, May 1939, doi: 10.1515/zpch-1939-4324.

[38] T. Liebert, “Cellulose Solvents – Remarkable History, Bright Future,” 2010, pp. 3–54. doi: 10.1021/bk-2010-1033.ch001.

[39] A. Isogai and R. H. Atalla, “Dissolution of Cellulose in Aqueous NaOH Solutions,” *Cellulose*, vol. 5, no. 4, pp. 309–319, 1998, doi: 10.1023/A:1009272632367.

[40] L. Yan and Z. Gao, “Dissolving of cellulose in PEG/NaOH aqueous solution,” *Cellulose*, vol. 15, no. 6, pp. 789–796, Dec. 2008, doi: 10.1007/s10570-008-9233-5.

[41] J. Cai *et al.*, “Dynamic Self-Assembly Induced Rapid Dissolution of Cellulose at Low Temperatures,” *Macromolecules*, vol. 41, no. 23, pp. 9345–9351, Dec. 2008, doi: 10.1021/ma801110g.

[42] R. Kadokawa, T. Endo, Y. Yasaka, K. Ninomiya, K. Takahashi, and K. Kuroda, “Cellulose Preferentially Dissolved over Xylan in Ionic Liquids through Precise Anion Interaction Regulated by Bulky Cations,” *ACS Sustain Chem Eng*, vol. 9, no. 26, pp. 8686–8691, Jul. 2021, doi: 10.1021/acssuschemeng.1c02492.

[43] S. Chrapava, D. Touraud, T. Rosenau, A. Potthast, and W. Kunz, “The investigation of the influence of water and temperature on the LiCl/DMAc/cellulose system,” *Physical Chemistry Chemical Physics*, vol. 5, no. 9, pp. 1842–1847, Apr. 2003, doi: 10.1039/b212665f.

[44] C. L. McCormick, P. A. Callais, and B. H. Hutchinson, “Solution studies of cellulose in lithium chloride and N,N-dimethylacetamide,” *Macromolecules*, vol. 18, no. 12, pp. 2394–2401, Dec. 1985, doi: 10.1021/ma00154a010.

[45] T. Heinze, R. Dicke, A. Koschella, A. H. Kull, E.-A. Klohr, and W. Koch, “Effective preparation of cellulose derivatives in a new simple cellulose solvent,” *Macromol*

Chem Phys, vol. 201, no. 6, pp. 627–631, Mar. 2000, doi: 10.1002/(SICI)1521-3935(20000301)201:6<627::AID-MACP627>3.0.CO;2-Y.

[46] S. Köhler and T. Heinze, "New Solvents for Cellulose: Dimethyl Sulfoxide/Ammonium Fluorides," *Macromol Biosci*, vol. 7, no. 3, pp. 307–314, Mar. 2007, doi: 10.1002/mabi.200600197.

[47] D. C. Boffito, F. Galli, C. Pirola, C. L. Bianchi, and G. S. Patience, "Ultrasonic free fatty acids esterification in tobacco and canola oil," *Ultrason Sonochem*, vol. 21, no. 6, pp. 1969–1975, Nov. 2014, doi: 10.1016/j.ultsonch.2014.01.026.

[48] D. Klemm, B. Philipp, T. Heinze, U. Heinze, and W. Wagenknecht, *Comprehensive Cellulose Chemistry*. Wiley, 1998. doi: 10.1002/3527601937.

[49] T. Heinze, T. Liebert, and A. Koschella, *Esterification of Polysaccharides*. Berlin/Heidelberg: Springer-Verlag, 2006. doi: 10.1007/3-540-32112-8.

[50] J. Zhang *et al.*, "Homogeneous esterification of cellulose in room temperature ionic liquids," *Polym Int*, vol. 64, no. 8, pp. 963–970, Aug. 2015, doi: 10.1002/pi.4883.

[51] Y. Zheng, J. Song, B. Cheng, X. Fang, and Y. Yuan, "Preparation and flame retardancy of 3-(hydroxyphenylphosphinyl)-propanoic acid esters of cellulose and their fibers," *Cellulose*, vol. 22, no. 1, pp. 229–244, Feb. 2015, doi: 10.1007/s10570-014-0486-x.

[52] H. Almasi, B. Ghanbarzadeh, J. Dehghannia, S. Pirsa, and M. Zandi, "Heterogeneous modification of softwoods cellulose nanofibers with oleic acid: Effect of reaction time and oleic acid concentration," *Fibers and Polymers*, vol. 16, no. 8, pp. 1715–1722, Aug. 2015, doi: 10.1007/s12221-015-4294-1.

[53] L. Duchatel-Crépy *et al.*, "Substitution degree and fatty chain length influence on structure and properties of fatty acid cellulose esters," *Carbohydr Polym*, vol. 234, p. 115912, Apr. 2020, doi: 10.1016/j.carbpol.2020.115912.

[54] K. J. Edgar *et al.*, "Advances in cellulose ester performance and application," *Prog Polym Sci*, vol. 26, no. 9, pp. 1605–1688, Nov. 2001, doi: 10.1016/S0079-6700(01)00027-2.

[55] T. Kulomaa, J. Matikainen, P. Karhunen, M. Heikkilä, J. Fiskari, and I. Kilpeläinen, "Cellulose fatty acid esters as sustainable film materials – effect of side chain structure on barrier and mechanical properties," *RSC Adv*, vol. 5, no. 98, pp. 80702–80708, 2015, doi: 10.1039/C5RA12671A.

[56] J. Bras, C. Vaca-Garcia, M.-E. Borredon, and W. Glasser, "Oxygen and water vapor permeability of fully substituted long chain cellulose esters (LCCE)," *Cellulose*, vol. 14, no. 4, pp. 367–374, Jul. 2007, doi: 10.1007/s10570-007-9123-2.

[57] R. D. Rogers and K. R. Seddon, "Ionic Liquids--Solvents of the Future?," *Science (1979)*, vol. 302, no. 5646, pp. 792–793, Oct. 2003, doi: 10.1126/science.1090313.

[58] T. L. Greaves, A. Weerawardena, C. Fong, I. Krodkiewska, and C. J. Drummond, "Protic Ionic Liquids: Solvents with Tunable Phase Behavior and Physicochemical Properties," *J Phys Chem B*, vol. 110, no. 45, pp. 22479–22487, Nov. 2006, doi: 10.1021/jp0634048.

[59] R. P. Swatloski, S. K. Spear, J. D. Holbrey, and R. D. Rogers, "Dissolution of Cellose with Ionic Liquids," *J Am Chem Soc*, vol. 124, no. 18, pp. 4974–4975, May 2002, doi: 10.1021/ja025790m.

[60] H. Wang, G. Gurau, and R. D. Rogers, "Ionic liquid processing of cellulose," *Chem Soc Rev*, vol. 41, no. 4, p. 1519, 2012, doi: 10.1039/c2cs15311d.

[61] T. Heinze, S. Dorn, M. Schöbitz, T. Liebert, S. Köhler, and F. Meister, "Interactions of Ionic Liquids with Polysaccharides – 2: Cellulose," *Macromol Symp*, vol. 262, no. 1, pp. 8–22, Jan. 2008, doi: 10.1002/masy.200850202.

[62] A. Xu, J. Wang, and H. Wang, "Effects of anionic structure and lithium salts addition on the dissolution of cellulose in 1-butyl-3-methylimidazolium-based ionic liquid solvent systems," *Green Chem.*, vol. 12, no. 2, pp. 268–275, 2010, doi: 10.1039/B916882F.

[63] H. Zhao, G. A. Baker, Z. Song, O. Olubajo, T. Crittle, and D. Peters, "Designing enzyme-compatible ionic liquids that can dissolve carbohydrates," *Green Chemistry*, vol. 10, no. 6, p. 696, 2008, doi: 10.1039/b801489b.

[64] A. R. Ferreira, M. G. Freire, J. C. Ribeiro, F. M. Lopes, J. G. Crespo, and J. A. P. Coutinho, “An Overview of the Liquid−Liquid Equilibria of (Ionic Liquid + Hydrocarbon) Binary Systems and Their Modeling by the Conductor-like Screening Model for Real Solvents,” *Ind Eng Chem Res*, vol. 50, no. 9, pp. 5279–5294, May 2011, doi: 10.1021/ie102471b.

[65] A. M. Fernandes, M. A. A. Rocha, M. G. Freire, I. M. Marrucho, J. A. P. Coutinho, and L. M. N. B. F. Santos, “Evaluation of Cation−Anion Interaction Strength in Ionic Liquids,” *J Phys Chem B*, vol. 115, no. 14, pp. 4033–4041, Apr. 2011, doi: 10.1021/jp201084x.

[66] L. Feng and Z. Chen, “Research progress on dissolution and functional modification of cellulose in ionic liquids,” *J Mol Liq*, vol. 142, no. 1–3, pp. 1–5, Aug. 2008, doi: 10.1016/j.molliq.2008.06.007.

[67] Y. Luan, J. Zhang, M. Zhan, J. Wu, J. Zhang, and J. He, “Highly efficient propionylation and butyralation of cellulose in an ionic liquid catalyzed by 4-dimethylminopyridine,” *Carbohydr Polym*, vol. 92, no. 1, pp. 307–311, Jan. 2013, doi: 10.1016/j.carbpol.2012.08.111.

[68] M. Granström *et al.*, “Tosylation and acylation of cellulose in 1-allyl-3-methylimidazolium chloride,” *Cellulose*, vol. 15, no. 3, 2008, doi: 10.1007/s10570-008-9197-5.

[69] S. Suzuki, Y. Hamano, S. C. Hernandez, N. Wada, and K. Takahashi, “Green Conversion of Total Lignocellulosic Components of Sugarcane Bagasse to Thermoplastics Through Transesterification Using Ionic Liquid,” *ACS Sustain Chem Eng*, vol. 9, no. 45, pp. 15249–15257, Nov. 2021, doi: 10.1021/acssuschemeng.1c05281.

[70] L. P. Hinner, J. L. Wissner, B. Hauer, and B. A. Nebel, “Efficient cellulose dissolution in a tertiary [EHEMIM]-[EMIM]OAc-water system,” *J Mol Liq*, vol. 281, pp. 236–242, May 2019, doi: 10.1016/j.molliq.2019.02.096.

[71] R. Milotskyi, G. Sharma, T. Fujie, D. Hirose, N. Wada, and K. Takahashi, “Continuous process of cellulose dissolution and transesterification reaction

catalysed by ionic liquid in twin screw extruder," *React Chem Eng*, vol. 8, no. 6, pp. 1395–1402, 2023, doi: 10.1039/D2RE00537A.

[72] R. Milotskyi, L. Szabó, T. Fujie, K. Sakata, N. Wada, and K. Takahashi, "Low waste process of rapid cellulose transesterification using ionic liquid/DMSO mixed solvent: Towards more sustainable reaction systems," *Carbohydr Polym*, vol. 256, p. 117560, Mar. 2021, doi: 10.1016/j.carbpol.2020.117560.

[73] E. Tarasova *et al.*, "Reactive extrusion of cellulose esters in ionic liquid: exploring properties and performance across different cellulose types and degrees of polymerization," *Cellulose*, Oct. 2024, doi: 10.1007/s10570-024-06203-1.

[74] C. S. R. Freire, A. J. D. Silvestre, C. P. Neto, M. N. Belgacem, and A. Gandini, "Controlled heterogeneous modification of cellulose fibers with fatty acids: Effect of reaction conditions on the extent of esterification and fiber properties," *J Appl Polym Sci*, vol. 100, no. 2, pp. 1093–1102, Apr. 2006, doi: 10.1002/app.23454.

[75] J. Lease, T. Kawano, and Y. Andou, "Esterification of Cellulose with Long Fatty Acid Chain through Mechanochemical Method," *Polymers (Basel)*, vol. 13, no. 24, p. 4397, Dec. 2021, doi: 10.3390/polym13244397.

[76] M. Ashokkumar *et al.*, *Handbook of Ultrasonics and Sonochemistry*. Singapore: Springer Singapore, 2016. doi: 10.1007/978-981-287-278-4.

[77] K. S. Suslick, "Sonochemistry," *Science (1979)*, vol. 247, no. 4949, pp. 1439–1445, Mar. 1990, doi: 10.1126/science.247.4949.1439.

[78] L. M. O. Vaz, M. I. Martins, U. Coutinho Filho, V. L. Cardoso, and M. H. M. Reis, "Ultrasound-assisted transesterification reactions for biodiesel production with sodium zirconate supported in polyvinyl alcohol as catalyst," *Environ Prog Sustain Energy*, vol. 36, no. 4, pp. 1262–1267, Jul. 2017, doi: 10.1002/ep.12571.

[79] A. Taha *et al.*, "Ultrasonic emulsification: An overview on the preparation of different emulsifiers-stabilized emulsions," *Trends Food Sci Technol*, vol. 105, pp. 363–377, Nov. 2020, doi: 10.1016/j.tifs.2020.09.024.

[80] J. Luo, Z. Fang, and R. L. Smith, “Ultrasound-enhanced conversion of biomass to biofuels,” *Prog Energy Combust Sci*, vol. 41, pp. 56–93, Apr. 2014, doi: 10.1016/j.pecs.2013.11.001.

[81] D. C. Boffito, S. Mansi, J.-M. Leveque, C. Pirola, C. L. Bianchi, and G. S. Patience, “Ultrafast Biodiesel Production Using Ultrasound in Batch and Continuous Reactors,” *ACS Sustain Chem Eng*, vol. 1, no. 11, pp. 1432–1439, Nov. 2013, doi: 10.1021/sc400161s.

[82] D. C. Boffito *et al.*, “Batch and Continuous Ultrasonic Reactors for the Production of Methyl Esters from Vegetable Oils,” 2015, pp. 87–114. doi: 10.1007/978-94-017-9624-8_3.

[83] E. Abedi, K. Pourmohammadi, and S. Abbasi, “Dual-frequency ultrasound for ultrasonic-assisted esterification,” *Food Sci Nutr*, vol. 7, no. 8, pp. 2613–2624, Aug. 2019, doi: 10.1002/fsn3.1115.

[84] A. Mohammad Amini, S. M. A. Razavi, and S. A. Mortazavi, “Morphological, physicochemical, and viscoelastic properties of sonicated corn starch,” *Carbohydr Polym*, vol. 122, pp. 282–292, May 2015, doi: 10.1016/j.carbpol.2015.01.020.

[85] A. Grönroos, P. Pirkonen, and O. Ruppert, “Ultrasonic depolymerization of aqueous carboxymethylcellulose,” *Ultrason Sonochem*, vol. 11, no. 1, pp. 9–12, Jan. 2004, doi: 10.1016/S1350-4177(03)00129-9.

[86] S. Haouache *et al.*, “Selective radical depolymerization of cellulose to glucose induced by high frequency ultrasound,” *Chem Sci*, vol. 11, no. 10, pp. 2664–2669, 2020, doi: 10.1039/D0SC00020E.

[87] P. Bhaumik and P. L. Dhepe, “Conversion of Biomass into Sugars,” in *Biomass Sugars for Non-Fuel Applications*, The Royal Society of Chemistry, 2015, pp. 1–53. doi: 10.1039/9781782622079-00001.

[88] W. Lan, C.-F. Liu, F.-X. Yue, R.-C. Sun, and J. F. Kennedy, “Ultrasound-assisted dissolution of cellulose in ionic liquid,” *Carbohydr Polym*, vol. 86, no. 2, pp. 672–677, Aug. 2011, doi: 10.1016/j.carbpol.2011.05.013.

[89] L. Tang *et al.*, "Ultrasonication-assisted manufacture of cellulose nanocrystals esterified with acetic acid," *Bioresour Technol*, vol. 127, pp. 100–105, Jan. 2013, doi: 10.1016/j.biortech.2012.09.133.

[90] J.-P. Mikkola *et al.*, "Ultrasound enhancement of cellulose processing in ionic liquids: from dissolution towards functionalization," *Green Chemistry*, vol. 9, no. 11, p. 1229, 2007, doi: 10.1039/b708533h.

[91] C. F. Liu *et al.*, "Succinoylation of sugarcane bagasse under ultrasound irradiation," *Bioresour Technol*, vol. 99, no. 5, pp. 1465–1473, Mar. 2008, doi: 10.1016/j.biortech.2007.01.062.

[92] S. Ma, X. Xue, S. Yu, and Z. Wang, "High-intensity ultrasound irradiated modification of sugarcane bagasse cellulose in an ionic liquid," *Ind Crops Prod*, vol. 35, no. 1, pp. 135–139, Jan. 2012, doi: 10.1016/j.indcrop.2011.06.023.

[93] S. Ma, S. Yu, Z. Wang, and X. Zheng, "Ultrasound-assisted modification of beet pulp cellulose with phthalic anhydride in ionic liquid ," *Cellulose Chemistry and Technology*, vol. 47, no. 7–8, pp. 527–533, 2013.

[94] D. Fernandez Rivas *et al.*, "Process intensification education contributes to sustainable development goals. Part 1," *Education for Chemical Engineers*, vol. 32, pp. 1–14, Jul. 2020, doi: 10.1016/j.ece.2020.04.003.

[95] D. Meroni, R. Djellabi, M. Ashokkumar, C. L. Bianchi, and D. C. Boffito, "Sonoprocessing: From Concepts to Large-Scale Reactors," *Chem Rev*, vol. 122, no. 3, pp. 3219–3258, Feb. 2022, doi: 10.1021/acs.chemrev.1c00438.

[96] D. C. Boffito and T. Van Gerven, "Process Intensification and Catalysis," in *Reference Module in Chemistry, Molecular Sciences and Chemical Engineering*, Elsevier, 2019. doi: 10.1016/B978-0-12-409547-2.14343-4.

[97] B. Gielen *et al.*, "Characterization of stable and transient cavitation bubbles in a milliflow reactor using a multibubble sonoluminescence quenching technique," *Ultrason Sonochem*, vol. 25, pp. 31–39, Jul. 2015, doi: 10.1016/j.ultsonch.2014.08.013.

[98] Y. Yao, Y. Pan, and S. Liu, “Power ultrasound and its applications: A state-of-the-art review,” *Ultrason Sonochem*, vol. 62, p. 104722, Apr. 2020, doi: 10.1016/j.ultsonch.2019.104722.

[99] T. G. Leighton, *The Acoustic Bubble*. Elsevier, 1994. doi: 10.1016/B978-0-12-441920-9.X5001-9.

[100] P. Riesz, D. Berdahl, and C. L. Christman, “Free radical generation by ultrasound in aqueous and nonaqueous solutions.,” *Environ Health Perspect*, vol. 64, pp. 233–252, Dec. 1985, doi: 10.1289/ehp.8564233.

[101] Y. T. Didenko and K. S. Suslick, “The energy efficiency of formation of photons, radicals and ions during single-bubble cavitation,” *Nature*, vol. 418, no. 6896, pp. 394–397, Jul. 2002, doi: 10.1038/nature00895.

[102] V. Mišík and P. Riesz, “EPR study of free radicals induced by ultrasound in organic liquids II. Probing the temperatures of cavitation regions,” *Ultrason Sonochem*, vol. 3, no. 1, pp. 25–37, Feb. 1996, doi: 10.1016/1350-4177(95)00036-4.

[103] J. Collins, T. G. McKenzie, M. D. Nothling, S. Allison-Logan, M. Ashokkumar, and G. G. Qiao, “Sonochemically Initiated RAFT Polymerization in Organic Solvents,” *Macromolecules*, vol. 52, no. 1, pp. 185–195, Jan. 2019, doi: 10.1021/acs.macromol.8b01845.

[104] D. Schieppati, A. Dreux, W. Gao, P. Fatehi, and D. C. Boffito, “Ultrasound-assisted carboxymethylation of LignoForce Kraft lignin to produce biodispersants,” *J Clean Prod*, vol. 366, p. 132776, Sep. 2022, doi: 10.1016/j.jclepro.2022.132776.

[105] D. Schieppati *et al.*, “Chemical and Biological Delignification of Biomass: A Review,” *Ind Eng Chem Res*, vol. 62, no. 33, pp. 12757–12794, Aug. 2023, doi: 10.1021/acs.iecr.3c01231.

[106] S. S. Rashwan, I. Dincer, and A. Mohany, “Investigation of acoustic and geometric effects on the sonoreactor performance,” *Ultrason Sonochem*, vol. 68, p. 105174, Nov. 2020, doi: 10.1016/j.ultsonch.2020.105174.

[107] I. Garcia-Vargas, L. Barthe, P. Tierce, and O. Louisnard, “Simulations of a full sonoreactor accounting for cavitation,” *Ultrason Sonochem*, vol. 91, p. 106226, Dec. 2022, doi: 10.1016/j.ultsonch.2022.106226.

[108] M. Girard, D. Vidal, F. Bertrand, J. R. Tavares, and M.-C. Heuzey, “Evidence-based guidelines for the ultrasonic dispersion of cellulose nanocrystals,” *Ultrason Sonochem*, vol. 71, p. 105378, Mar. 2021, doi: 10.1016/j.ultsonch.2020.105378.

[109] H. Laajimi, K. Fattahi, and D. C. Boffito, “Numerical investigation of the ultrasound-assisted biodiesel transesterification with a polyalcohol,” *Chemical Engineering and Processing - Process Intensification*, vol. 181, p. 109139, Nov. 2022, doi: 10.1016/j.cep.2022.109139.

[110] Y. Son, Y. No, and J. Kim, “Geometric and operational optimization of 20-kHz probe-type sonoreactor for enhancing sonochemical activity,” *Ultrason Sonochem*, vol. 65, p. 105065, Jul. 2020, doi: 10.1016/j.ultsonch.2020.105065.

[111] Y. Fang, T. Yamamoto, and S. Komarov, “Cavitation and acoustic streaming generated by different sonotrode tips,” *Ultrason Sonochem*, vol. 48, pp. 79–87, Nov. 2018, doi: 10.1016/j.ultsonch.2018.05.011.

[112] R. Jamshidi, B. Pohl, U. A. Peuker, and G. Brenner, “Numerical investigation of sonochemical reactors considering the effect of inhomogeneous bubble clouds on ultrasonic wave propagation,” *Chemical Engineering Journal*, vol. 189–190, pp. 364–375, May 2012, doi: 10.1016/j.cej.2012.02.029.

[113] K. W. Commander and A. Prosperetti, “Linear pressure waves in bubbly liquids: Comparison between theory and experiments,” *J Acoust Soc Am*, vol. 85, no. 2, pp. 732–746, Feb. 1989, doi: 10.1121/1.397599.

[114] S. Dähnke and F. Keil, “Modeling of Sound Fields in Liquids with a Nonhomogeneous Distribution of Cavitation Bubbles as a Basis for the Design of Sonochemical Reactors,” *Chem Eng Technol*, vol. 21, no. 11, pp. 873–877, Nov. 1998, doi: 10.1002/(SICI)1521-4125(199811)21:11<873::AID-CEAT873>3.0.CO;2-V.

[115] S. W. Dähnke and F. J. Keil, “Modeling of linear pressure fields in sonochemical reactors considering an inhomogeneous density distribution of cavitation bubbles,” *Chem Eng Sci*, vol. 54, no. 13–14, pp. 2865–2872, Jul. 1999, doi: 10.1016/S0009-2509(98)00340-6.

[116] O. Dahlem, J. Reisse, and V. Halloin, “The radially vibrating horn: A scaling-up possibility for sonochemical reactions,” *Chem Eng Sci*, vol. 54, no. 13–14, pp. 2829–2838, Jul. 1999, doi: 10.1016/S0009-2509(98)00356-X.

[117] Z. Xu, K. Yasuda, and S. Koda, “Numerical simulation of liquid velocity distribution in a sonochemical reactor,” *Ultrason Sonochem*, vol. 20, no. 1, pp. 452–459, Jan. 2013, doi: 10.1016/j.ultsonch.2012.04.011.

[118] Y. Kojima, Y. Asakura, G. Sugiyama, and S. Koda, “The effects of acoustic flow and mechanical flow on the sonochemical efficiency in a rectangular sonochemical reactor,” *Ultrason Sonochem*, vol. 17, no. 6, pp. 978–984, Aug. 2010, doi: 10.1016/j.ultsonch.2009.11.020.

[119] J. Jordens, A. Honings, J. Degrève, L. Braeken, and T. Van Gerven, “Investigation of design parameters in ultrasound reactors with confined channels,” *Ultrason Sonochem*, vol. 20, no. 6, pp. 1345–1352, Nov. 2013, doi: 10.1016/j.ultsonch.2013.03.012.

[120] B. Sajjadi, A. A. A. Raman, and S. Ibrahim, “Influence of ultrasound power on acoustic streaming and micro-bubbles formations in a low frequency sono-reactor: Mathematical and 3D computational simulation,” *Ultrason Sonochem*, vol. 24, pp. 193–203, May 2015, doi: 10.1016/j.ultsonch.2014.11.013.

[121] P. R. Gogate, S. Mujumdar, and A. B. Pandit, “Sonochemical reactors for waste water treatment: comparison using formic acid degradation as a model reaction,” *Advances in Environmental Research*, vol. 7, no. 2, pp. 283–299, Jan. 2003, doi: 10.1016/S1093-0191(01)00133-2.

[122] S. Manickam, V. N. D. Arigela, and P. R. Gogate, “Intensification of synthesis of biodiesel from palm oil using multiple frequency ultrasonic flow cell,” *Fuel*

Processing Technology, vol. 128, pp. 388–393, Dec. 2014, doi: 10.1016/j.fuproc.2014.08.002.

[123] A. V. Prabhu, P. R. Gogate, and A. B. Pandit, "Optimization of multiple-frequency sonochemical reactors," *Chem Eng Sci*, vol. 59, no. 22–23, pp. 4991–4998, Nov. 2004, doi: 10.1016/j.ces.2004.09.033.

[124] A. Kumar, P. R. Gogate, and A. B. Pandit, "Mapping the efficacy of new designs for large scale sonochemical reactors," *Ultrason Sonochem*, vol. 14, no. 5, pp. 538–544, Jul. 2007, doi: 10.1016/j.ultsonch.2006.11.005.

[125] S. M. B. Hashemi, M. Akbari, R. Roohi, and Y. Phimolsiripol, "Thermosonication process of sour cherries: Microbial inactivation kinetics, experimental and computational fluid dynamics simulation," *Innovative Food Science & Emerging Technologies*, vol. 94, p. 103692, Jun. 2024, doi: 10.1016/j.ifset.2024.103692.

[126] P. R. Gogate, V. S. Sutkar, and A. B. Pandit, "Sonochemical reactors: Important design and scale up considerations with a special emphasis on heterogeneous systems," *Chemical Engineering Journal*, vol. 166, no. 3, pp. 1066–1082, Feb. 2011, doi: 10.1016/j.cej.2010.11.069.

[127] M. Hodnett, M. J. Choi, and B. Zeqiri, "Towards a reference ultrasonic cavitation vessel. Part 1: Preliminary investigation of the acoustic field distribution in a 25 kHz cylindrical cell," *Ultrason Sonochem*, vol. 14, no. 1, pp. 29–40, Jan. 2007, doi: 10.1016/j.ultsonch.2006.01.003.

[128] J. K. Chu, T. J. Tiong, S. Chong, U. A. Asli, and Y. H. Yap, "Multi-frequency sonoreactor characterisation in the frequency domain using a semi-empirical bubbly liquid model," *Ultrason Sonochem*, vol. 80, p. 105818, Dec. 2021, doi: 10.1016/j.ultsonch.2021.105818.

[129] S. Glegg and W. Devenport, "Linear acoustics," in *Aeroacoustics of Low Mach Number Flows*, Elsevier, 2017, pp. 49–72. doi: 10.1016/B978-0-12-809651-2.00003-5.

[130] L. Van Wijngaarden, “On the equations of motion for mixtures of liquid and gas bubbles,” *J Fluid Mech*, vol. 33, no. 3, pp. 465–474, Sep. 1968, doi: 10.1017/S002211206800145X.

[131] A. Prosperetti, L. A. Crum, and K. W. Commander, “Nonlinear bubble dynamics,” *J Acoust Soc Am*, vol. 83, no. 2, pp. 502–514, Feb. 1988, doi: 10.1121/1.396145.

[132] D. Schieppati *et al.*, “Characterization of the acoustic cavitation in ionic liquids in a horn-type ultrasound reactor,” *Ultrason Sonochem*, vol. 102, p. 106721, Jan. 2024, doi: 10.1016/j.ultsonch.2023.106721.

[133] K. Fattahi, E. Robert, and D. C. Boffito, “Numerical and experimental investigation of the cavitation field in horn-type sonochemical reactors,” *Chemical Engineering and Processing - Process Intensification*, vol. 182, p. 109186, Dec. 2022, doi: 10.1016/j.cep.2022.109186.

[134] P. García-Giménez, J. F. Martínez-López, S. T. Blanco, I. Velasco, and S. Otín, “Densities and Isothermal Compressibilities at Pressures up to 20 MPa of the Systems N,N-Dimethylformamide or N,N-Dimethylacetamide + α,ω-Dichloroalkane,” *J Chem Eng Data*, vol. 52, no. 6, pp. 2368–2374, Nov. 2007, doi: 10.1021/je700339f.

[135] D. Lide, *CRC Handbook of Chemistry and Physics, 2009-2010, 90th ed.* CRC Press, 2009.

[136] A. Wahab and S. Mahiuddin, “Isentropic compressibility and viscosity of aqueous and methanolic lithium chloride solutions,” *Can J Chem*, vol. 80, no. 2, pp. 175–182, Feb. 2002, doi: 10.1139/v02-007.

[137] A. Brotchie, F. Grieser, and M. Ashokkumar, “Effect of Power and Frequency on Bubble-Size Distributions in Acoustic Cavitation,” *Phys Rev Lett*, vol. 102, no. 8, p. 084302, Feb. 2009, doi: 10.1103/PhysRevLett.102.084302.

[138] A. Dehane, S. Merouani, O. Hamdaoui, and A. Alghyamah, “Insight into the impact of excluding mass transport, heat exchange and chemical reactions heat on the sonochemical bubble yield: Bubble size-dependency,” *Ultrason Sonochem*, vol. 73, p. 105511, May 2021, doi: 10.1016/j.ultsonch.2021.105511.

[139] S. Dähnke, K. M. Swamy, and F. J. Keil, “Modeling of three-dimensional pressure fields in sonochemical reactors with an inhomogeneous density distribution of cavitation bubbles,” *Ultrason Sonochem*, vol. 6, no. 1–2, pp. 31–41, Mar. 1999, doi: 10.1016/S1350-4177(98)00026-1.

[140] G. Servant, J.-L. Laborde, A. Hita, J.-P. Caltagirone, and A. Gérard, “Spatio-temporal dynamics of cavitation bubble clouds in a low frequency reactor: comparison between theoretical and experimental results,” *Ultrason Sonochem*, vol. 8, no. 3, pp. 163–174, Jul. 2001, doi: 10.1016/S1350-4177(01)00074-8.

[141] A. V. Pandit, V. P. Sarvothaman, and V. V. Ranade, “Estimation of chemical and physical effects of cavitation by analysis of cavitating single bubble dynamics,” *Ultrason Sonochem*, vol. 77, p. 105677, Sep. 2021, doi: 10.1016/j.ultsonch.2021.105677.

[142] B. Avvaru and A. B. Pandit, “Oscillating bubble concentration and its size distribution using acoustic emission spectra,” *Ultrason Sonochem*, vol. 16, no. 1, pp. 105–115, Jan. 2009, doi: 10.1016/j.ultsonch.2008.07.003.

[143] Comsol AB, “Acoustics Module User’s Guide.”

[144] R. Roohi, S. Baroumand, R. Hosseinie, and G. Ahmadi, “Numerical simulation of HIFU with dual transducers: The implementation of dual-phase lag bioheat and non-linear Westervelt equations,” *International Communications in Heat and Mass Transfer*, vol. 120, p. 105002, Jan. 2021, doi: 10.1016/j.icheatmasstransfer.2020.105002.

[145] K. Hynynen, “Demonstration of enhanced temperature elevation due to nonlinear propagation of focussed ultrasound in dog’s thigh in vivo,” *Ultrasound Med Biol*, vol. 13, no. 2, pp. 85–91, Feb. 1987, doi: 10.1016/0301-5629(87)90078-0.

[146] P. Hariharan, M. R. Myers, and R. K. Banerjee, “HIFU procedures at moderate intensities—effect of large blood vessels,” *Phys Med Biol*, vol. 52, no. 12, pp. 3493–3513, Jul. 2007, doi: 10.1088/0031-9155/52/12/011.

[147] K. Rahn, M. Diamantoglou, D. Klemm, H. Berghmans, and T. Heinze, “Homogeneous synthesis of cellulose p-toluenesulfonates in N,N-

dimethylacetamide/LiCl solvent system," *Die Angewandte Makromolekulare Chemie*, vol. 238, no. 1, pp. 143–163, Jun. 1996, doi: 10.1002/apmc.1996.052380113.

[148] Olympus, "Vitesse de propagation des ondes ultrasonores dans les matériaux," https://www.olympus-ims.com/fr/ndt-tutorials/thickness-gauge/appendices-velocities/.

[149] P. R. Gogate, A. M. Wilhelm, and A. B. Pandit, "Some aspects of the design of sonochemical reactors," *Ultrason Sonochem*, vol. 10, no. 6, pp. 325–330, Oct. 2003, doi: 10.1016/S1350-4177(03)00103-2.

[150] S. Tanaka, T. Iwata, and M. Iji, "Long/Short Chain Mixed Cellulose Esters: Effects of Long Acyl Chain Structures on Mechanical and Thermal Properties," *ACS Sustain Chem Eng*, vol. 5, no. 2, pp. 1485–1493, Feb. 2017, doi: 10.1021/acssuschemeng.6b02066.

[151] C. Vaca-Garcia and M. E. Borredon, "Solvent-free fatty acylation of cellulose and lignocellulosic wastes. Part 2: reactions with fatty acids1The first paper of this series is: Thiebaud, S., Borredon, M.E., 1995. Solvent-free wood esterification with fatty acid chlorides. Bioresour. Technol., 52, 169–173.1," *Bioresour Technol*, vol. 70, no. 2, pp. 135–142, Nov. 1999, doi: 10.1016/S0960-8524(99)00034-6.

[152] X. Huang *et al.*, "Enhanced volatile fatty acids production from waste activated sludge anaerobic fermentation by adding tofu residue," *Bioresour Technol*, vol. 274, pp. 430–438, Feb. 2019, doi: 10.1016/j.biortech.2018.12.010.

[153] P. Uschanov, L.-S. Johansson, S. L. Maunu, and J. Laine, "Heterogeneous modification of various celluloses with fatty acids," *Cellulose*, vol. 18, no. 2, pp. 393–404, Apr. 2011, doi: 10.1007/s10570-010-9478-7.

[154] C. Costa, C. Silva, E. F. Marques, and N. G. Azoia, "Long-chain cellulose esters from recycling textile waste as highly effective superhydrophobic additive: synthesis and evaluation," *Cellulose*, vol. 30, no. 5, pp. 2913–2928, Mar. 2023, doi: 10.1007/s10570-023-05065-3.

[155] L. Huang, Q. Wu, Q. Wang, and M. Wolcott, “One-Step Activation and Surface Fatty Acylation of Cellulose Fibers in a Solvent-Free Condition,” *ACS Sustain Chem Eng*, vol. 7, no. 19, pp. 15920–15927, Oct. 2019, doi: 10.1021/acssuschemeng.9b01974.

[156] D.-F. Hou *et al.*, “Mechanochemical preparation of thermoplastic cellulose oleate by ball milling,” *Green Chemistry*, vol. 23, no. 5, pp. 2069–2078, 2021, doi: 10.1039/D0GC03853A.

[157] J.-P. Mikkola, B. Toukoniitty, E. Toukoniitty, J. Aumo, and T. Salmi, “Utilisation of on-line acoustic irradiation as a means to counter-effect catalyst deactivation in heterogeneous catalysis,” *Ultrason Sonochem*, vol. 11, no. 3–4, pp. 233–239, May 2004, doi: 10.1016/j.ultsonch.2004.01.020.

[158] A. M. Bochek, “Effect of Hydrogen Bonding on Cellulose Solubility in Aqueous and Nonaqueous Solvents,” *Russian Journal of Applied Chemistry*, vol. 76, no. 11, pp. 1711–1719, Nov. 2003, doi: 10.1023/B:RJAC.0000018669.88546.56.

[159] T. Heinze, O. El Seoud, and A. Koschella, *Cellulose Derivatives: Synthesis, Structure, and Properties*. Springer, 2018.

[160] Y. Habibi, “Key advances in the chemical modification of nanocelluloses,” *Chem. Soc. Rev.*, vol. 43, no. 5, pp. 1519–1542, 2014, doi: 10.1039/C3CS60204D.

[161] N. Abdul Hadi, B. Wiege, S. Stabenau, A. Marefati, and M. Rayner, “Comparison of Three Methods to Determine the Degree of Substitution of Quinoa and Rice Starch Acetates, Propionates, and Butyrates: Direct Stoichiometry, FTIR, and 1H-NMR,” *Foods*, vol. 9, no. 1, p. 83, Jan. 2020, doi: 10.3390/foods9010083.

[162] M. Ferro *et al.*, “Non-destructive and direct determination of the degree of substitution of carboxymethyl cellulose by HR-MAS 13C NMR spectroscopy,” *Carbohydr Polym*, vol. 169, pp. 16–22, Aug. 2017, doi: 10.1016/j.carbpol.2017.03.097.

[163] A. Li, R. Zhong, X. Li, and J. Zhang, “Enhancement of sonochemical efficiency using combination of ultrasound with ultraviolet irradiation and water flow in a horn-type reactor,” *Chemical Engineering and Processing - Process Intensification*, vol. 150, p. 107884, Apr. 2020, doi: 10.1016/j.cep.2020.107884.

[164] L. Crépy, L. Chaveriat, J. Banoub, P. Martin, and N. Joly, “Synthesis of Cellulose Fatty Esters as Plastics—Influence of the Degree of Substitution and the Fatty Chain Length on Mechanical Properties,” *ChemSusChem*, vol. 2, no. 2, pp. 165–170, Feb. 2009, doi: 10.1002/cssc.200800171.

[165] A. C. Rustan and C. A. Drevon, “Fatty Acids: Structures and Properties,” in *Encyclopedia of Life Sciences*, Wiley, 2005. doi: 10.1038/npg.els.0003894.

[166] P. Willberg-Keyriläinen, R. Talja, S. Asikainen, A. Harlin, and J. Ropponen, “The effect of cellulose molar mass on the properties of palmitate esters,” *Carbohydr Polym*, vol. 151, pp. 988–995, Oct. 2016, doi: 10.1016/j.carbpol.2016.06.048.

[167] S. Barthel and T. Heinze, “Acylation and carbanilation of cellulose in ionic liquids,” *Green Chem.*, vol. 8, no. 3, pp. 301–306, 2006, doi: 10.1039/B513157J.

[168] P. Jandura, B. Riedl, and B. V. Kokta, “Thermal degradation behavior of cellulose fibers partially esterified with some long chain organic acids,” *Polym Degrad Stab*, vol. 70, no. 3, pp. 387–394, Jan. 2000, doi: 10.1016/S0141-3910(00)00132-4.

[169] M. Jebrane, N. Terziev, and I. Heinmaa, “Biobased and Sustainable Alternative Route to Long-Chain Cellulose Esters,” *Biomacromolecules*, vol. 18, no. 2, pp. 498–504, Feb. 2017, doi: 10.1021/acs.biomac.6b01584.

[170] P. Jandura, B. V. Kokta, and B. Riedl, “Fibrous long-chain organic acid cellulose esters and their characterization by diffuse reflectance FTIR spectroscopy, solid-state CP/MAS13C-NMR, and X-ray diffraction,” *J Appl Polym Sci*, vol. 78, no. 7, pp. 1354–1365, Nov. 2000, doi: 10.1002/1097-4628(20001114)78:7<1354::AID-APP60>3.0.CO;2-V.

[171] P. Liang *et al.*, “Application of Fourier Transform Infrared Spectroscopy for the Oxidation and Peroxide Value Evaluation in Virgin Walnut Oil,” *Journal of Spectroscopy*, vol. 2013, pp. 1–5, 2013, doi: 10.1155/2013/138728.

[172] L. A. García-Zapateiro, J. M. Franco, C. Valencia, M. A. Delgado, and C. Gallegos, “Viscous, thermal and tribological characterization of oleic and ricinoleic acids-derived estolides and their blends with vegetable oils,” *Journal of Industrial and*

Engineering Chemistry, vol. 19, no. 4, pp. 1289–1298, Jul. 2013, doi: 10.1016/j.jiec.2012.12.030.

[173] M. D. M. Morselli Ribeiro, D. Barrera Arellano, and C. R. Ferreira Grosso, "The effect of adding oleic acid in the production of stearic acid lipid microparticles with a hydrophilic core by a spray-cooling process," *Food Research International*, vol. 47, no. 1, pp. 38–44, Jun. 2012, doi: 10.1016/j.foodres.2012.01.007.

[174] J. E. Sealey, G. Samaranayake, J. G. Todd, and W. G. Glasser, "Novel cellulose derivatives. IV. Preparation and thermal analysis of waxy esters of cellulose," *J Polym Sci B Polym Phys*, vol. 34, no. 9, pp. 1613–1620, Jul. 1996, doi: 10.1002/(SICI)1099-0488(19960715)34:9<1613::AID-POLB10>3.0.CO;2-A.

[175] P. S. Sejati, F. Obounou Akong, C. Torloting, F. Fradet, and P. Gérardin, "Thermoplastic translucent film from wood and fatty acids by solvent free esterification: Influence of fatty acid chain length," *Eur Polym J*, vol. 196, p. 112276, Sep. 2023, doi: 10.1016/j.eurpolymj.2023.112276.

[176] B. Stefanovic, T. Rosenau, and A. Potthast, "Effect of sonochemical treatments on the integrity and oxidation state of cellulose," *Carbohydr Polym*, vol. 92, no. 1, pp. 921–927, Jan. 2013, doi: 10.1016/j.carbpol.2012.09.039.

[177] Y. Liu, S. Li, Z. Wang, and L. Wang, "Ultrasound in cellulose-based hydrogel for biomedical use: From extraction to preparation," *Colloids Surf B Biointerfaces*, vol. 212, p. 112368, Apr. 2022, doi: 10.1016/j.colsurfb.2022.112368.

[178] X. Niu, Y. Liu, A. W. T. King, S. Hietala, H. Pan, and O. J. Rojas, "Plasticized Cellulosic Films by Partial Esterification and Welding in Low-Concentration Ionic Liquid Electrolyte," *Biomacromolecules*, vol. 20, no. 5, pp. 2105–2114, May 2019, doi: 10.1021/acs.biomac.9b00325.

[179] F. Ahmed *et al.*, "Ultrasonic-assisted deacetylation of cellulose acetate nanofibers: A rapid method to produce cellulose nanofibers," *Ultrason Sonochem*, vol. 36, pp. 319–325, May 2017, doi: 10.1016/j.ultsonch.2016.12.013.

[180] R. Zhang *et al.*, "High-intensity ultrasound promoted the aldol-type condensation as an alternative mean of synthesizing pyrazines in a Maillard reaction model system of

D-glucose-13C6 and L-glycine," *Ultrason Sonochem*, vol. 82, p. 105913, Jan. 2022, doi: 10.1016/j.ultsonch.2022.105913.

[181] M. Sivakumar and A. B. Pandit, "Ultrasound enhanced degradation of Rhodamine B: optimization with power density," *Ultrason Sonochem*, vol. 8, no. 3, pp. 233–240, Jul. 2001, doi: 10.1016/S1350-4177(01)00082-7.

[182] M. Ioelovich, "Structural characteristics of cellulose esters with different degrees of substitution," *World Journal of Advanced Research and Reviews*, vol. 15, no. 1, pp. 730–738, Jul. 2022, doi: 10.30574/wjarr.2022.15.1.0772.

[183] T. Yamagishi, T. Fukuda, T. Miyamoto, Y. Takashina, Y. Yakoh, and J. Watanabe, "Thermotropic cellulose derivatives with flexible substituents IV. Columnar liquid crystals from ester-type derivatives of cellulose," *Liq Cryst*, vol. 10, no. 4, pp. 467–473, Oct. 1991, doi: 10.1080/02678299108036436.

[184] D. C. Boffito and D. Fernandez Rivas, "Process intensification connects scales and disciplines towards sustainability," *Can J Chem Eng*, vol. 98, no. 12, pp. 2489–2506, Dec. 2020, doi: 10.1002/cjce.23871.

[185] D. C. Boffito, "Scaling process intensification technologies: what does it take to deploy?," *Chemical Engineering and Processing - Process Intensification*, vol. 212, p. 110275, Jun. 2025, doi: 10.1016/j.cep.2025.110275.

[186] P. Dal, A. Jean-Fulcrand, J.-M. Lévêque, J.-M. Raquez, and D. C. Boffito, "Ultrasound-assisted esterification of cotton cellulose with long chain free fatty acids," *Submitted to Cleaner Chemical Engineering*, 2025.

[187] X. Gao *et al.*, "Rapid transesterification of cellulose in a novel DBU-derived ionic liquid: Efficient synthesis of highly substituted cellulose acetate," *Int J Biol Macromol*, vol. 242, p. 125133, Jul. 2023, doi: 10.1016/j.ijbiomac.2023.125133.

[188] A. R. Todorov, A. W. T. King, and I. Kilpeläinen, "Transesterification of cellulose with unactivated esters in superbase–acid conjugate ionic liquids," *RSC Adv*, vol. 13, no. 9, pp. 5983–5992, 2023, doi: 10.1039/D2RA08186E.

[189] E. Tarasova *et al.*, “Preparation of Thermoplastic Cellulose Esters in [mTBNH][OAC] Ionic Liquid by Transesterification Reaction,” *Polymers (Basel)*, vol. 15, no. 19, p. 3979, Oct. 2023, doi: 10.3390/polym15193979.

[190] A. Schenzel, A. Hufendiek, C. Barner-Kowollik, and M. A. R. Meier, “Catalytic transesterification of cellulose in ionic liquids: sustainable access to cellulose esters,” *Green Chemistry*, vol. 16, no. 6, p. 3266, 2014, doi: 10.1039/c4gc00312h.

[191] R. K. Singh, P. Gupta, O. P. Sharma, and S. S. Ray, “Homogeneous synthesis of cellulose fatty esters in ionic liquid (1-butyl-3-methylimidazolium chloride) and study of their comparative antifriction property,” *Journal of Industrial and Engineering Chemistry*, vol. 24, pp. 14–19, Apr. 2015, doi: 10.1016/j.jiec.2014.09.031.

[192] K. Huang, J. Xia, M. Li, J. Lian, X. Yang, and G. Lin, “Homogeneous synthesis of cellulose stearates with different degrees of substitution in ionic liquid 1-butyl-3-methylimidazolium chloride,” *Carbohydr Polym*, vol. 83, no. 4, pp. 1631–1635, Feb. 2011, doi: 10.1016/j.carbpol.2010.10.020.

[193] S. Men *et al.*, “Synthesis of Cellulose Long-Chain Esters in 1-Butyl-3-methylimidazolium Acetate: Structure-Property Relations,” *Polymer Science, Series B*, vol. 60, no. 3, pp. 349–353, May 2018, doi: 10.1134/S1560090418030144.

[194] M. Granström, W. Mormann, and P. Frank, “Method of chlorinating polysaccharides or oligosaccharides,” WO2011086082A1, 2011

[195] K. S. Egorova, M. M. Seitkalieva, A. V. Posvyatenko, and V. P. Ananikov, “An unexpected increase of toxicity of amino acid-containing ionic liquids,” *Toxicol Res (Camb)*, vol. 4, no. 1, pp. 152–159, 2015, doi: 10.1039/C4TX00079J.

[196] Y. Zhou *et al.*, “The solution state and dissolution process of cellulose in ionic-liquid-based solvents with different hydrogen-bonding basicity and microstructures,” *Green Chemistry*, vol. 24, no. 9, pp. 3824–3833, 2022, doi: 10.1039/D2GC00374K.

[197] K. S. Salem *et al.*, “Comparison and assessment of methods for cellulose crystallinity determination,” *Chem Soc Rev*, vol. 52, no. 18, pp. 6417–6446, 2023, doi: 10.1039/D2CS00569G.

[198] M. B. Agustin, F. Nakatsubo, and H. Yano, “Improving the thermal stability of wood-based cellulose by esterification,” *Carbohydr Polym*, vol. 192, pp. 28–36, Jul. 2018, doi: 10.1016/j.carbpol.2018.02.071.

[199] T. Huang, K. D. Li, and M. Ek, “Hydrophobization of cellulose oxalate using oleic acid in a catalyst-free esterification suitable for preparing reinforcement in polymeric composites,” *Carbohydr Polym*, vol. 257, p. 117615, Apr. 2021, doi: 10.1016/j.carbpol.2021.117615.

[200] H. Satani, M. Kuwata, and A. Shimizu, “Simple and environmentally friendly preparation of cellulose hydrogels using an ionic liquid,” *Carbohydr Res*, vol. 494, p. 108054, Aug. 2020, doi: 10.1016/j.carres.2020.108054.

[201] K. J. Walst, “Synthesis and Characterization of Triaminocyclopropenium Ionic Liquids,” University of Canterbury, 2013.

[202] G. Chauvelon *et al.*, “Acidic activation of cellulose and its esterification by long-chain fatty acid,” *J Appl Polym Sci*, vol. 74, no. 8, pp. 1933–1940, 1999.

[203] T. Heinze, T. F. Liebert, K. S. Pfeiffer, and M. A. Hussain, “Unconventional Cellulose Esters: Synthesis, Characterization and Structure–Property Relations,” *Cellulose*, vol. 10, no. 3, pp. 283–296, 2003, doi: 10.1023/A:1025117327970.

[204] S. Cichosz and A. Masek, “IR Study on Cellulose with the Varied Moisture Contents: Insight into the Supramolecular Structure,” *Materials*, vol. 13, no. 20, p. 4573, Oct. 2020, doi: 10.3390/ma13204573.

[205] Y. Cao, J. Wu, J. Zhang, H. Li, Y. Zhang, and J. He, “Room temperature ionic liquids (RTILs): A new and versatile platform for cellulose processing and derivatization,” *Chemical Engineering Journal*, vol. 147, no. 1, pp. 13–21, Apr. 2009, doi: 10.1016/j.cej.2008.11.011.

[206] J.-M. Andanson, E. Bordes, J. Devémy, F. Leroux, A. A. H. Pádua, and M. F. C. Gomes, “Understanding the role of co-solvents in the dissolution of cellulose in ionic liquids,” *Green Chemistry*, vol. 16, no. 5, p. 2528, 2014, doi: 10.1039/c3gc42244e.

[207] Y. Lv *et al.*, “Rheological properties of cellulose/ionic liquid/dimethylsulfoxide (DMSO) solutions,” *Polymer (Guildf)*, vol. 53, no. 12, pp. 2524–2531, May 2012, doi: 10.1016/j.polymer.2012.03.037.

[208] S.-L. Quan, S.-G. Kang, and I.-J. Chin, “Characterization of cellulose fibers electrospun using ionic liquid,” *Cellulose*, vol. 17, no. 2, pp. 223–230, Apr. 2010, doi: 10.1007/s10570-009-9386-x.

[209] C. Costa, A. Viana, C. Silva, E. F. Marques, and N. G. Azoia, “Recycling of textile wastes, by acid hydrolysis, into new cellulosic raw materials,” *Waste Management*, vol. 153, pp. 99–109, Nov. 2022, doi: 10.1016/j.wasman.2022.08.019.

[210] J. M. Rieland, S. Nikafshar, Z. Hu, M. Nejad, and B. J. Love, “Ionic Liquid-Mediated Biopolymer Extraction from Coffee Fruit,” *Macromol Mater Eng*, vol. 308, no. 12, Dec. 2023, doi: 10.1002/mame.202300145.

[211] K. K. Puss, P. Paaver, M. Loog, and S. Salmar, “Ultrasound effect on a biorefinery lignin-cellulose mixture,” *Ultrason Sonochem*, vol. 111, p. 107071, Dec. 2024, doi: 10.1016/j.ultsonch.2024.107071.

[212] D. C. Boffito *et al.*, “Ultrasonic enhancement of the acidity, surface area and free fatty acids esterification catalytic activity of sulphated ZrO 2 –TiO 2 systems,” *J Catal*, vol. 297, pp. 17–26, Jan. 2013, doi: 10.1016/j.jcat.2012.09.013.

[213] L. Sun, J. Y. Chen, W. Jiang, and V. Lynch, “Crystalline characteristics of cellulose fiber and film regenerated from ionic liquid solution,” *Carbohydr Polym*, vol. 118, pp. 150–155, Mar. 2015, doi: 10.1016/j.carbpol.2014.11.008.

[214] I. Hacisalioglu, F. Yildiz, A. Alsaran, and G. Purcek, “Wear behavior of the plasma and thermal oxidized Ti-15Mo and Ti-6Al-4V alloys,” *IOP Conf Ser Mater Sci Eng*, vol. 174, p. 012055, Feb. 2017, doi: 10.1088/1757-899X/174/1/012055.

[215] P. Willberg-Keyriläinen, J. Vartiainen, A. Harlin, and J. Ropponen, “The effect of side-chain length of cellulose fatty acid esters on their thermal, barrier and mechanical properties,” *Cellulose*, vol. 24, no. 2, pp. 505–517, Feb. 2017, doi: 10.1007/s10570-016-1165-x.

[216] A. Rachocki, E. Markiewicz, and J. Tritt-Goc, “Dielectric Relaxation in Cellulose and its Derivatives,” *Acta Phys Pol A*, vol. 108, no. 1, pp. 137–145, Jul. 2005, doi: 10.12693/APhysPolA.108.137.

[217] M. Dawy and A. -A. M. A. Nada, “IR and Dielectric Analysis of Cellulose and Its Derivatives,” *Polym Plast Technol Eng*, vol. 42, no. 4, pp. 643–658, Jan. 2003, doi: 10.1081/PPT-120023100.

[218] S. Takechi, Y. Teramoto, and Y. Nishio, “Improvement of dielectric properties of cyanoethyl cellulose via esterification and film stretching,” *Cellulose*, vol. 23, no. 1, pp. 765–777, Feb. 2016, doi: 10.1007/s10570-015-0852-3.

[219] T. Morooka, M. Norimoto, T. Yamada, and N. Shiraishi, “Dielectric properties of cellulose acylates,” *J Appl Polym Sci*, vol. 29, no. 12, pp. 3981–3990, Dec. 1984, doi: 10.1002/app.1984.070291230.

[220] J. Einfeldt, D. Meißner, and A. Kwasniewski, “Polymerdynamics of cellulose and other polysaccharides in solid state-secondary dielectric relaxation processes,” *Prog Polym Sci*, vol. 26, no. 9, pp. 1419–1472, Nov. 2001, doi: 10.1016/S0079-6700(01)00020-X.

[221] A. Geissler, F. Loyal, M. Biesalski, and K. Zhang, “Thermo-responsive superhydrophobic paper using nanostructured cellulose stearoyl ester,” *Cellulose*, vol. 21, no. 1, pp. 357–366, Feb. 2014, doi: 10.1007/s10570-013-0160-8.

[222] S. J. Lighthill, “Acoustic streaming,” *J Sound Vib*, vol. 61, no. 3, pp. 391–418, Dec. 1978, doi: 10.1016/0022-460X(78)90388-7.

[223] F. J. Trujillo and K. Knoerzer, “A computational modeling approach of the jet-like acoustic streaming and heat generation induced by low frequency high power ultrasonic horn reactors,” *Ultrason Sonochem*, vol. 18, no. 6, pp. 1263–1273, Nov. 2011, doi: 10.1016/j.ultsonch.2011.04.004.

[224] O. J. Curnow, D. R. MacFarlane, and K. J. Walst, “Triaminocyclopropenium salts as ionic liquids,” *Chemical Communications*, vol. 47, no. 37, p. 10248, 2011, doi: 10.1039/c1cc13979g.

APPENDIX A SUPPLEMENTARY INFORMATION TO ARTICLE 1: NUMERICAL SIMULATION OF A CONTINUOUS SONOREACTOR FOR BIOMASS RESIDUES RECOVERY

Pierre Dal, Julie Kring, Dalma Schieppati, Daria C. Boffito

Submitted to Ultrasonics Sonochemistry on 7 October 2024

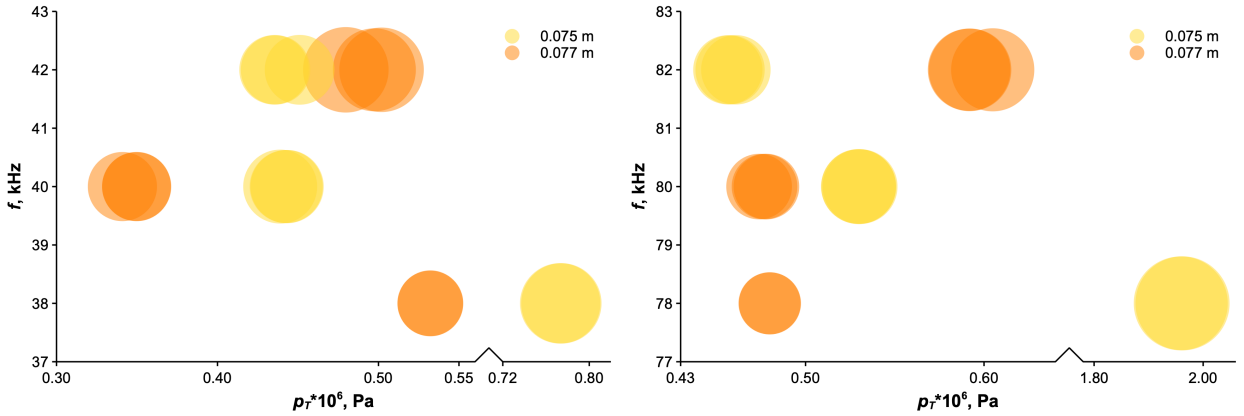

Figure A.1 Bubble plot representing the relationship between f and p_T for various h, from 38 kHz to 42 kHz on the left and from 78 kHz to 82 kHz on the right, with the bubble size representing V.

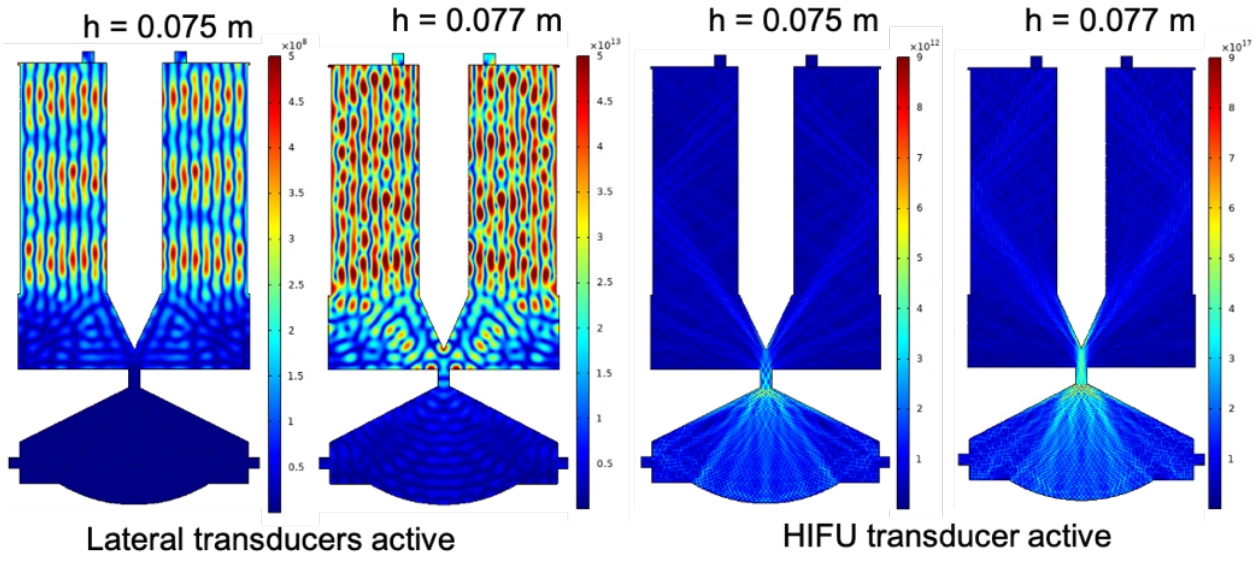

Figure A.2 Profiles of bubble number density at 78 kHz and b = 0.1 m. Comparison between h = 0.075 m and h = 0.077 m, for the lateral transducers active and for the HIFU active.

APPENDIX B SUPPLEMENTARY INFORMATION TO ARTICLE 2: ULTRASOUND-ASSISTED ESTERIFICATION OF COTTON CELLULOSE WITH LONG-CHAIN FREE FATTY ACIDS

Pierre Dal, Annelise Jean-Fulcrand, Jean-Marc Lévêque, Jean-Marie Raquez, Daria C. Boffito

Submitted to Cleaner Chemical Engineering on 7 April 2025

Contents

B.1 Cellulose sources

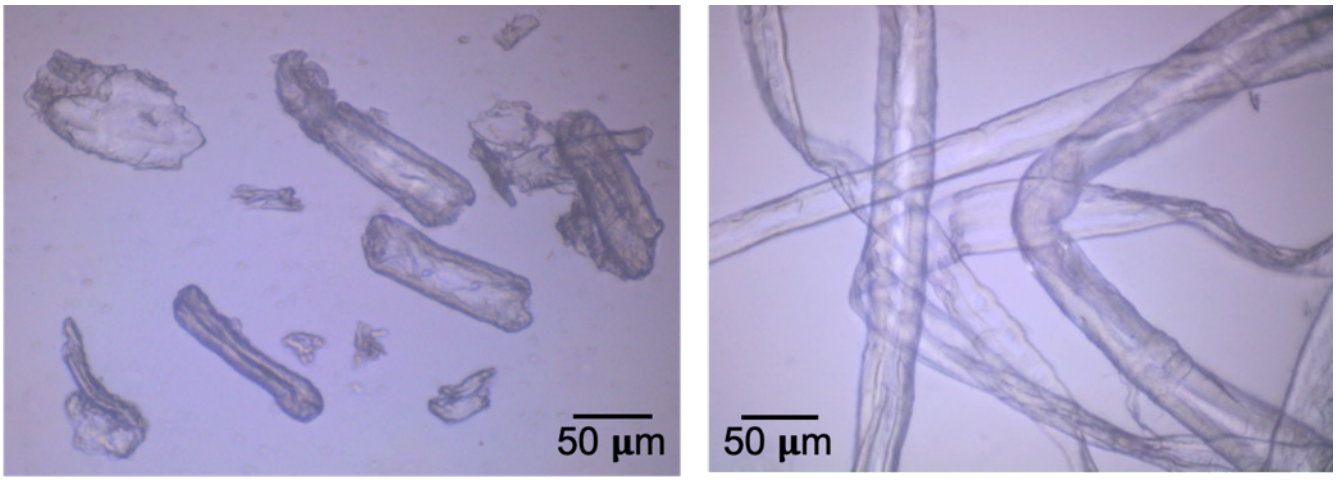

Figure B.1 Cellulose sources images, cellulose linters referred as C1 (left) and cellulose fibers referred as C2 (right).

B.2 Synthesis of cellulose esters

The conventional esterification process began with the dissolution of cellulose in a solvent. Initially, the cellulose was dried in an oven at 100 °C for 1h. For the dissolution in DMAc/LiCl, a solution of 10 mL of DMAc at 130 °C activated 0.25 g of cellulose for 2h under stirring at 1150 rpm, the mixture cooled down to 100 °C, we added 0.75 g of LiCl. When the mixture reached the room temperature, and was transparent, we added 1.77 g of p-Tos and 2.63 g of oleic acid (for a molar ratio cellulose : FFA : p-Tos of 1 : 6 : 6), each dissolved separately in 2.5 mL of DMAc. The reaction mixture was maintained in an oil bath for 24 h and 300 rpm at 40 °C, 60 °C or 80 °C, according to the set experimental conditions (Table 4.1). 200 mL of anhydrous ethanol precipitated the reaction mixture under stirring at 300 rpm for 5 min. the resulting mixture was then centrifuged at 5 000 rpm for 15 min to separate solid and liquid phases. The recovered solid phase dried at 50 °C for at least 24 h before analysis.

As a reference material, we produced cellulose esters in pyridine with oleoyl chloride as esterification agent [221]. After drying at 100 °C for 1h, we activated cellulose in pyridine (same concentration mentioned above) at 700 rpm and 100 °C for 30 min. We added oleoyl chloride (molar ratio cellulose:oleoyl chloride of 1 : 6). The esterification took place in an oil bath on a heating and stirring plate for 1 h at 100 °C [221]. The post-reaction procedure to recover the solid material was the same procedure abovementioned.

For the reactions under US, the dissolution procedure as well as esterification reaction followed the same procedures as described above, with half of the engaged quantities to meet the equipment requirements of our ultrasonic reactor, with a similar setup as described in previous work [104]. The ultrasonic liquid processor was a Vibra Cell from Sonics & Materials Inc. with a nominal output power of 500 W and 20 kHz frequency. The transducer was a piezoelectric ceramic transducer made of a Ti-6Al-V alloy and with a diameter of 13 mm. The US reactor was a glass jacketed beaker of 50 mL capacity, connected to a heating/cooling system. We immersed the probe at 1 cm depth in the mixture and it sonicated the reaction for 30 min, at various reaction temperatures and various amplitudes, according to the set experiment (Table 4.1). No matter the total volume of reaction, the concentration of cellulose, the molar ratio cellulose : FFA : p-Tos, and the ratio of anhydrous ethanol : reaction volume were unchanged. The washing procedure was the same as described above. The oven dried the flocculated solids at 50 °C for at least 24 h before

analysis. We did all experiments in duplicate. We determined the uncertainty on the *DS* measuring the *DS* four times on the same sample.

B.3 Determination of the *DS* by ^{1}H NMR

For the ^{1}H NMR measurements, the repetition time was 15 s, acquisition time 1.2 s, spectrum range 50 ppm (20 000 Hz) and impulsion 8 µs (90°). The rotational speed was 3.5 kHz. The analysis included a spin echo sequence with a period of 2.2 ms, synchronized with the rotational speed, in order to attenuate the cellulose signal. We prepared the rotor (4) inserting 10 to 20 mg of sample and 30 µL of solution of 0.35 mg of standard sodium trimethylsilylpropanesulfonate (DSS) in dimethylsulfoxide (DMSO). To make sure we have a homogeneous sample, we did this sample preparation in 3 steps, mixing the sample between each step. We let the rotor settle for 15 minutes for the solvent to impregnate the powder sample. For the degree of substitution (*DS*) determination, we normalized the peaks with DSS as a reference. We set the area of the DSS peak at 100. The calculation of the *DS* followed these steps:

1. Determination of the number of moles of DSS based on its weight, density and molecular weight;
2. Determination of the number of moles and weight of each species based on their peak's area and the number of moles of DSS;
3. Determination of the weight of cellulose by difference;
4. Determination of the DS by the ratio of oleic acid moles to cellulose moles.

B.4 Mathematical model and governing equations

B.4.1 Equations for acoustic pressure

The Helmholtz equation represents the steady-state form of the wave equation. We assumed that the fluid was homogeneous and incompressible, the sound waves exhibited linear behavior, and the shear stress could be neglected [106]. Additionally, we considered the acoustic pressure to have a harmonic time dependence, expressed as $p(r,t) = p(r).e^{i\omega t}$ [129], where $\omega = 2\pi f$ is the wave's angular frequency in rad s^{-1}, with f the ultrasonic frequency in Hz. COMSOL was employed to solve the Helmholtz equation (Eq. (B.1)), for the acoustic pressure distribution in the liquid:

$$\frac{1}{\rho}\nabla^2 p + \frac{\omega^2}{\rho c^2} p = 0 \qquad \text{(B. 1)}$$

As highlighted in Section 4.1 of the manuscript, the application of US in liquids at specific intensities and frequencies induces acoustic cavitation. This process leads to the formation and accumulation of bubbles at the tip of the ultrasound probe, which in turn attenuates the propagation of sound waves. Wijngaarden derived equations that describe the one-dimensional propagation of sound waves in a mixture of liquid and bubbles [130]. Building on the continuity equation and Wijngaarden's work, Commander and Prosperetti developed a model to characterize sound wave propagation in bubble-containing liquids. Their model, a modified version of the Helmholtz equation, incorporates the damping effects of bubbles, which result from viscous, thermal, and acoustic mechanisms (factor *b* defined in Eq. (B.4)). However, they noted that their model is not applicable in cases involving significant bubble resonance effects but is effective for bubble volume fractions up to 2% [113]. The modified Helmholtz equation they proposed is:

$$\nabla^2 p + k_m^2 p = 0 \tag{B.2}$$

where k_m is the complex wave number in m^{-1} in the fluid and bubbles mixture. For a monodisperse bubble distribution, k_m^2 is [112]:

$$k_m^2 = \frac{\omega^2}{c^2}\left(1 + \frac{4\pi c^2 n_b R_0}{\omega_0^2 - \omega^2 + 2ib\omega}\right) \tag{B.3}$$

Here, n_b represents the number of bubbles per unit volume in m^{-3}, R_0 is the initial radius of a bubble in m, and ω_0 denotes the resonant angular frequency of the bubbles in rad s^{-1}, i refers to the imaginary unit, while b is the damping factor, accounting for viscous, thermal, and acoustic effects [113]:

$$b = \frac{2\mu}{\rho R_{eq}^2} + \frac{p_0}{2\rho\omega R_{eq}^2} Im\Phi + \frac{\omega^2 R_{eq}}{2c} \tag{B.4}$$

where, p_0 represents the undisturbed pressure at the bubble's position in Pa, which is given by $p_{atm} + (2\sigma/R_{eq})$, σ is the surface tension of the liquid in N m^{-1}. R_{eq} denotes the equilibrium radius of the bubbles in m, accounting for effects such as coalescence and rectified diffusion. μ is the dynamic viscosity of the liquid in Pa s, and Φ is a complex dimensionless parameter. The resonant angular frequency of the bubbles, ω_0 in Eq. (B.3) is expressed as:

$$\omega_0^2 = \frac{p_0}{\rho R_{eq}^2}\left(Re\Phi - \frac{2\sigma}{p_0 R_{eq}}\right) \tag{B.5}$$

The parameter Φ in Eq. (B.4) and in Eq. (B.5) is a function of the specific heat ratio of the gas inside bubbles (γ), and χ [131]:

$$\Phi = \frac{3\gamma}{1 - 3(\gamma - 1)i\chi\left[\left(\frac{i}{\chi}\right)^{\frac{1}{2}}\coth\left(\frac{i}{\chi}\right)^{\frac{1}{2}} - 1\right]} \tag{B.6}$$

χ is expressed as:

$$\chi = D/\omega R_{eq}^2 \tag{B.7}$$

with D the thermal diffusivity of the gas. The bubbles number density n_b in Eq. (B.3) depends on β, the volume of the gas fraction within the bubbles in the reactor with respect to the total volume:

$$n_b = \frac{3\beta}{4\pi R_0^3} \tag{B.8}$$

B.4.2 Equations for acoustic cavitation zones

We assumed that bubbles grow and eventually collapse, generating cavitation when the pressure exceeds the threshold pressure for cavitation, p_c [133]. This cavitation threshold is influenced by the properties of the sonicated fluid, its temperature and gas content, and is described by:

$$p_c = p_0 - p_v + \frac{\frac{2}{3\sqrt{3}}\sqrt[3]{\left(\frac{2\sigma}{R_{eq}}\right)^2}}{\sqrt{p_0 - p_v + \frac{2\sigma}{R_{eq}}}} \tag{B.9}$$

where p_v is the vapour pressure of the sonicated liquid in Pa. To visualize the cavitation zones within the reactor, we set the acoustic pressure to p_c whenever the pressure exceeded this threshold value.

B.4.3 Equations for acoustic streaming

Acoustic streaming refers to the fluid motion induced by pressure fluctuations generated by US. Within the frequency range of 20 kHz to 20 MHz, and at power levels exceeding 0.0004 W, the acoustic streaming is a turbulent flow [222]. To determine the streaming velocity (u), COMSOL solved the Navier-Stokes equation:

$$\rho\left(\frac{\delta\vec{u}}{\delta t}+\vec{u}\cdot\nabla\vec{u}\right)=-\nabla\vec{p}+\mu\nabla^2\vec{u}+\vec{F} \quad (B.10)$$

With *F* the volumetric force acting on the reaction. Indeed, origins of the acoustic streaming are the Bjerknes forces acting on bubbles in the acoustic field [111].

$$F=-\beta\cdot\nabla|p| \quad (B.11)$$

We replaced Eq. (B.11)**Erreur! Source du renvoi introuvable.** into Eq. (B.10) to calculate the fluid velocity and map the flow pattern. The pressure calculated from Eq. (B.2) directs *F*.

B.4.4 Assumptions of the model

For Eq. (B.1), Eq. (B.2) and Eq. (B.10), we assume:

1. The fluid is incompressible and Newtonian.
2. The bubble to liquid volume ratio is low so we compute the system as a single-phase fluid [113].
3. The properties of the sonicated fluid are independent of the temperature and bubble volume fraction.
4. The bubble size R_0 was predefined in our model. Brotchie et al. and Dehane et al. observed that an increase in acoustic frequency reduced the mean size of cavitation bubbles, whereas an increase in acoustic power led to larger cavitation bubbles [137], [138]. Servant et al. and Dähnke et al. assumed bubble radii ranged between $5\cdot10^{-6}$ m and $3\cdot10^{-3}$ m [139], [140]. Similarly, Pandit et al. considered bubble radii between 2 μm and 50 μm for acoustic frequencies ranging from 10 kHz to 80 kHz [141]. For our study, we selected a bubble equilibrium radius of 250 μm at an US frequency of 20 kHz, consistent with the order of magnitude predicted by Minnaert's equation: $R_{eq}\approx 3/f$ [137]. Under acoustic excitation and coalescence, cavitation bubbles grow to approximately 50 times their initial radius R_0 [142]. We set R_0 to 5 μm for an US frequency of 20 kHz.
5. The bubble concentration was assumed to be homogeneously distributed throughout the reactor, with β ranging from 10^{-4} to 10^{-1}. When $\beta > 10^{-1}$, cavitation bubbles attenuate acoustic waves to the point of complete scattering [112]. For our calculations, we followed Dähnke et al. by assuming that the bubble volume fraction linearly depends on the acoustic pressure amplitude in the fluid, expressed as $\beta = K\cdot p$ where K is a constant [139].

Jamshidi et al. validated this model in water, determining $K = 2 \cdot 10^{-9}$ [112]. We adopted the same value for K in our simulations.

6. The US transducer generates an acoustic pressure amplitude that is maximal at the center of the transducer and decreases as the distance from the center increases [133]. This reduction in pressure amplitude follows a Gaussian function.

B.5 Simulation

COMSOL Multiphysics 6.1 solved the equations presented in Section 4.4, determining the acoustic pressure distribution within the sonoreactor, both with and without bubble-induced attenuation, as well as the acoustic streaming velocity. The simulations were conducted in 2D axisymmetric mode and followed three sequential steps:

1. Using the COMSOL Acoustic Module – Pressure Acoustics, Eq. (B.1) was solved in the Frequency Domain to simulate a continuous wave. The simulation accounted for the attenuation of the acoustic pressure (α), which depends on the fluid's properties [106]. The attenuation coefficient was calculated using:

$$\alpha = \frac{8\mu\pi^2 f^2}{3\rho c^3} \tag{B.12}$$

This step provided the acoustic pressure distribution in the absence of cavitation bubbles, serving as the starting point for step 2.

2. We included the attenuation caused by cavitation bubbles implementing Eq. (B.2) through the Stabilized Convection-Diffusion Equation. Parameters defined in Eq. (B.3) to Eq. (B.8) were included in this step. The software calculated β using the acoustic pressure obtained in step 1. Subsequently, it solved Eq. (B.8) and Eq. (B.3) to determine n_b and k_m. The modified Helmholtz equation (Eq. (B.2)) was solved until steady state.
3. Using the COMSOL turbulent flow k–ε Module, the Navier-Stokes equation was solved, incorporating the acoustic pressure from step 2. This step calculated the acoustic streaming velocity within the sonoreactor.

B.5.1 Geometry

The reactor is a 50 mL thermostatic glass beaker, of internal diameter 3.5 cm and height 6.8 cm. The ultrasound probe is made of a titanium alloy Ti-6Al-V, and has a diameter of 1.3 cm. We

maintained the immersion depth constant at 1 cm vertically. The ultrasonic generator operates at 20 kHz. The sonicated liquid is the simulation domain, whose dimensions vary with the liquid volume.

B.5.2 Boundary conditions

Jamshidi et al. and Fang et al. considered the reactor's walls and the probe's walls completely rigid, meaning that they reflect the sound waves perfectly ($\frac{\delta p}{\delta x} = 0$ for $x = 0$), and the liquid-air boundary as soft, meaning that the acoustic pressure vanishes ($p = 0$) [111], [112]. However, US waves reflect with a deviation of acoustic impedance (Z). Z is product of the material's density and speed of sound. We applied the following boundary conditions (Figure B.2):

1. At the boundary liquid-glass, Z = 2230 kg m^{-3}·5640 m s^{-1}, for steps 1 and 2. For step 3, we applied a no-slip boundary condition.

2. At the boundary liquid-air Z = 1.2 kg m^{-3}·343 m s^{-1}, for steps 1 and 2. For step 3, we applied a pressure outlet, with a pressure of 0 Pa.

3. At the boundary liquid-probe Z = 4470 kg m^{-3}·4987 m s^{-1}, for steps 1 and 2. For step 3, we applied a slip boundary condition.

4. At the tip of the probe, we set a pressure amplitude p_a for steps 1 and 2:

$$p_a = \sqrt{\frac{2Pc\rho}{\pi R^2}} \tag{B.13}$$

With P being the US power delivered to the liquid, calculated by calorimetric calibration. R is the radius of the probe. For step 3, p_a is the pressure inlet with velocity directed toward the liquid. The turbulence length scale is the size of the vortices in the turbulent flow, which we set at 0.07·R [223].

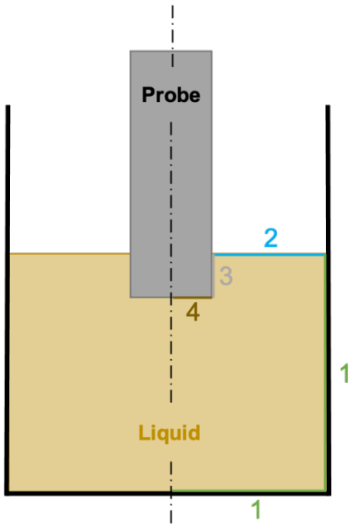

Figure B.2 Sonochemical reactor with simulation domain and boundaries.

B.5.3 Mesh

COMSOL Multiphysics generated automatically a 2D computational mesh, composed of triangles and quadrilaterals (6371 triangles and 1090 quadrilaterals for 32.2 mL). We made sure we had at least 8 mesh elements per wavelength [106]. At 20 kHz, the wavelength in water is 7.5 cm, and in cellulose solutions, the wavelength is between 7.5 cm and 7.7 cm. We chose a *normal mesh* size with a maximum element size of 0.09 cm, a minimum element size of 0.004 cm, a curvature factor of 0.3, and a growth rate of 1.15.

B.6 Thermal analysis

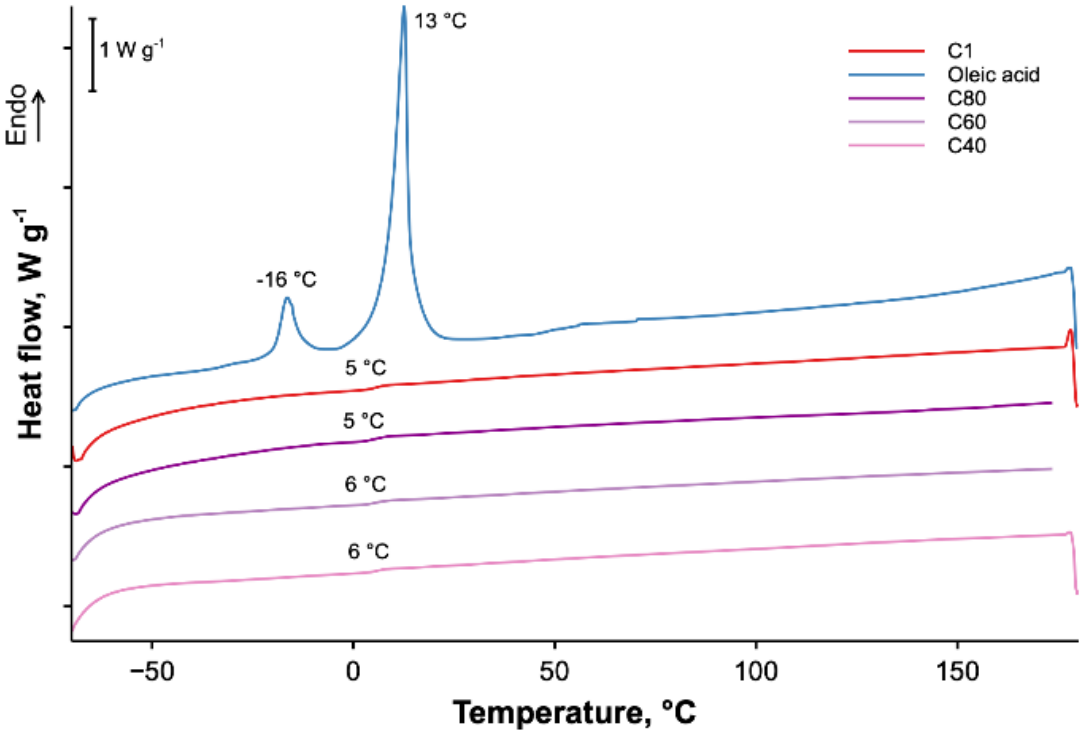

Figure B.3 DSC curves of the reference cellulose C1 and oleic acid, and the cellulose esters produced at various temperatures.

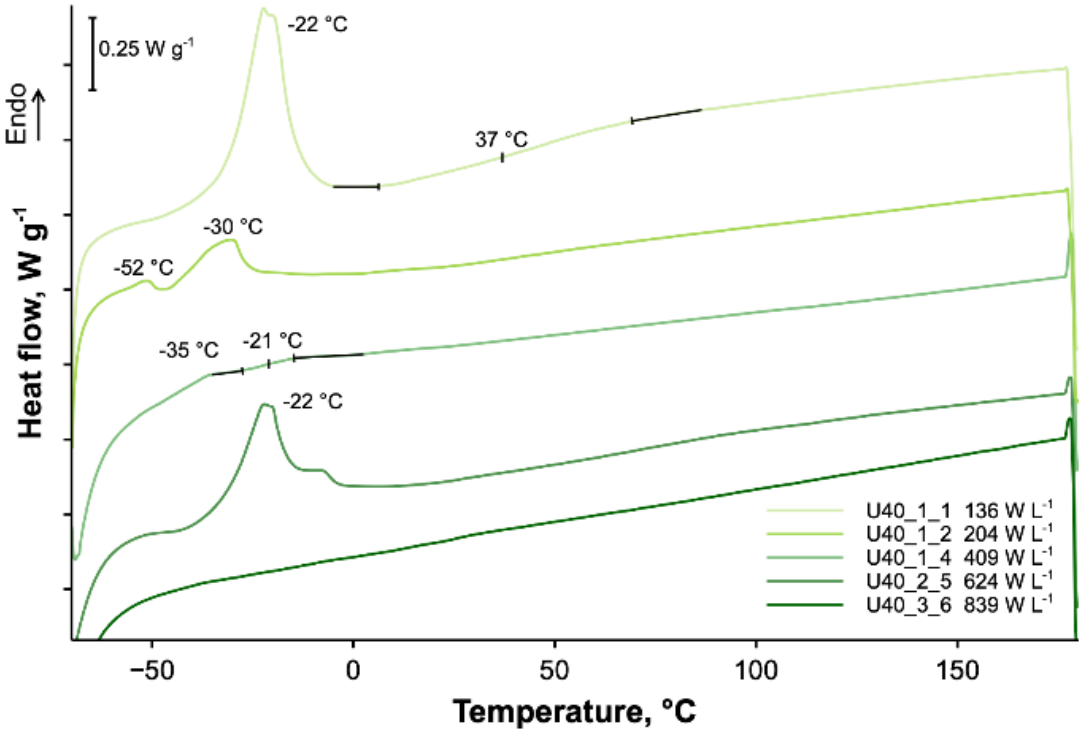

Figure B.4 DSC curves of cellulose esters produced at 40 ˚C at various US power densities.

APPENDIX C SUPPLEMENTARY INFORMATION TO ARTICLE 3: ULTRASOUND-ASSISTED ESTERIFICATION OF COTTON CELLULOSE IN IONIC LIQUIDS

Pierre Dal, Owen J. Curnow, Jean-Marie Raquez, Daria C. Boffito

Submitted to Carbohydrate Polymers on 14 May 2025

Contents

C.1 Synthesis of tris(dibutylamino)cyclopropenium chloride ($[C_3(NBu_2)_3]Cl$) salt

C.1.1 Materials

All chemicals and solvents have been used as received unless specified: dibutylamine (≥ 99%, Merck), dichloromethane (≥ 99.8%, Fisher), pentachlorocyclopropane (Biosynth), acetone (≥ 99.8%, Fisher), Triethylamine (≥ 99%, Merck).

C.1.2 Synthesis

A 250 mL round bottom flask with 40.5 mL of dibutylamine (Bu) and 100 mL of dichloromethane was cooled in an ice bath and stirred at 350 rpm. After heating the reaction mixture to ambient temperature, pentachlorocyclopropane (3.85 mL) was added dropwise (Figure C.1). The temperature was then increased to 60 °C for 4 h. The crude reaction mixture was washed five times with 20 mL of acetone, which were added to the reaction flask, stirred, and then filtered through a silica filter. Finally, the solid part, the unreacted Bu, was washed with 20 mL of acetone. The solvents were then removed from the liquid mixture by a rotary evaporator. Deionized water (200 mL) was then added, followed by four washes with 50 mL of petroleum ether to remove unreacted amine. The product was then extracted four times with 50 mL of chloroform to give 30 mmol (67% yield) of a yellowish liquid [201], [224]. The purity of $[C_3(NBu_2)_3]Cl$ was verified by ^{1}H-NMR (Figure C.2) in deuterated chloroform and eventually washed with aqueous hydrochloric acid. ^{1}H

NMR (500 MHz, $CDCl_3$): δ 3.33 (t, $^3J_{HH}$= 8.1 Hz, 12H, 3-H_2), 1.61 (m, 12H, 4-H_2), 1.33 (m, 12H, 5-H_2), 0.96 (t, $^3J_{HH}$ = 7.3 Hz, 18H, 6-H_3).

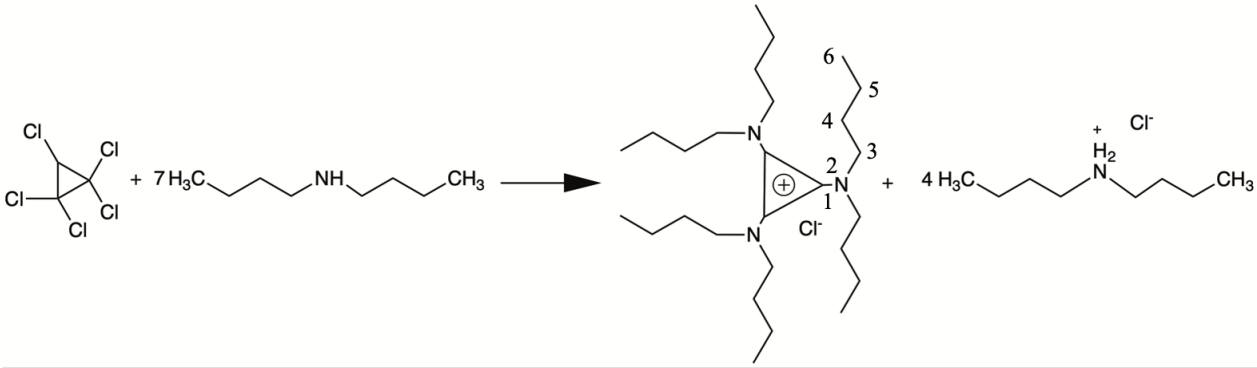

Figure C.1 Synthesis of the $[C_3(NBu_2)_3]Cl$ salt (the numbering refers to the ^{1}H-NMR assignments, ^{1}H-NMR spectrum in Figure C.2).

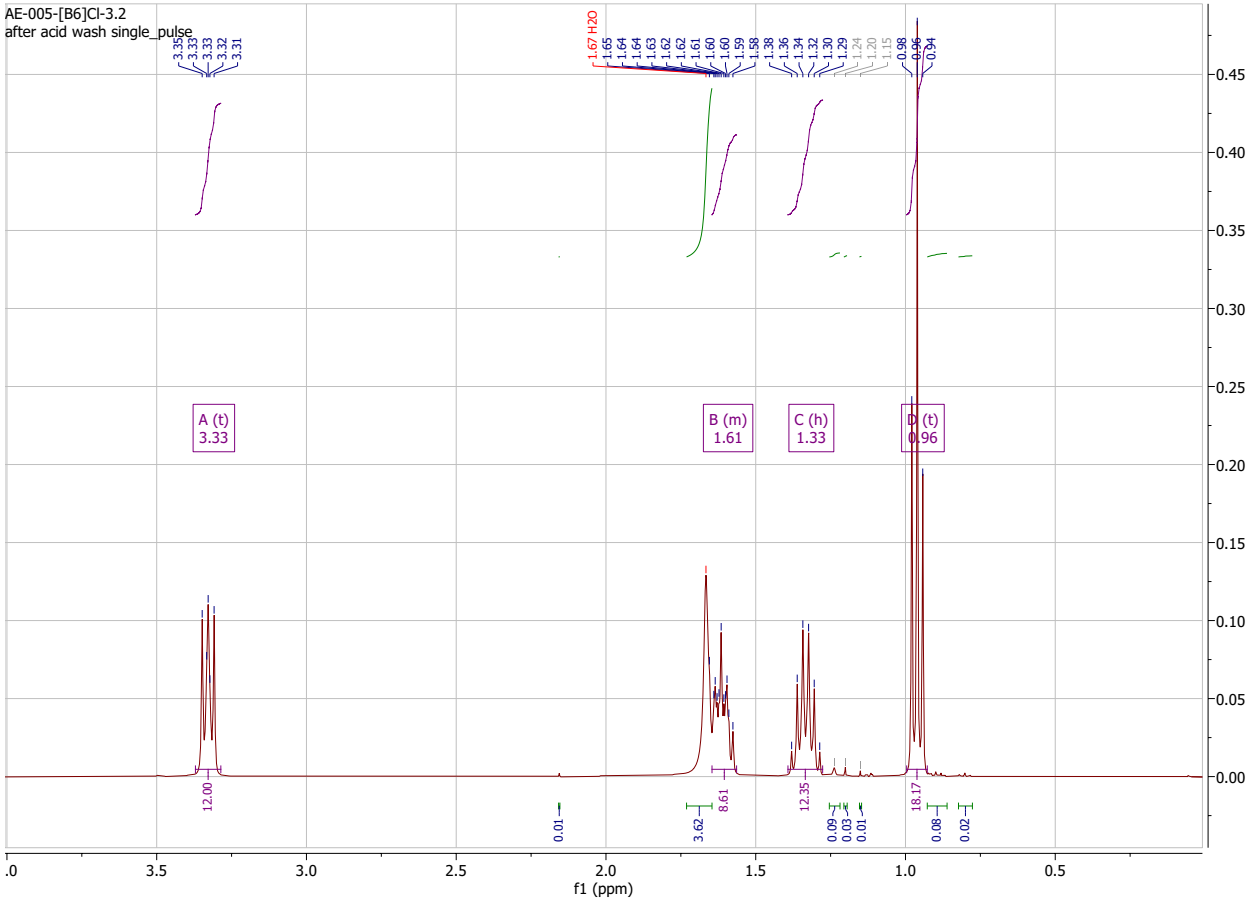

Figure C.2 ^{1}H-NMR spectra of $[C_3(NBu_2)_3]Cl$ salt.

C.2 Chemical structure of cellulose esters

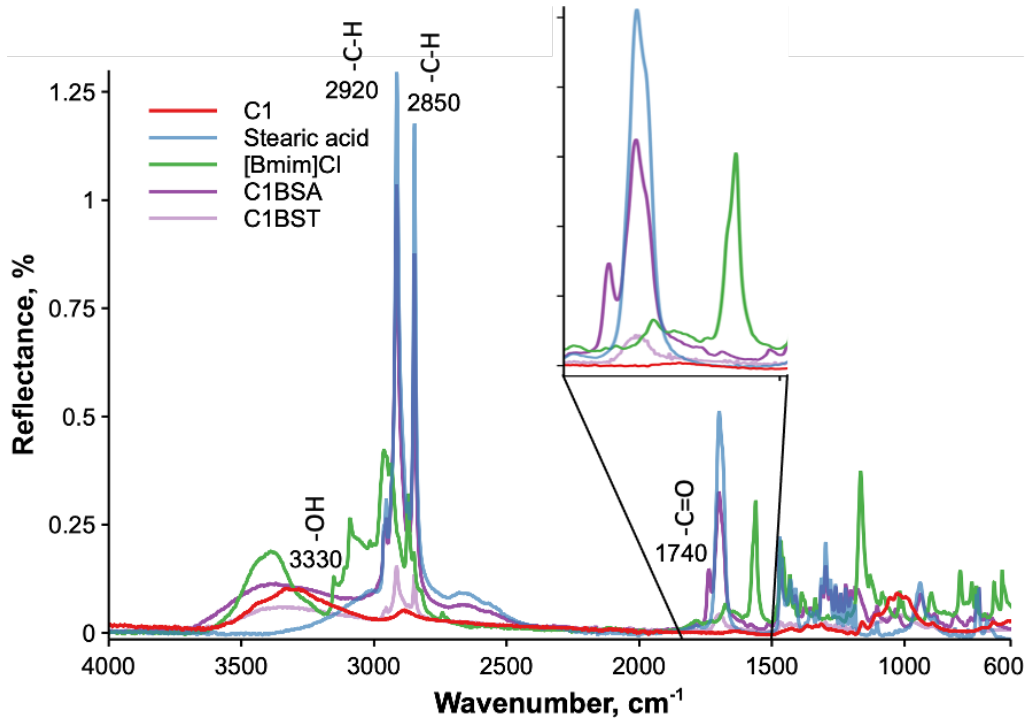

Figure C.3 FTIR spectra of cellulose esters produced in [Bmim]Cl with stearic acid and various catalysts. Labels are the wavenumber (in cm^{-1}) of the associated peak.

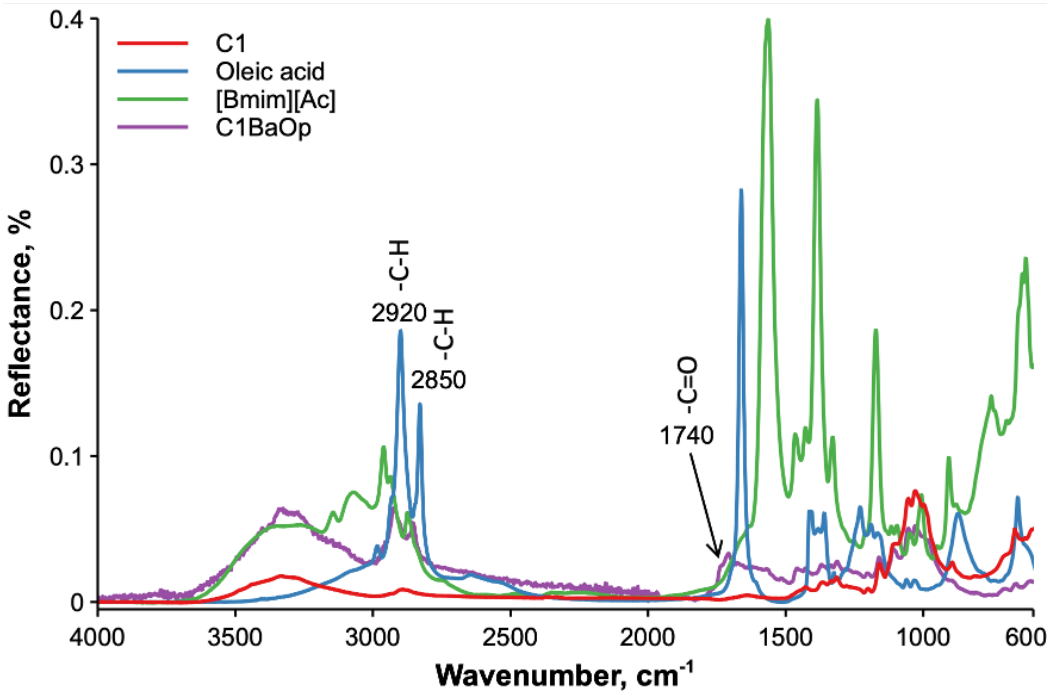

Figure C.4 FTIR spectra of cellulose esters produced in [Bmim][Ac] with oleic acid. Labels are the wavenumber (in cm^{-1}) of the associated peak.

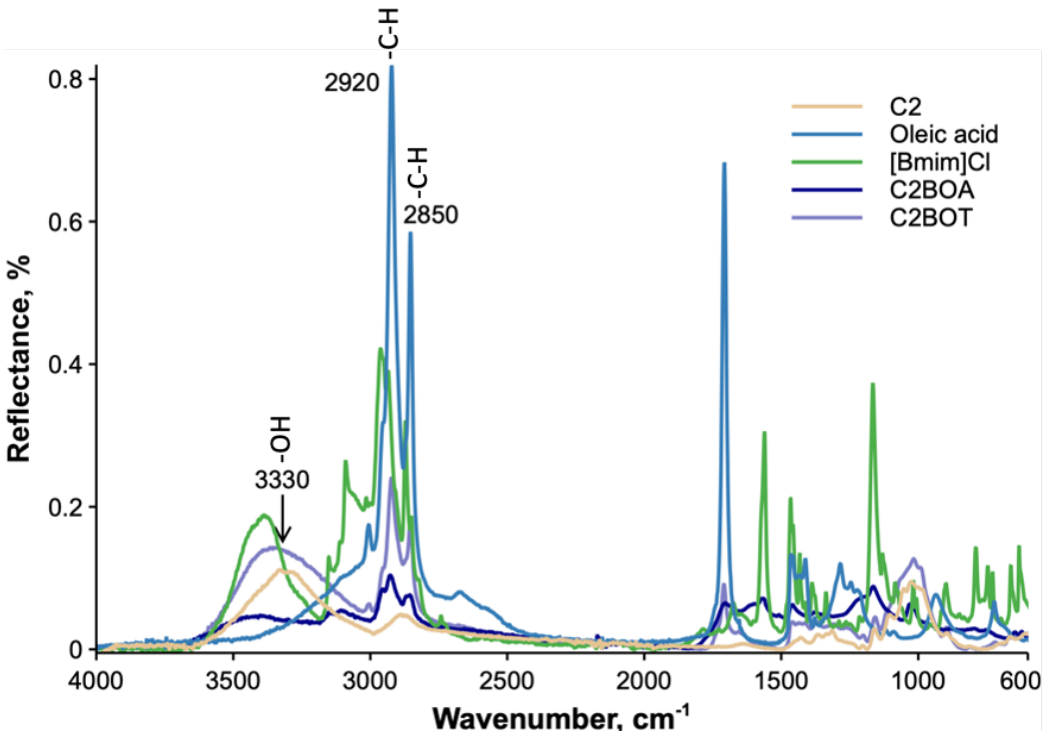

Figure C.5 FTIR spectra of cellulose esters produced from cellulose fibers, in [Bmim]Cl with oleic acid and various catalysts. Labels are the wavenumber (in cm^{-1}) of the associated peak.

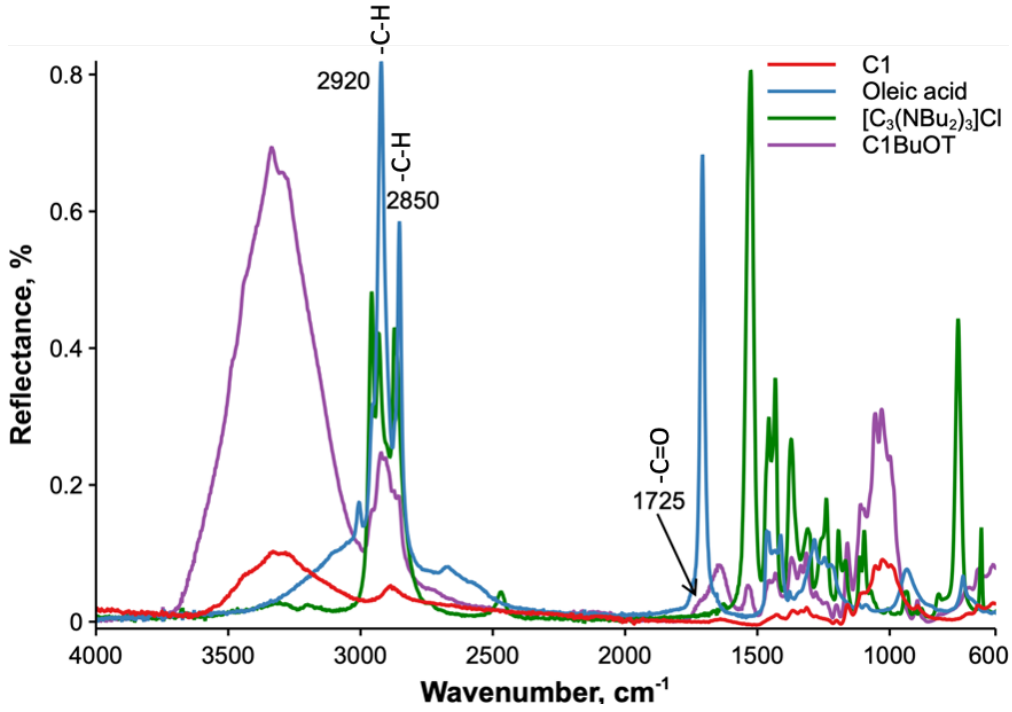

Figure C.6 FTIR spectra of cellulose esters produced in $[C_3(NBu_2)_3]Cl$ with oleic acid. Labels are the wavenumber (in cm^{-1}) of the associated peak.

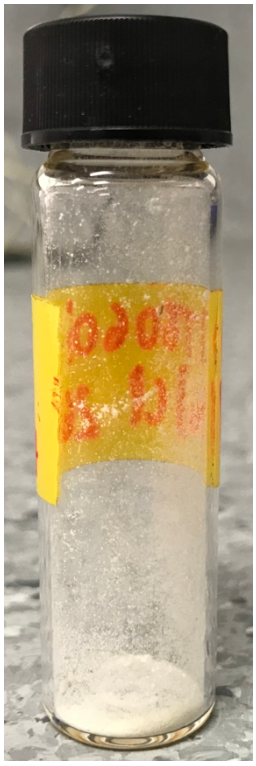

Figure C.7 Ester's sample C1BuOT produced in $[C_3(NBu_2)_3]Cl$ with oleic acid.

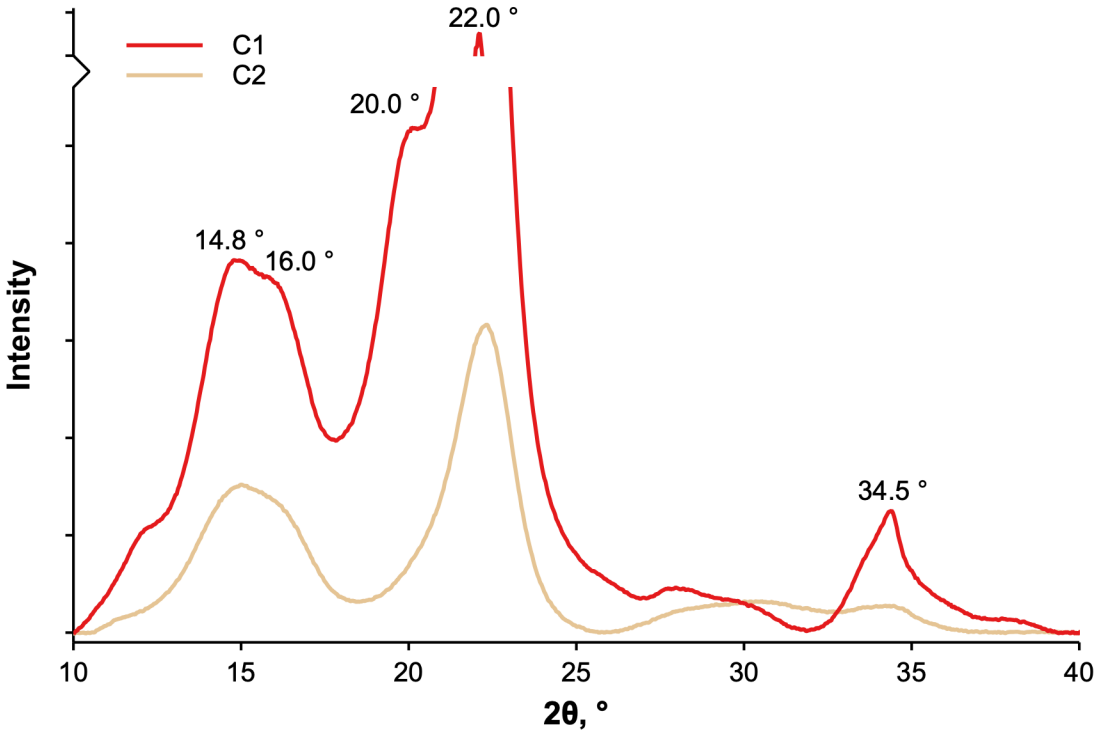

Figure C.8 XRD diffractogram of unmodified celluloses C1 and C2.

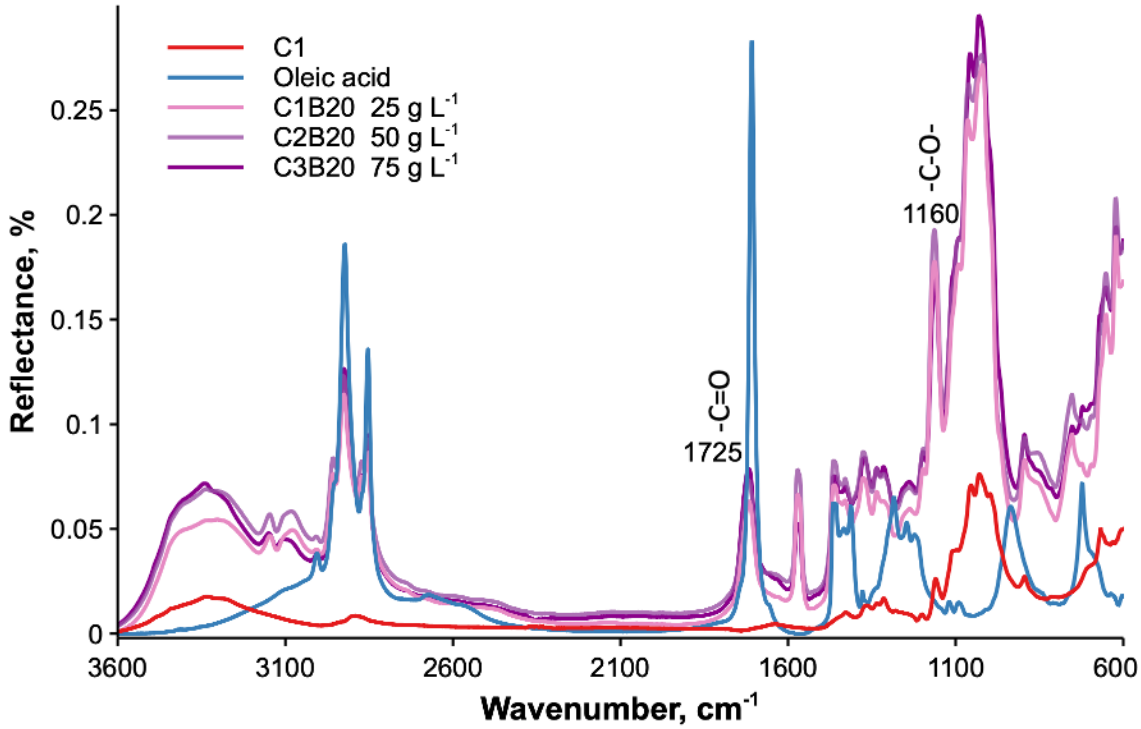

Figure C.9 FTIR spectra of cellulose esters produced with US and various concentrations of cellulose. Labels are the wavenumber (in cm^{-1}) of the associated peak.

C.3 Thermal analysis

Table C.1 T_g of DoE2. Some samples show two glass transitions.

Experiment	*DS*	T_g, °C	
		1	2
C1B	0.73 ± 0.05	-21	36
C1Ba	0.04 ± 0.003	-9	-
C1B_30	0.13 ± 0.009	-	-
C1Ba_30	0.0	-	-
C1B20_80	0.83 ± 0.06	-	-
C1B20	0.92 ± 0.06	60	-
C2B20	1.05 ± 0.07	-10	-
C3B20	0.33 ± 0.02	-	-
C3B30	0.34 ± 0.02	-8	-
C3B40	0.41 ± 0.03	-	-
R1B20	1.09 ± 0.08	125	-
R1B40	2.34 ± 0.16	21	117
C1Ba20	0.16 ± 0.01	35	115
C1Ba20_80	1.62 ± 0.11	36	-

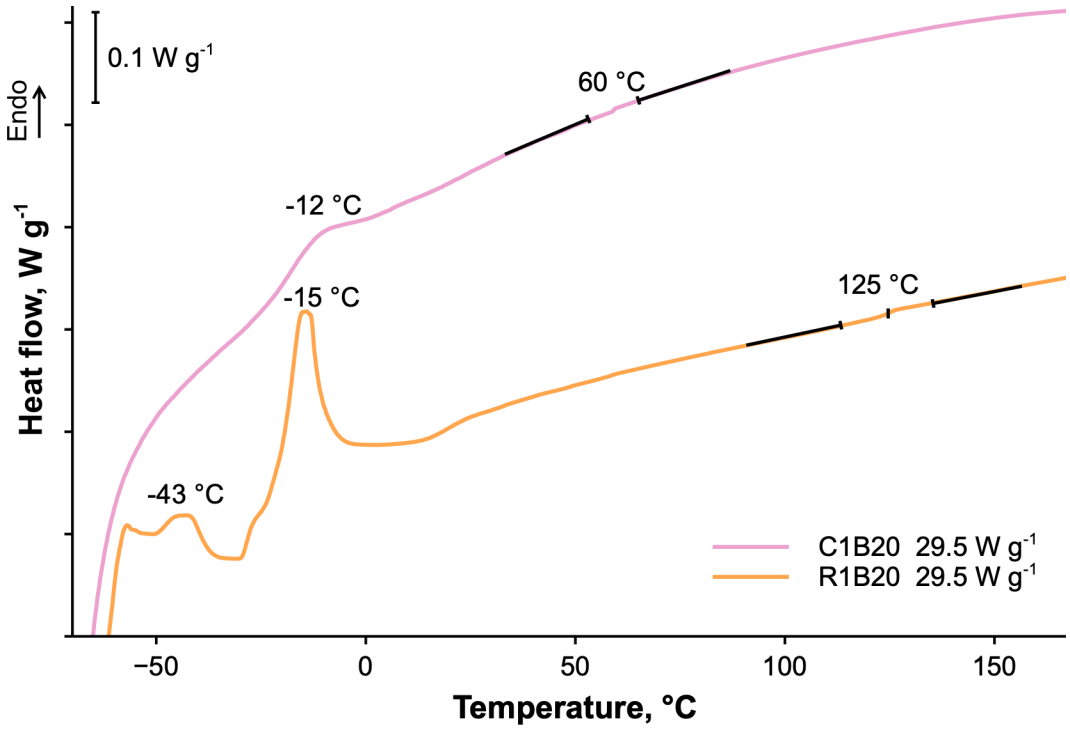

Figure C.10 DSC curves of cellulose esters produced in [Bmim]Cl/DMSO at 40 °C and 29.5 W g^{-1}, from C1 (C1B20) and C2 (R1B20).

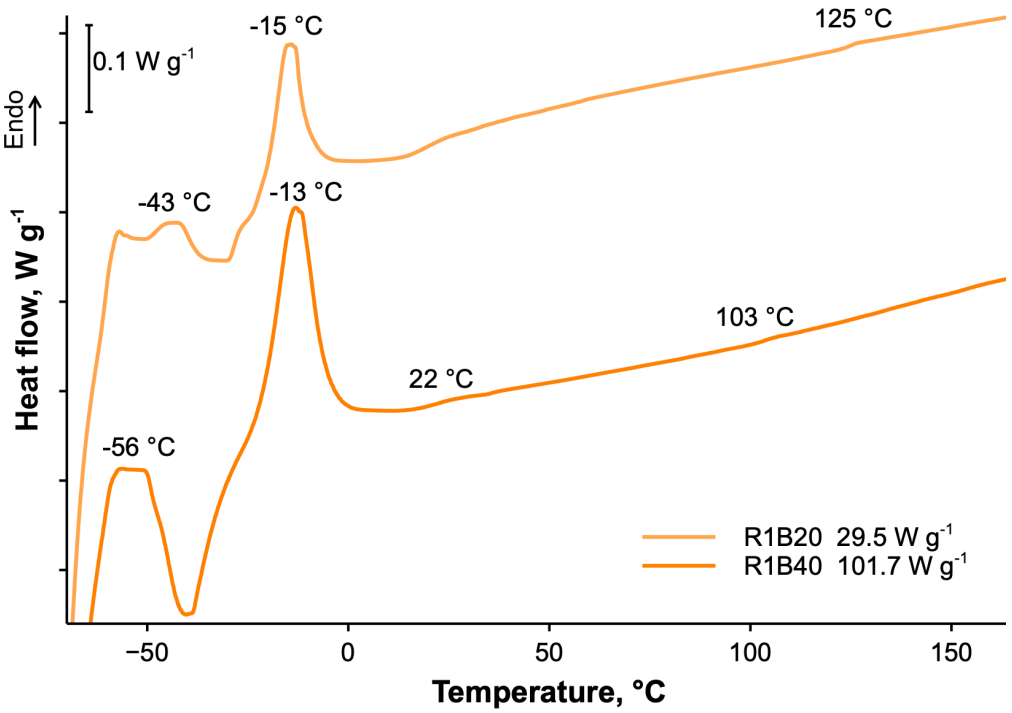

Figure C.11 DSC curves of cellulose esters produced from C2 in [Bmim]Cl/DMSO at 25 g L^{-1}, at various US *PD*.

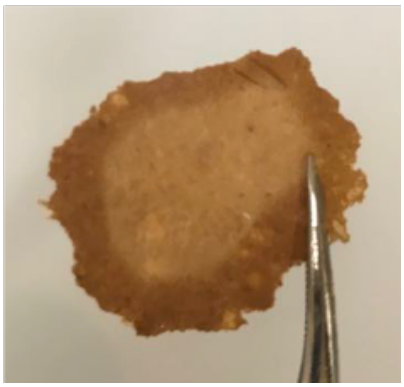

Figure C.12 Aspect of pressed sample C3B20.

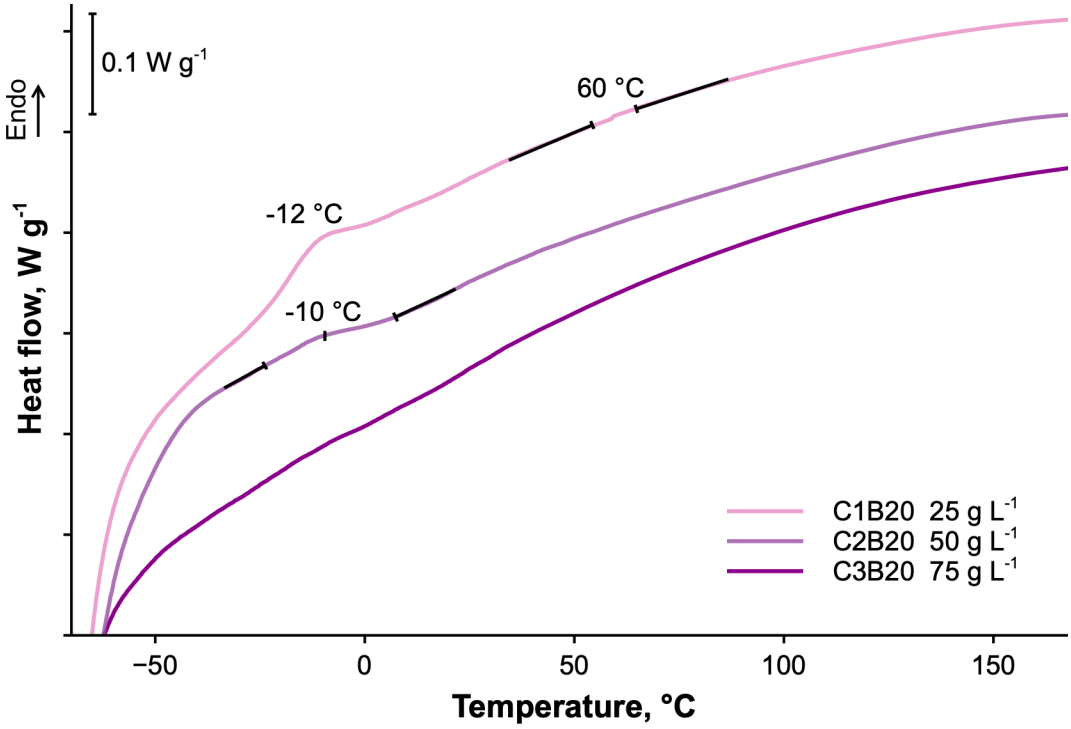

Figure C.13 DSC curves of cellulose esters produced in [Bmim]Cl/DMSO at various cellulose concentrations.

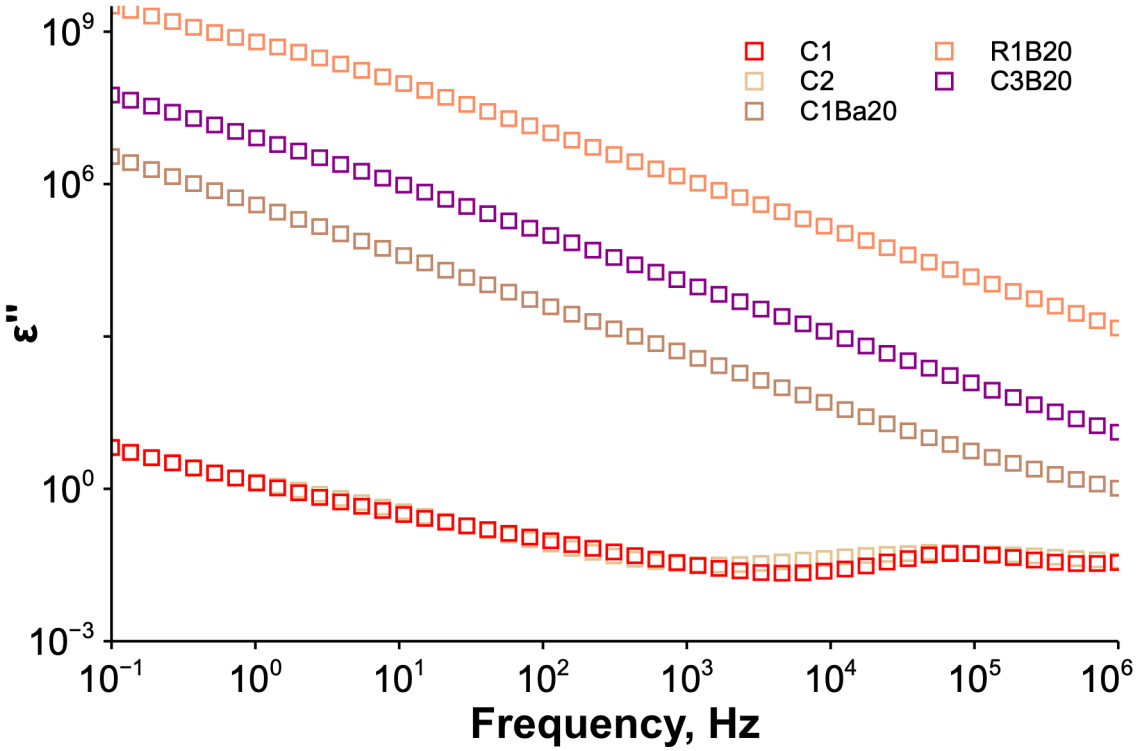

Figure C.14 Dielectric loss as a function of frequency at 120 °C for unmodified celluloses and pressed samples C1Ba20, R1B20 and C3B20.

Table C.2 Parameters of regression lines for unmodified cellulose and esters samples (esters samples have two distinct regression lines).

Sample	Slope	Intersection	R^2
C1	415	-8.56	0.857
C2	355	-8.55	0.987
C3B20	261	-5.11	0.957
	17.9	-2.56	0.856
R1B20	63.4	-3.48	0.978
	8.09	-1.88	0.919
C1Ba20	128	-2.53	0.987
	8.19	-0.163	0.691